TURBULENT ACIDIC DISCHARGES INTO SEAWATER

Hendrik Ülpre

A thesis submitted for the degree of Doctor of Philosophy

April 2015

Declaration

I, Hendrik Ülpre confirm that the work presented in this thesis is my own. Where information has been derived from other sources, I confirm that this has been indicated in the thesis.

Abstract

This thesis analyses the chemistry and physics behind acidic jets and plumes. The research was motivated from the discussions between industry and regulatory bodies concerning the dispersion of highly acidic discharges from exhaust gas scrubbers on ships into seawater. The industrial problem is simplified in an analytical model for acidic jets and plumes, which is then validated through an experimental study. The analytical model allows for the construction of an optimisation tool that considers the acidity of the discharge, the alkalinity of local seawater and the required scrubber flow rate to propose optimal discharge pipe configurations. This tool can be used for designing discharge pipe configurations in compliance with regulation MEPC 59/24/Add.1 Annex 9.

The analytical model was then extended to also take into account the effects of ambient flow and buoyancy on the discharge trajectory. Existing regulatory compliance tests for scrubber discharges assume that no deflection occurs, however, the experimental study shows that an offset of one jet radius leads to an overestimation of pH recovery by one unit. Simplified expressions are developed to improve the accuracy of regulatory compliance tests by taking into account the effects of buoyancy and ambient flow.

A general purpose computational fluid dynamics code was written to study the dispersion of contaminants in the wake of a ship. The study suggests that rapid dilution occurs in the near field as a result of the turbulence generated by propulsion, and further dilution occurs more slowly through the widening of the ship wake. Different velocity profiles are generated when the ship is either decelerating, accelerating or moving at a steady pace, but the widening of the wake is relatively insensitive to these factors in the near field.

Contents

List of figures

List of tables

List of symbols

A^- = acid ion

A_W = cross-sectional area of the wake

B = buoyancy flux

B_0 = initial buoyancy flux

b = jet/plume radius

b_0 = initial jet/plume radius

$\tilde{B} = B/B_0$ = dimensionless buoyancy flux

$\bar{C}$ = average dye concentration

C_a = acid concentration in a package of fluid

C_a^0 = initial acid concentration in a package of fluid

C_b = alkali concentration in a package of fluid

C_b^0 = initial alkali concentration in a package of fluid

C_{max} = maximum concentration of contaminant

$\mathcal{D}$ = dilution of acid

$\mathcal{D}_N$ = dilution for neutralisation

$\mathcal{D}_{onboard}$ = dilution onboard the ship

$\mathcal{D}_{jet}$ = dilution offboard the ship

$\mathcal{D}_T$ = total dilution onboard and offboard the ship

D = characteristic lengthscale, *e.g.* nozzle diameter, ship width

F_D = drag force

F_F = form drag

F_T = thrust force

F_W = wave drag

Fr = Froude number

g = gravity

H^+ = hydrogen ion

$[H^+]$ = concentration of hydrogen ions

K_a = acid dissociation constant

K_b = alkali dissociation constant

K_w = water dissociation constant

L = length of the experimental tank or the ship

L_{exp} = experimentally useful length of the tank

M = momentum flux

M_0 = initial momentum flux

M^+ = alkaline ion

$[M^+]$ = concentration of alkaline ions

$\tilde{M} = M/M_0$ = dimensionless momentum flux

P = pressure

P_v = cavitation pressure

P_a = cavitation pressure

Q = volume flux

$\tilde{Q} = Q/Q_0$ = dimensionless volume flux

Q_w = additional volume flux of seawater added for dilution

Re = Reynolds number

Re_c = critical Reynolds number for a fully turbulent flow

Re_T = turbulent Reynolds number

Re_W = wake Reynolds number

$\tilde{t} = \frac{2\alpha M_0 t}{Q_0 b_0}$ = dimensionless residence time

t_{local} = local timescale for the jet/plume

u_1 = horizontal velocity

u_2 = vertical velocity

u_d = wake velocity deficit

u_m = maximum wake velocity deficit

u_x = local velocity

U_∞ = free stream velocity

Q_0 = initial volume flux

w = jet/plume velocity

w_E = entrainment velocity

x_1 = distance downstream from a ship

x_2 = distance tangential to the ship travel direction

Y_W = wake width

$Y_{50\%}$ = 50% of the maximum value of vorticity in across the wake

z = jet/plume distance from the source

$\tilde{z} = 2\alpha z/b_0$ dimensionless jet/plume distance

$\tilde{z}_N$ dimensionless jet/plume neutralisation distance

α_E = entrainment coefficient

Γ = jet/plume parameter

Γ_0 = jet/plume source parameter

$\Delta\rho$ = density contrast

μ = dynamic viscosity

ν = kinematic viscosity

ν_T = turbulent viscosity

ρ = density

ρ_0 = initial density

ω = vorticity

Chapter 1

Introduction

1.1 Introduction

The main products in the combustion of fossil fuels in air are carbon oxides (CO_x) and water (H_2O). Carbon oxides are major contributors to ocean acidification (Raven *et al.*, 2005). Due to fuel impurities and incomplete combustion a number of by-products may also be produced; the main ones being sulphur oxides (SO_x), nitrogen oxides (NO_x) and carbon based matter (soot, smoke). These by-products exist in small quantities but have a disproportionate effect on the environment. Sulphur and nitrogen oxides in the atmosphere form either wet precipitates (acid rain, snow and fog) or dry precipitates (acidic gases and salts). One source of nitric oxides is combustion at high temperatures. The release of nitric oxides can be mitigated through a number of methods inside and outside of the engine (Blatcher & Eames, 2013). Carbon based matter is formed due to incomplete combustion. It has a long airborne residence time that has been proven to be detrimental to human health (Jacobson, 2010) and it also reduces the reflection coefficient of snow and ice, raising their melting point (Hansen & Nazarenko, 2004). This is of particular concern in the Arctic and Antarctica areas.

These combustion by-products affect the acid-alkali balance especially in fresh water systems, in which pH recovery to original levels takes a long time because of reduced concentrations of dissolved alkaline substances (Schindler, 1988). Sulphur is naturally present in fossil fuels, but its quantity depends on the originating region and fuel type. At a significant cost, fuel sulphur content can be reduced by refining but it is also possible to 'wash' the exhaust gases via an exhaust gas scrubber.

1.2 Exhaust gas scrubbers

The majority of sulphur oxide scrubbers are used to clean the exhaust gases of coal power stations where the sulphur content ranges from less than 0.1% to over 10% on a dry weight basis (Casagrande, 1987) - the most common scrubber being the lime or lime stone absorption scrubber. The basic principle is to pass the exhaust gases through a packed bed absorber filled with hydrated and granulated lime. On contact with sulphur oxides in the exhaust gases, calcium sulphate ($CaSO_4$) is formed (Raja *et al.*, 2006). This is a harmless substance that is used in the manufacture of wallboard. The water used in this system is recovered and recycled. The disadvantage in the context of shipping is that significant amounts of lime and the resulting waste products need to be stored onboard the ship.

In areas where water is abundant (*e.g.* coastal regions, rivers or estuaries) heavy industries (*e.g.* mining, chemical and power generation) use wet scrubbers to reduce polluting by-products in exhaust gases. The most common, spray type scrubber works by bringing the exhaust gas into contact with alkaline water in the scrubber tower. The resulting wash water contains sulphuric acid (H_2SO_4) formed from the chemical reactions between sulphur oxides and water. In the past, River Thames water has been used by the scrubber of the Battersea Power Station from the 1925 to 1960's where the discharge was supplemented with the addition of alkali agents. Wet scrubbers are very effective at removing solid particles from the exhaust gases (10 μm or larger) by hydrating them (Arora & Domkundwar, 1997). Additionally, in a wet scrubber the pressure drop through the scrubber tower is small and the design is simple in comparison to lime or lime stone absorption scrubbers. The disadvantages are that the liquid to gas ratio has to be quite high and the exhaust gas wash water is highly corrosive, requiring corrosion resistant materials (*e.g.* fibre-reinforced plastic). In the case of ships, see figure 1.1, open loop wet scrubbers are used where the wash water is then filtered of particulate matter that is stored onboard and the acidic liquid is discharged back into the natural environment. Due to its high acidity, the wash water needs to be diluted or treated prior to discharge. The configuration of the scrubber discharge pipe controls the depth, angle and rate of discharge.

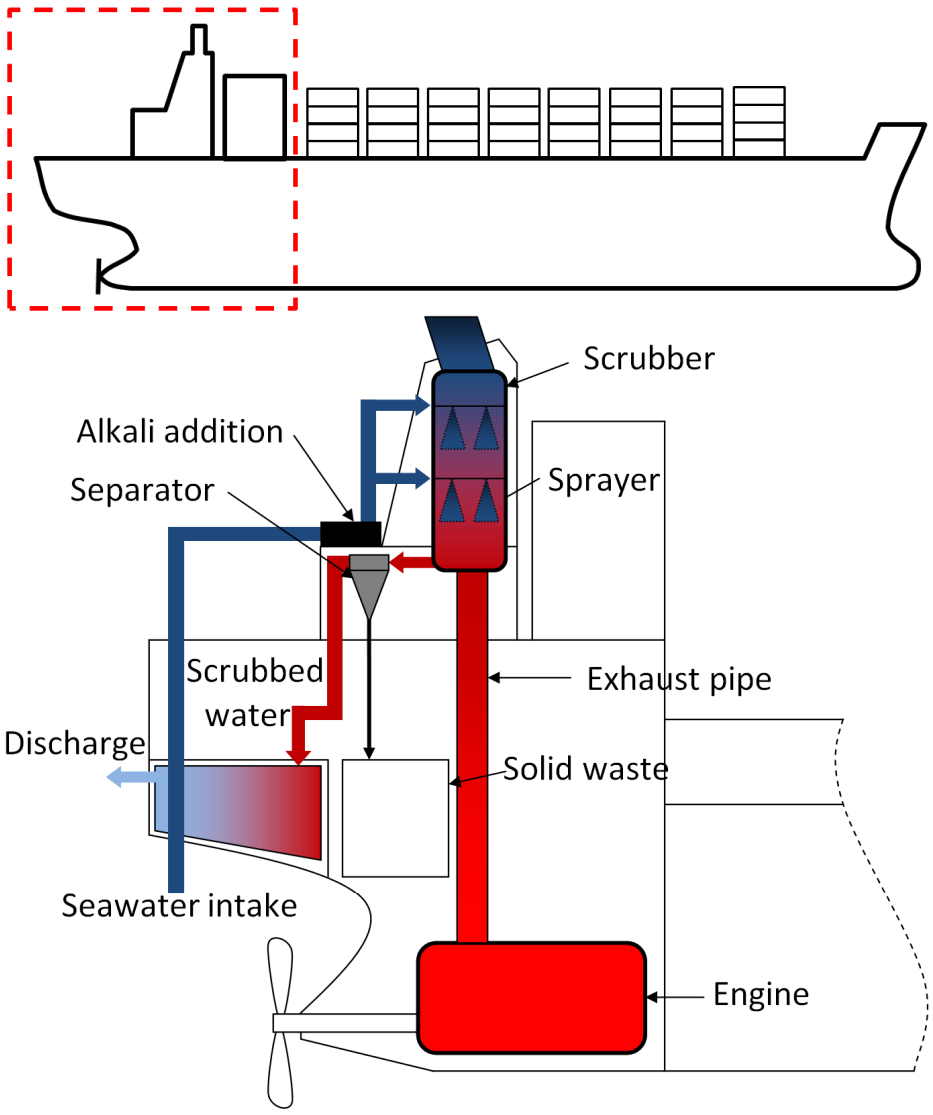

Figure 1.1: Schematic of a typical wet open loop exhaust gas scrubber setup at the stern of a container ship. Hot exhaust gases from the engine are sprayed with seawater in the scrubber after which the wash water is separated into dischargeable and storable (sludge) components.

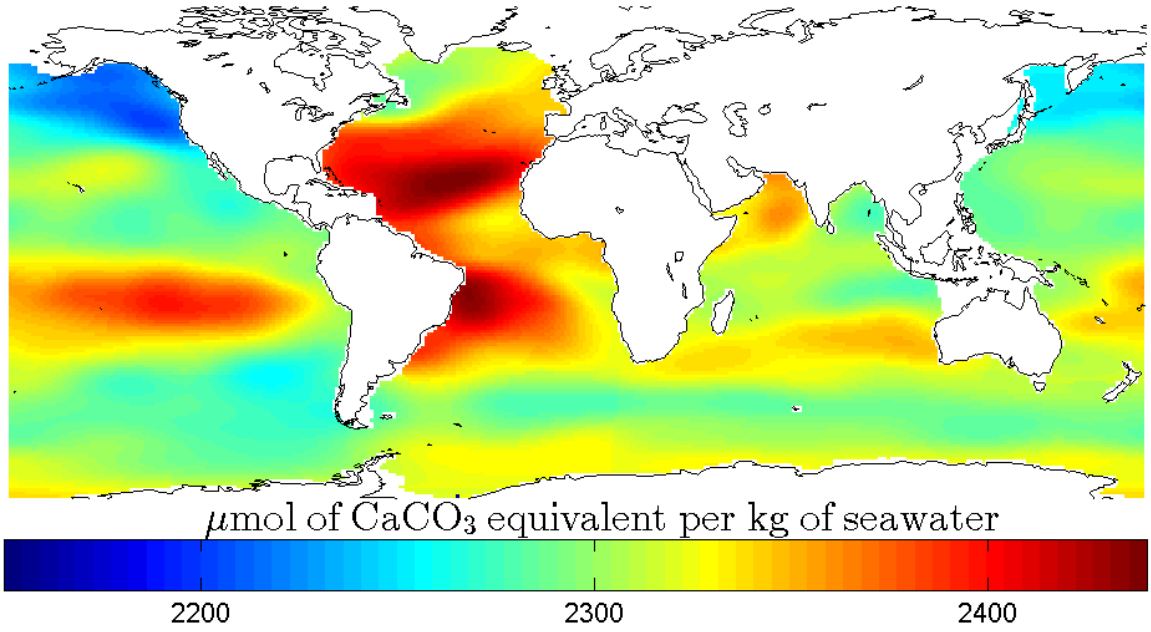

Figure 1.2: The global estimate of the total potential seawater alkalinity (μmol/kg) based on seawater salinity (Key *et al.*, 2004). The Emissions Control Areas (ECA) are highlighted with bold black lines.

1.3 Acid-alkali chemistry

The Brønsted-Lowry definition of acids and alkalis (Brønsted, 1923; Lowry, 1923) states that acids are substances which donate hydrogen ions (H^+) and alkalis are substances which add hydrogen ions. The pH scale, introduced by Sørensen (1909), is a measure of concentration of H^+ or OH^- ions on a logarithmic scale. At atmospheric pressure and 25 ^{o}C a solution is considered acidic at pH < 7, neutral at pH $= 7$ and alkaline at pH > 7. A neutral pH is temperature dependent and varies from pH $=$ 7.47 at 0 ^{o}C, pH $= 7$ at 25 ^{o}C and pH $= 6.92$ at 30 ^{o}C. The effect of pressure on pH is negligible within the context of wet scrubber discharges (Kitamura & Itoh, 1987). It is important to note that 'strong' and 'weak' in the context of acids/alkalis refers to their dissociability and not concentration. In solution, strong acids/alkalis dissociate fully into ions (H^+ and the anion, A^-, in the case of the acid and OH^- and the cation, M^+, in the case of the alkali). Weak acids and alkalis dissociate incompletely and reach equilibrium at a point described by a constant K_a for acids and K_b for alkalis (Gordus, 1985).

1.4 Marine environment

Seawater is a weak alkaline buffer solution which contains a large number of dissolved salts (Drever, 1988), some of which affect its pH. Alkaline buffer solutions resist changes to pH by absorbing hydrogen ions (H^+) when small amounts of strong acid are added. The majority of the seawater buffering capacity comes from carbonate (CO_3^{2-}) and bicarbonate (HCO_3^-) ions, which react with H^+ ions in a reversible reaction to form carbonic acid, which can in turn dissociate to form water and gaseous carbon dioxide (Frankignoulle, 1994). Calcium carbonate ($CaCO_3$) is a sparingly soluble alkaline salt common in seawater, therefore, the seawater alkalinity is frequently estimated in calcium carbonate equivalent moles. The buffering capacity of seawater is also influenced by water temperature, depth, salinity and coastal runoffs. For example, glacial ice melting in the summer introduces fresh water into seawater reducing the acid buffering capacity. Typical values of seawater alkalinity around the globe range from 2200-2400 μmol/kg (figure 1.2). In parts of the Baltic Sea, however, alkalinity is far lower at 800 μmol/kg (figure 1.3). The brackish characteristic of the Baltic Sea is due to the large number of rivers flowing into it and the limited exchange with the North Sea. Additionally, the pH of seawater is always lower at the free surface because carbonic acid is produced when the seawater absorbs atmospheric carbon dioxide. Marine organisms frequently experience pH fluctuations but prolonged periods of depressed pH can cause considerable harm (Knutzen, 1981). To avoid permanent damage to the local ecosystem, the scrubber discharge pH recovery must occur very rapidly.

Acids are corrosive and some, such as sulphuric acid, are also toxic to marine life. Bell & Nebeker (1969) observed that most marine insects seem to be able to tolerate an environment with a pH of 5 for 96 hours, however, survival rates dropped significantly when the pH was reduced to 3 with some species not surviving at all. Trent *et al.* (1978) investigated the effects of sulphuric acid on a range of marine animals and plants with exposure times of up to 96 hours. They also concluded that with varying mortality rates, most organisms were able to survive in an environment with a pH of 5 for up to 96 hours. However, snails were affected more than other organisms and died rapidly. With the exception of midges and mosquitofish, all of the tested organisms died within the 24 hour exposure period in an environment with a pH of 3. In the long term, a reduction in the average pH of seawater also poses a

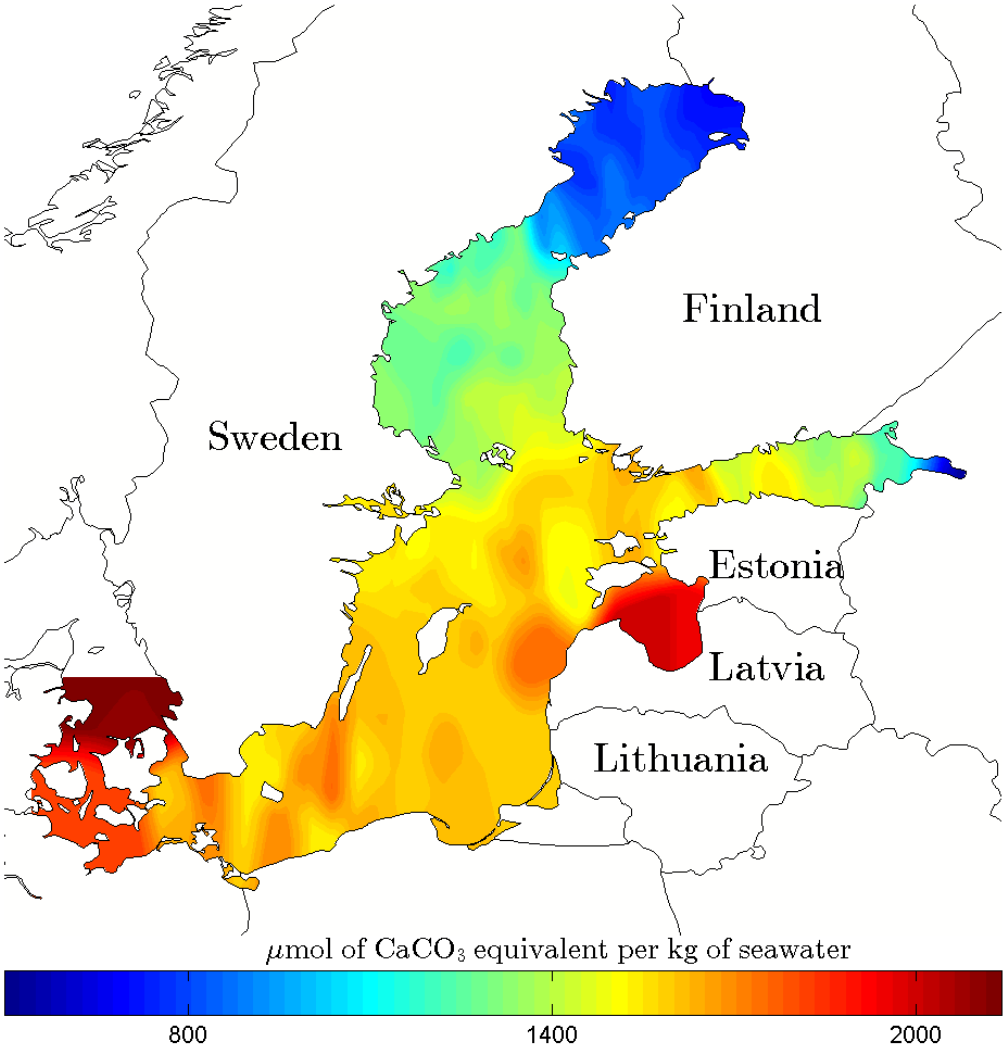

Figure 1.3: The estimate of the average seawater alkalinity (μmol/kg) between 2000-2012 in the Baltic Sea (ICES, 2011) is shown. The Savitzky-Golay filter is applied to the data in Matlab R2013b.

Outside an ECA established limit to SO_x emissions	Inside an ECA established limit to SO_x emissions
4.50% m/m prior to 1/1/2012	1.50% m/m prior to 1/7/2010
3.50% m/m on and after 1/1/2012	1.00% m/m on and after 1/7/2010
0.50% m/m on and after 1/1/2020	0.10% m/m on and after 1/1/2015

Table 1.1: Sulphur oxide emission limits inside and outside of the ECA expressed in terms of weight.

significant risk to fauna, in particular to calcifying organisms with calcium carbonate shells, skeletons and coral reefs (Raven *et al.*, 2005). Additionally, acidic seawater dissolves their defensive properties, making them more vulnerable to predators.

1.5 Environmental legislation

The legislative body for shipping emissions is the International Maritime Organisation (IMO). Nitric oxide emissions fall under IMO Regulation 13 and sulphur oxide emissions under Regulation 14. In the context of exhaust gas scrubbers IMO Regulation 14 is the most relevant because it sets limits for sulphur oxide and soot emissions (see table 1.1). Emissions Control Areas (ECA), shown in figure 1.2, cover the Pacific and Atlantic coasts of the United States and Canada, the Gulf of Mexico, Hawaiian Islands and the North and Baltic seas. The ECA are defined in MEPC.190(60) for the Americas and the limits of the North Sea are defined by the International Hydrographic Organization. In these regions the SO_x emissions limits are very severe (a maximum of 1% of fuel weight can be sulphur as of 1st of July 2010) meaning that exhaust gas scrubbers are likely to be used. Outside of the ECA the sulphur content can be up to 3.5% of fuel weight. Modern diesel and gas turbine ships are supported by auxiliary engines that are used for electricity generation and manoeuvring. Depending on the size of the ship a number of scrubbers may be fitted to allow for the independent running of main and auxiliary engines. The acidic scrubber discharges need to comply with the MEPC 59/24/Add.1 Annex 9 regulation. An extract from the regulation states:

> The wash water pH should comply with one of the following requirements which should be recorded in the ETM-A or ETM-B as applicable:
>
> (I) The discharge wash water should have a pH of no less than 6.5 measured at the ship's overboard discharge with the exception that during

manoeuvring and transit, the maximum difference between inlet and outlet of 2 pH units is allowed measured at the ships inlet and overboard discharge.

(II) During commissioning of the unit(s) after installation, the discharged wash water plume should be measured externally from the ship (at rest in harbour) and the discharge pH at the ship's overboard pH monitoring point will be recorded when the plume at 4 m from the discharge point equals or is above pH 6.5. The discharged pH to achieve a minimum pH units of 6.5 will become the overboard pH discharge limit recorded in the ETM-A or ETM-B.

Complying with (II) is easier because it permits a lower discharge pH than (I). Regulation compliance requires monitoring of pH, polycyclic aromatic hydrocarbons (PAH) content, turbidity and temperature. These measurements need to be recorded continuously while the scrubber is operational. Compliance is demonstrated by measuring the pH at a fixed depth and 4 m in front of the discharge port. This requires the ship engine to be running and driving the propeller in order for the scrubber to operate in typical working conditions. This means that an ambient flow will be present deviating the discharge in combination with buoyancy originating from the wash water's contact with hot exhaust gases. As a result the accuracy of measuring the pH 4 m in front of the discharge port is compromised.

1.6 Problem statement and thesis structure

The starting point is an industry problem on whether legislation on scrubber discharges is being met. The second matter is environmental, it is necessary to understand what happens to the acidic discharges outside of the regulated 4 m. These questions can be broken down into the following:

1. What processes affect the pH recovery in the ambient seawater?
2. How is the trajectory of the discharge affected by buoyancy and cross flow?
3. What are the mixing processes in the ship wake?
4. What are the design and engineering best practices for scrubber discharge nozzle sizes and configurations?

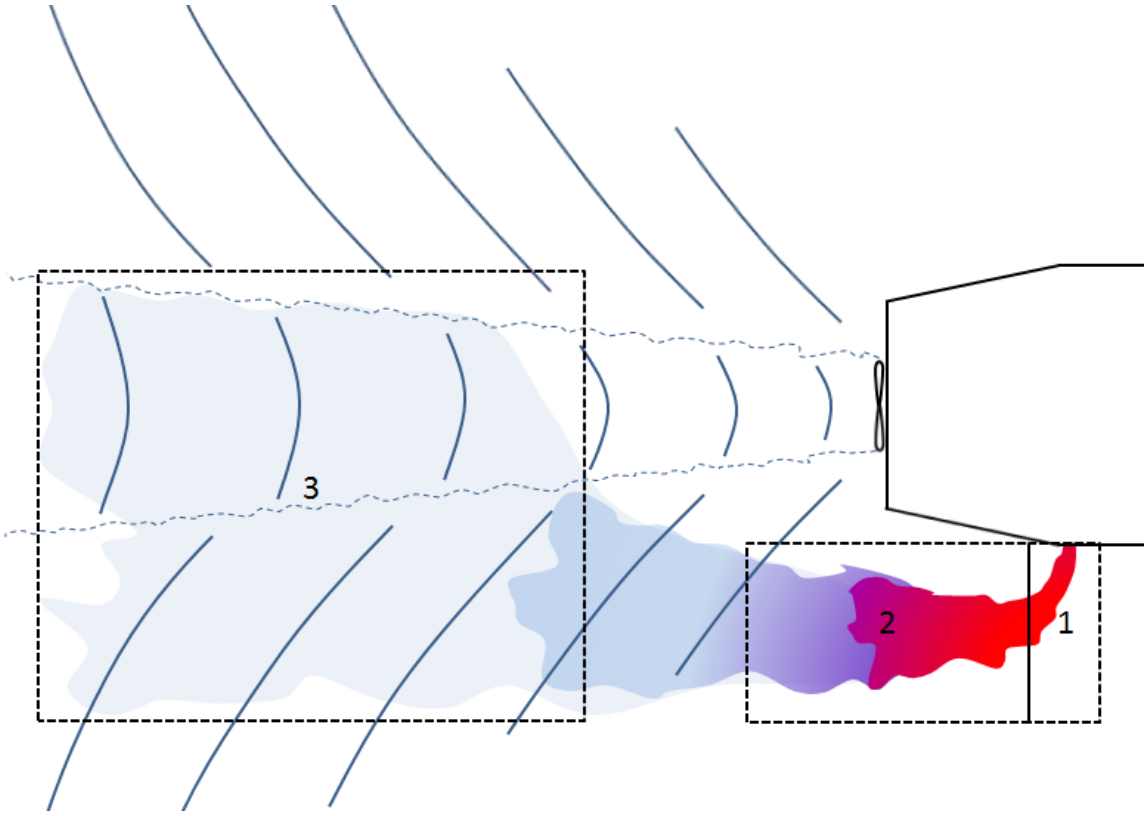

Figure 1.4: Schematic of an acidic discharge spreading in the wake of ship moving at a constant speed. The problem of acidic discharges into seawater is divided into three sections. In the first section we look at an undeflected acidic jet, in the second section we also include the influence of bending and in the third section we examine mixing in the wake.

Points 1 and 2 are addressed in Chapter 2, where a mathematical fluid flow and chemistry model is presented that describes the behaviour of an acidic jet in an alkaline environment. In order to provide a basis for testing the predictions, a series of experiments are undertaken and described in Chapter 3. Point 3 is addressed through a numerical study where the literature is presented in Chapter 4, the numerical model in Chapter 5 and the numerical results in Chapter 6. Point 4 is addressed in Chapter 7 where the challenges to measuring the discharge acidity in practice are discussed and design solutions are proposed to satisfy the necessary IMO MEPC guidelines for acidic discharges, which take into account the discharge acidity, required flow rate, seawater alkalinity, ship power, the size of the discharge port and dilution prior to discharge. Conclusions and findings are summarised in Chapter 8.

Chapter 2

Mathematical model of acidic jets and plumes

2.1 Introduction

When estimating the impact of scrubber discharge on marine environments, it is important to evaluate how pH changes with distance from the point of discharge and how long aquatic animals spend in regions of depressed pH. The change in pH depends on the dilution of the discharge due to entrainment of ambient fluid and on acid-alkali reactions between the discharge and seawater. Entrainment is the transport of fluid across an interface, in this case from the ambient seawater into the acidic jet. The purpose of this chapter is to develop an analytical model for acidic jets (momentum dominated) and Boussinesq plumes (Boussinesq, 1903) (influenced by buoyancy) discharged into an alkaline environment. In the context of warm discharges from ships, the jets and plumes will be affected by an ambient cross flow and buoyancy which needs to be taken into account. The depth of discharge is dependent on the individual configuration of the discharge pipe, however, draughts of more than 20 m are unusual, therefore, the effects of stratification tend to be weak. Consequently we limit our attention to an unstratified environment and discharges at a constant rate. Based on the chemical make up of the marine environment and the practical context described in Chapter 1, the chemistry analysis will be limited to monoprotic acids and to monoprotic and diprotic alkalis. Monoprotic acids yield only one H^+ ion per molecule upon ionization while diprotic acids yield two. In relation to alkalis, two OH^- ions are yielded instead of one. This analytical analysis will the form the basis for comparison with experiments in Chapter 3.

2.2 Literature review

Here we review the literature specific to turbulent jets and plumes in uniform environments. Additional literature with regards the the addition of an ambient flow can be found later on in the chapter.

2.2.1 Circular jet and plume models

The two most common integral models for turbulent jets and plumes are Gaussian (Reichardt, 1941, 1942) and top-hat (Morton *et al.*, 1956) which are shown in the schematic in figure 2.1. The key difference between the two models is the shape of the self-similar profile. In both cases the turbulent jet or plume can dynamically be described as quasi-steady if the eddy turnover time is shorter than the timescale over which horizontally averaged (tangential to the trajectory) volume, momentum and buoyancy fluxes are estimated. The approximation in the top-hat case is less accurate but the governing equations in the Gaussian are far more complex (Davidson, 1986). List (1982) summarises other integral models that differ due to either an entrainment assumption or the source conditions. Additional extensions include non-Boussinesq behaviour (Woods, 1997; Carlotti & Hunt, 2005), internal generation of buoyancy (Hunt & Kaye, 2005) and the effects of momentum or buoyancy of sources varying in time (Scase *et al.*, 2006*a*,*b*).

The assumptions in Morton *et al.* (1956) (page 5, equation 2) are based on a top-hat profile for jets and plumes which is consistent with the recent work by Westerweel and others (Westerweel *et al.*, 2005; Hunt *et al.*, 2006; Westerweel *et al.*, 2009) in which the conditionally averaged properties (velocity and concentration) (Bisset *et al.*, 2002) exhibit a large jump at the interface between the turbulent and non-turbulent regions *i.e.*

$$w(z,r) = wH\left[1-\frac{r}{b}\right], \tag{2.1}$$

where r is the tangential distance from the centre line, z is the distance along the trajectory, w the streamwise velocity of the discharge and $H[n]$ is the Heaviside step function that is 1 when n is positive and 0 when n is negative. The velocity profile of a Gaussian jet is

$$w(z,r) = w_{max}\exp\left(-\frac{r^2}{2\sigma^2}\right), \tag{2.2}$$

where w_{max} is the velocity on the discharge centre line and σ is the radius (standard

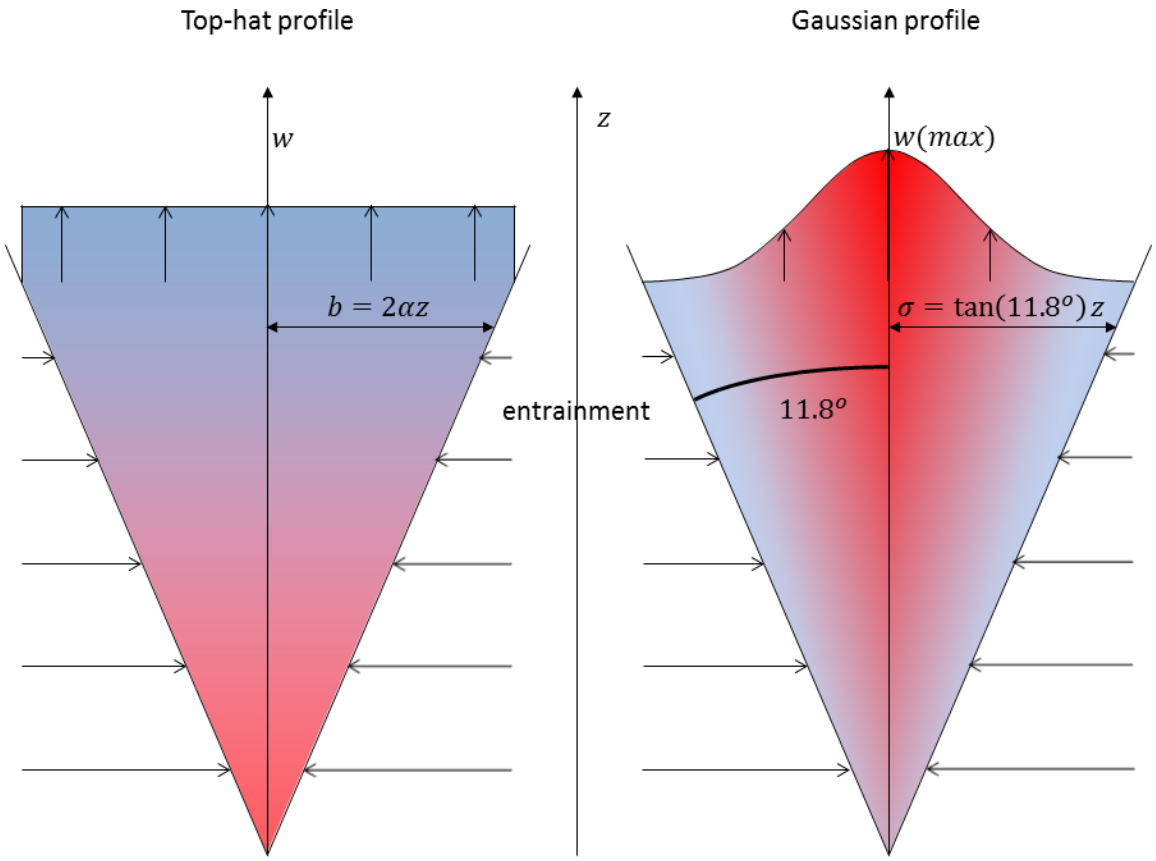

Figure 2.1: Illustration of point source jet profiles for top-hat and Gaussian models. The radius of the jet increases linearly from the source in either case. The symbols on the figure represent the centre line velocity w, the radius of the jet b, the entrainment coefficient α and distance from the origin z. The variation of colour indicates the averaging assumption for each of the integral models. In the top-hat case the properties of the jet are averaged across the width of the jet while in the Gaussian case the maximum values are found on the centre line than then decrease towards the edges of the jet. The horizontal black arrows indicate the relative magnitude of the entrainment velocity. Its magnitude is directly proportional to the velocity of the jet along its centre line and as it decreases so does the entrainment velocity.

deviation). In the Gaussian model of Hunt & Kaye (2005) (page 2, equation 2.1) the velocity at the edge of the jet has reduced to 95% of the maximum value. Averaging experimental measurements over time provides velocity and concentration profiles which appear to be close to Gaussian in form (Turner, 1969), largely as a consequence of the random meandering of the interface between the turbulent plume and non-turbulent ambient. Gaussian profiles have been the basis of many theoretical models as well, *e.g.* Jirka (2004); Hunt & van den Bremer (2011).

Depending on the source momentum and buoyancy contributions of the discharge, jets and plumes can be categorised as either jets, forced plumes, pure plumes or lazy plumes. In one extreme are jets that are wholly momentum based with no contribution from buoyancy. On the other extreme are lazy plumes that are initially buoyancy driven but momentum is picked up as they rises, for example the movement of hot air from a fire. Van Den Bremer & Hunt (2010) showed that in the far field forced plumes and lazy plumes locally become pure plumes.

2.2.2 Entrainment

Entrainment occurs at the edges of the jet or plume and it has been studied in detail over the last 50 years. It is a process through which the jet or plume volume flux increases by small fluid packages being incorporated into the jet or plume (Woods, 2010). There is a debate on the detailed elements of entrainment, such as on the dominance of nibbling versus engulfment (Hunt *et al.*, 2006, 2011). In the top-hat and Gaussian models the entrainment rate at the edges of a jet or plume is proportional to the local centre line velocity. The constant of proportionality is α, the entrainment coefficient. Under the top-hat velocity profile assumption, Morton (1959) suggested that the most reliable way of determining the entrainment coefficient was to measure experimentally the spreading rate of pure jets, from which he determined $\alpha = 0.082$. There are a number of ways of determining the entrainment coefficient, such as measuring the spreading angle, measuring the velocity profiles at different distances from the source or by measuring the inflow into the jet or plume directly. Baines (1983) developed a method for measuring the entrainment coefficient by placing the plume in a vertical coflow channel. The advantage of this method is that a fixed interface develops that can be measured to infer the changes in volume flux. Ricou & Spalding (1961) determined that the entrainment coefficient for jets is close to

0.08 while for plumes they determined 0.12. Kaminski *et al.* (2005) suggested that the enhancement of entrainment in plumes is partly explained by the increase in baroclinically generated turbulence. Turner (1969) noted that the resulting similarity solutions are not sensitive to the value of α, therefore, reasonably accurate solutions can be made on the assumption α is constant. In the following analysis we assume $\alpha = 0.1$ for top-hat jets and plumes, however, in the work of Hunt & Kaye (2005) it is suggested that this approach slightly underestimates the entrainment rate in a pure plume.

In the case of Gaussian jets and plume model, the entrainment coefficients are different due to the jet velocity being defined as the axial velocity and jet width as the distance to the point where jet velocity is reduced by the factor $1/e$ (Turner, 1969). To convert the entrainment coefficient of a top-hat plume to that of a Gaussian plume it needs to be divided by a factor of $\sqrt{2}$ (Kaye, 2008).

2.2.3 Chemistry with jets and plumes

A number of studies have examined the chemistry of reacting jets and plumes. Conroy & Llewellyn-Smith (2008) analysed second order irreversible exothermic and endothermic reactions between a point source plume and a second species in the ambient. Campbell & Cardoso (2010) and Cardoso & McHugh (2010) examined the influence of internal buoyancy generation through irreversible reactions resulting in phase change on the development of plumes in stratified and unstratified environments. Cardoso & McHugh (2010) studied experimentally a plume containing calcium carbonate particles descending in an acidic aqueous solution where the generation of carbon dioxide bubbles on the surface of the particles modified the buoyancy flux of the plume. A number of studies have used acid alkali reactions combined with pH sensitive dyes as a visualisation tool to examine mixing in jets (Corriveau & Baines, 1993; Dimotakis & Brown, 1976). A thorough review of jets and plumes has been published (Woods, 2010), however, what appears to be currently missing from the jet/plume research literature is a detailed understanding of reversible reactions, such as acid-alkali reactions that do not have an effect on the flow by affecting the fluid density. This essentially forms one novel aspect of this thesis.

2.3 Mathematical model

The following analysis is based on the top-hat model as described in figure 2.1. The aim of the analysis is to determine the neutralisation distance along the jet/plume centre line, therefore, the simpler top-hat model is used over the more complex Gaussian model.

An acidic fluid issues with a mean vertical speed of w_0 from a circular orifice of radius b_0 into an otherwise stagnant ambient body of water. The injected fluid has a density ρ_0 and contains a concentration C_a^0 of monoprotic strong acid HA. The ambient fluid has a density ρ_a and a concentration C_b^0 of alkali MOH. It is assumed that the issuing fluid is perfectly mixed across the width of the jet or plume. The analysis describes a purely acidic jet or plume injected into a purely alkaline environment. It can be straight forwardly extended to account for alkali in the jet or plume, as indeed we do to interpret experiments and apply analysis to practical situations in Chapter 3. It is also assumed that the mixing processes have a far longer timescale than the chemical processes that happen very rapidly on timescales less than 10^{-9} s (Eigen, 1954). For analytical simplicity, our discussion is centred around strong monoprotic acids (*e.g.* nitric acid) which donate one H^+ ion per molecule. The limit of the acid being strong is in keeping with the practical context, although ambient fluid may be a weak alkali or dilute strong alkali.

2.3.1 Chemistry model

We first analyse a strong acid and a strong or weak alkali reacting in an aqueous solution. Consider a fixed volume of acidic fluid V_a that is being diluted through the addition of alkaline fluid V_b. The chemical reaction is governed by the conservation of charge

$$[H^+] + [M^+] = [OH^-] + [A^-], \tag{2.3}$$

and the conservation of mass of alkali and acid, respectively

$$C_b^0 V_b = ([MOH] + [M^+])(V_a + V_b), \quad C_a^0 V_a = [A^-](V_a + V_b). \tag{2.4a, b}$$

The square brackets denote the molar concentration (mol/l) of the species. The condition (2.4b) occurs because the acid is strong and fully dissociates, *i.e.* $HA \rightarrow H^+ + A^-$. Both water and a weak alkali dissociate reversibly, *i.e.* $H_2O \rightleftharpoons H^+ + OH^-$

and MOH $\rightleftharpoons$ $M^+ + OH^-$. The dissociation constant of water K_w and alkali K_b are defined by

$$K_w = [OH^-][H^+], \quad K_b = \frac{[M^+][OH^-]}{[MOH]}. \tag{2.5a, b}$$

At 25 ^{o}C and at atmospheric pressure, $K_w = 10^{-14}$ mol^2/l^2. In the standard notation, it is important to note that K_w and K_b have different units, *e.g.* Atkins & De Paula (2006). Combining (2.3), (2.5a) and (2.5b) generates an implicit equation which relates the H^+ ion concentration to the dilution of the acid by the alkali. The first step is to substitute (2.3) into (2.4b) to eliminate $[A^-]$

$$([H^+] + [M^+] - [OH^-])(V_a + V_b) = C_a^0 V_a. \tag{2.6}$$

Eliminate $[M^+]$ by substituting (2.6) into (2.4a)

$$\left([MOH] + \frac{C_a^0 V_a}{V_a + V_b} - [H^+] + [OH^-]\right)(V_a + V_b) = C_b^0 V_b, \tag{2.7}$$

and rearranging the equation with V_a and V_b on separate sides while keeping the $[MOH](V_a + V_b)$ intact gives

$$V_a(C_a^0 - [H^+] + [OH^-]) = V_b(C_b^0 + [H^+] - [OH^-]) - [MOH](V_a + V_b). \tag{2.8}$$

Rearrange (2.4a) in terms of $[MOH](V_a + V_b)$

$$[MOH](V_a + V_b) = C_b^0 V_b - [M^+](V_a + V_b), \tag{2.9}$$

and manipulate it with (2.5b) to give

$$[MOH](V_a + V_b) = C_b^0 V_b - \left(\frac{C_b V_b}{\frac{[OH]}{K_b} + 1}\right). \tag{2.10}$$

Substitute (2.10) into (2.8)

$$V_a(C_a^0 - [H^+] + [OH^-]) = V_b([H^+] - [OH^-]) + \left(\frac{C_b^0 V_b}{\frac{[OH^-]}{K_b} + 1}\right), \tag{2.11}$$

replace $[OH^-]$ with $K_w/[H^+]$ and rearrange to get the standard acid-alkali titration equation

$$\frac{V_b}{V_a} = \frac{C_a^0 - [H^+] + \frac{K_w}{[H^+]}}{\frac{C_b^0}{1 + K_w/([H^+]K_b)} + [H^+] - \frac{K_w}{[H^+]}} = \mathcal{D}, \tag{2.12}$$

where the fraction V_a/V_b can be expressed as the dilution factor $\mathcal{D}$. The pH of the resultant solution is defined in terms of the H^+ concentration

$$\mathrm{pH} = -\log_{10}[\mathrm{H}^+], \tag{2.13}$$

as introduced by Sørensen (1909). The point of neutralisation is defined as $[\mathrm{H}^+] = [\mathrm{OH}^-]$ which, therefore, occurs when the hydrogen ion concentration is equal to $[\mathrm{H}^+] = K_w^{\frac{1}{2}}$. In this scenario the dilution needed for neutralisation from (2.12) reduces to

$$\mathcal{D} = \frac{C_a^0}{C_b^0}\left(\frac{K_w^{1/2}}{K_b} + 1\right). \tag{2.14}$$

For a strong alkali, $\mathcal{D} = C_a^0/C_b^0$ and corresponds to the ratio of acid to alkali concentrations. When the alkali is weak, more dilution is required because of incomplete dissociation. Therefore, the strong acid - strong alkali and a strong acid - weak alkali reaction need to be considered separately. A strong alkali is characterized by $K_b/K_w^{1/2} \gg 1$, and in this limit the hydrogen ion concentration has a quadratic relationship, with that the titration equation in (2.12) can be reduced to

$$[\mathrm{H}^+]^2 - \left(\frac{V_a C_a^0 - V_b C_b^0}{V_a + V_b}\right)[\mathrm{H}^+] - K_w = 0. \tag{2.15}$$

Rearrange (2.15) and multiplying with $(1+\frac{V_b}{V_a})$

$$[\mathrm{H}^+]^2\left(1 + \frac{V_b}{V_a}\right) - \left(C_a^0 - \frac{V_b}{V_a}C_b^0\right)[\mathrm{H}^+] - \left(1 + \frac{V_b}{V_a}\right)K_w = 0, \tag{2.16}$$

where dilution can be substituted in reducing the expression to

$$[\mathrm{H}^+]^2(1+\mathcal{D}) - (C_a^0 - \mathcal{D}C_b^0)[\mathrm{H}^+] - (1+\mathcal{D})K_w = 0. \tag{2.17}$$

The solution to the quadratic equation for a positive root is

$$[\mathrm{H}^+] = \frac{1}{2}\left(\frac{C_a^0 - \mathcal{D}C_b^0}{1+\mathcal{D}} + \sqrt{\left(\frac{C_a^0 - \mathcal{D}C_b^0}{1+\mathcal{D}}\right)^2 + 4K_w}\right). \tag{2.18}$$

When the reaction is far from neutralisation and acidic (*i.e.* $(C_a^0 - \mathcal{D}C_b^0)/(1+\mathcal{D}) \gg K_w^{1/2}$), the hydrogen ion concentration is

$$[\mathrm{H}^+] \simeq \frac{1}{2}\left(\frac{C_a^0 - \mathcal{D}C_b^0}{1+\mathcal{D}} + \frac{C_a^0 - \mathcal{D}C_b^0}{1+\mathcal{D}}\right), \tag{2.19}$$

that reduces to

$$[\mathrm{H}^+] \simeq \frac{C_a^0 - \mathcal{D}C_b^0}{1+\mathcal{D}}. \tag{2.20}$$

Physically (2.20) shows that $[\mathrm{H}^+]$ decreases due to the reaction (*i.e.* the numerator $C_a^0 - \mathcal{D}C_b^0$) and the dilution (*i.e.* the denominator $1/(1+\mathcal{D})$). Beyond neutralisation (*i.e.* $\mathcal{D}C_b^0 > C_a^0$ and $[\mathrm{H}^+] \ll K_w^{1/2}$), the first term in (2.17) ($[\mathrm{H}^+]^2(\mathcal{D}+1)$) is small compared to the last and (2.17) reduceds to

$$-(C_a^0 - \mathcal{D}C_b^0)[\mathrm{H}^+] - (1+\mathcal{D})K_w \simeq 0. \tag{2.21}$$

Rearranging (2.21) and equating it to $[\mathrm{H}^+]$ gives

$$[\mathrm{H}^+] \simeq \frac{(1+\mathcal{D})K_w}{\mathcal{D}C_b^0 - C_a^0}. \tag{2.22}$$

For a weak alkali, characterised by $K_w/[\mathrm{H}^+] \gg K_b$, the balance in (2.12) reduces to

$$\mathcal{D} = \frac{C_a^0 - [\mathrm{H}^+] + \frac{K_w}{[\mathrm{H}^+]}}{\frac{C_b^0 K_b}{K_w/[\mathrm{H}^+]} + [\mathrm{H}^+] - \frac{K_w}{[\mathrm{H}^+]}}. \tag{2.23}$$

This can be rearranged to give a cubic in $[\mathrm{H}^+]$,

$$[\mathrm{H}^+]^2(C_b^0 K_b \mathcal{D}/K_w + 1 + \mathcal{D}) - [\mathrm{H}^+]C_a^0 - (1+\mathcal{D})K_w = 0. \tag{2.24}$$

Figure 2.2 shows the pH variation of a mixture formed by titrating a strong acid against an alkali at 25 ^{o}C. Figure 2.2*a* shows the case of a strong acid - strong alkali reaction for varying concentration of the alkali, where the concentration of acid is the same in each curve. The comparison between (2.20) (for pH < 7) and (2.22) (for pH > 7) is good and finally asymptotes to

$$\mathrm{pH} = -\log_{10}\left(\frac{K_w}{C_b^0}\right) = 14 + \log_{10}(C_b^0). \tag{2.25}$$

We see that close to neutralisation the pH varies rapidly with $\mathcal{D}$. Figure 2.2*b* shows the reaction strong acid - weak alkali reaction, the dashed lines correspond to (2.18) for pH < 5 and (2.24) for pH > 5.

The presented chemistry model can be extended for a strong or weak diprotic acid (*e.g.* sulphuric acid) reacting with a strong or weak monoprotic alkali. Diprotic acids are characterized by two dissociation constants (K_{a1} and K_{a2}) that describe the ease

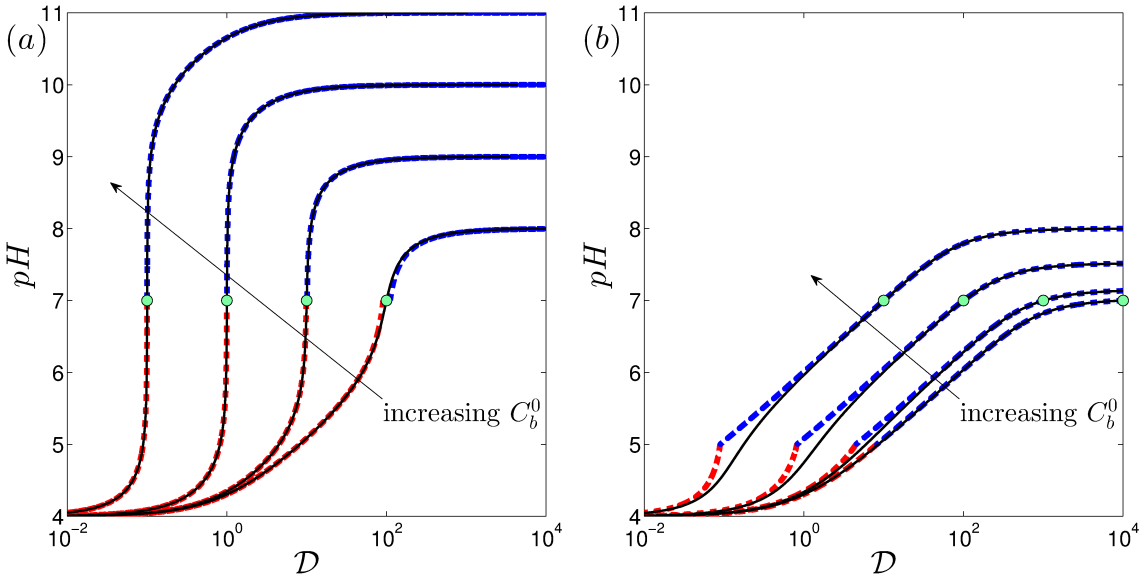

Figure 2.2: Theoretical titration curves for (a) strong acid - strong alkali reaction ($K_b = 10^1$ mol/l) and (b) strong acid - weak alkali reaction ($K_b = 10^{-9}$ mol/l) at 25 ^{o}C ($K_w = 10^{-14}$ mol^2/l^2) are described by solid black lines (2.12) in the limit of $\mathcal{D} \to \infty$. In both cases $C_a^0 = 10^{-4}$ mol/l and $C_b^0 = 10^{-6}$, 10^{-5}, 10^{-4}, 10^{-3} mol/l. The dashed lines denote simplified expressions. In (a) they correspond to (2.20) for pH $<$ 7 and (2.22) for pH $>$ 7. In (b), they correspond to (2.18) for pH $<$ 5 and (2.24) for pH $>$ 5. Points of neutralisation are displayed as circles that correspond to (2.14).

of dissociation of the first and the second H^+ ion

$$K_{a1} = \frac{[H^+][HA^-]}{[H_2A]}, \quad K_{a2} = \frac{[H^+][A^{2-}]}{[HA^-]}. \tag{2.26a, b}$$

The charge balance equation is

$$[H^+] + [M^+] = [OH^-] + [HA^-] + 2[A^{2-}], \tag{2.27}$$

and the expressions for mass conservation of the acid and the alkali are

$$C_a^0 V_a = (V_a + V_b)([H_2A] + [HA^-] + [A^{2-}]), \tag{2.28}$$

$$C_b^0 V_b = (V_a + V_b)([MOH] + [M^+]). \tag{2.29}$$

The $[H_2A]$, $[HA^-]$ and $[A^{2-}]$ can be eliminated from (2.28) by substitution of (2.26a), (2.26b) and (2.27) to give

$$C_a^0 V_a = (V_a + V_b) \left(\frac{[H^+] + [M^+] - [OH^-]}{1 + \frac{2K_{a2}}{[H^+]}} \right) \left(\frac{[H^+]}{K_{a1}} + 1 + \frac{K_{a2}}{[H^+]} \right). \tag{2.30}$$

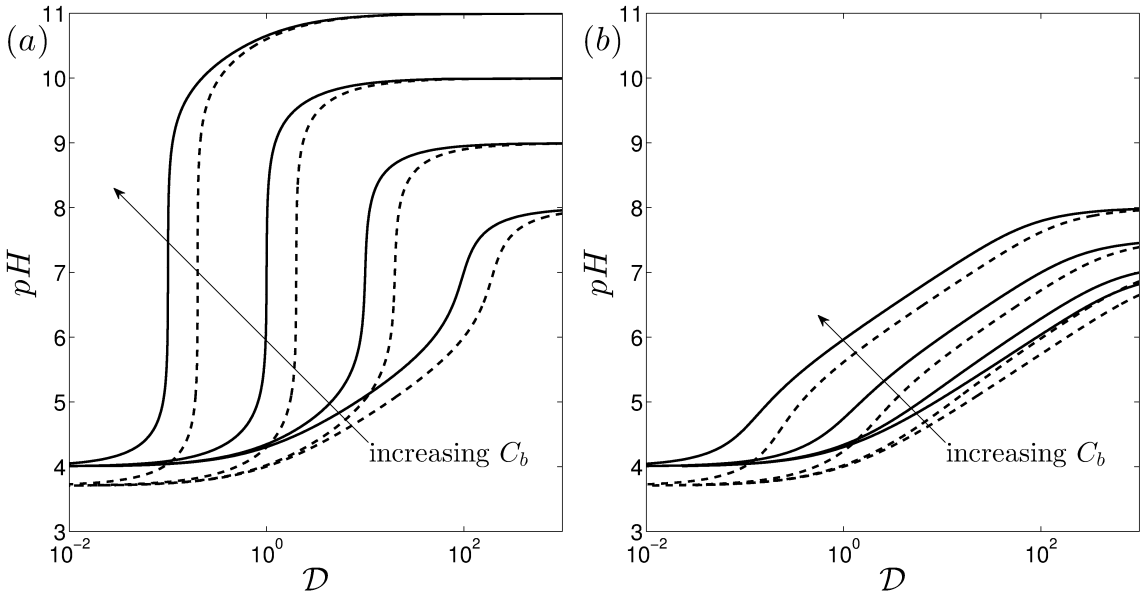

Figure 2.3: The pH of a jet or a plume is plotted for four cases corresponding to a strong acid - strong(a)/weak(b) alkali reaction. The solid line is for nitric acid and corresponds to (2.12) while the dashed line is for sulphuric acid and corresponds to (2.33). The value of C_a^0 is 10^{-4} mol/l and C_b^0 correspond to 10^{-6}, 10^{-5}, 10^{-4} and 10^{-3} mol/l.

An expression for $[\mathrm{M}^+]$ can be formed from substitution of (2.5b) into (2.29) to give

$$[\mathrm{M}^+] = \left(\frac{C_b^0 V_b}{V_a + V_b}\right)\left(\frac{1}{1 + \frac{[\mathrm{OH}^-]}{K_b}}\right). \tag{2.31}$$

To eliminate $[\mathrm{M}^+]$ from (2.30) we need to substitute (2.31) into it and after significant algebra the following expression can be obtained

$$\frac{V_a}{V_b} = \frac{C_a^0 K_{a1} V_b([\mathrm{H}^+] + 2K_{a2})}{(V_a + V_b)\left([\mathrm{H}^+] - [\mathrm{OH}^-] + \frac{C_b K_b V_b}{(V_a+V_b)(K_b+[\mathrm{OH}^-])}\right)([\mathrm{H}^+]^2 + K_{a1}[\mathrm{H}^+] + K_{a1}K_{a2})}, \tag{2.32}$$

which can be rearranged and the $[\mathrm{OH}^-]$ term eliminated via (2.5a) to result in

$$\frac{V_b}{V_a} = \frac{\frac{C_a^0(K_{a1}[\mathrm{H}^+]+2K_{a1}K_{a2})}{[\mathrm{H}^+]^2+K_{a1}[\mathrm{H}^+]+K_{a1}K_{a2}} - [\mathrm{H}^+] + \frac{K_w}{[\mathrm{H}^+]}}{\frac{C_b^0}{1+K_w/([\mathrm{H}^+]K_b)} + [\mathrm{H}^+] - \frac{K_w}{[\mathrm{H}^+]}} = \mathcal{D}. \tag{2.33}$$

The titration curves from (2.33) for sulphuric acid (K_{a1}= 1mol/l; $K_{a2} = 1.2 \times 10^{-2}$ mol/l) are plotted in figure 2.3 and it is evident that both of the H^+ ions dissociate with ease. As a result, in the case of sulphuric acid we can estimate the total acid concentration to be twice that of the monoprotic acid.

2.3.2 Top-hat jets and plumes in a stationary ambient

The starting point is the conservation of momentum and mass (with an empirical closure for entrainment), which for a top-hat profile are defined in the classic paper of Morton *et al.* (1956) as

$$\frac{\mathrm{d}}{\mathrm{d}z}(\pi b^2 w) = 2\pi\alpha w b, \tag{2.34}$$

$$\frac{\mathrm{d}}{\mathrm{d}z}(\pi b^2 w^2) = g\pi b^2 \left(\frac{\rho_a - \rho}{\rho_0}\right), \tag{2.35}$$

$$\frac{\mathrm{d}}{\mathrm{d}z}\left[\pi b^2 w g \left(\frac{\rho_a - \rho}{\rho_0}\right)\right] = 0, \tag{2.36}$$

where b is the radius, w is the vertical velocity and g is the acceleration due to gravity. The density terms ρ_a, ρ and ρ_0 stand for the density of the ambient fluid, density within the plume and initial density of the plume at its source. The system of equations can be re-expressed in terms of specific fluid momentum ($M = \pi b^2 w^2$), volume flux ($Q = \pi b^2 w$) and buoyancy flux ($B = \pi b^2 w g(\rho_a - \rho)/\rho_0$) as

$$\frac{\mathrm{d}Q}{\mathrm{d}z} = 2\pi\alpha w b = 2\pi^{1/2}\alpha(\pi^{1/2} w b) = 2\pi^{1/2}\alpha M^{1/2} \tag{2.37}$$

$$\frac{\mathrm{d}M}{\mathrm{d}z} = g\pi b^2 \left(\frac{\rho_a - \rho}{\rho_0}\right) = \frac{B}{w} = \frac{BQ}{M} \tag{2.38}$$

$$\frac{\mathrm{d}B}{\mathrm{d}z} = 0. \tag{2.39}$$

The above expressions can be rendered dimensionless through $\tilde{Q} = Q/Q_0$, $\tilde{M} = M/M_0$, $\tilde{B} = B/B_0 = 1$ and $\tilde{z} = 2\alpha z/b_0$. The volume flux increases due to entrainment as

$$\frac{\mathrm{d}\tilde{Q}}{\mathrm{d}\tilde{z}} = \tilde{M}^{1/2}. \tag{2.40}$$

The specific momentum flux, after rearranging, becomes

$$\frac{\mathrm{d}\tilde{M}}{\mathrm{d}\tilde{z}} = \frac{1}{2}\left(\frac{\tilde{B}\tilde{Q}}{\tilde{M}}\right)\frac{B_0 Q_0^2}{\alpha\pi^{1/2} M_0^{5/2}}, \tag{2.41}$$

where the following term can be substituted in

$$\Gamma_0 = \frac{5 B_0 Q_0^2}{8\alpha\pi^{1/2} M_0^{5/2}}, \tag{2.42}$$

resulting in

$$\frac{\mathrm{d}\tilde{M}}{\mathrm{d}\tilde{z}} = \frac{4}{5}\frac{\tilde{B}\tilde{Q}}{\tilde{M}}\Gamma_0. \tag{2.43}$$

Γ_0 in (2.42) is a dimensionless measure of the relative strength of the source buoyancy flux of the plume and can be used to classify the nature of the source, *i.e.* for jets $\Gamma_0 = 0$, forced plumes $0 < \Gamma_0 < 1$, pure plumes $\Gamma_0 = 1$, lazy plumes $\Gamma_0 > 1$ (Hunt & Kaye, 2001, 2005). The equations (2.40) and (2.43) can be solved using the relationship between $\tilde{M}$ and $\tilde{Q}$. Start with rearranging (2.37) in terms of $\mathrm{d}\tilde{z}$

$$\mathrm{d}\tilde{z} = \frac{1}{\tilde{M}^{1/2}}\mathrm{d}\tilde{Q}, \tag{2.44}$$

similarly, rearrange (2.43) into

$$\mathrm{d}\tilde{z} = \frac{5}{4}\frac{\tilde{M}}{\tilde{B}\tilde{Q}\Gamma_0}\mathrm{d}\tilde{M}. \tag{2.45}$$

Equate (2.44) to (2.45) and move the integration constants to the appropriate sides of the equation

$$\frac{5}{4\tilde{B}\Gamma_0}\int_1^{\tilde{M}} \tilde{M}^{3/2}\mathrm{d}\tilde{M} = \int_1^{\tilde{Q}} \tilde{Q}\mathrm{d}\tilde{Q}. \tag{2.46}$$

Integrating (2.46) gives

$$\frac{5}{4\Gamma_0\tilde{B}}\left(\frac{2}{5}(\tilde{M}^{5/2} - 1)\right) = \frac{1}{2}(\tilde{Q}^2 - 1), \tag{2.47}$$

that can be expressed in terms of $\tilde{M}$ as

$$\tilde{M} = (\Gamma_0\tilde{B}(\tilde{Q}^2 - 1) + 1)^{2/5}. \tag{2.48}$$

The volume flux $\tilde{Q}$ can be expressed implicitly in terms of the distance $\tilde{z}$ from the source by substituting (2.48) into (2.44)

$$\tilde{z} = \int_1^{\tilde{Q}} \frac{\mathrm{d}\tilde{Q}}{(\Gamma_0(\tilde{Q}^2 - 1) + 1)^{1/5}}. \tag{2.49}$$

For a pure jet source ($\Gamma_0 = 0$), the radius and volume flux increase linearly with distance. In the case of volume flux

$$\tilde{z} = \int_1^{\tilde{Q}} \mathrm{d}\tilde{Q} = \tilde{Q} - 1. \tag{2.50}$$

The relationship between $\tilde{z}$ and $\tilde{Q}$ can be derived from (2.50) and reduce the equation to

$$b = b_0 + 2\alpha z. \tag{2.51}$$

For $\Gamma_0 > 0$, the asymptotic form can be obtained by writing (2.49), in the limit of $\tilde{Q} \to \infty$ asymptotic spread in the far field, accounting for the virtual origin $\tilde{z}$. A series expansion of the first term of (2.49) gives

$$\int_{\tilde{z}_0}^{\tilde{z}} \mathrm{d}\tilde{z} \simeq \int_1^{\tilde{Q}} \frac{\mathrm{d}\tilde{Q}}{(\Gamma_0 \tilde{Q}^2)^{1/5}}, \tag{2.52}$$

that can be integrated to give

$$\tilde{z} - \tilde{z}_0 \sim \frac{5}{3}\frac{\tilde{Q}^{3/5}}{\Gamma_0^{1/5}} - \frac{5}{3}\frac{1}{\Gamma_0^{1/5}}, \tag{2.53}$$

and rearranging in terms of $\tilde{Q}$ results in

$$\tilde{Q} \sim \left(\frac{3}{5}(\tilde{z} - \tilde{z}_0)\right)^{5/3} \Gamma_0^{1/3}. \tag{2.54}$$

The virtual origin can be evaluated to be

$$\tilde{z}_0 = -\frac{1}{\Gamma_0^{1/5}} \int_1^{\infty} \left(\frac{1}{(\tilde{Q}^2 - 1 + \Gamma_0^{-1})^{1/5}} - \frac{1}{\tilde{Q}^{2/5}} \right) \mathrm{d}\tilde{Q} - \frac{5}{3}\Gamma_0^{1/5}. \tag{2.55}$$

When $\Gamma_0 = 1$, equations (2.52) reduces to

$$\tilde{z} = \int_1^{\tilde{Q}} \frac{1}{(\tilde{Q}^2)^{1/5}} \mathrm{d}\tilde{Q} = \int_1^{\tilde{Q}} \frac{1}{\tilde{Q}^{2/5}} \mathrm{d}\tilde{Q} = \frac{5}{3}\tilde{Q}^{3/5} - \frac{5}{3}, \tag{2.56}$$

that can be rearranged in terms of $\tilde{Q}$ to

$$\tilde{Q} = \left(\frac{3}{5}\tilde{z} + 1\right)^{5/3}, \tag{2.57}$$

in the case when $\tilde{z}_0 = 5/3$. From (2.57) the increase in radius can be determined

$$b = b_0 + \frac{6}{5}\frac{\alpha z}{b_0} \tag{2.58}$$

Figure 2.4*a* shows the variation of $\tilde{Q}$ with $\tilde{z}$ for a range of Γ_0 values. For $|\Gamma_0 -$

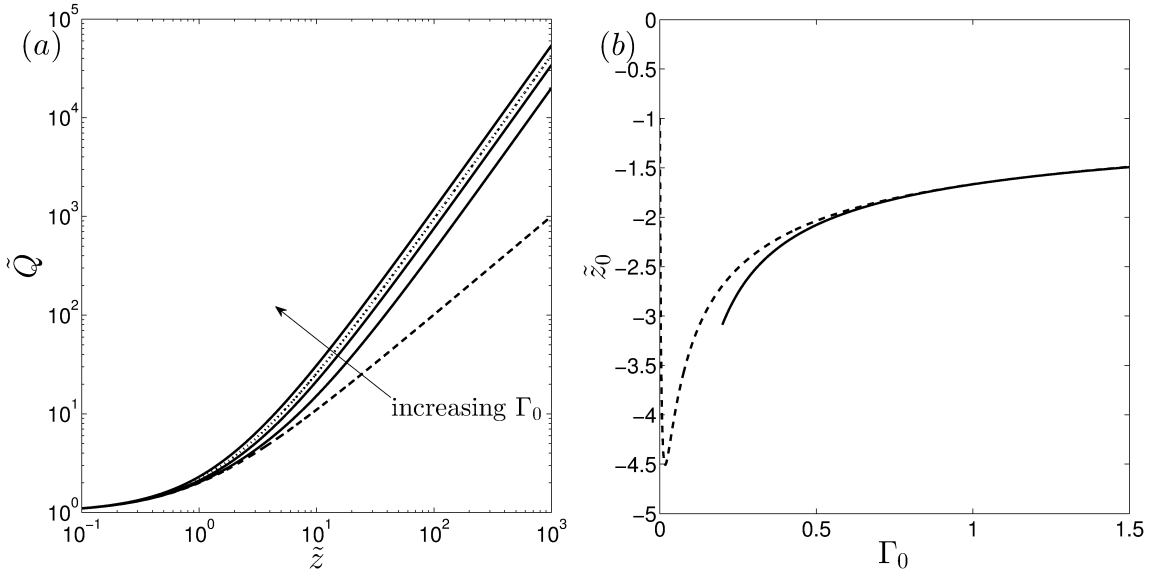

Figure 2.4: In (a) the numerical volume flux against distance for a range of $\Gamma_0 = 0$ (dashed line), 0.1, 0.5, 1 (dotted line), 2. In (b) the variation of the virtual origin $\tilde{z}_0$ as a function Γ_0 (2.55) (dashed line) compared against the analytical approximation (2.59) (solid line).

$1|/(\tilde{Q}^2\Gamma_0) \ll 1$, the virtual origin can be approximated as

$$\tilde{z}_0 \sim -\frac{32}{21\Gamma_0^{1/5}} - \frac{1}{7\Gamma_0^{6/5}}. \tag{2.59}$$

From figure 2.4b it can be concluded that the variation of the virtual origin with Γ_0 in expression (2.59) is a reasonable approximation for $\Gamma_0 > 0.2$.

The travel time of the fluid which is either formed as a part of the source discharge or is entrained by the jet or plume from the point of origin to a distance z is defined as

$$t(z) = \int_0^z \frac{\mathrm{d}z}{w}. \tag{2.60}$$

Equation (2.60) is evaluated in a dimensionless form, $\tilde{t} = 2\alpha w_0 t/b_0$, where

$$\tilde{t} = \int_1^{\tilde{z}} \frac{\tilde{Q}}{\tilde{M}} \mathrm{d}\tilde{z} = \int_1^{\tilde{Q}} \frac{\tilde{Q}\mathrm{d}\tilde{Q}}{(1+\Gamma_0(\tilde{Q}^2-1))^{3/5}}. \tag{2.61}$$

Again, there are two limiting cases, the first one is for a pure jet ($\Gamma_0 = 0$)

$$\tilde{t} = \int_1^{\tilde{Q}} \tilde{Q}\mathrm{d}\tilde{Q} = \frac{1}{2}(\tilde{Q}^2 - 1). \tag{2.62}$$

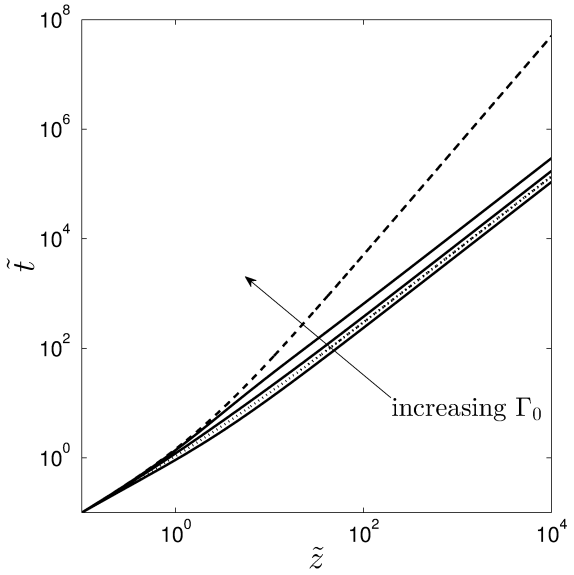

Figure 2.5: The numerical travel time against distance where $\Gamma_0 = 0$ (dashed line), 0.1, 0.5, 1 (dotted line) and 2.

Substituting in (2.50) gives

$$\tilde{t} = \frac{1}{2}\tilde{z}^2 + \tilde{z}. \tag{2.63}$$

The second case is for a plume ($\Gamma_0 > 0$) and can be evaluated through the same series expansion as in the case of (2.54) to give

$$\tilde{t} \sim \frac{5}{4}\left(\frac{5\tilde{z}}{3}\right)^{4/3}\Gamma_0^{-1/3}. \tag{2.64}$$

Figure 2.5 shows the variation of travel time with distance and volume flux. The velocity in the jet decays as $w \sim z^{-2}$ and in the plume as $w \sim z^{-1/3}$. Due to the different rates of velocity decay the travel time increases much more rapidly with distance from the nozzle for a jet than for a plume.

2.3.3 Combined chemistry and fluid flow model

The concentration of acid in a jet or plume decreases with distance from the point of origin through the combination of dilution and chemical reactions. The mass conservation equations for the jet and plume are

$$\frac{\mathrm{d}}{\mathrm{d}z}(\pi b^2 w[\mathrm{A}^-]) = 0, \tag{2.65}$$

$$\frac{\mathrm{d}}{\mathrm{d}z}(\pi b^2 w([\mathrm{MOH}] + [\mathrm{M}^+])) = 2\alpha\pi b w C_b^0. \tag{2.66}$$

The amount of acid within the jet or plume is described by (2.65) while (2.66) describes the increase in the alkali component within the jet or plume due to entrainment. The source conditions at $\tilde{z} = 0$ are

$$[\mathrm{A}^-] = C_a^0, \quad [\mathrm{MOH}] + [\mathrm{M}^+] = 0. \tag{2.67}$$

The concentration of acid decreases due to dilution, where

$$\tilde{Q} = 1 + \mathcal{D} = 1 + \frac{V_b}{V_a}. \tag{2.68}$$

The solutions to (2.65) and (2.66) can be expressed in terms of volume flux as this determines the dilution of the acid and the increase in concentration of the alkali within the jet or plume, *i.e.*

$$[\mathrm{A}^-] = \frac{C_a^0 V_a}{V_a + V_b} = \frac{C_a^0}{\tilde{Q}}, \quad [\mathrm{MOH}] + [\mathrm{M}^+] = \frac{C_b^0 V_b}{V_a + V_b} = \frac{C_b^0(\tilde{Q} - 1)}{\tilde{Q}}. \tag{2.69a, b}$$

The terms in (2.69*a, b*) are the rearranged from (2.4*a, b*) and are strictly valid for when the anion A^- is not present in the ambient and the alkali in the ambient has a uniform concentration of MOH. The condition for neutralisation is stated in (2.14). The expressions for neutralisation of a jet ($\Gamma_0 = 0$) can be obtained by combining (2.50), (2.68) and (2.14) resulting in

$$\tilde{z}_N = \frac{C_a^0}{C_b^0}\left(\frac{K_w^{1/2}}{K_b} + 1\right). \tag{2.70}$$

In the case of a plume ($\Gamma_0 > 0$), combining (2.54), (2.68) and (2.14) results in

$$\tilde{z}_N = \frac{5}{3\Gamma_0^{1/5}}\left[1 + \frac{C_a^0}{C_b^0}\left(\frac{K_w^{1/2}}{K_b} + 1\right)\right]^{3/5} + \tilde{z}_0. \tag{2.71}$$

Figure 2.6*a, b* shows the pH along the centre line in the jet and plume as a function of distance from the inlet, for the case of a strong acid injected into a strong alkali. In the case when the concentrations of acid and alkali are both high the results are insensitive to Γ_0 because the alkali solution is so strong that neutralisation occurs in the region $\tilde{Q} \sim 1$ and where the jet and plume dynamics are dominated by the source volume flux. When the concentration of the alkali is reduced then neutralisation occurs further away from the nozzle. As the neutralisation distance increases so does the

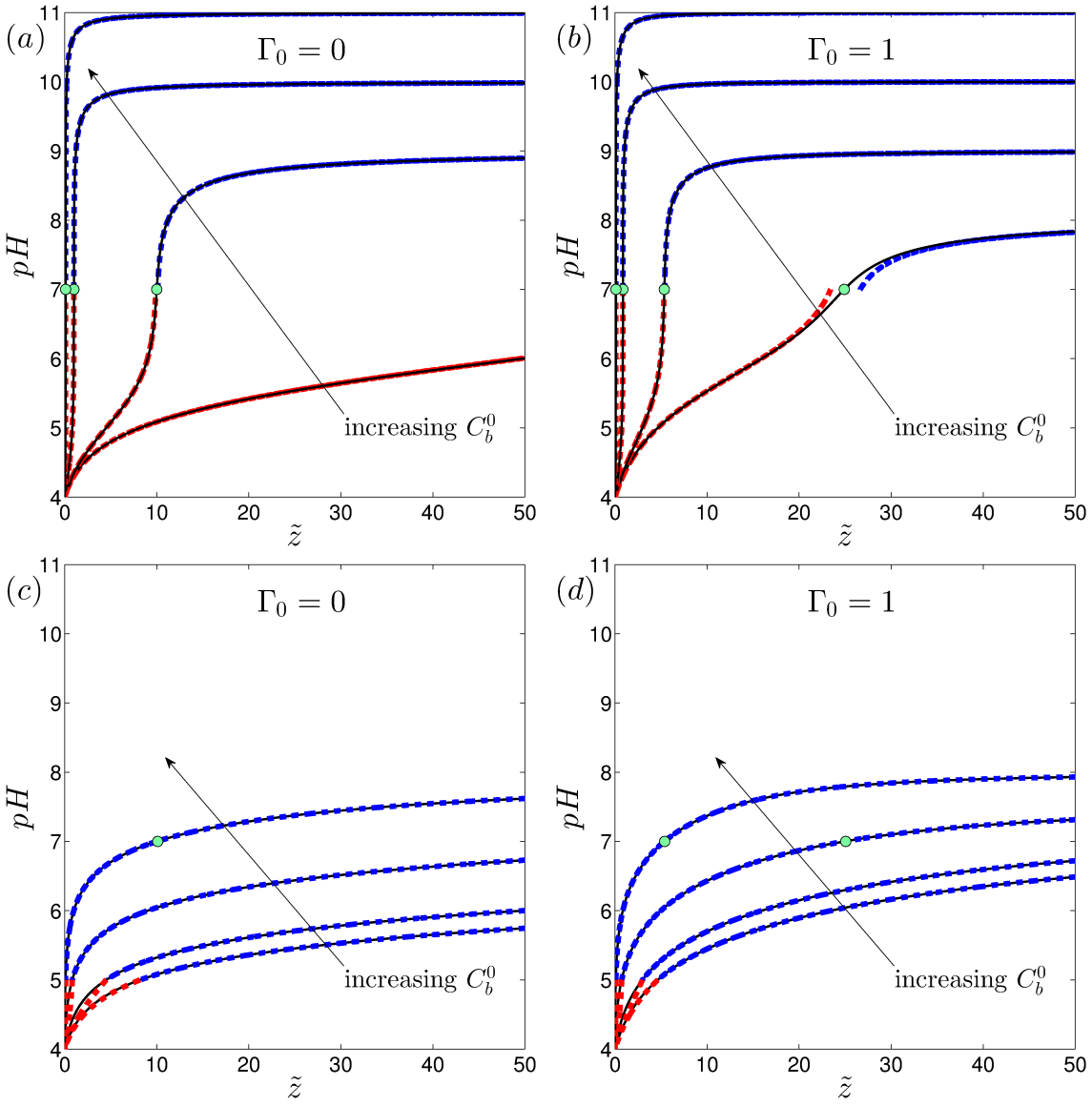

Figure 2.6: The pH of an acidic $C_a^0 = 10^{-4}$ mol/l jet (*a, c*) and plume (*b, d*) is plotted for four cases of initial ambient alkaline concentration $C_b^0 = 10^{-6}$, 10^{-5}, 10^{-4}, 10^{-3} mol/l. In (*a, b*) the alkaline ambient is strong ($K_b = 1$ mol/l) and in (*c, d*) the alkaline ambient is weak ($K_b = 10^{-9}$ mol/l). The points of neutralization are plotted as circles that are defined by (2.70) in the case of the jet and by (2.71) in the case of a plume. The solid lines correspond to (2.12) where $\mathcal{D} = \tilde{Q} - 1$ is expressed as a function of $\tilde{z}$ and the dashed lines are the same as in figure 2.2.

momentum flux in the case of a plume and that has a significant effect on increasing the neutralisation distance. The variation of the pH in the acidic discharge can then be calculated by expressing $\mathcal{D} = \tilde{Q} - 1$ as a function of $\tilde{z}$ and substituting this into (2.12) to determine $[H^+]$. The results for a strong acid injected into a weak alkali are shown in figure 2.6*c, d*. Both the weak and strong alkalis increase the acidic discharge pH by the same amount in approximately the same distance, $\tilde{z}$, up until a pH of 5. Far downstream, the pH of the discharge into a weak alkali solution has a minor dependence on C_b^0 than for the strong alkali case and a much lower pH.

2.4 Jets and plumes injected into a moving ambient

We now extend the analysis to include a moving ambient to account for the fact that the ship may be discharging whilst in transit. There are a number of contrasting models for describing the influence of an ambient flow on the dynamics of a turbulent plume. Models such as that of Fan (1967) and Jirka (2004) are based on semi-empirical relationships for entrainment that include drag in the momentum equations. The approach and discussions regarding closure reflect similar discussions regarding vortices in an ambient flow, where a number of researchers (*e.g.* Maxworthy (1972, 1974, 1977)) have incorporated drag forces (*i.e.* an integrated pressure over the surface of a jet) to account for the reduction of momentum in the jet due to ambient vortices. While there are circumstances where this is important, there is no support physically for a drag force as it requires a rigid surface. An alternative physical interpretation is that it arises from the detrainment of material from the plume (or vortex). The primary influence of an ambient flow is to generate a thrust on the plume due to entrainment which gives rise to the Lamb force (Lamb, 1932). Lamb force causes the jet to bend due to the entrainment of the jet being non uniformly affected by the cross flow. The model that we discuss in the following section incorporates this effect. The entrainment velocity depends on the relative velocity between the plume flow and ambient flow.

2.4.1 Defining equations

The conservation of mass and momentum are expressed in terms of how the volume flux Q and specific momentum flux parallel to the plume M evolve with distance s along

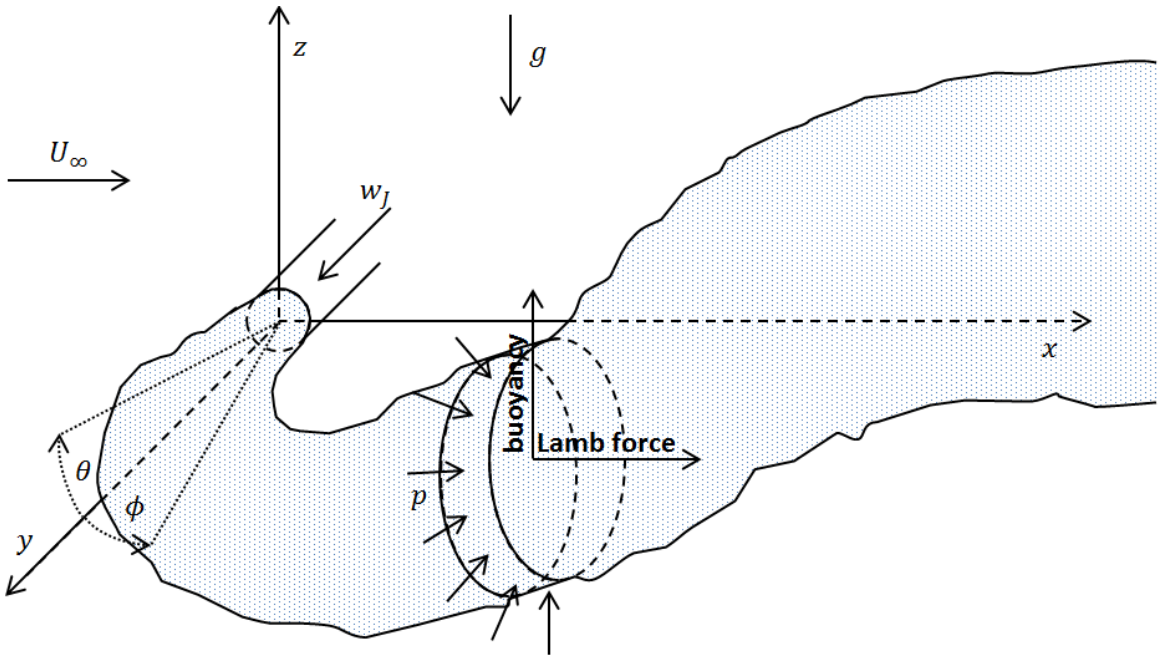

Figure 2.7: Schematic of a buoyant jet in a cross flow. In the case of horizontal discharges into a tangential ambient cross flow, at the source the angle of elevation θ_0 is 0 and the angle of azimuth ϕ_0 is $\pi/2$. The cross flow affects the entrainment velocity of the jet resulting in its deflection. This effect is described by the Lamb force.

the plume arc. The plume has a local radius b, velocity w_s along the plume trajectory and an entrainment velocity w_E. Two forces act on the plume - a vertical buoyancy force and a streamwise inviscid Lamb force. Consequently the general equations are described as

$$\frac{\mathrm{d}Q}{\mathrm{d}s} = 2\pi b w_E, \tag{2.72}$$

$$\frac{\mathrm{d}M_x}{\mathrm{d}s} = F_x, \tag{2.73}$$

$$\frac{\mathrm{d}M_y}{\mathrm{d}s} = 0, \tag{2.74}$$

$$\frac{\mathrm{d}M_z}{\mathrm{d}s} = F_z, \tag{2.75}$$

where the directions of x, y and z are indicated in figure 2.7.

We start our discussion of the streamwise force F_x. The Lamb force is generated when fluid is injected or removed at a constant rate in a uniform stream. The force is estimated from the loss of momentum flux from the ambient flow. In the absence of viscous effects the net force on the source can be evaluated using the momentum flux

argument based on a control surface

$$\boldsymbol{F} = \int_{S_B} p\hat{\boldsymbol{n}} \mathrm{d}S, \tag{2.76}$$

where $\hat{\boldsymbol{n}}$ is a unit vector. The force balance between the source and the rest of the domain is (including the momentum term where $\boldsymbol{w}$ is the velocity vector)

$$\boldsymbol{F} = -\int_{S_\infty = S_1 + S_2} p\hat{\boldsymbol{n}} \mathrm{d}S - \int_{S_\infty = S_1 + S_2} \rho(\boldsymbol{w} \cdot \hat{\boldsymbol{n}})\boldsymbol{w} \mathrm{d}S, \tag{2.77}$$

Since

$$p = p_\infty - \frac{1}{2}\rho w^2, \tag{2.78}$$

we can express (2.77) as

$$\boldsymbol{F} = -\int_{S_\infty} \left[\left(p_\infty - \frac{1}{2}\rho w^2 \right) \hat{\boldsymbol{n}} + \rho(\boldsymbol{w} \cdot \hat{\boldsymbol{n}})\boldsymbol{w} \right] \mathrm{d}S. \tag{2.79}$$

The force can be evaluated by considering the momentum flux through a control volume in the far field. For a three dimensional flow, we can take a long cylindrical tube of radius M and length $2L$. The source flow rate from a three dimensional source is expressed as

$$\boldsymbol{w} = \frac{Q}{4\pi r^2}\boldsymbol{r} + U_\infty, \tag{2.80}$$

where $\boldsymbol{r}$ is the position vector. In the limit of $L/M \gg 1$

$$\boldsymbol{F} = -\int_{S_1, S_2} \left[\frac{\rho U_\infty Q cos\theta}{2\pi r} n_y + \frac{\rho Q sin\theta}{2\pi r} n_y \left(\frac{U_\infty Q cos\theta}{2\pi r} \right) \right] \mathrm{d}S\hat{\boldsymbol{x}}, \tag{2.81}$$

$$\boldsymbol{F} = -\int_{-L}^{L} 2\rho \frac{QMU_\infty}{2\pi r(M^2 + x^2)} \mathrm{d}x\hat{\boldsymbol{x}}, \tag{2.82}$$

$$\boldsymbol{F} = \frac{-\rho Q U_\infty}{\pi} \left[\tan^{-1} \frac{x}{M} \right]_{-L}^{L} \hat{\boldsymbol{x}}, \tag{2.83}$$

$$\boldsymbol{F} = -\rho Q U_\infty \hat{\boldsymbol{x}}. \tag{2.84}$$

Thus for a sink flow, for instance entrainment, there is a force in the positive x-direction. This force is the basis of the jet description of Coelho & Hunt (1989); Eames & Hunt (2004).

In combination with Lamb and buoyancy forces, the governing equations can be

updated

$$\frac{\mathrm{d}Q}{\mathrm{d}s} = 2\pi\alpha w_E b, \tag{2.85}$$

$$\frac{\mathrm{d}(M\cos\theta\cos\phi)}{\mathrm{d}s} = 2\pi\alpha w_E U_\infty b\rho, \tag{2.86}$$

$$\frac{\mathrm{d}(M\cos\theta\sin\phi)}{\mathrm{d}s} = 0, \tag{2.87}$$

$$\frac{\mathrm{d}(M\sin\theta)}{\mathrm{d}s} = \pi b^2 g\left(\frac{\rho_a-\rho}{\rho_0}\right). \tag{2.88}$$

The relationship of the volume flux rate increase along the discharge trajectory is the same as in the stationary ambient case shown in (2.37) along the axis of discharge. The angles θ and ϕ are related to position through

$$\frac{\mathrm{d}x}{\mathrm{d}s} = \cos\theta\cos\phi, \tag{2.89}$$

$$\frac{\mathrm{d}y}{\mathrm{d}s} = \cos\theta\sin\theta, \tag{2.90}$$

$$\frac{\mathrm{d}z}{\mathrm{d}s} = \sin\theta. \tag{2.91}$$

The entrainment velocity w_E is defined here to depend on the relative velocity between the mean plume velocity and the ambient flow, *i.e.*

$$w_E = |w_s\sin\theta| + |w_s\cos\theta\cos\phi - U_\infty| + |w_s\cos\theta\sin\phi|. \tag{2.92}$$

The same closure was used by Woodhouse *et al.* (2013). The relationship between w_E and the properties of the flow is empirical, a number of alternatives are also available. In the study of Jirka (2004) with the Gaussian jet model, the entrainment rate is described as

$$\begin{aligned} w_E = 2\pi W w_c\left(\alpha_1 + \alpha_2\frac{\sin\theta}{F_r^2} + \alpha_3\frac{U_\infty\cos\theta\cos\phi}{w_c+U_\infty}\right) \\ + 2\pi\beta U_\infty\sqrt{1-\cos^2\theta\cos^2\phi}\alpha_4|\cos\theta\cos\phi|, \end{aligned} \tag{2.93}$$

where w_c is the velocity along the centre line and β is the width of a Gaussian jet. The entrainment coefficients α_1, α_2 and α_3 correspond to a pure jet, pure plume and pure wake. The last coefficient α_4 corresponds to a line puff and a thermal. F_r is the densimetric Froude number $F_r = w_c/\sqrt{\Delta g b}$ where Δg is the buoyancy on the centre line.

2.4.2 Dimensionless form of equations

The cross flow jet/plume model adopted here reduces to that of Morton *et al.* (1956) (2.34 - 2.36) in the limit of $U_\infty \to 0$ and for vertical discharges ($\theta = \pi/2$). The model is non-dimensionalised using $\tilde{Q} = Q/Q_0$, $\tilde{M} = M/M_0$, $\tilde{s} = s/L$, where $L = Q_0/2\pi^{1/2}\alpha(M_0\rho_0)^{1/2}$ giving

$$\frac{\mathrm{d}\tilde{Q}}{\mathrm{d}\tilde{s}} = \tilde{M}^{1/2}\tilde{w}_E, \tag{2.94}$$

$$\frac{\mathrm{d}(\tilde{M}\cos\theta\cos\phi)}{\mathrm{d}\tilde{s}} = \Lambda\tilde{M}^{1/2}\tilde{w}_E, \tag{2.95}$$

$$\frac{\mathrm{d}(\tilde{M}\cos\theta\sin\phi)}{\mathrm{d}\tilde{s}} = 0, \tag{2.96}$$

$$\frac{\mathrm{d}(\tilde{M}\sin\theta)}{\mathrm{d}\tilde{s}} = \frac{\Gamma_0\tilde{Q}}{\tilde{M}}, \tag{2.97}$$

where

$$\Gamma_0 = \frac{5B_0Q_0^2}{8\alpha\pi^{1/2}M_0^{5/2}}, \tag{2.98}$$

and

$$\Lambda = \frac{U_\infty}{w_J}. \tag{2.99}$$

The focus is on unstratified environments where the buoyancy flux $B = \pi b^2 w_J(\rho_a - \rho/\rho_0)g = B_0$ is constant. The dimensionless entrainment velocity is

$$\tilde{w}_E = |\sin\theta| + \left|\frac{\cos\theta_0\cos\phi_0 + \Lambda}{\tilde{M}}\right| + |\cos\theta\sin\phi|\,. \tag{2.100}$$

The system of equations (2.94), (2.95), (2.96), (2.97) and (2.100) is closed and contain four unknowns M, Q, θ and ϕ that are solved as a function of s. Combining (2.85), (2.86), (2.87) and (2.88) and we obtain

$$\tilde{M}\cos\theta\cos\phi = \cos\theta_0\cos\phi_0 + \Lambda(\tilde{Q} - 1). \tag{2.101}$$

The system of equations can be reduced to a system of coupled equations in M, θ and ϕ with dependence on s by eliminating $\tilde{Q}$. Most are usually solved analytically as functions of position $\tilde{x}$, we analyse the problem as a function of, S, distance along the trajectory. The plume trajectory can be reconstructed by integration

$$\frac{\mathrm{d}\tilde{x}}{\mathrm{d}\tilde{s}} = \cos\theta\cos\phi, \qquad \frac{\mathrm{d}\tilde{y}}{\mathrm{d}\tilde{s}} = \cos\theta\sin\phi, \qquad \frac{\mathrm{d}\tilde{z}}{\mathrm{d}\tilde{s}} = \sin\theta. \tag{2.102}$$

Order-of-magnitude estimates for each term are given below

$$\underbrace{\frac{\mathrm{d}}{\mathrm{d}\tilde{s}}\left(\tilde{M}\frac{\mathrm{d}\tilde{x}}{\mathrm{d}\tilde{s}}\right)}_{\tilde{M}\tilde{x}/\tilde{s}^2} = \Lambda\tilde{M}^{\frac{1}{2}}\left(\underbrace{\left|\frac{\mathrm{d}\tilde{z}}{\mathrm{d}\tilde{s}}\right|}_{\tilde{z}/\tilde{s}} + \underbrace{\frac{|\cos\theta_0\cos\phi_0+\Lambda|+|\cos\theta_0\sin\phi_0|}{\tilde{M}}}_{(|\cos\theta_0\cos\phi_0+\Lambda|+|\cos\theta_0\sin\theta_0|)M^{-1}}\right), \tag{2.103}$$

$$\underbrace{\frac{\mathrm{d}}{\mathrm{d}\tilde{s}}\left(\tilde{M}\frac{\mathrm{d}\tilde{z}}{\mathrm{d}\tilde{s}}\right)}_{\tilde{M}\tilde{z}/\tilde{s}^2} = \frac{\Gamma_0}{\tilde{M}}\left(\underbrace{\frac{\tilde{M}}{\Lambda}\frac{\mathrm{d}\tilde{x}}{\mathrm{d}\tilde{s}}}_{\tilde{x}/\Lambda\tilde{s}} + \underbrace{1-\frac{1}{\Lambda}\cos\theta_0\cos\phi_0}_{(1-\Lambda^{-1}\cos\theta_0\cos\phi_0)}\right), \tag{2.104}$$

$$\underbrace{\frac{\mathrm{d}\tilde{y}}{\mathrm{d}\tilde{s}}}_{\tilde{y}/\tilde{s}} = \underbrace{\frac{\cos\theta_0\sin\phi_0}{\tilde{M}}}_{\cos\theta_0\sin\phi_0/\tilde{M}}. \tag{2.105}$$

The fourth equation required for closing the above system is

$$\left(\frac{\mathrm{d}\tilde{x}}{\mathrm{d}\tilde{s}}\right)^2 + \left(\frac{\mathrm{d}\tilde{y}}{\mathrm{d}\tilde{s}}\right)^2 + \left(\frac{\mathrm{d}\tilde{z}}{\mathrm{d}\tilde{s}}\right)^2 = 1. \tag{2.106}$$

Equations (2.103), (2.104), (2.105) and (2.106) are solved subject to an source condition that at $\tilde{s}=0$,

$$\tilde{M}=1, \qquad \frac{\mathrm{d}\tilde{x}}{\mathrm{d}\tilde{s}}=\cos\theta_0\cos\phi_0, \qquad \frac{\mathrm{d}\tilde{y}}{\mathrm{d}\tilde{s}}=\cos\theta_0\sin\phi_0, \qquad \frac{\mathrm{d}\tilde{z}}{\mathrm{d}\tilde{s}}=\sin\theta_0. \tag{2.107}$$

The various regimes and scaling analysis for the turbulent plumes injected into an ambient flow are analysed. The focus on the scaling analysis is to determine the shape of the plume and the volume flux $\tilde{Q}$ as a function of distance from the plume nozzle. These quantities can be used to estimate the pH of a discharge with distance from the origin.

In practice the scrubber effluent is discharged horizontally ($\theta_0=0$) into seawater at a right angle to the ambient flow ($\phi_0=\pi/2$). Container ships reach a maximum speed of 26 knots which equates to 13.4 m/s. As a result the ratio between the ship speed and rate of discharge Λ varies approximately from 0 to 10.

2.4.3 Asymptotic expressions for vertical jets ($\theta_0 = \pi/2$, $\phi_0 = \pi/2$, $\Gamma_0 = 0$)

The conservation of momentum in the streamwise and vertical directions reduce to

$$\frac{\mathrm{d}}{\mathrm{d}\tilde{s}}\left(\tilde{M}\frac{\mathrm{d}\tilde{x}}{\mathrm{d}\tilde{s}}\right) = \Lambda\tilde{M}^{1/2}\left(\frac{\mathrm{d}\tilde{z}}{\mathrm{d}\tilde{s}} + \frac{\Lambda}{\tilde{M}}\right), \tag{2.108}$$

$$\frac{\mathrm{d}}{\mathrm{d}\tilde{s}}\left(\tilde{M}\frac{\mathrm{d}\tilde{z}}{\mathrm{d}\tilde{s}}\right) = 0, \tag{2.109}$$

respectively. It is assumed that $\mathrm{d}\tilde{z}/\mathrm{d}\tilde{s} > 0$. Rearranging (2.109), we obtain a relationship between the vertical position and momentum flux

$$\frac{\mathrm{d}\tilde{z}}{\mathrm{d}\tilde{s}} = \frac{1}{\tilde{M}} \quad \Rightarrow \quad \tilde{z} = \int_0^{\tilde{s}} \frac{1}{\tilde{M}}\mathrm{d}\tilde{s}. \tag{2.110}$$

Substituting (2.110) into (2.108) gives

$$\frac{\mathrm{d}}{\mathrm{d}\tilde{s}}\left(\tilde{M}\frac{\mathrm{d}\tilde{x}}{\mathrm{d}\tilde{s}}\right) = \frac{\Lambda}{\tilde{M}^{1/2}}\left(1+\Lambda\right), \tag{2.111}$$

and using (2.106)

$$\frac{\mathrm{d}\tilde{x}}{\mathrm{d}\tilde{s}} = \left(1 - \left(\frac{1}{\tilde{M}}\right)^2\right)^{1/2}, \tag{2.112}$$

that combined with (2.111) gives

$$\frac{\mathrm{d}}{\mathrm{d}\tilde{s}}\left(\tilde{M}\left(1 - \left(\frac{1}{\tilde{M}}\right)^2\right)^{1/2}\right) = \frac{\Lambda}{\tilde{M}^{1/2}}(1+\Lambda), \tag{2.113}$$

or

$$\Lambda(1+\Lambda)\tilde{s} = \int_1^{\tilde{M}} \frac{\tilde{M}^{3/2}}{(\tilde{M}^2-1)^{1/2}}\mathrm{d}\tilde{M}. \tag{2.114}$$

This gives an exact, but implicit, relationship between $\tilde{M}$ and $\tilde{s}$. The relationship between $\tilde{Q} = \mathcal{D} + 1$ and $\tilde{M}$ in (2.101) enables the jet dilution to be determined from

$$\mathcal{D} = \frac{\tilde{M}}{\Lambda}\frac{\mathrm{d}\tilde{x}}{\mathrm{d}\tilde{s}} = \frac{(\tilde{M}^2-1)^{1/2}}{\Lambda}. \tag{2.115}$$

There is no closed form solution to (2.114) but approximate solutions can be obtained in the near and far field.

Near field ($\mathrm{d}\tilde{z}/\mathrm{d}\tilde{s} = 1$)

In the near field region $\tilde{M} \simeq 1$, therefore, the integral in (2.114) can be manipulated through a quadratic inequality to become

$$\Lambda(1+\Lambda)\tilde{s} = \int_1^{\tilde{M}} \frac{\tilde{M}^{3/2}}{(\tilde{M}^2-1)^{1/2}}\mathrm{d}\tilde{M} \approx \int_1^{\tilde{M}} \frac{1}{\sqrt{2}(\tilde{M}-1)^{1/2}}\mathrm{d}\tilde{M} = \sqrt{2}(\tilde{M}-1)^{1/2}. \quad (2.116)$$

An expression for $\tilde{M}$, therefore, becomes

$$\tilde{M} \simeq 1 + \frac{1}{2}(\Lambda(1+\Lambda))^2\tilde{s}^2. \quad (2.117)$$

Rearranging (2.112) results in

$$\frac{\mathrm{d}\tilde{x}}{\mathrm{d}\tilde{s}} = \frac{(\tilde{M}^2-1)^{1/2}}{\tilde{M}} = \frac{\sqrt{2}(\tilde{M}-1)^{1/2}}{\tilde{M}}. \quad (2.118)$$

The denominator in (2.118) can be ignored due to $\tilde{M} \approx 1$ and (2.116) can be substituted into (2.118) to give an expression for $\tilde{x}$

$$\tilde{x} \approx \frac{1}{2}\Lambda(\Lambda+1)\tilde{s}^2. \quad (2.119)$$

In the near field scenario ($\tilde{M} \approx 1$), $\tilde{z} \approx \tilde{s}$ eliminating $\tilde{s}$ from (2.119) to give

$$\tilde{z} \simeq \left(\frac{2\tilde{x}}{\Lambda(\Lambda+1)}\right)^{1/2}. \quad (2.120)$$

The quadratic dependence of $\tilde{z}$ on $\tilde{x}$ is anticipated because of the constant Lamb body force, giving a result similar to what is expected for particles falling under gravity (*e.g.* $\tilde{x} \sim (1/2)gt^2$). From the substitution of (2.115) into (2.116), dilution along the discharge trajectory is

$$\mathcal{D} = (1+\Lambda)\tilde{s}. \quad (2.121)$$

In the limit of $\Lambda \to 0$, we retrieve the results for a jet in a stagnant ambient *i.e.* $\mathcal{D} \simeq \tilde{s}$. It can be determined that in the near field, the influence of the cross flow is to increase entrainment. The near field analysis is valid when $|\tilde{M}-1| \ll 1$, which requires

$$\tilde{s} \ll \frac{\mathcal{D}}{\Lambda(1+\Lambda)}. \quad (2.122)$$

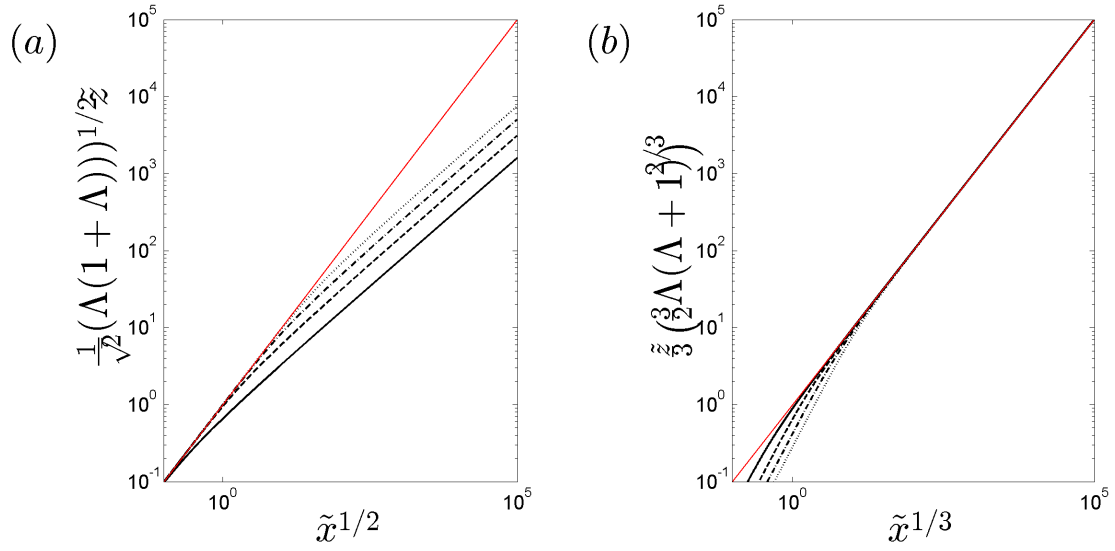

Figure 2.8: Deflection of a vertical jet in near (a), corresponding to (2.120), and far (b), corresponding to (2.125), fields for a range of $\Lambda = 10$ (solid line), 1 (dashed line), 0.1 (dash-dot line) and 0.01 (dotted line).

Far field ($\mathrm{d}\tilde{x}/\mathrm{d}\tilde{s} = 1$)

The integral in (2.114) can be simplified under the assumption that $\tilde{M} \gg 1$, to give

$$\Lambda(1+\Lambda)\tilde{s} = \int_1^{\tilde{M}} \frac{\tilde{M}^{3/2}}{(\tilde{M}^2-1)^{1/2}}\mathrm{d}\tilde{M} \approx \int_1^{\tilde{M}} \tilde{M}^{1/2}\mathrm{d}\tilde{M} \approx \frac{2}{3}(\tilde{M}^{3/2}-1), \tag{2.123}$$

or

$$\tilde{M} \approx \left(\frac{3\Lambda}{2}(1+\Lambda)\tilde{s}+1\right)^{2/3}. \tag{2.124}$$

In this regime the relationship between $\tilde{z}$ and $\tilde{s}$ is given in (2.110). Substituting (2.124) into (2.110) results in

$$\tilde{z} = \int_0^{\tilde{s}} \frac{\mathrm{d}\tilde{s}}{\left(\frac{3}{2}\Lambda(\Lambda+1)\tilde{s}+1\right)^{2/3}} \simeq 3\left(\frac{3}{2}\Lambda(\Lambda+1)\right)^{-2/3}\tilde{s}^{1/3}. \tag{2.125}$$

The dilution in the far field, where ($\mathrm{d}\tilde{x}/\mathrm{d}\tilde{s}$) term becomes 1, can be obtained from the substitution of (2.124) into (2.115) that results in

$$\mathcal{D} \approx \frac{\left(\frac{3}{2}\Lambda(1+\Lambda)\tilde{s}+1\right)^{2/3}}{\Lambda} = \left(\frac{3}{2}\right)^{2/3}\Lambda^{-1/3}(1+\Lambda)^{2/3}\tilde{x}^{2/3}. \tag{2.126}$$

To assess the influence of near and far fields, a numerical study was undertaken that is presented in figures 2.8 and 2.9. In the near field the dilution is affected significantly

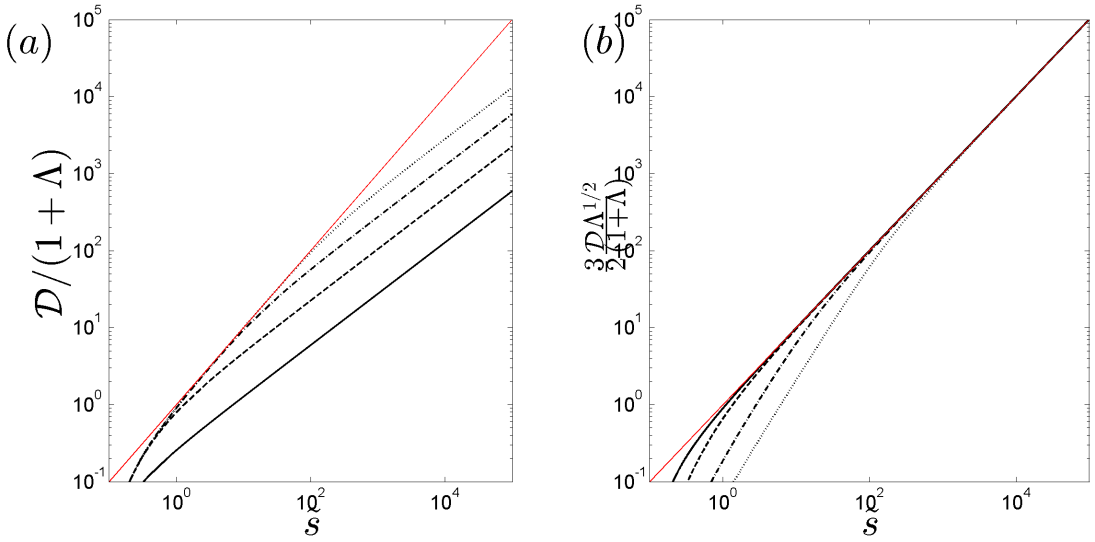

Figure 2.9: Dilution of a vertical jet in near (a), corresponding to (2.121), and far (b), corresponding to (2.126), fields for a range of $\Lambda = 10$ (solid line), 1 (dashed line), 0.1 (dash-dot line) and 0.01 (dotted line).

by the cross flow but its influence decreases with distance from the point of discharge. For the far field analysis to be valid, we require $\tilde{M} \gg 1$ or $\Lambda(1+\Lambda)\tilde{s} \sim 1$.

2.4.4 Asymptotic expressions for vertical plumes ($\theta_0 = \pi/2$, $\phi_0 = \pi/2$, $\Gamma_0 = 1$)

The change in momentum in the direction of $\tilde{x}$ has already been manipulated to give (2.114). The change in momentum in the $\tilde{z}$ direction has a dependence on Γ_0 and after the application of source conditions it reduces to

$$\frac{\mathrm{d}}{\mathrm{d}\tilde{s}}\left(\tilde{M}\frac{\mathrm{d}\tilde{z}}{\mathrm{d}\tilde{s}}\right) = \frac{\Gamma_0}{\tilde{M}}\left(\frac{\tilde{M}}{\Lambda}\frac{\mathrm{d}\tilde{x}}{\mathrm{d}\tilde{s}} + 1\right). \tag{2.127}$$

Near field ($\mathrm{d}\tilde{z}/\mathrm{d}\tilde{s} = 1$)

From (2.127)

$$\frac{\mathrm{d}\tilde{x}}{\mathrm{d}\tilde{s}} = \frac{\Lambda}{\Gamma_0}\frac{\mathrm{d}\tilde{M}}{\mathrm{d}\tilde{s}} - \frac{\Lambda}{\tilde{M}}. \tag{2.128}$$

Combining (2.128) and (2.111) gives

$$\frac{\mathrm{d}^2\tilde{M}^2}{\mathrm{d}\tilde{s}^2} = 2\Gamma_0\tilde{M}^{1/2}\left(1 + \frac{\Lambda}{\tilde{M}}\right). \tag{2.129}$$

This is a second order ordinary differential equation which can be analysed using standard analytical techniques by substituting $N = \tilde{M}^2$, to give

$$\frac{\mathrm{d}^2 N}{\mathrm{d}\tilde{s}^2} = 2\Gamma_0 N^{1/4}\left(1 + \frac{\Lambda}{N^{1/2}}\right). \tag{2.130}$$

By equating $L = \mathrm{d}N/\mathrm{d}\tilde{s}$, we generate an ordinary differential equation with two variables (L,N),

$$L\frac{\mathrm{d}L}{\mathrm{d}N} = 2\Gamma_0 N^{1/4}\left(1 + \frac{\Lambda}{N^{1/2}}\right). \tag{2.131}$$

Since $\mathrm{d}M/\mathrm{d}\tilde{s} = 0$ at $\tilde{s} = 0$ and after some manipulation, integrating (2.131) gives

$$L = \frac{4}{\sqrt{5}}\Gamma_0^{1/2} N^{5/8} + \frac{4}{\sqrt{3}}\Gamma_0^{1/2}\Lambda^{1/2} N^{3/8}. \tag{2.132}$$

Substituting $\mathrm{d}N/\mathrm{d}\tilde{s} = L$ into (2.132) and integrating, we obtain the scaling of

$$\tilde{M} \sim \tilde{s}^{4/3}, \quad \tilde{M} \sim \tilde{s}^{4/5}. \tag{2.133}$$

In the near field the influence of the cross flow on the deflection of the jet is less significant, therefore, justifying the use of the scaling without Λ, *i.e.* $\tilde{M} \sim \tilde{s}^{4/3}$. Using this scaling and substituting into (2.128), we obtain

$$\tilde{z} \sim \frac{\Lambda}{\Gamma_0}\tilde{x}^{4/3}. \tag{2.134}$$

The plume rises much more rapidly than a jet in the near field with a weaker dependence on the ambient flow. Using (2.133) and (2.101) the scaling for dilution in the near field is

$$\mathcal{D} \sim \tilde{s}^{4/3}, \tag{2.135}$$

and it is shown in figure 2.11*a*.

Far field ($\mathrm{d}\tilde{x}/\mathrm{d}\tilde{s} = 1$)

In the far field the plume has turned sufficiently so that (2.127) can be rearranged into

$$\frac{\mathrm{d}\tilde{z}}{\mathrm{d}\tilde{s}} = \frac{1}{\Lambda\tilde{M}^{1/2}}\frac{\mathrm{d}\tilde{M}}{\mathrm{d}\tilde{s}} - \frac{\Lambda}{\tilde{M}}. \tag{2.136}$$

Substituting (2.136) into (2.103) gives

$$\frac{\mathrm{d}}{\mathrm{d}\tilde{s}}\left(\frac{\tilde{M}^{1/2}}{\Lambda}\left(\frac{\mathrm{d}\tilde{M}}{\mathrm{d}\tilde{s}}\right)\right)=\frac{\Gamma_0}{\tilde{M}}\left(1+\frac{\tilde{M}}{\Lambda}\right), \tag{2.137}$$

that after manipulation becomes

$$\frac{2}{3}\frac{\mathrm{d}\tilde{M}^{3/2}}{\mathrm{d}\tilde{s}^2}=\frac{\Lambda\Gamma_0}{\tilde{M}}\left(1+\frac{\tilde{M}}{\Lambda}\right), \tag{2.138}$$

and can be approximated to give

$$\tilde{M}\simeq\left(\frac{4}{3}\right)^{2/3}\Gamma_0^{2/3}\tilde{s}^{4/3}. \tag{2.139}$$

Since

$$\tilde{z}=\frac{2}{\Lambda}(\tilde{M}^{1/2}-1)-\int_1^{\tilde{s}}\frac{\Lambda+1}{\tilde{M}}\mathrm{d}\tilde{s}, \tag{2.140}$$

then

$$\tilde{z}=\frac{2}{\Lambda}\left(\frac{3}{4}\right)^{1/2}\Gamma_0^{1/3}\tilde{x}^{2/3}-\frac{4(\Lambda+1)}{3\Gamma_0^{2/3}}\left[\frac{-3}{\tilde{x}^{1/3}}\right]_1^{\tilde{x}}, \tag{2.141}$$

that approximately scales as

$$\tilde{z}\sim\frac{2}{\Lambda}\left(\frac{3}{4}\right)^{1/2}\Gamma_0^{1/3}\tilde{x}^{2/3}. \tag{2.142}$$

A range of Λ values are plotted in figure 2.10 for the deflection of a vertical plume. The dilution increases as

$$\mathcal{D}=\frac{\tilde{M}-1}{\Lambda}\sim\frac{3}{4}\Gamma_0^{2/3}\Lambda^{-1}\tilde{x}^{4/3}, \tag{2.143}$$

which grows significantly faster than in the case of a jet. The scaling analysis shows a trajectory collapse of $\tilde{z}\sim\tilde{x}^{\gamma}$ for a range of $\gamma=2/3-3/4$. A comparison with the dilution in the near field analysis is shown in figure 2.11. It is clear that the effect of cross flow is to increase the amount of dilution in the plume, however, when the plume is turned over into the direction of the ambient flow the near field scaling does not apply any more and the far field scaling should be followed.

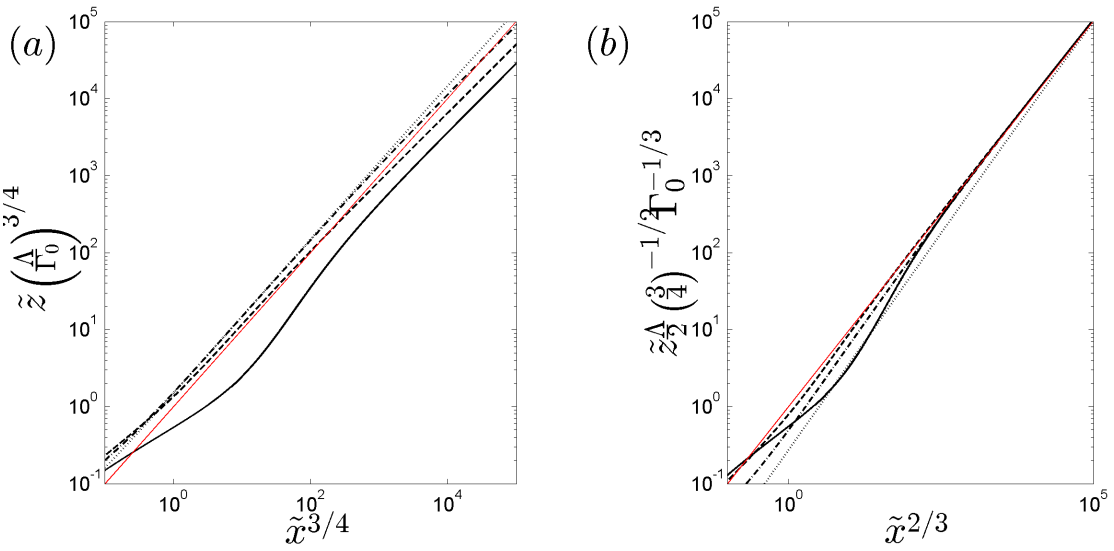

Figure 2.10: Vertical plume deflection in the near field (a) and far field (b) corresponding to (2.134) and (2.142) for a range of $\Lambda = 10$ (solid line), 1 (dashed line), 0.1 (dash-dot line) and 0.01 (dotted line).

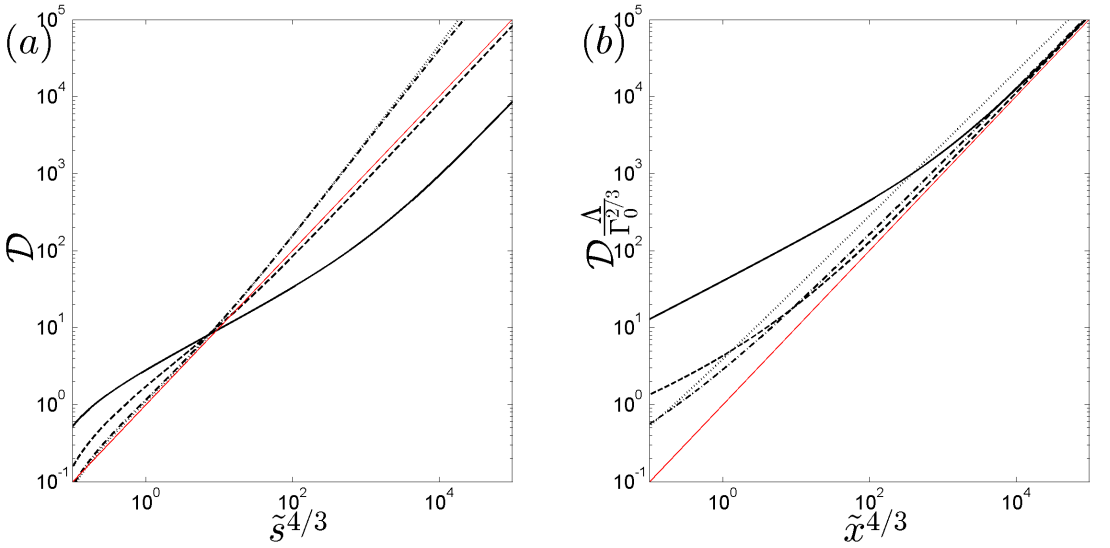

Figure 2.11: Vertical plume dilution in the near (a) and (b) far fields corresponding to (2.135) and (2.143) respectively for a range of $\Lambda = 10$ (solid line), 1 (dashed line), 0.1 (dash-dot line) and 0.01 (dotted line).

2.4.5 Horizontal discharges into a moving ambient ($\theta_0 = 0$, $\phi_0 = \pi/2$)

For a horizontal jet, where $\Gamma_0 = 0$, the discharge behaves the same way as vertical injection with the direction of travel in the $x - y$ plane since

$$\frac{\mathrm{d}\tilde{z}}{\mathrm{d}\tilde{s}} = 0. \tag{2.144}$$

Since

$$\frac{\mathrm{d}\tilde{y}}{\mathrm{d}\tilde{s}} = \frac{1}{\tilde{M}}, \tag{2.145}$$

the rate of progress downstream is

$$\frac{\mathrm{d}\tilde{x}}{\mathrm{d}\tilde{s}} = \left(1 - \frac{1}{\tilde{M}^2}\right)^{1/2}, \tag{2.146}$$

the same as (2.112). Therefore, the (y, x) trajectory is the same as the (z, x) trajectory of a vertical jet. For a plume the trajectory is now three dimensional.

Near field ($\mathrm{d}\tilde{y}/\mathrm{d}\tilde{s} = 1$)

In this regime we can determine

$$M = 1, \tag{2.147}$$

from (2.105). The other governing equations (2.103) and (2.104) give

$$\frac{\mathrm{d}}{\mathrm{d}\tilde{s}}\left(\tilde{M}\frac{\mathrm{d}\tilde{x}}{\mathrm{d}\tilde{s}}\right) \simeq \Lambda(\Lambda + 1), \tag{2.148}$$

and

$$\frac{\mathrm{d}}{\mathrm{d}\tilde{s}}\left(\tilde{M}\frac{\mathrm{d}\tilde{z}}{\mathrm{d}\tilde{s}}\right) \simeq \Gamma_0. \tag{2.149}$$

These expressions can be integrated to produce scalings of

$$\tilde{x} = \frac{1}{2}\tilde{y}^2\Lambda(\Lambda + 1), \tag{2.150}$$

and

$$\tilde{z} = \frac{1}{2}\tilde{y}^2\Gamma_0. \tag{2.151}$$

It can be shown that the near field scaling is valid for $\Lambda \leq 1$ and $\tilde{y} < 1$. In this regime the dilution and deflection have the same relationship as the vertical jet.

Far field ($\mathrm{d}\tilde{x}/\mathrm{d}\tilde{s} = 1$)

In the far field

$$\frac{\mathrm{d}\tilde{z}}{\mathrm{d}\tilde{s}} = \frac{1}{\Lambda \tilde{M}^{1/2}} \frac{\mathrm{d}\tilde{M}}{\mathrm{d}\tilde{s}}, \tag{2.152}$$

so that

$$\frac{\mathrm{d}}{\mathrm{d}\tilde{s}} \left(\frac{\tilde{M}^{1/2}}{\Lambda} \frac{\mathrm{d}\tilde{M}}{\mathrm{d}\tilde{s}} \right) = \frac{\Gamma_0}{\Lambda}. \tag{2.153}$$

The momentum flux can be inferred from

$$\tilde{M} \sim \left(\frac{3}{4} \Gamma_0 \tilde{s}^2 + 1 \right)^{2/3}. \tag{2.154}$$

The first order approximation of the momentum flux can be used to estimate the penetration distance $\tilde{y}_\infty$, into the ambient flow, *i.e.*

$$\tilde{y}_\infty \simeq \int_0^\infty \frac{\mathrm{d}\tilde{s}}{\tilde{M}} \sim \int_0^\infty \frac{\mathrm{d}\tilde{s}}{\left(\frac{3}{4} \Gamma_0 \tilde{s}^2 + 1 \right)^{2/3}} \sim \frac{1}{\Gamma_0^{2/3}}. \tag{2.155}$$

The deflection due to buoyancy is

$$\tilde{z} \sim \frac{2\tilde{M}^{1/2}}{\Lambda} \sim \frac{(6\Gamma_0 \tilde{s}^2)^{1/3}}{\Lambda}. \tag{2.156}$$

The expressions for deflection are plotted in figure 2.12 for a range of Λ values. The maximum distance in the direction of discharge ($\tilde{y}_\infty$) reached for a horizontal plume is shown in figure 2.13*b*. For low values of $\Lambda < 0.1$ the distance scales to the power of -2/3, however, a sharp transition occurs beyond that point to a scaling of -1. The expression for dilution can be obtained by substituting (2.154) into (2.101) to give

$$\mathcal{D} = \frac{1}{\Lambda} \left(\frac{3}{4} \Gamma_0 \tilde{s}^2 + 1 \right)^{2/3}, \tag{2.157}$$

the results are plotted in figure 2.13*a*.

2.4.6 pH variation of discharges in a moving ambient

The cross flow model is applied to examine the pH of a buoyant horizontal discharge into a river or sea. The difference between discharges into a cross flow as opposed to a stationary ambient is that the volume flow rate of the jet/plume increases faster as it is being turned in the direction of the ambient flow. The relationship between volume flux increase and dilution is the same as described in §2.3.3. The typical values of Λ

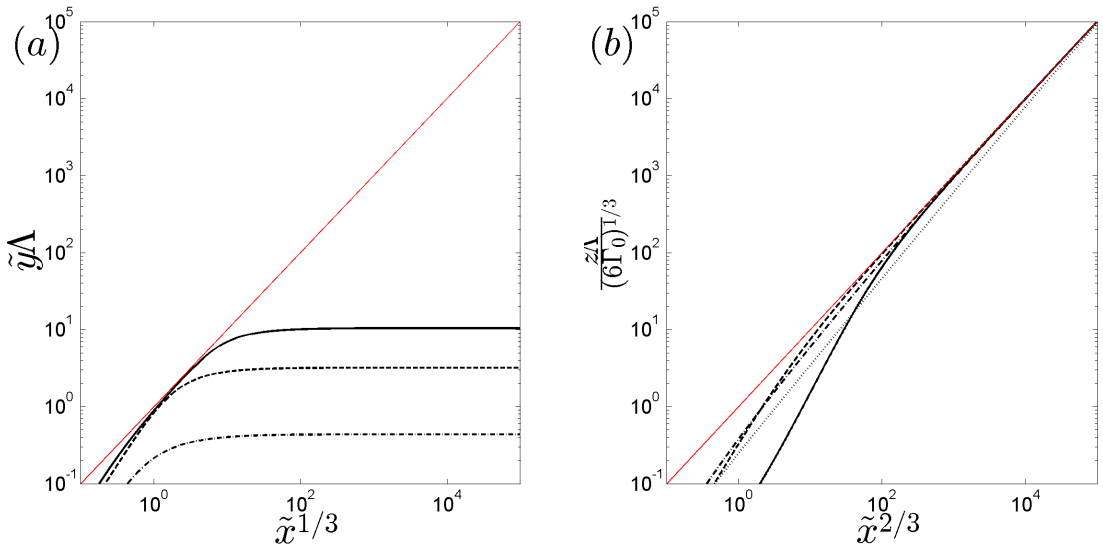

Figure 2.12: Deflection of a horizontal plume in the far field corresponding to (2.156) for a range of $\Lambda = 10$ (solid line), 1 (dashed line), 0.1 (dash-dot line) and 0.01 (dotted line).

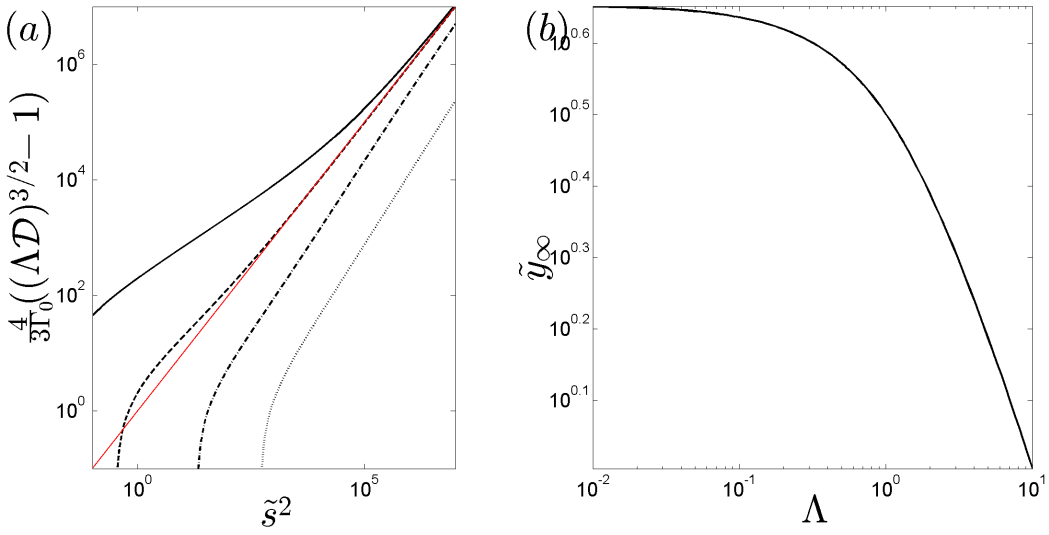

Figure 2.13: In (a) the far field dilution of a horizontal plume in cross flow for a range of $\Lambda = 10$ (solid line), 1 (dashed line), 0.1 (dash-dot line) and 0.01 (dotted line). In (b) the maximum distance along the axis of discharge reached by a horizontal plume

are around 10 where the typical speed of a ship is 13.4 m/s and the discharge rate between 1-2 m/s. Additionally, the rate of discharge is quite rapid, therefore, $\Gamma_0 \ll 1$ so figure 2.8 is applicable where

$$\tilde{z} = 3\left(\frac{3}{2}\Lambda(\Lambda+1)\right)^{-2/3}\tilde{x}^{1/3}, \tag{2.158}$$

and

$$\mathcal{D} \sim \left(\frac{3}{2}\right)^{2/3}\Lambda^{-1/3}(1+\Lambda)^{2/3}\tilde{x}^{2/3}. \tag{2.159}$$

In this regime the H^+ concentration change can be predicted based on the substitution of (2.159) into (2.20)

$$[H^+] \simeq \frac{C_a^0 - \left(\frac{3}{2}\right)^{2/3}\Lambda^{-1/3}(1+\Lambda)^{2/3}\tilde{x}^{2/3}C_b}{1+\left(\frac{3}{2}\right)^{2/3}\Lambda^{-1/3}(1+\Lambda)^{2/3}\tilde{x}^{2/3}}, \tag{2.160}$$

when it is far from neutralisation. In the case of a strong cross flow, the important length scale is distance downstream as opposed to the discharge direction in the case of a stationary ambient. The rate of neutralisation is significantly increased mainly due to the cross flow component boosting dilution from a linear increase to the power of 3/2 in the case of a jet.

In figures 2.14 and 2.15 a comparison is made with earlier work in figure 2.6. Overall there is very little variation in the pH recovery along the trajectory of the jet/plume $\tilde{s}$ for the non cross flow and cross flow case. In the case of a jet the effect of cross flow is to significantly increase the dilution and therefore pH recovery in the discharge. In the plume case a subtle change is observed in how cross flow increases dilution in the near field but then reduces it further along the trajectory. This means that the entrainment mechanism of the plume is negatively affected by the presence of a strong cross flow.

Figure 2.16 shows qualitatively the dilution of an acidic plume in an ambient stream. The source pH of the discharge is 3 and the pH of the ambient is 8. The relationship between distance and dilution is solved numerically and as expected, the dilution rapidly raises the source pH of the discharge but the rate of pH recovery decreases with distance from the point of discharge.

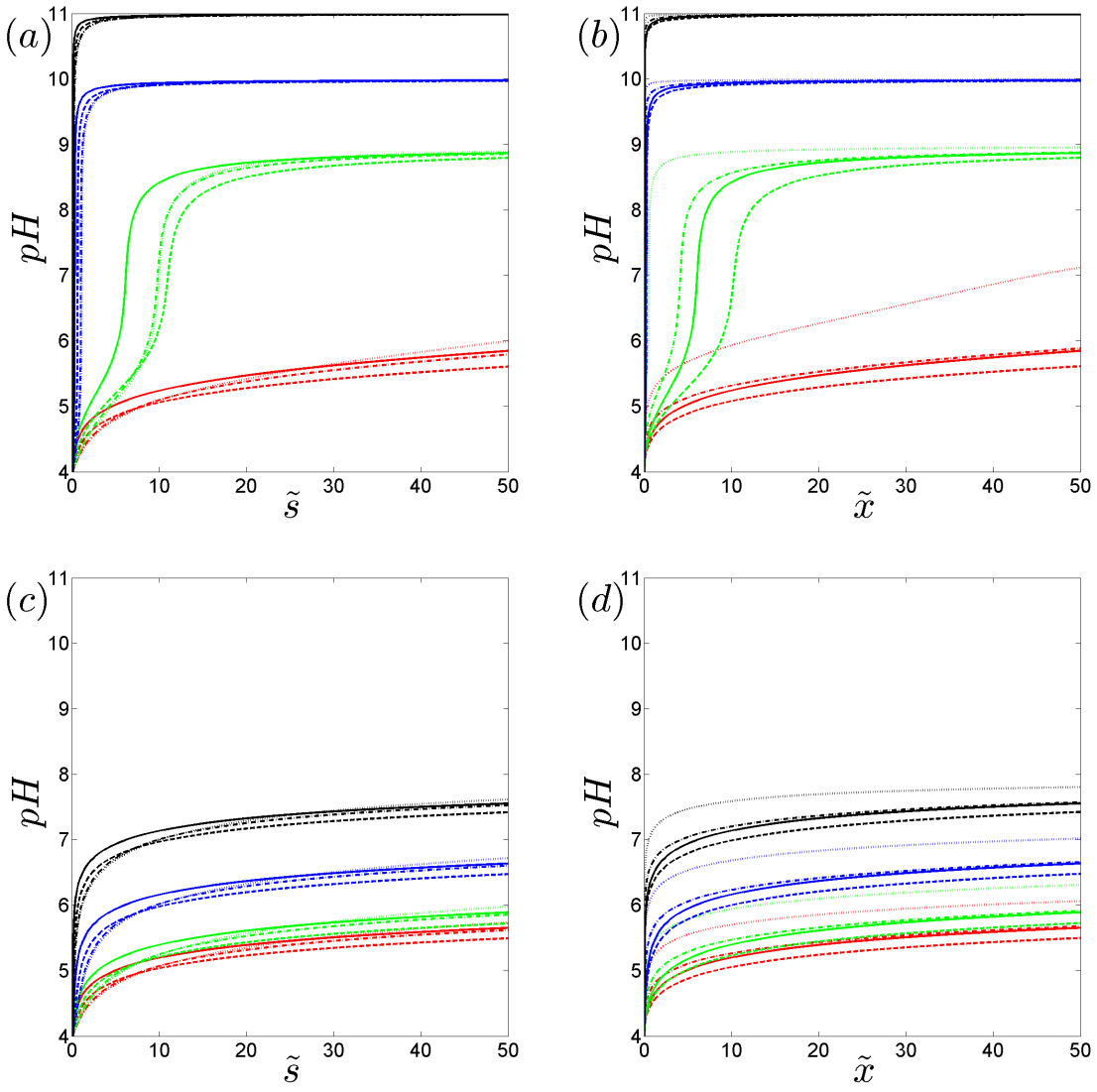

Figure 2.14: The pH of a strong acidic jet ($\Gamma_0 = 0$; $C_a^0 = 10^{-4}$ mol/l) varies as it is discharged ($\theta_0 = 0$, $\psi_0 = \pi/2$) into an alkaline ambient fluid $C_b^0 = 10^{-6}$, 10^{-5}, 10^{-4} and 10^{-3} mol/l corresponding to red, green, blue and black lines. The value of $\Lambda = 10$, 1, 0.1 and 0.01 for solid, dashed, dash-dot and dotted lines. In (a) and (b) $K_b = 10$, typical of a strong alkali. In (c) and (d) $K_b = 10^{-9}$, typical of a weak acid.

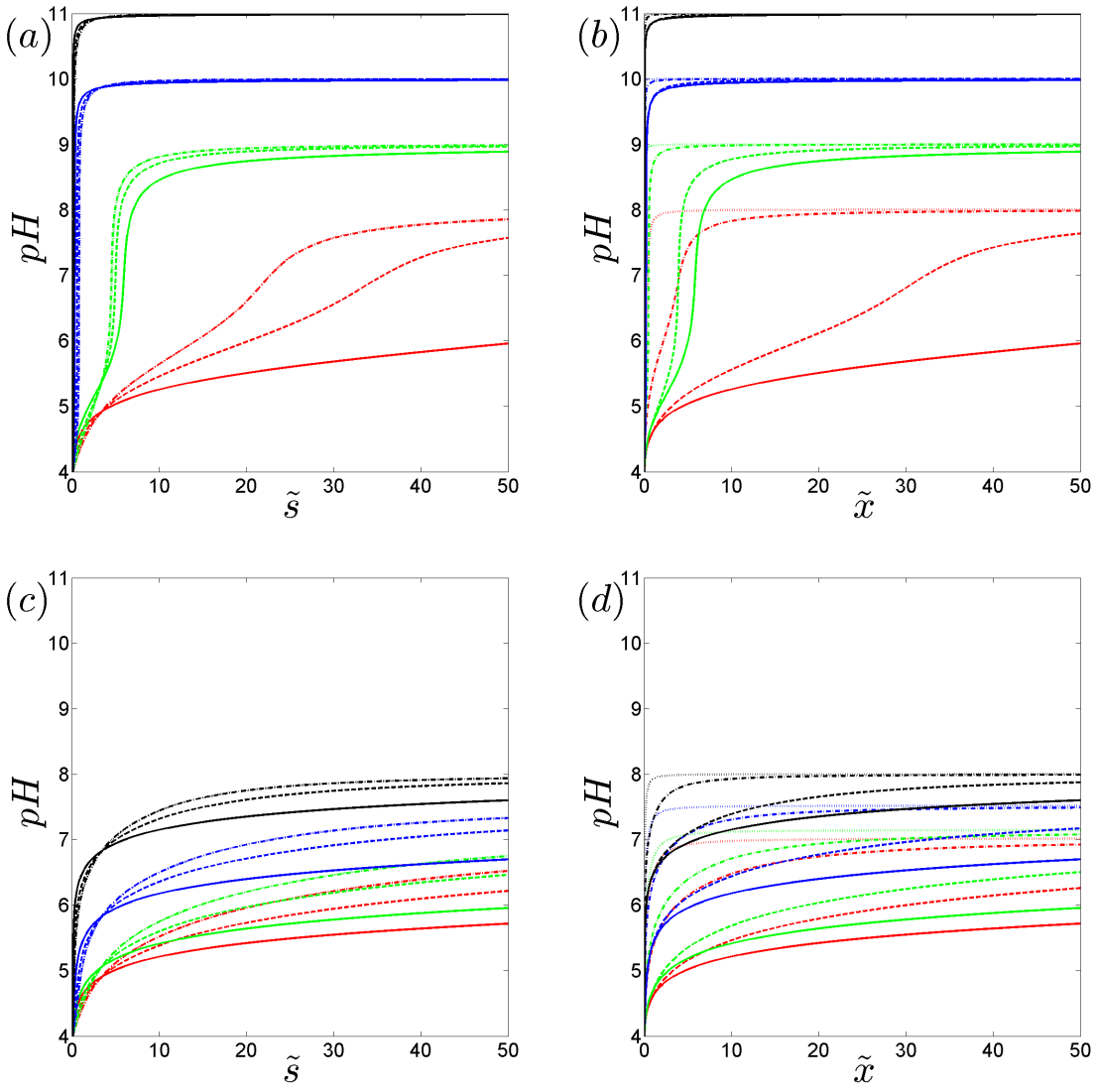

Figure 2.15: The pH of a strong acidic plume ($\Gamma_0 = 1$; $C_a^0 = 10^{-4}$ mol/l) varies as it is discharged ($\theta_0 = 0$, $\psi_0 = \pi/2$) into an alkaline ambient fluid $C_b^0 = 10^{-6}$, 10^{-5}, 10^{-4} and 10^{-3} mol/l corresponding to red, green, blue and black lines. The value of $\Lambda = 10$, 1, 0.1 and 0.01 for solid, dashed, dash-dot and dotted lines. In (a) and (b) $K_b = 10$, typical of a strong alkali. In (c) and (d) $K_b = 10^{-9}$, typical of a weak acid.

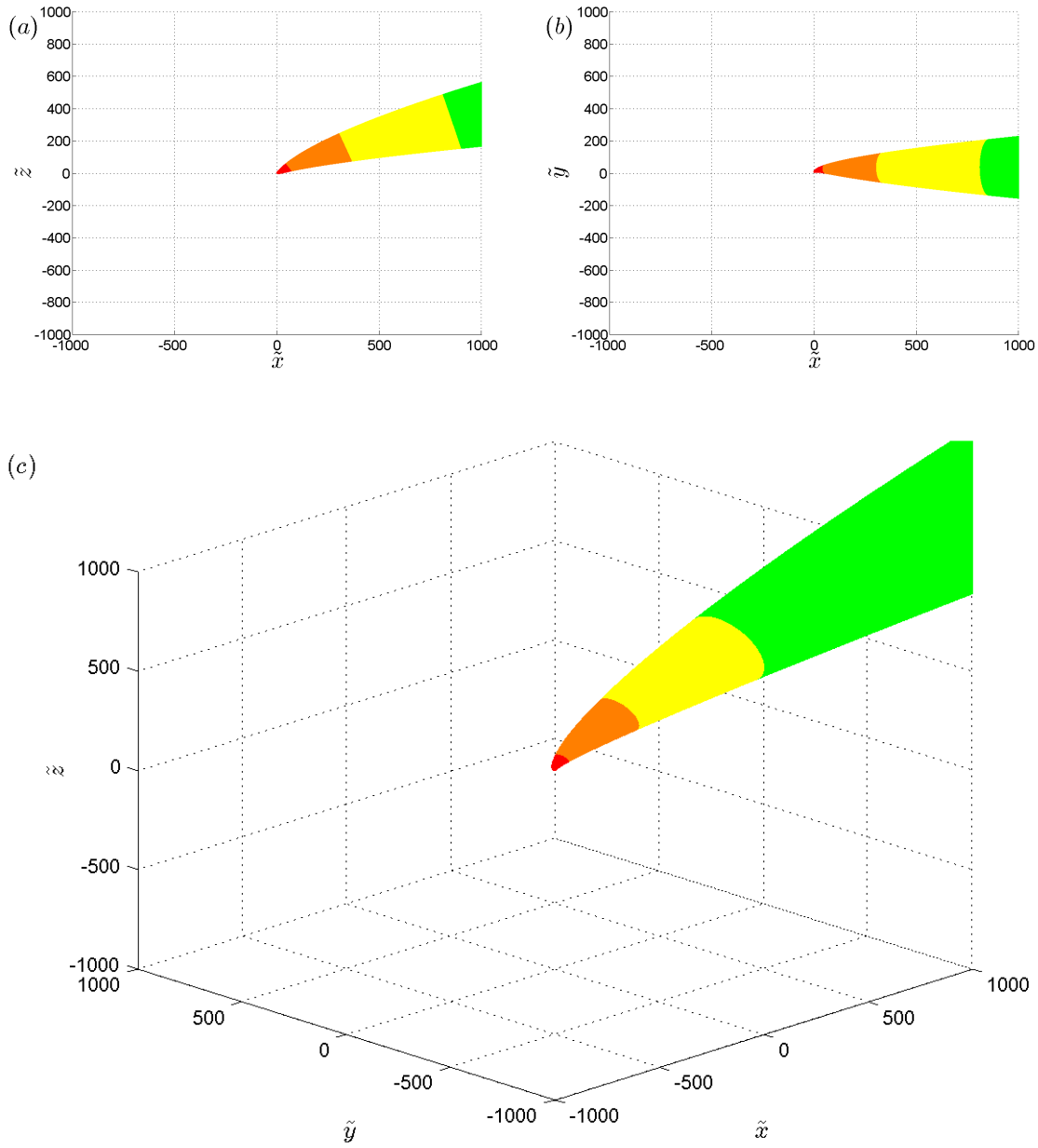

Figure 2.16: A buoyant acidic plume ($\Gamma_0 = 0.01$) discharged into a tangential alkaline ambient stream ($\theta = 0$; $\phi = \pi/2$; $\Lambda = 0.1$). The source pH of the discharge is 3 and the ambient is weakly alkaline with $K_b = 10^{-9}$ with a pH of 8. The colours correspond to pH of 3-5 for red, 5-6 for orange, 6-6.5 for yellow and 6.5+ for green.

	Far field	Jirka (2004) (Table 1)
Vertical jet		
$\mathcal{D}$	$\left(\frac{3}{2}\right)^{2/3}\left[(1+\Lambda)^{2/3}\right]\left(\frac{\tilde{x}^2}{\Lambda}\right)^{1/3}$	$\left(\frac{3}{2}\right)^{2/3}\left[\frac{2^{2/3}\lambda^2}{4}\right]\left(\frac{\tilde{x}^2}{\Lambda}\right)^{1/3}$
Elevation $\tilde{z}$	$3^{1/3}\left[\frac{2}{(\Lambda+1)}\right]^{2/3}\left(\frac{\tilde{x}}{\Lambda^2}\right)^{1/3}$	$3^{1/3}\left[2\right]\left(\frac{\tilde{x}}{\Lambda^2}\right)^{1/3}$
Hor. plume		
$\mathcal{D}$	$\frac{1}{\Lambda}\left(\frac{3}{4}\Gamma_0\tilde{x}^2+1\right)^{2/3}$	$\frac{1}{\Lambda}\left(\frac{3}{4}\Gamma_0\tilde{x}^2\right)^{2/3}\frac{\lambda^{4/3}}{5^{2/3}}$
Elevation $\tilde{z}$	$\frac{(6\Gamma_0\tilde{s}^2)^{1/3}}{\Lambda}$	$\left[\left(\frac{8}{5\lambda}\right)^{1/3}\right]\frac{(6\Gamma_0\tilde{x}^2)^{1/3}}{\Lambda}$

Table 2.1: Comparison between the scaling analysis presented in this chapter and in Jirka (2004). The turbulent Schmidt number is denoted by λ with a value of 1.2.

2.5 Conclusions

A mathematical model was developed to analyse the characteristics of a monoprotic or diprotic acid injected into an alkaline environment. Fundamentally, two processes were shown to be important: (a) dilution, caused by the mixing of acid with the alkaline ambient and (b) chemical reactions. In the case of a strong acid and a strong alkali that have fully dissociated, the alkali tended to mop up the excess hydrogen ions after mixing leading to a rapid reduction of the hydrogen ion concentration and a more rapid increase in the pH along the edges of the plume. At the point of neutralisation the ratio of alkali to acid is equal to the ratio of hydrogen ions and hydroxide ions. Above the point of neutralisation, dilution is the dominant process in the increase of alkali concentration. A similar picture emerged for the case of a weak alkali where the hydroxide ions are only partially dissociated. As a result the pH showed a weaker dependence on the concentration of the alkali.

In the case of jets and plumes in a cross flow, figure 2.16 illustrates that even a small cross flow ($\Lambda = 0.1$) will have a significant effect on the bending of the jet/plume. In practice Λ is usually of the order of 10 meaning that the acidic jets/plumes discharged from the side of the ship will certainly interact with the hull immediately after discharge. Corrosion could occur, therefore, it could be beneficial if the discharges were to be discharged from the stern directly into the highly turbulent wake.

The mathematical model was extended to include the effect of cross flow. A near and far field scaling analysis was performed to determine the rates of deflection and dilution for jets and plumes. As a result of the scaling analysis, the dilution and consequently the pH can be estimated for a range of discharge configurations. A

comparison with scaling analysis of Jirka (2004) is made in table 2.1. The scalings agree provided that Λ is small, the results of Jirka (2004) are valid for small values of Λ. The variation of scalars is due to different entrainment coefficients used in top-hat and Gaussian models.

Chapter 3

Experimental study of acidic jets and plumes

3.1 Introduction

The purpose of the experimental study is to validate the analytical model developed in Chapter 2. The challenges that needed to be overcome were:

1. How to accurately measure the pH in the jet or plume.

2. How to ensure reproducibility of creating a turbulent plume.

The pH in the discharge was determined from a pH sensitive dye due to the difficulty of measuring the pH in a turbulent environment with a pH probe. Intrusive methods such as using a pH probe also affect the flow properties of the jet or plume. A video camera was used to record the dye in the jet or plume, which changed colour with variations in the pH. The results were time-averaged and processed to measure distance from the source to the point of neutralisation.

3.2 Experimental setup

In the jet experiments the discharge was generated by a head of water from a header tank that was drained into the pool of alkaline water for each experiment. A small tank was placed 1.8 m higher than the point of discharge and the head difference experienced over the course of the experiment was 0.2 m. An extensive network of piping needed to be constructed which would also have contributed to a stabilising the flow rate at the point of discharge over the course of the experiment.

In the plume experiments the volumes of water involved were reduced significantly, therefore, a comparably larger header tank was used where the tank volume changed less than 5% over the course of the experiment. The aim was to minimize the flow rate variation caused by the change in tank head. In the case of plume experiments, maintaining a fixed flow rate is important to sustaining a fixed ratio between momentum and buoyancy.

The experiments are conducted with London tap water due to ease of access. Using seawater is impractical because of the logistics of transporting large quantities into central London. Similarly, distilled water can not be used because the process of boiling and condensing the water to remove impurities is far too slow for the quantities required. A viable alternative would be the use of deionised water but this approach was not cost effective in this case.

To reduce the number of variables in the experiments: acid type (nitric acid), acid concentration and flow rate were fixed in the jet and plume as well as the buoyancy flux in the case of the plume. The alkalinity as well as the chemical composition of the water in the tank was varied.

3.2.1 Design considerations

The jet experiments took place in a wide rectangular tank with planform dimensions of 1.46 m $\times$ 0.97 m, filled to a depth of 0.46 m (see figure 3.1). The tank was illuminated by diffuse light sources from the bottom and along one of its sides. In the case of the plume, the tank planform dimensions were 0.5 m $\times$ 0.5 m, filled to a depth of 0.66 m. Since the tank was smaller, only diffuse light sources were installed on one side of the tank only (see figure 3.2). The internal radius of the nozzle was fixed at $b_0 =$ 0.011 m for the jets and $b_0 = 0.004$ m for the plumes. The nozzle design for the plume is a derivation from the Cooper nozzle (see figure 3.3) that is described by Hunt & Linden (2001), the key difference is that a mesh at the end of the nozzle could not be used to straighten the flow. The reason for this is that litmus dye powder is not fully soluble in water and residual extremely fine particles caused blockages in the mesh. To counter this, a short pipe was used to straighten the flow without causing it to become laminar. The average jet flow rate over the course of the experiment was calculated to be $Q = 1.31 \times 10^{-4}$ m^3/s. A dense plume was created by adding sodium chloride, that has no influence on the acid-alkali reactions, to a vertical discharge. For the case

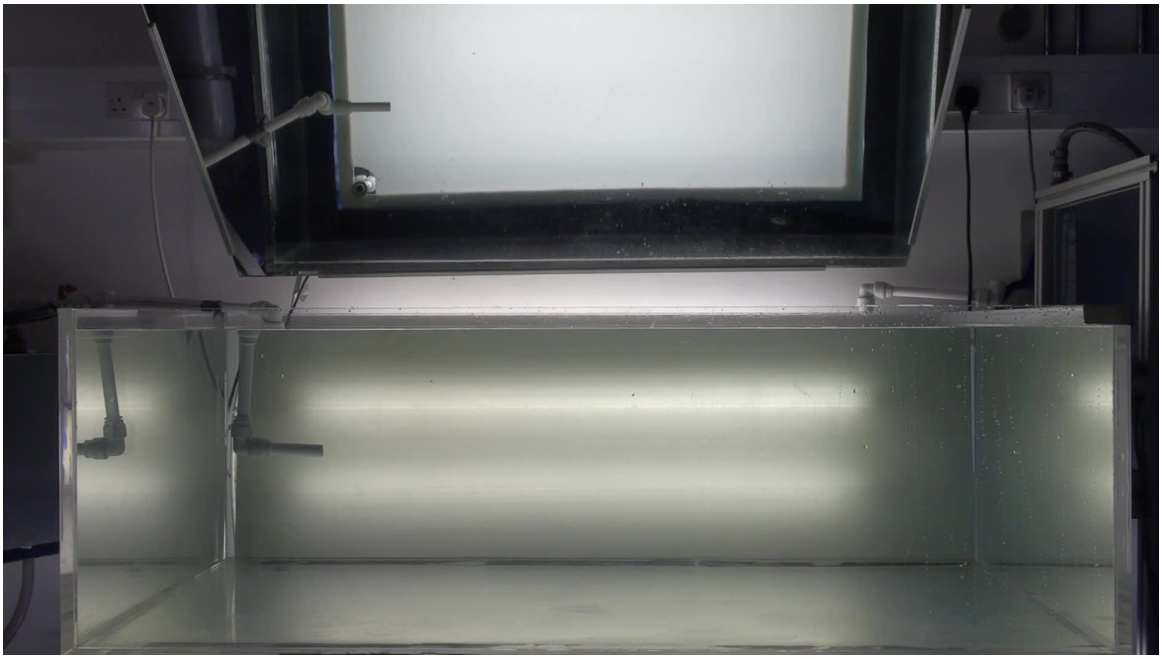

Figure 3.1: Experimental setup for the jet experiments. The total tank length is 1.46 m but the length usable for experiments is 1.3 m.

of a plume, $Q = 2.53 \times 10^{-6}$ m^3/s, $\Delta\rho_0 = 36.59$ kg/m^3 resulting in $\Gamma_0 = 3.55$ at the point of discharge. The nozzle radii were chosen to provide a range of neutralisation distances, up to 40 nozzle diameters, without influence from pooling at the end of the tank. The experimentally useful length of the tank was determined from the pooled dye depth in the tank at the end of the experiment (see figures 3.5 and 3.6). The maximum dilution in the jet/plume at that point can be calculated from

$$\mathcal{D}_{\text{jet}} = \frac{2\alpha z}{b_0} = 23.6; \quad \mathcal{D}_{\text{plume}} = \left(\frac{3}{5}\left(\frac{2\alpha z}{b_0} - \tilde{z}_0\right)\right)^{5/3} \Gamma_0^{1/3} - 1 = 122. \tag{3.1}$$

The expressions in (3.1) can be derived from (2.50) and (2.54) in Chapter 2. In this range the effects of pooling at the end of the tank are negligible. Litmus dye was diluted in a tabletop experiment and it was determined that when the dilution became greater than 100, it became too difficult to detect the dye by eye. The camera, however, could still differentiate between the different colour components at dilution of 122.

The requirements are for the discharge to be turbulent (in order to agree with the theory in Chapter 2) and to neutralise within the confines of a tank. The characteristic Reynolds number ($Re = 2Q_0/(\pi b_0 \nu)$) for the jet is 7500 (turbulent) and for the plume is 400 (non-turbulent). The use of a nozzle design (see figure 3.3) similar to that of the Cooper nozzle, in the case of the plume, enables the flow to be tripped turbulent.

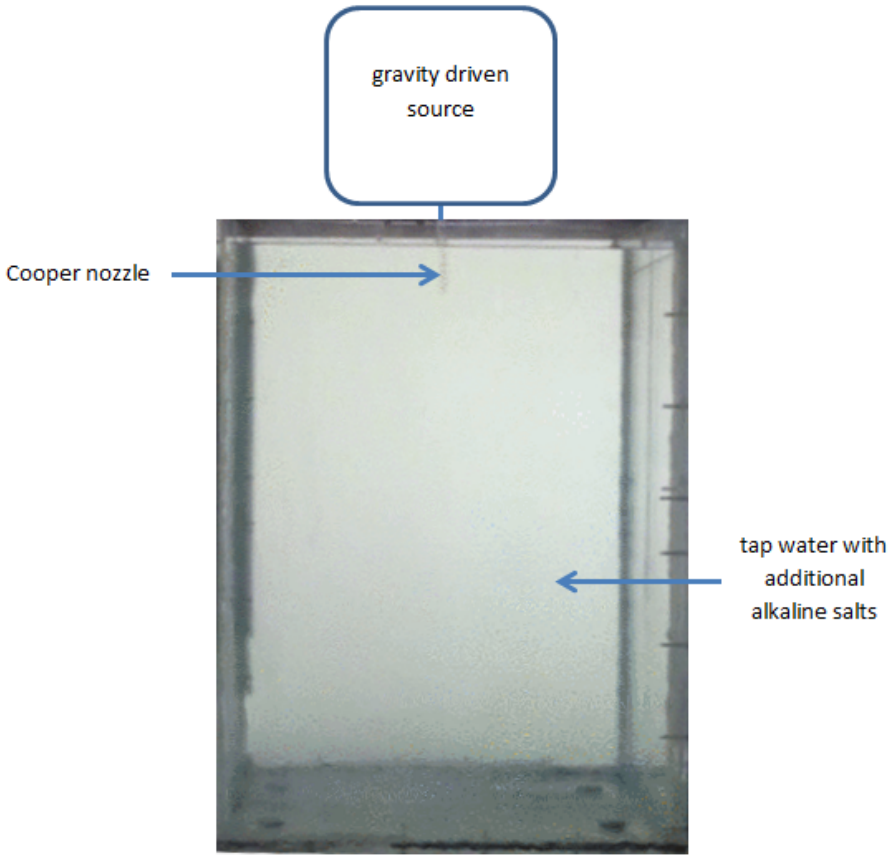

Figure 3.2: Experimental setup for the plume experiments. The total tank length is 0.66 m but the length usable for experiments is 0.44 m.

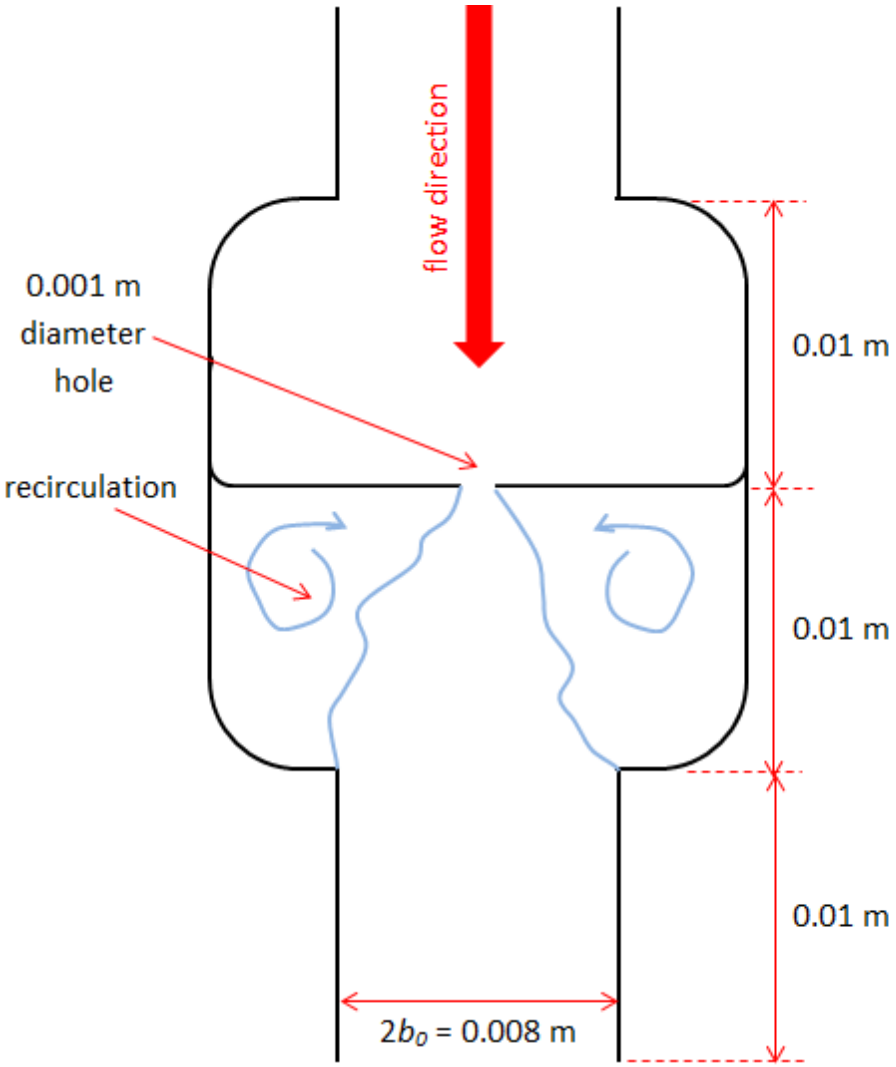

Figure 3.3: The plume nozzle design (Cooper nozzle) based on Hunt & Linden (2001). The small hole creates a recirculating region within the enlarged compartment before leaving the nozzle.

The flow is restricted to pass through a 0.001 m hole and as a result the effective Reynolds number becomes 3200 (turbulent). After a 0.01 m long pooling region, the flow is straightened in a short 0.01 m pipe with a diameter of 0.008 m and exists the nozzle in a turbulent state. With distance along the discharge trajectory Re stays constant in the case of a jet but in the case of a plume there is a gradual increase due to buoyancy (see Chapter 2). As described in Chapter 2 the neutralisation occurs when the concentration of hydrogen and hydroxide ions is equal within a fixed volume of fluid. We can express the dilution required for neutralisation as

$$D_N \simeq \frac{C_a^0}{C_b^0}. \tag{3.2}$$

Substituting in the volume flux of the discharge

$$\frac{C_a^0}{C_b^0} = \frac{Q}{Q_0} - 1, \tag{3.3}$$

allows to express the neutralisation distance of the jet or the plume in terms of its volume flux. In the case of the jet

$$\frac{C_a^0}{C_b^0} = \frac{2\alpha z}{b_0}, \tag{3.4}$$

and in the case of the plume

$$\frac{C_a^0}{C_b^0} = \left[\frac{3}{5}\left(\frac{2\alpha z}{b_0} - \tilde{z}_0\right)\right]^{5/3} \Gamma_0^{1/3} - 1, \tag{3.5}$$

where

$$\tilde{z}_0 = \frac{32}{21\Gamma_0^{1/5}} - \frac{1}{7\Gamma_0^{6/5}}. \tag{3.6}$$

Two limits must be imposed onto the neutralisation distance. Data accuracy suffers in the proximity of the nozzle due to the narrow jet/plume profile that is captured by the camera on a small number of pixels, this places a constraint of

$$\frac{z_N}{2b_0} > 5b_0. \tag{3.7}$$

In order to counter the effects of pooling at the back of the tank, the neutralisation distances should be within 3/4 of the distance down the experimental length of the tank

$$L_{exp} < \lambda_2 L, \tag{3.8}$$

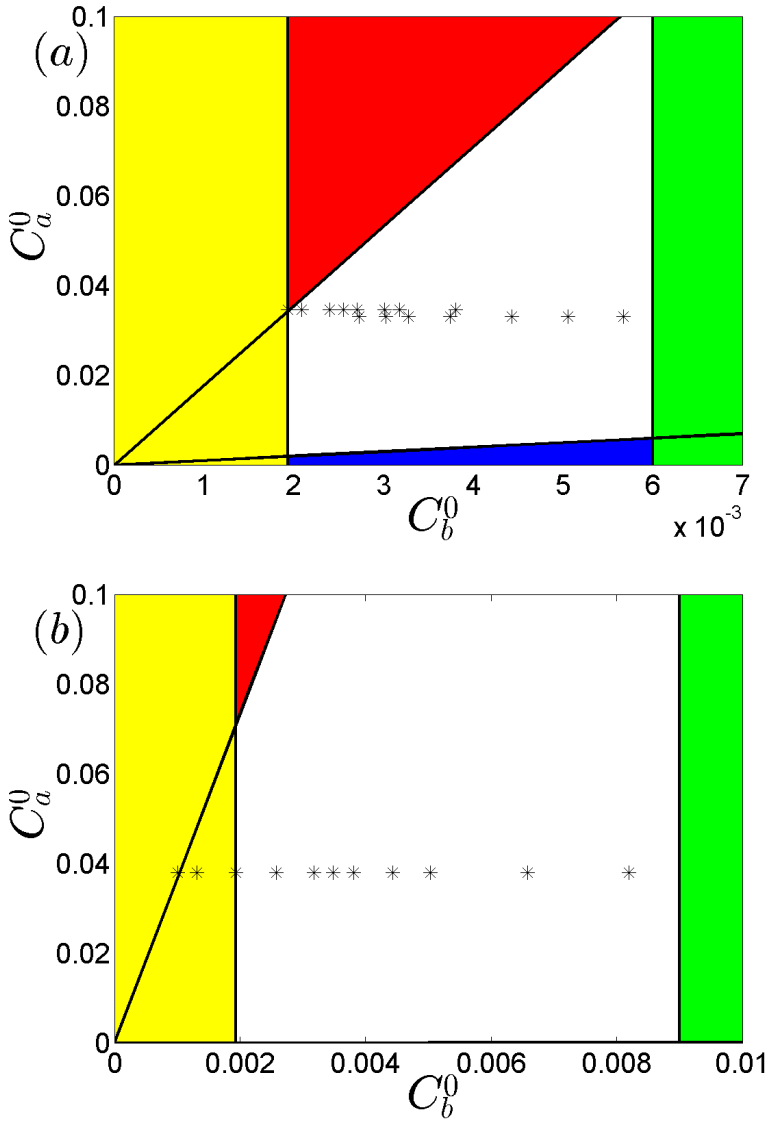

Figure 3.4: In (a) jet and in (b) plume experiments are indicated with stars for their respective acid and alkali concentrations. The values of C_a^0 and C_b^0 in the experiments were designed to fall into the unshaded region of the plot. In the red region the concentration of the acid would have been too strong for the jet to neutralise within the useful length of the tank (not affected by pooling) and in the blue region the acid concentration would have been too weak and neutralised within the first 5 nozzle diameters. The yellow region indicates where acid would have to be added to reduce the concentration of the alkali in the tap water and the green region shows where no more alkaline salts can be added due to the tank becoming opaque.

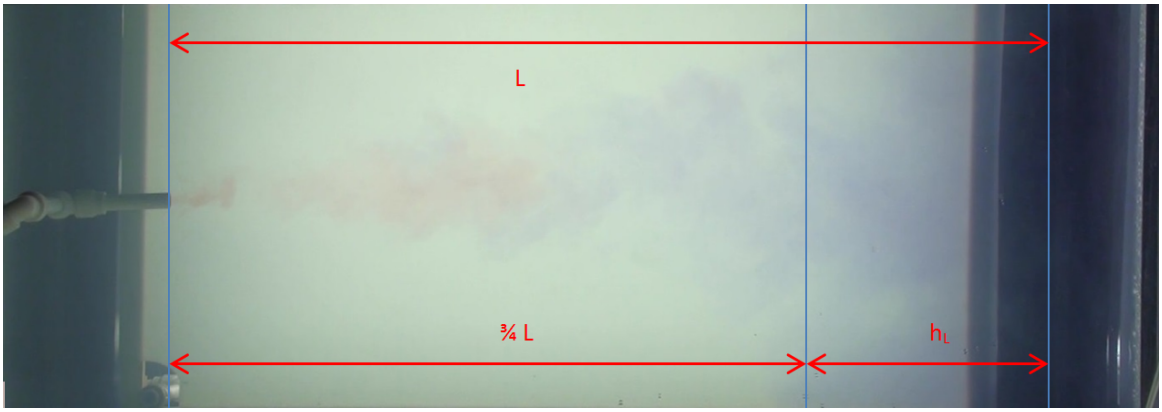

Figure 3.5: Pooling at the back of the tank at the end of a jet experiment.

where $\lambda_2 = 3/4$. The value of λ_2 was estimated from the state of the dye within the tank at the end of the experiment when the discharge of fluid had stopped, see figures 3.5 and 3.6.

The experimental recordings need to be time-averaged in order to obtain accurate centre line measurements. The camera is focused at the centre of the tanks and the travel distance to that point is the half length of the tank minus the distance from the end of the tank to the point of discharge, resulting in 0.58 m for jets and 0.27 m for plumes. The local timescale at that point can be determined as

$$t_{\text{local}} = \frac{b}{w} = \frac{Q^2}{M^{3/2}\pi^{1/2}}. \tag{3.9}$$

The expressions for M and Q can be found in Chapter 2 in (2.48) and (2.49). This results in local timescales of 4.25 for the jet and 0.76 for the plume. The experiments were time-averaged over 7 seconds in both cases, meaning that at least two timescales were considered. It can also be observed that the data for the plumes is slightly smoother due to averaging over a larger number of local timescales.

3.2.2 Data acquisition

The neutralisation distances of the jets and plumes were determined optically from the litmus dye in the discharge. The significant quantities of water involved in these experiments precluded the use of distilled or deionised water, therefore, central London tap water at a temperature of 19 ^{o}C was used in all of the experiments. In the absence of any additional alkaline salts, the jet neutralisation distance was used to infer the concentration of dissolved salts in the tank ($C_w^0 = 0.0019$ mol/l). The

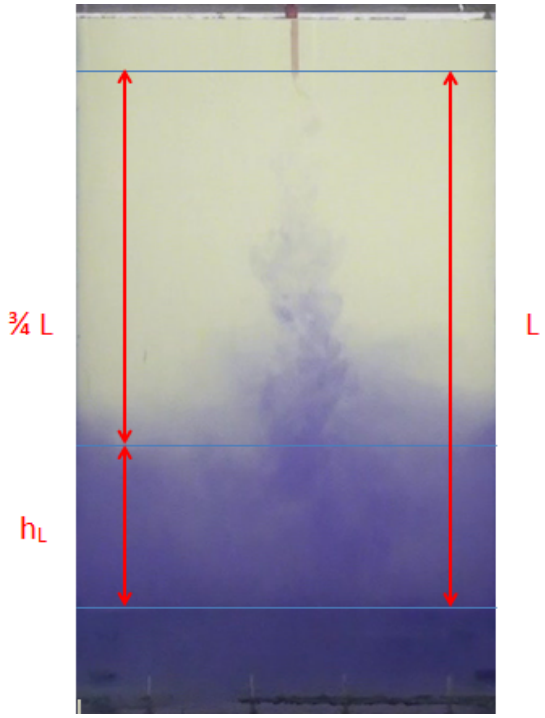

Figure 3.6: Pooling at the back of the tank at the end of the plume experiment. The base of the tank is visible due to parallax because the camera is focused at the centre of the tank.

chemical characteristics of the tank water were changed by the addition of a buffer salt combination, a single alkaline salt, an alkaline solution or an acidic solution. By adding alkali salts, the water became increasingly opaque to the point where the presence of the pH indicator dye could no longer be detected in the tank by the camera. This limited the shortest neutralisation distance that could be observed. When additional alkaline salts were added to the tank the total alkaline molar concentration was estimated to be the sum of the added alkalis (C_b^0) and the alkalinity of tap water (C_w).

All the experiments were recorded with a colour camera (Sony HDR-SR12E) at a resolution of 1920 × 1080 pixels, 24 bit colour depth and 25 frames per second. The videos were converted into a sequence of images at the video frame rate. A number of routines were written in Matlab R2012a using the Image Processing Toolbox to gain either an instantaneous view of the colour intensity fields or a time-averaged measure. The averaged images were created over a time period of 7 seconds. The images were split into red, green and blue colour components to gain a quantitative overview of how the colour intensity along the jet and plume centre line changed with distance from the nozzle. In the RGB colour model the colour intensity is within the range of 0

to 255 for each colour. The maximum colour intensity varies greatly depending on the opacity of the water in the tank, however, the relationship between the different colour components remains the same as distance from the nozzle increases.

3.3 Experimental results

Titration experiments were undertaken to examine how the pH and colour of the indicator dye changed as acid reacted with an alkaline fluid. A diluted acid solution was created from a 1N standard nitric acid solution (Fluka Analytical) in distilled water and titrated against a sodium hydroxide solution in distilled water. The titration experiments involved increasing the volume of an initially acidic solution with an alkaline solution that was then stirred for a short period of time. The pH was measured using the Hannah Instruments HI 8428NEW probe two minutes after stirring. Litmus and Universal indicator dyes were also used to determine the colour of the solution that corresponded with the probe measurements. The reaction occurred in a transparent glass beaker, placed on top of a small diffuse light box.

Figure 3.7 shows the variation of pH in a nitric acid solution as it is diluted with concentrated sodium hydroxide solution. The titration curve shows that when C_b^0 is large, the pH changes rapidly through the point of neutralisation. As discussed in Chapter 2 pH titration curves are affected by both chemical reactions and dilution. The titration of acid against distilled water ($C_b^0 = 0$ mol/l) shows a change in the pH occurring wholly due to dilution. It is worth noting that the experiments involving distilled water are very sensitive to contamination.

Figure 3.8 shows how the colour of the litmus dye changes due to nitric acid being titrated against sodium hydroxide. As the amount of alkali added increases, the pH quickly passes through the point of neutralisation and a corresponding rapid change in colour from red to blue is observed. Based on the colour intensity difference we are able to identify the point of neutralisation.

The mixing in the jet was examined using litmus dye without the addition of acid and the results are shown in figure 3.9. The instantaneous image (a) shows a sharp jet edge, but averaging over time (b), generates a gradual variation from the jet centre line to the edge of the jet. The entrainment of packets of fluid from the edges of the jet or plume to the centre is characterised by a turbulent diffusivity which scales as $\mathcal{D} \sim \lambda w b \sim \lambda M^{\frac{1}{2}}$, where $\lambda \sim 0.1$ (Prandtl, 1954). This means that the mixing at

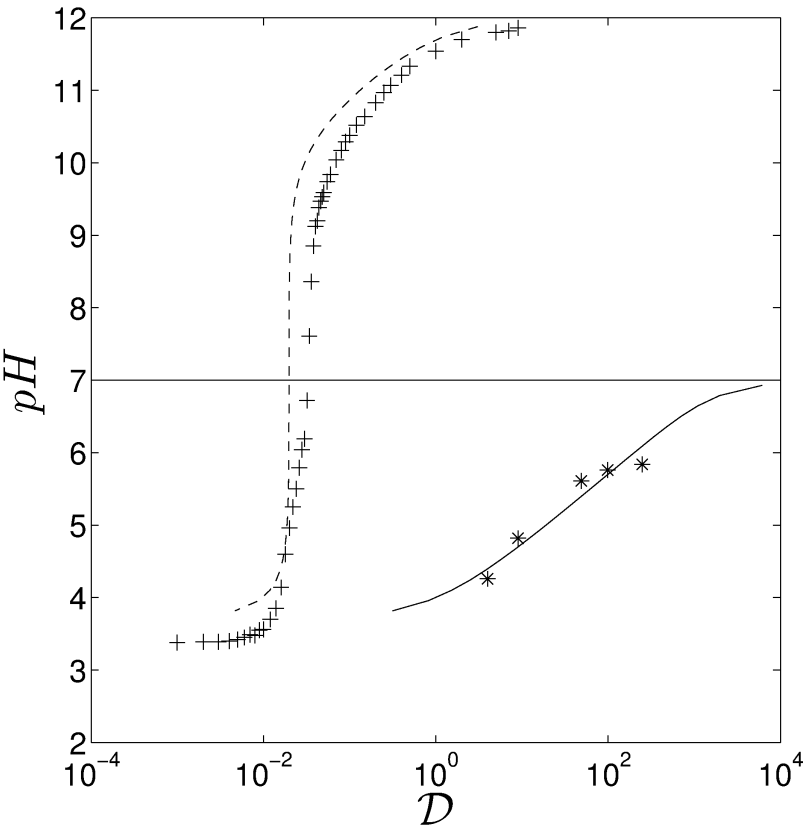

Figure 3.7: The pH titration curves of nitric acid ($C_a^0 = 0.0002$ mol/l) being titrated against a sodium hydroxide solution $C_b^0 = 0.01$ mol/l (dashed line) and distilled water $C_b^0 = 0$ mol/l (solid line). The solid and dashed lines show the theoretical predictions (2.12) while the symbols correspond to experimental data.

Chemistry	C_a^0	C_b^0	$\frac{C_a^0 - C_l - C_w}{C_b^0 + C_w}$	Exp. $\tilde{z}_N$	Theo. $\tilde{z}_N$
Jets					
None	0.0364	0.0000	17.90	17.90	17.90
NaOH (aq.)	0.0364	0.0002	16.57	15.75	16.57
NaOH (aq.)	0.0364	0.0005	14.43	14.73	14.43
NaOH (aq.)	0.0364	0.0008	12.78	14.29	12.78
NaOH (aq.)	0.0364	0.0011	11.48	10.86	11.48
Buffer (50%)	0.0364	0.0006	13.54	11.43	13.54
Buffer (100%)	0.0364	0.0012	10.88	9.14	10.88
Buffer (150%)	0.0364	0.0019	9.10	9.40	9.10
Buffer (200%)	0.0348	0.0025	7.47	7.75	7.47
Buffer (250%)	0.0348	0.0031	6.55	8.06	6.55
Buffer (300%)	0.0348	0.0037	5.83	6.22	5.83
NaOH (salt)	0.0348	0.0008	12.11	14.03	12.11
NaOH (salt)	0.0348	0.0011	10.94	11.49	10.94
NaOH (salt)	0.0348	0.0013	10.09	11.49	10.09
NaOH (salt)	0.0348	0.0018	8.83	9.53	8.83
Plumes					
None	0.0400	0.0000	19.68	7.18	7.00
NaOH (salt)	0.0400	0.0006	14.76	5.56	5.83
NaOH (salt)	0.0400	0.0013	11.95	4.91	5.10
NaOH (salt)	0.0400	0.0016	10.92	4.93	4.81
NaOH (salt)	0.0400	0.0019	9.99	3.09	4.23
NaOH (salt)	0.0400	0.0025	8.58	2.09	3.84
NaOH (salt)	0.0400	0.0031	7.55	3.88	3.82
NaOH (salt)	0.0400	0.0047	5.77	1.91	2.99
NaOH (salt)	0.0400	0.0063	4.64	2.15	2.83
HNO_3	0.0400	-0.0006	28.97	8.51	8.95
HNO_3	0.0400	-0.0009	37.91	10.72	10.62

Table 3.1: List of the chemical composition of the jet, plume and tank water. The dimensionless experimental neutralisation distance $\tilde{z}_N$ is measured from time-averaged jet or plume images. The 100% buffer solution is created from 0.057 g/l of sodium bicarbonate (molar mass 84 g/mol) and 0.163 g/l of sodium carbonate decahydrate (molar mass 286 g/mol). The molar mass of sodium hydroxide is 40 g/mol. The molarity of London tap water was estimated to be $C_w = 0.0019$ mol/l from the jet experiments and $C_l = 3.5 \times 10^{-5}$ mol/l is the concentration of litmus solution alkalinity.

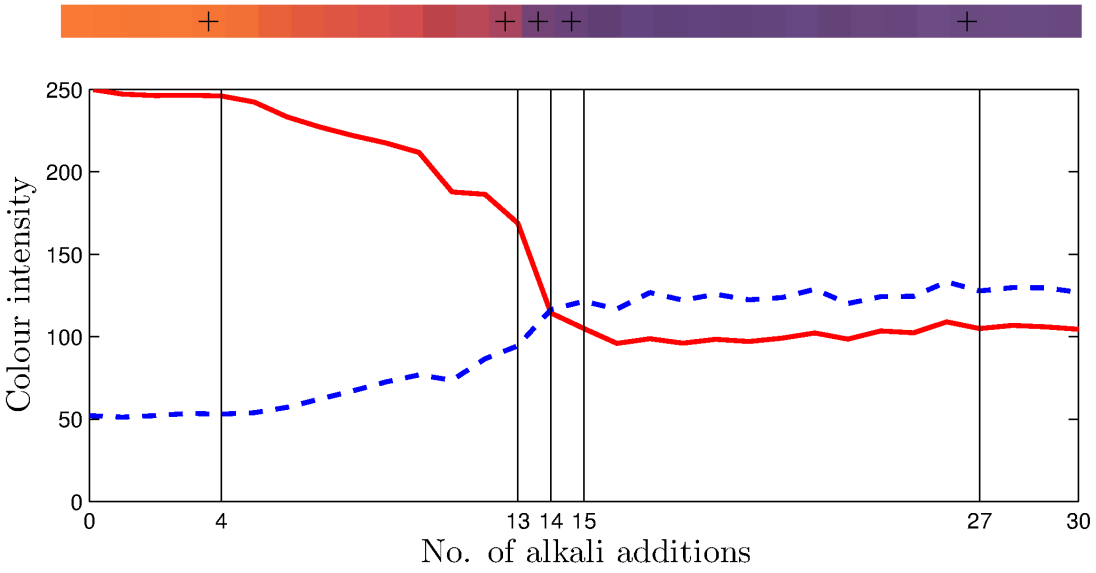

Figure 3.8: Experimental results from the titration experiments of nitric acid and sodium hydroxide in distilled water. The initial volume (200 ml) and alkalinity ($C_a^0 =$ 0.0014 mol/l) of the acidified solution increases through the addition of a fixed volume (2 ml) of alkali ($C_b^0 = 0.01$ mol/l) at every step for 30 steps. The colour component intensity (dashed line - blue component; solid line - red component) of the pH sensitive dye, Litmus, varies and is highlighted at the following steps: step 4, pH ≈ 3; step 13, pH ≈ 4; step 14, pH ≈ 7; step 15, pH ≈ 10; step 27, pH ≈ 11.

a fixed distance z from the nozzle is not instantaneous and explains why the edges are neutralized first and the centre line last. The distance between the concentration variation from the nozzle to point z along centre of the jet and from the nozzle to point z along the edge of the jet scales as $\mathcal{D}/w \sim \lambda b$. This is a fraction of the local width of a turbulent jet or plume. The molecular diffusivity of the chemical species is low and characterised by a diffusivity $\mathcal{D}_{mol} \sim 10^{-9}$ m^2/s. The small scale mixing process quickly generates concentration filaments of the scale $(\mathcal{D}_{mol} L/u')^{1/2}$ where L is the integral scale and u' the RMS velocity; this broadly explains when the small scale mixing has a weak dependence on $\mathcal{D}_{mols}$ (da Silva *et al.*, 2014).

An instantaneous image of an acidic jet is shown in figure 3.10*a* and quantitative view where the change from red (acidic) to blue (alkaline) occurs in a time-averaged jet is show in figure 3.10*b,c*. With distance from the nozzle the jet fluid becomes increasingly alkaline due to dilution and chemical reactions. Mixing between the ambient fluid and the jet or plume first occurs on the edges of the discharge where a gradual neutralisation gradient is formed towards the centre line. An overview of the blue and red colour components intensity along a jet centre line is shown in figure 3.11.

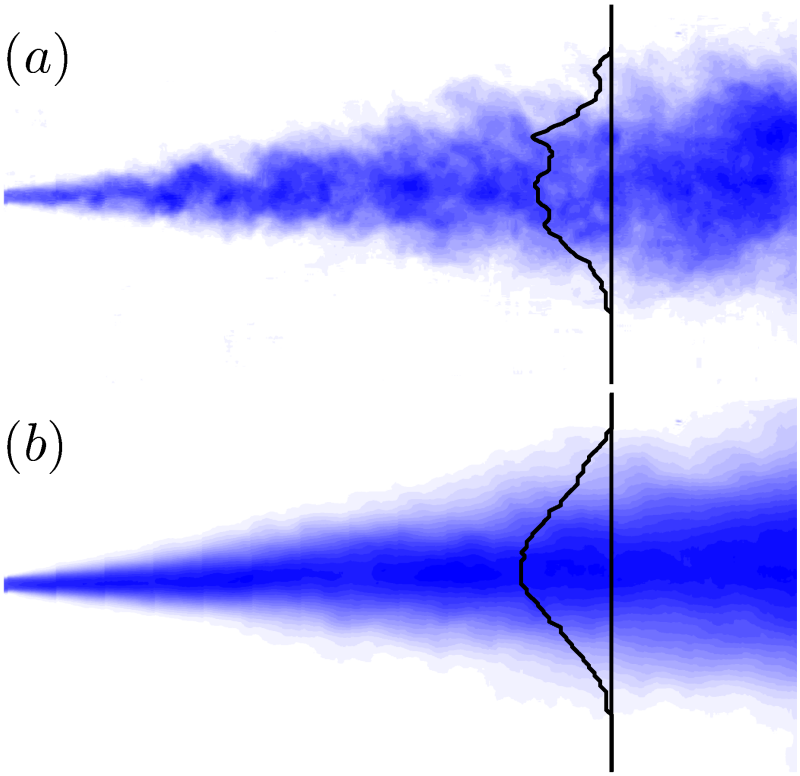

Figure 3.9: The blue colour component intensity for a jet experiment with litmus dye and no acid-alkali neutralisation reactions, where (a) is the instantaneous image and (b) the time-averaged image. The colour component intensity across the jet has been plotted along the vertical straight line.

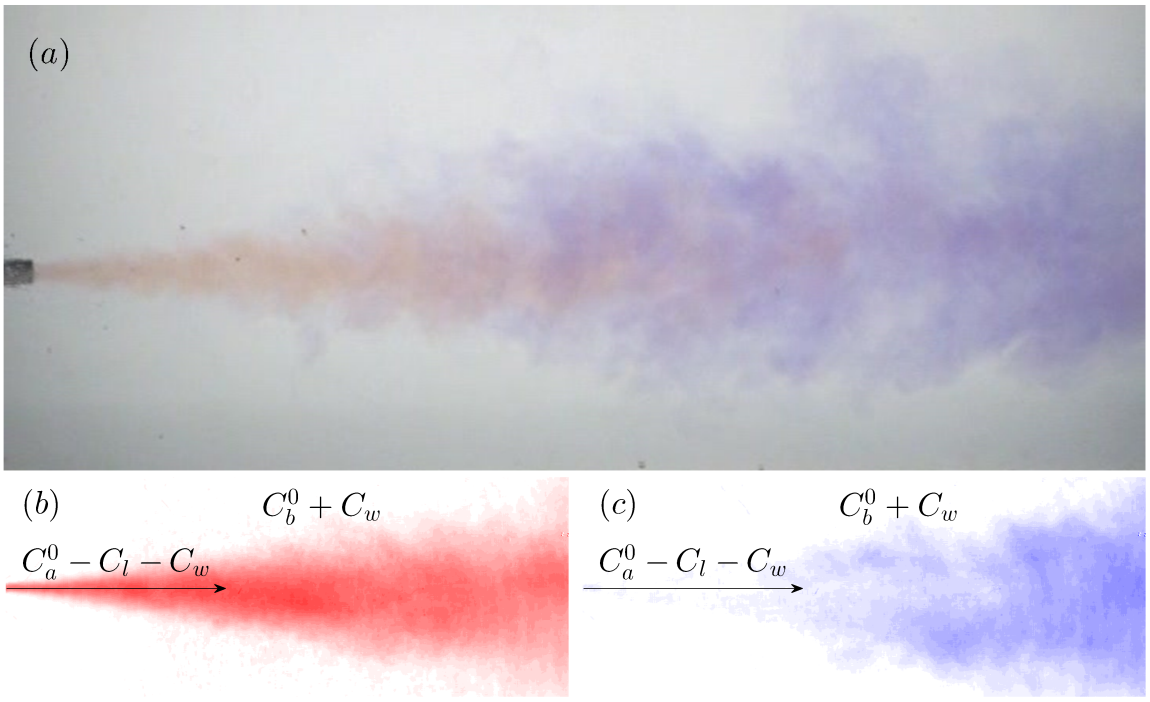

Figure 3.10: An instantaneous image of an acidic turbulent jet (a). A time-averaged jet has been decomposed into (b) red and (c) blue colour components. The jet contains litmus indicator that changes from red to blue as the acidic jet is gradually neutralised.

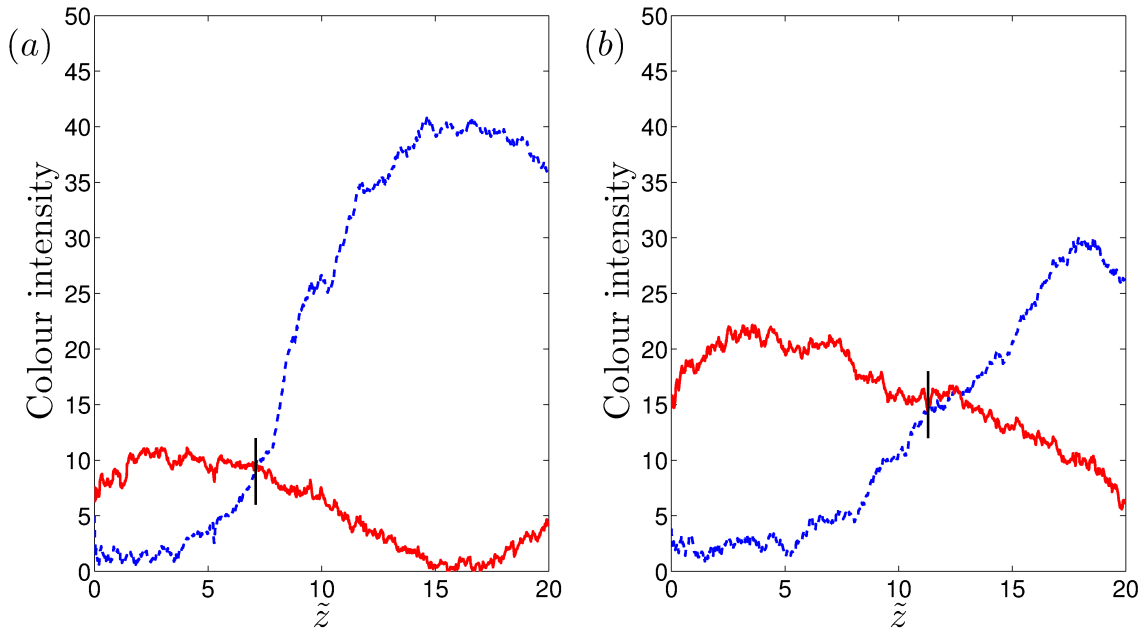

Figure 3.11: The time-averaged centre line red (solid line) and blue (dashed line) colour component intensity of a turbulent acidic jet with litmus dye plotted against $\tilde{z}$. Neutralisation occurs when the blue colour component intensity becomes greater than the red colour component intensity (highlighted by a short vertical black bar). Two contrasting cases are shown for a high concentration alkaline ambient in (a) and for a low concentration alkaline ambient in (b).

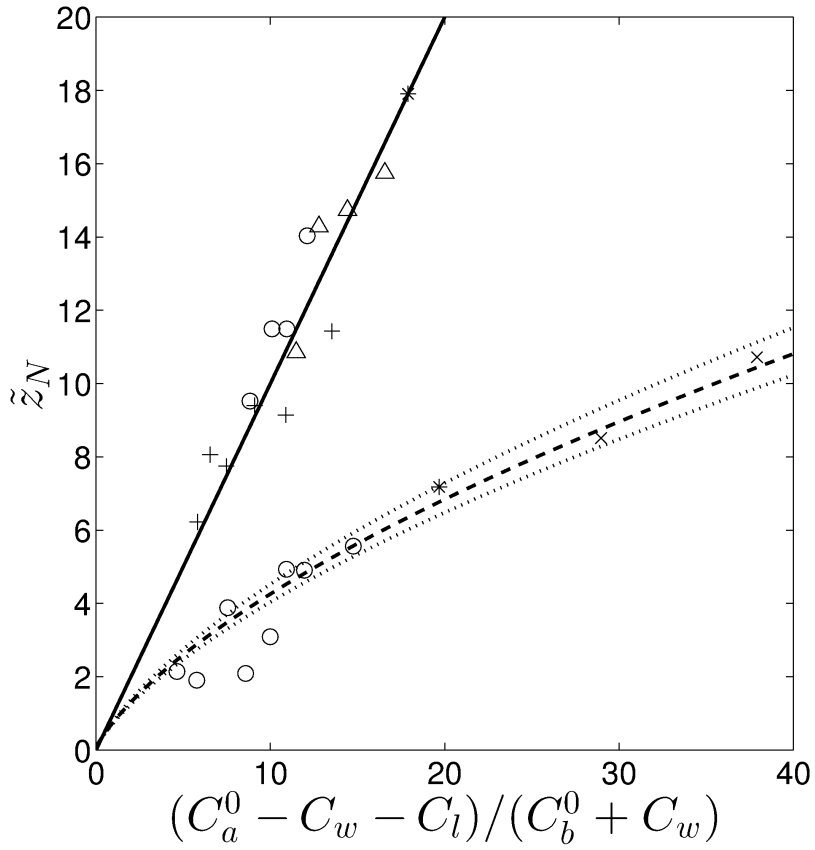

Figure 3.12: The experimental results from table 3.1 where the $(*)$ symbols are for London tap water, (Δ) are for sodium hydroxide solution, $(+)$ for buffer solution, $(\circ)$ for sodium hydroxide salt and $(\times)$ for nitric acid. The solid $(\Gamma_0 = 0)$ and dashed $(\Gamma_0 = 3.55)$ curves correspond to (2.70) and (2.71) respectively while the dotted curves give an estimation of error in measuring the plume flow rate.

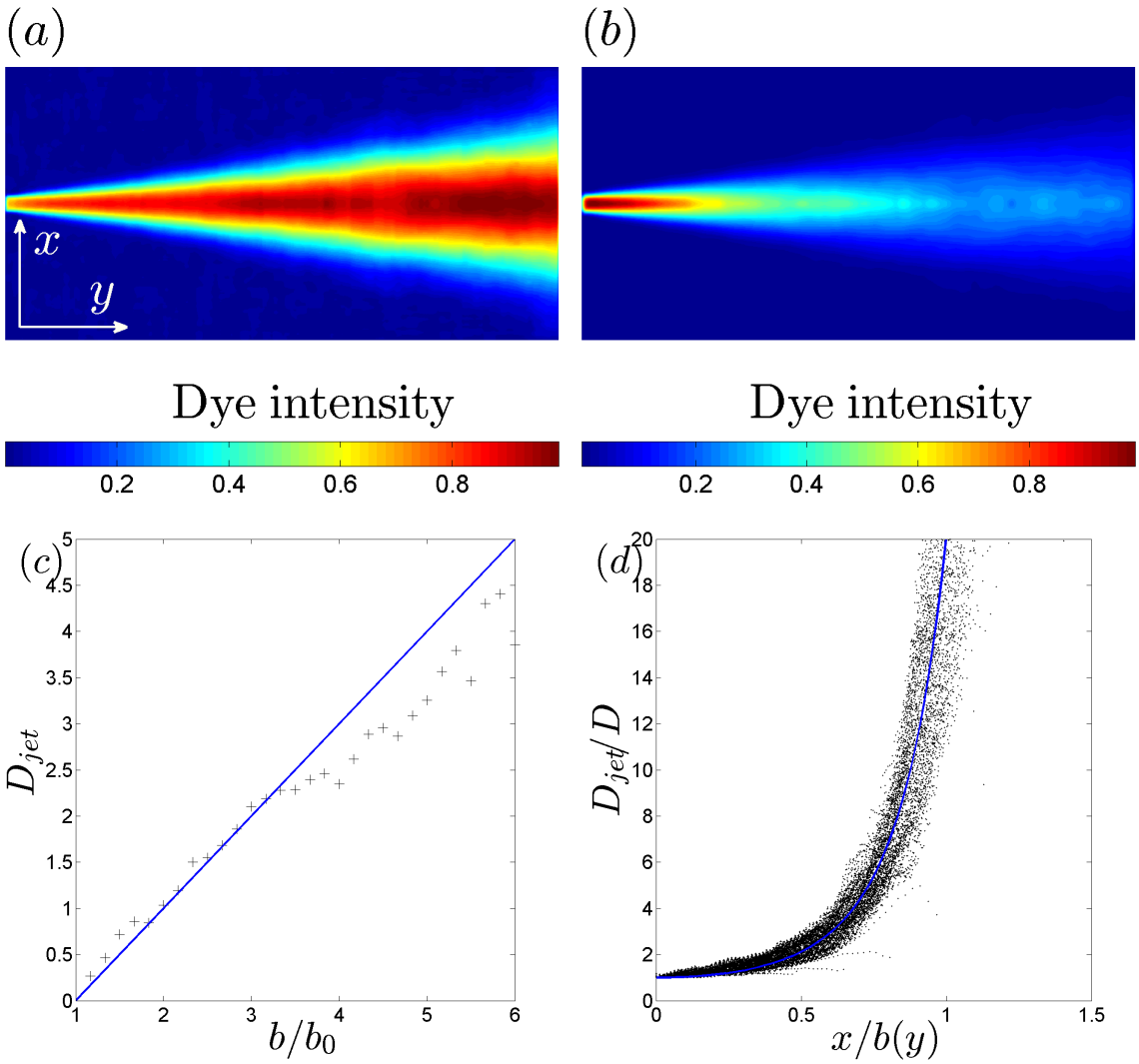

Figure 3.13: In (a), a depth integrated and time-averaged image of an experimental jet with passive dye is shown. In (b), an inverse Abel transformation (3.10) is performed to extract the average dye concentration through the centre line. The dye intensity is normalized in the range of minimum to maximum, *i.e.* 0 to 1. In (c), the dye dilution is plotted against distance along the jet trajectory and the solid blue line corresponds to $b/b_0 = 1 + \mathcal{D}_{jet}$ which is consistent with Chapter 2. In (d), the dye dilution is related to the tangential distance from the jet centre line and the solid blue line corresponds to (3.13).

The crossover point corresponds to the point of neutralisation, distance z_N from the nozzle, but in the case that the lines cross multiple times, as shown in figure 3.11*b*, the first point of contact closest to the nozzle is used. With increasing concentration of alkali salts in the ambient, the neutralisation distance z_N is reduced. It is necessary to take into account the influence of the dissolved salts in the London tap water. In the absence of any additional alkali salts added to the London tap water, the neutralisation distance was measured to be $\tilde{z}_N = 17.9$ in a jet, resulting in an alkali concentration of $C_w = 0.0019$ mol/l. The effective concentration of basic salts in the tank is estimated to be $C_w + C_b^0$. The alkalinity of the litmus dye in the discharge is denoted by $C_l = 3.5{\times}10^{-5}$ mol/l that was determined from titration experiments. The total molarity of the acid in the jet and plume is given by $C_a^0 - C_w - C_l$. The resulting molarity values were substituted into (2.70) for a jet and (2.71) for a plume to obtain theoretical predictions. Figure 3.12 shows a comparison between the experimentally determined neutralisation distance and theoretical predictions for jets and plumes, respectively.

Additional information is required to understand how average dilution varies across the jet width. To examine this effect we analysed the dilution of a jet containing passive dye as it is gradually diluted. Figure 3.13*a* shows the concentration field of a jet containing passive dye and provides information about the depth integrated and time-averaged dye concentration ($C_{DI}(x, y)$). An inverse Abel transformation (Abel, 1826) was performed to reconstruct the axisymmetric form of the dye concentration through the jet using

$$\bar{C}(x, z) = -\frac{1}{\pi} \int_r^\infty \frac{\mathrm{d}\bar{C}_{DI}}{\mathrm{d}m} \frac{\mathrm{d}m}{\sqrt{m^2 - r^2}}. \tag{3.10}$$

Figure 3.13*b* shows the reconstructed concentration profile. It has been known that the time-averaged concentration field ($\bar{C}$) across the jet is approximately Gaussian (*e.g.* Turner (1969), *etc.*) *i.e.*

$$\bar{C} = \frac{\bar{C}_0}{1 + (2\alpha y/b_0)} \exp\left(-\frac{\lambda x^2}{b^2}\right). \tag{3.11}$$

The dilution at any location in the jet ($D(x, y)$) can be estimated by relating the centre line concentration (C) to the value at the nozzle (C_0) and radius (b) to the value that captures 95% of the jet fluid (giving $\lambda = \log(20) \simeq 3$). This relationship

can, therefore, be related to the dilution anywhere through

$$D_{jet} = \frac{\bar{C}_0}{\bar{C}} - 1, \tag{3.12}$$

that is confirmed in figure 3.13c where there is a linear relationship between dilution and the jet radius growth. The depth integrated concentration is related to the concentration profile

$$D(x, y) = \left(1 + \frac{2\alpha y}{b_0}\right) \exp\left(\frac{3x^2}{(b_0 + 2\alpha y)^2}\right) - 1. \tag{3.13}$$

Figure 3.13d confirms (3.13) and demonstrates a rapid increase in dilution as we move away from the centre line.

3.4 Conclusions

To provide support for our models, experiments on both the chemistry and fluid mechanical aspects were conducted. The chemistry model is consistent with the titration measurements. As was expected, for mixtures of strong acid and strong alkali, the pH changed rapidly around the point of neutralisation. In contrast to the usual titration studies, where the volume of fluid used for titration is often small, we examined dilute strong alkalis where the pH changed much more slowly through the point of neutralisation and the volume of the alkali was significant. Titrating a strong acid against distilled water shows that the pH rose by 1 unit when the acid was diluted by a factor of 10, except close to neutralisation where the dissociation of H_2O is important. The dilution of the acid with distance from the outlet was analysed using a passive dye and an optical method of estimating the integrated concentration through a side view of the plume. The specific point highlighted in this component of the study was the contrasting view between an instantaneous snap shot and a time-averaged view, where the latter gave a near Gaussian distribution.

The variation of the pH with distance from the outlet was examined using litmus indicator dye that was first calibrated against pH. The neutralisation distance was measured from the colour component intensity variations along the centre line of the jet and plume. The measured neutralisation distances (correcting for the alkalinity of the water) were consistent with the distances predicted by the analysis for a variety of acid and alkali combinations. The agreement between predictions and observations

of neutralisation distances is good, confirming that the model captures the salient physics of the problem.

The results from this study provide predictions about the behaviour of strong acids when mixed with river and seawater. In this configuration, the pH as a function of distance, volume flux and discharge diameter were discussed. In the context of the environmental application to wet scrubber discharges from ships, when the ship is under way the discharges tend to be swept into the wake of the ship where dilution is extremely rapid. This alone will probably lead to the pH recovery even when the ambient fluid is fresh water. When a ship starts from rest or is in port, pH recovery occurs by both chemistry and dilution of the acid by entrainment. The engineering parameter which largely controls the pH recovery of a jet discharge is the diameter of the nozzle, where an initially narrow jet significantly shortens the recovery distance. Since there are constraints on the exit flow rate (due to pressure head constraints and piping), halving the jet diameter (from 0.4 m to 0.2 m) halves the neutralisation distance. Further work focussing on the design constraints of scrubber discharge ports due to policy is discussed in Chapter 7.

Chapter 4

Dilution and mixing in the wake of a ship

4.1 Introduction

In the previous chapters, the dilution of an acidic discharge was analysed in the near and intermediate fields where the discharge contained within an inclined jet or plume. Further downstream from the discharge port, the discharge is swept into the wake of the ship. In this chapter, we examine the spread and dilution of a passive material downstream in the wake of a ship that is moving steadily in time. Dilution occurs due to turbulent mixing within the wake and by the wake widening. In contrast to the dilution process which occurs in jets and plumes, there is no entrainment process at the edge of a wake ($u_E = 0$) although the boundary spreads (Hunt *et al.*, 2011). The dilution in the wake is not only relevant in the context of scrubber discharges but also to the discharge of ballast tank water.

The following three chapters (4, 5 and 6), related to numerical analysis of ship wakes, use subscript notation for the coordinate system, *e.g.* $x_i = (x_1, x_2, x_3)$ instead of x, y and z in the case of jets and plumes. This allows the governing equations to be written in a more compact and legible form.

4.2 Literature review

The first step is to understand the characteristics of the flow field. For instance in the case of a ship, propulsion can be due to an external propeller which induces a thrust force on the fluid or a duct flow where fluid is drawn from the bottom of the ship

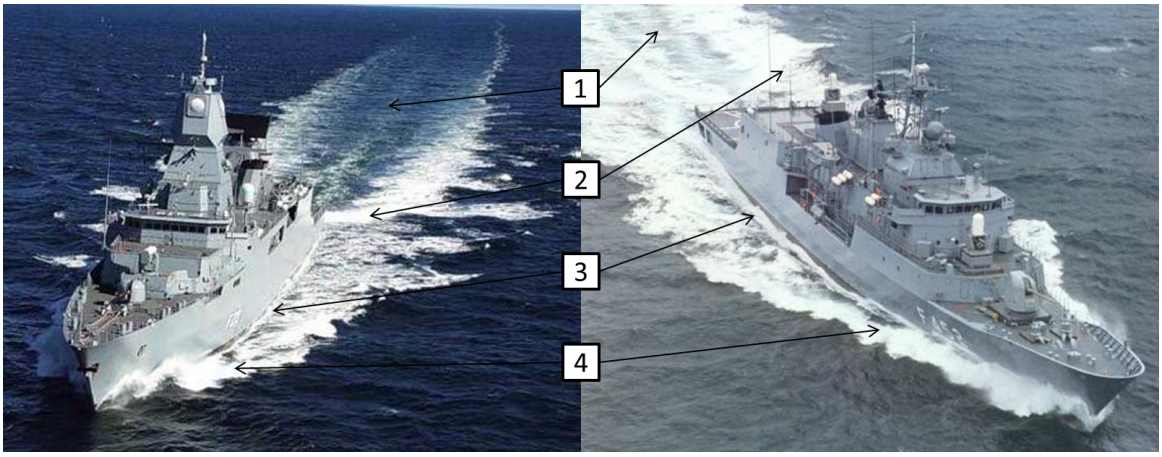

Figure 4.1: Frigates of the Sachsen-class, on the left, and Hydra-class, on the right (`http://www.naval-technology.com/`). Flow features around the ships have been highlighted where *1* is the turbulent wake, *2* is the stern divergent wave, *3* is the boundary layer and *4* is the bow divergent wave.

and propelled out through the rear, *e.g.* a jet boat (Secondo, 1935). In the animal kingdom propulsion can be generated either through shape change (*e.g.* squid, fish) or by exerting a thrust on the fluid. Figure 4.1 illustrates some of the different flow features in the wake of a ship. The boundary layer is the result of friction on the rigid body (the ship), in this region the viscous forces dominate the fluid flow. Ships tend to have a streamlined bow and a rectangular stern. The stern divergent waves are the result of the boundary layer separation due to the geometry of the stern. Bow waves are generated through a hydraulic jump at the bow and propagate at an angle similar to an oblique shock. Dong *et al.* (1997) analysed the mechanisms of formation of bow waves for a streamlined body. The turbulent wake is the result of propulsion from the ship's screw. The general downstream wake features from a rigid body have been described in detail by Batchelor (2001) and Williamson (1996).

The typical momentumless unbounded wake (*e.g.* free wake) is described by the Kelvin wave system (see figure 4.2). The wake spreads in a wedge shape also known as the Kelvin wedge that consists of transverse (in the turbulent wake region) and diverging wave crests (on the edges). The spreading angle of the wake is dependent on the Froude number of the ship (Darmon *et al.*, 2014)

$$Fr = \frac{U_\infty}{\sqrt{gL}}, \tag{4.1}$$

where U_∞ is the speed of the ship, g is acceleration due to gravity and L is the length

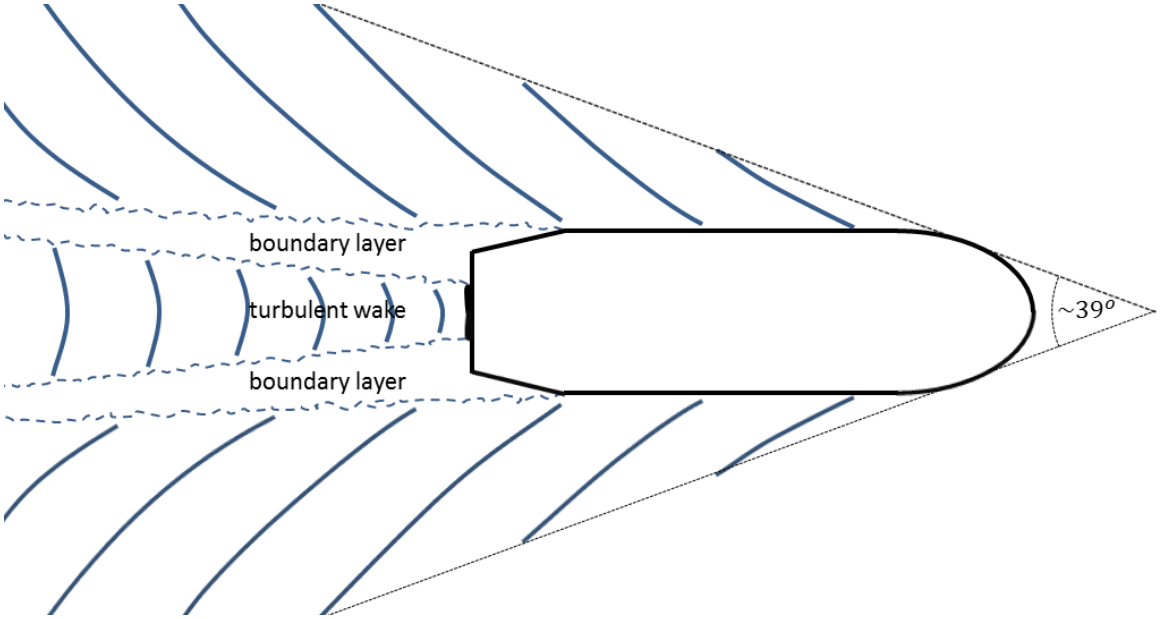

Figure 4.2: A schematic of wave patterns produced on the water surface around a self-propelled body. The Kelvin wake envelope was initially thought to expand at $\sim 39^o$ (Dias, 2014), however, Darmon *et al.* (2014) has shown that it is dependent on the Froude number.

of the ship.

Figure 4.3 shows the experimental results for a conventional merchant-ship hull where beam/draft ratios are 2.25, 3 and 3.75. The experimental data was obtained from Gertler (1954) and Graff *et al.* (1964). Commercial ships are designed to take advantage of the low wave drag at $Fr < 0.3$ where the majority of the drag force comes from form drag. Increasing the length of the ship has a significant effect on reducing its wave drag and allowing it to travel faster. Extremely fast ships, whose weight is supported by hydrodynamic lift as opposed to hydrostatic lift, can reach $Fr \approx 3$.

4.2.1 The self-propelled state

In this section we describe the classic analysis of Tennekes & Lumley (1972). In order for a ship to propel through water its thrust force F_T must be equal to (moving at a steady speed) or greater than (accelerating) that the drag force F_D. For a ship moving on the sea surface the main drag force components are form (F_F) and wave drag (F_W)

$$F_D = F_F + F_W. \tag{4.2}$$

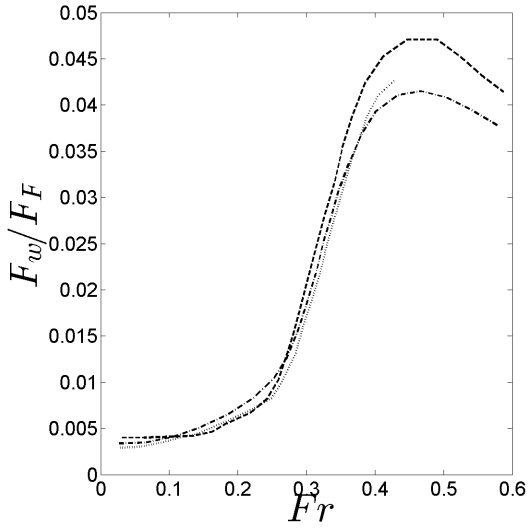

Figure 4.3: Increasing wave resistance against Fr for a standard merchant-ship with beam/draft ratios of 2.25 (dashed line), 3 (dash-dot line) and 3.75 (dotted line) based on the experimental studies of Gertler (1954) and Graff *et al.* (1964).

The characteristics of the wake flow are usually expressed in terms of wake width Y_W and maximum velocity deficit u_m (see figure 4.4). It is widely recognised, *e.g.* Tennekes & Lumley (1972) that both Y_W and u_m are ultimately affected by the excess of $F_D - F_T$.

The influence of the body is usually characterised in terms of the time-averaged velocity deficit, defined as

$$u_d(x_1, x_2) = U_\infty - u_x. \tag{4.3}$$

The centre line velocity deficit is

$$u_m = |u_d(x_1, x_2)|. \tag{4.4}$$

There are a number of ways to define the wake width, such as analysing at the dilution of dye in the wake with distance from the ship or magnitude of the velocity deficit across the width of the wake. For the jets and jets and plumes case in Chapters 2 and 3 the edge was defined to be where the concentration field had dropped to 5% of the centre line value. Morton *et al.* (1956) defined the 'effective' wake width to be the distance from the centre line to where the velocity deficit has fallen to 1% of the ambient value. The wake width can also be determined from the pressure contour lines from the point of flow separation from the body (Roshko, 1961). The case of spheres

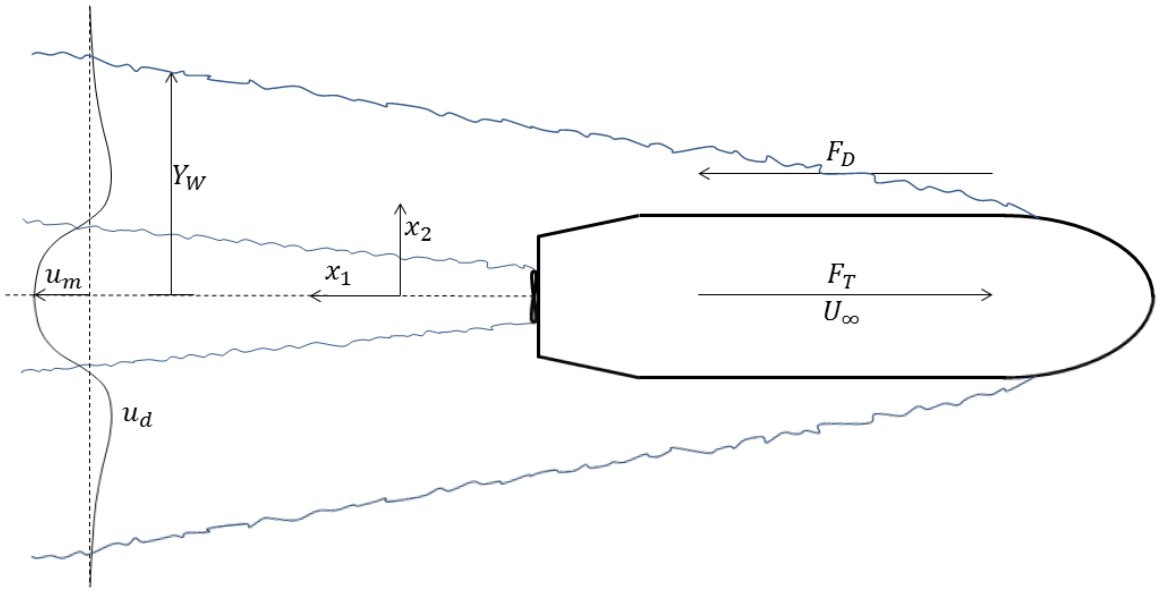

Figure 4.4: A schematic of a propelled ship showing the notation for the analysis.

and cylinders forms the basis of most studies but they differ from ships because ships are streamlined. The velocity deficit and wake width are linked through the volume flux Q

$$Q = \int_{-\infty}^{\infty} u_d \mathrm{d}A, \tag{4.5}$$

where

$$u_d = u_m \exp\left(\frac{-x_2^2}{2Y_W^2}\right), \tag{4.6}$$

for a Gaussian decay. The wake volume flux can be related to the drag force F_D on a towed body through

$$F_D = \rho Q U_\infty. \tag{4.7}$$

For an axisymmetric wake (Betz, 1925)

$$Q = \int_{-\infty}^{\infty} u_{dx_2} \mathrm{d}x_2 \simeq \pi Y_W^2 u_m, \tag{4.8}$$

likewise for a two-dimensional wake

$$Q = \int_{-\infty}^{\infty} u_d \mathrm{d}x_2 = \sqrt{\frac{\pi}{2}} Y_W u_m. \tag{4.9}$$

It is useful to estimate the Reynolds number associated with the wake

$$Re_W = \frac{u_m Y_W}{\nu}. \tag{4.10}$$

From (4.9), we see that the Reynolds number associated with the wake of a planar two-dimensional body is constant downstream (similar to a circular jet described in Chapter 2). For an axisymmetric wake

$$Re_W = \frac{Q}{\pi Y_W \nu}, \tag{4.11}$$

decreases downstream as the wake is circular. Thus, in many cases the influence of viscous effects becomes more important downstream for three-dimensional wakes. For a self-propelled body, the form of the velocity deficit is completely different. The first main difference lies in the fact that the volume flux in the wake is zero, *i.e.*

$$Q = \int_{A_W} u_d \mathrm{d}A = 0, \tag{4.12}$$

where A_W is the cross-sectional area of the wake. Physically this means that the wake behind a self-propelled body consists of four shear layers while in the case of a body fixed in the flow there are two shear layers (see Chapter 6, figure 6.6 for an illustration). Since the vorticity changes sign across the wake twice in the case of the self-propelled wake the vorticity annihilation is strong in both two and three dimensions reducing the velocity deficit faster than for a rigid body fixed in the flow. Since $Q = 0$, an alternative closure is required to estimate the downstream wake profile.

Tennekes & Lumley (1972) describe the classic view of the self-propelled state where the body does not move near the interface between two fluids, so that there is no wave drag. The main aim was to explore the scaling that describes how the wake width and velocity deficit decay downstream and this has been the starting point for most computational and experimental studies on self-propelled bodies. Their analysis starts off by assuming that the turbulent viscosity ν_t is constant, which as they noted, is quite a poor assumption. Their model gives a qualitative estimate of the processes - the self-similar form for a wake with momentum does not depend on the form of the turbulent viscosity, but for a self-propelled wake, a similarity solution can only be determined by assuming ν_t is independent of x_2. Their analysis first considered the case of a two-dimensional wake, where the streamwise momentum equation is written as

$$\frac{\partial}{\partial x_1}[U_\infty(u_{x_1} - U_\infty)] = \nu_t \frac{\partial^2}{\partial x_2^2}(u_{x_1} - U_\infty), \tag{4.13}$$

where ν_t is a constant. The assumption in (4.13) is valid far downstream where viscous

stress are ignored and the mean pressure gradient is weak. Multiplying (4.13) by x_2^n and integrating by parts twice gives

$$\frac{\mathrm{d}}{\mathrm{d}x_1}\int_{-\infty}^{\infty} x_2^n U_\infty(u_{x_1}-U_\infty)\mathrm{d}x_2 = \nu_t n(n-1)\int_{-\infty}^{\infty} x_2^{n-2}(u_{x_1}-U_\infty)\mathrm{d}x_2. \tag{4.14}$$

When $n=2$, the right-hand side of (4.14) is proportional to the volume flux (Q) which is zero for a self-propelled state (4.12) because the momentum flux is zero. For a non self-propelled state

$$\frac{\mathrm{d}I}{\mathrm{d}x_1} = 2\nu_T Q, \tag{4.15}$$

so

$$I = I_0 + 2\nu_T Q x_1. \tag{4.16}$$

Therefore, we can integrate (4.14) and show that

$$\int_{-\infty}^{\infty} x_2^2 U_\infty(u_{x_1}-U_\infty)\mathrm{d}x_2 = \text{constant}. \tag{4.17}$$

Assuming that the velocity-deficit profile is self-preserving (the velocity deficit and Reynolds stresses are independent of x if expressed in terms of the local length and velocity scales), (4.17) can be reduced to

$$u_m Y_W^3 \int_{-\infty}^{\infty} \tilde{x}_2^2 f(\tilde{x}_2)\mathrm{d}(\tilde{x}_2) = \text{constant}, \tag{4.18}$$

where $\tilde{x}_2 = x_2/Y_W$ and $u_{x_1}-U_\infty = u_m f(\tilde{x_2})$, *i.e.* $u_m Y_W \beta = \text{constant}$. This determines the first relationship between the width of the wake and the maximum velocity deficit. The second closure is obtained by assuming that the equations of motion are self-preserving. The self-preserving hypothesis arises from the momentum equation

$$U_\infty \frac{\partial u_{x_1}}{\partial x_1} = -\frac{\partial}{\partial x_2}(\overline{u'_{x_1} v'_{x_2}}). \tag{4.19}$$

The Reynolds stress scales as

$$-\overline{u'_{x_1} v'_{x_2}} = u_m^2 g(\tilde{x_2}), \tag{4.20}$$

and

$$u_x = u_m f(\tilde{x_2}). \tag{4.21}$$

Substituting into (4.19) we have

$$U_\infty \frac{\mathrm{d}u_m}{\mathrm{d}x_1} f(\tilde{x}_2) - \frac{U_\infty}{Y_W}\frac{\mathrm{d}Y_W}{\mathrm{d}x_1} u_m \frac{\mathrm{d}f}{\mathrm{d}\tilde{x}_2} = -\frac{u_m^2}{Y_m}\frac{\mathrm{d}^2 g}{\mathrm{d}\tilde{x}_2^2}, \tag{4.22}$$

or

$$U_\infty \frac{Y_W}{u_m^2}\frac{\mathrm{d}u_m}{\mathrm{d}x_1} f(\tilde{x}_2) - \frac{U_\infty}{u_m}\frac{\mathrm{d}Y_w}{\mathrm{d}x_1}\frac{\mathrm{d}f}{\mathrm{d}\tilde{x}_2} = -\frac{\mathrm{d}^2 g}{\mathrm{d}\tilde{x}_2^2}. \tag{4.23}$$

For a solution to exist, we would require the prefactors to be constant. Given the predictions consist of $u_m Y_m =$ constant,

$$\frac{1}{u_m}\frac{\mathrm{d}u_m}{\mathrm{d}x_1} = -\frac{\beta}{Y_W}\frac{\mathrm{d}Y_W}{\mathrm{d}x_1}. \tag{4.24}$$

The first constraint is

$$\frac{\beta U_\infty Y_W^{1+\beta}}{Y_W}\frac{\mathrm{d}Y_W}{\mathrm{d}x_1} = \text{constant}, \tag{4.25}$$

and the second

$$Y_W^\beta \frac{\mathrm{d}Y_W}{\mathrm{d}x_1} = \text{constant}. \tag{4.26}$$

Both constraints can be combined to give

$$\frac{\mathrm{d}Y_W^{\beta+1}}{\mathrm{d}x_1} = \text{constant}, \tag{4.27}$$

or

$$Y_W^{\beta+1} = Y_W^{\beta+1}(0) + Kx_1, \tag{4.28}$$

therefore,

$$Y_W = Y_W(0)\left(1 + \frac{Kx_1}{Y_W^{\beta+1}}\right)^{1/(\beta+1)}. \tag{4.29}$$

By dimensional analysis we could expect $K \simeq D^\beta$

$$Y_W = Y_W(0)\left(1 + \frac{\lambda x_1}{D}\right)^{1/(\beta+1)}, \tag{4.30}$$

where $\lambda \ll 1$. The self-preserving hypothesis is not consistent with the constant turbulent viscosity assumption

$$\nu_t = -\frac{\overline{u'_{x_1} v'_{x_2}}}{\partial u_{x_1}/\partial x_1} = \frac{u_m^2 g(\overline{x}_2)}{u_m/Y_W \mathrm{d}f(\overline{x}_2)/\mathrm{d}\overline{x}_2}. \tag{4.31}$$

Tennekes & Lumley (1972)	self-propelled			under-propelled		
	u_d	Y_W	ω	u_d	Y_W	ω
2D	$x_1^{-3/4}$	$x_1^{1/4}$	x_1^{-1}	$x_1^{-1/2}$	$x_1^{1/2}$	x_1^{-1}
axisymmetric/3D	$x_1^{-4/5}$	$x_1^{1/5}$	x_1^{-1}	$x_1^{-2/3}$	$x_1^{1/3}$	x_1^{-1}

ν_T = constant	self-propelled			under-propelled		
	u_d	Y_W	ω	u_d	Y_W	ω
2D	$x_1^{-3/2}$	$x_1^{1/2}$	x_1^{-2}	$x_1^{-1/2}$	$x_1^{1/2}$	x_1^{-1}
axisymmetric/3D	$x_1^{-5/2}$	$x_1^{1/2}$	x_1^{-3}	x_1^{-1}	$x_1^{1/3}$	$x_1^{-3/2}$

Table 4.1: Velocity deficit, wake width and maximum vorticity scalings for the Tennekes & Lumley (1972) (turbulent and self-similar) and Re_T = constant (laminar and self-similar) wake profiles.

This is because

$$\nu_t = \frac{u_m^2 g(\tilde{y})}{\frac{u_m}{Y_W}\frac{\mathrm{d}f(\tilde{x}_2)}{\mathrm{d}\tilde{x}_2}} = Y_W u_m \frac{g(\tilde{x}_2)}{\mathrm{d}f/\mathrm{d}\tilde{x}_2} = C\frac{g(\tilde{x}_2)}{\mathrm{d}f/\mathrm{d}\tilde{x}_2} Y_W^{1-\beta} \neq \text{constant}. \tag{4.32}$$

The predicted scalings are shown in table 4.1.

Since the velocity field is sensitive to $F_D - F_T$, the question is then how does the difference affect the velocity field. To assess the flow field, three integral quantities (Tennekes & Lumley (1972) integral (I), momentum flux (M) and volume flux (Q)). are calculated as a function of downstream distance

$$I = \int_{A_D} x_2^2 u_d \mathrm{d}A, \tag{4.33}$$

$$M = \int_{A_D} u_d^2 \mathrm{d}A, \tag{4.34}$$

$$Q = \int_{A_D} u_d \mathrm{d}A, \tag{4.35}$$

where A_D is the cross-sectional area of the domain which leads to $\mathrm{d}A = \mathrm{d}x_2$ in two dimensions and for an axisymmetric problem

$$\mathrm{d}A = 2\pi x_2 \mathrm{d}x_2, \tag{4.36}$$

and x_2 varies from $x_2 = 0$ to the edge of the computational domain.

Figure 4.5: Wake width behind a self-propelled ferry. Note that the turbulent region of the wake does not increase in width as opposed to the Kelvin wave structure on either side of it.

4.2.2 Mixing in the wake

The dumping of industrial and sewage waste into seawater is generally banned worldwide with a few exceptions. The Convention on the Prevention of Marine Pollution by Dumping of Wastes and Other Matter of 1972 was the first of such global agreements. In authorised and controlled cases the waste is tested for toxicity and the rate of release is restricted to ensure sufficient dilution in order to minimise potential toxic effects. In the UK the emission of waste into the environment is enforced by the Department of Environment, Food and Rural Affairs (DEFRA). Qualitatively the contaminant is most likely to remain within the turbulent region of the wake as opposed to spreading out like the Kelvin wave pattern. This is due to the lack of transport mechanisms, *e.g.* entrainment out of the turbulent region. Figure 4.5 shows an image of a ferry wake and it is evident that the width of the turbulent region remains relatively constant in the near and mid field.

The dilution in the wake of a self-propelled body can be understood by considering the development of the mean concentration in the wake. Following Tennekes & Lumley (1972), it can be assumed that $\mathcal{D}_t/\nu_t \simeq 1$. The mean flux of contaminant in the wake is,

$$Q_0 = \int U_\infty C \mathrm{d}A. \tag{4.37}$$

Writing

$$C = C_{max} \exp\left(-\frac{1}{2}\frac{x_2^2}{Y_W^2}\right), \tag{4.38}$$

then

$$Q_0 = U_\infty \pi Y_W^2 C_{max}. \tag{4.39}$$

From (4.39), we find that

$$C_{max} = \frac{Q_0}{U_\infty \pi Y_W^2} \sim x_1^{-2/5}. \tag{4.40}$$

Thus the dilution in the wake is

$$\mathcal{D}(x_1) = \frac{C_0}{C_{max}}. \tag{4.41}$$

at a fixed point downstream of the ship. This argument explains the basis of the IMO seawater dumping formula developed from full scale experiments of Dahl & Tollan (1972, 1973, 1975). Since the 1970 dumping of industrial and agricultural waste into seawater has gradually been severely restricted or outright banned. The following formula has been used to estimates the dilution of waste water in a ship wake

$$\mathcal{D}(t) = \beta \left(\frac{x_1}{L}\right)^{2/5} \frac{U_\infty L^2}{Q_0}, \tag{4.42}$$

where Q_0 and L correspond to the discharge rate (m^3/s) and waterline ship length (m). The IMO dumping formula in (4.42) has been expressed in terms of distance

$$3 < \frac{x}{L} < 40, \tag{4.43}$$

for consistency it is applicable 300 s or more after the ship's passing. The term β is a coefficient that is 0.003 for a single discharge port and 0.0045 for two ports located symmetrically from the ship's centre line. In a full scale study by Delvigne (1983) it was determined that the near field dilution is far higher than what Dahl predicted.

Additionally, the number of ports or their location on the ship did not affect the far field dilution. The IMO requires that the waste in the ship wake is diluted to below 96 hour LC_{50} in no more than 300 s after discharge. The term, 96 hour LC_{50}, is the lethal concentration of a contaminating substance that causes half of a specific population of species to die if they spend 96 hours within the contaminated region. Byrne *et al.* (1988) pointed out that the IMO dumping formula does not adequately predict dilution on the basis of an experimental study. It was estimated that the formula is accurate only within an order of magnitude for the estimation of dilution. It was also pointed out that obtaining empirical samples is very difficult.

Lewis (1985) developed an analytical model to improve the accuracy of predictions of dilution within a ship's wake by proposing two different expressions of dilution for the mid and far fields. Lewis (1985) indicated that the rate of dilution decays with time after discharge due to the turbulence generated by the ship (assumed to be isotropic) becoming close to that of the ambient seawater. The processes of dilution in the wake takes place in three stages: near, mid and far field. The near field is within the period of time from wake creation to when the influence of the dispersing wake is replaced by natural diffusion processes.

The most recent and detailed study was that of Chou (1996) who identified different physics that control dilution. Chou (1996) introduced the concept of near wake, intermediate wake and far wake that correspond to $x_1/D < 7$, $7 < x_1/D < 100$ and $x_1/D > 100$ where x_1 is the distance downstream of the ship and D is the characteristic width of the ship. In the near wake the fluid flow is characterised by the propulsion generation method and the ship geometry. In the intermediate wake, Chou (1996) proposed that dilution was a result of the cross-stream wake diffusion where the maximum concentration along the centre line of the wake is

$$\mathcal{C}_{max}(x_1) = C_{max}\left(\frac{x_2}{7D}\right)^{-0.552}. \tag{4.44}$$

The dilution can, therefore, be expressed as

$$\mathcal{D}(x_1) = \frac{C_0}{C_{max}(x_1)} = 0.556(I_1 + 0.134I_2)\frac{U_0B^2}{Q_E}\left(\frac{U_0t}{D}\right)^{0.522}, \tag{4.45}$$

where $I_1 = 0.374$ and $I_2 = 0.0388$ for an axisymmetric wake. At a later stage, the velocity deficit is negligible and mixing then occurs due to turbulence in the ambient

flow. The influence of ambient turbulence can be understood by the recent work of Eames *et al.* (2011*b*,*a*). This process is important when $u_d \sim u'_{RMS}$ where u_{RMS} is the RMS of the natural ambient turbulence. In the natural environment, the integral length scale is large and the RMS velocity decays slowly. Chou (1996) tested his predictions against the work of Delvigne (1983) with reasonable agreement. He commented on the possible influence of Kelvin wake drag, which is important for high speed ships, where a component of the drag does not have a submerged wake component.

4.2.3 Recent computational and experimental studies

Most computational studies of self-propelled bodies do not explicitly place a rigid body into the flow but initialize the inlet with a flow profile that satisfied the self-propelled state. Moreover most studies initialize the whole length of the channel using periodic inlet and outlet conditions (Rind & Castro, 2012; Redford *et al.*, 2012). The near field flow features of the self-propelled state are determined by the specific nature of the problem.

The numerical study of Diamessis *et al.* (2011) examined the wake behind a towed sphere for a range of Re up to 10^5 in a stably stratified environment with the LES model. The effect of stratification was to generate quasi two-dimensional large-scale vortices, however, the results did not agree with the decay laws of a two-dimensional wake as described by Tennekes & Lumley (1972). This is because the wake was not purely two-dimensional, however, almost all of the kinetic energy of the wake resided in the large quasi two-dimensional vortices.

An experimental study in a stratified environment was undertaken by Meunier & Spedding (2006). They investigated the wake behind a towed streamlined body with a propeller for the cases of under-, self- and over-propelled. It was determined that the self-propelled case is captured when the towing velocity did not differ more than 2% from the momentumless towing velocity, highlighting the fragility of capturing the momentumless wake. They determined that no consistent wake scaling could be found for self-propelled bodies in a stratified environment.

Linden (2011) indicated in an experimental study of a self-propelled streamlined body that pulsed jet propulsion can be more efficient than continuous jet propulsion. This is due to the increased entrainment of ambient fluid into the wake near the body

that leads to the increased downstream acceleration of the vortex rings.

Cimbala & Park (1990) examined experimentally the momentumless wake of a body with a streamlined front and a bluff rear at $Re = 5400$ in a non-stratified environment. It was found that the mean centre line velocity decayed as $x^{-0.92}$ (as opposed to $x^{-3/4}$ by Tennekes & Lumley (1972)) and the wake became isotropic 45 body diameters downstream.

4.3 Conclusions

From this literature review of self-propelled wakes and dilution we can identify a number of challenges and a number of gaps in the knowledge.

(a) The self-propelled state is quite special because it requires an exact balance between thrust and total drag. The pressure of wake drag, which conservatively could represent up to 5% of total drag means that there is some over thrust. This is a small fraction but as noted by Tennekes & Lumley (1972) the self-propelled state is very sensitive to excess momentum. In the case that the momentum mismatch is even 1% one body width downstream then the wake can be expected to lose its self-propelled state 100 widths downstream.

(b) Much of the literature suggests that the form of a downstream wake only depends on the integral measurements of Q_0 and I_0 (or mean drag). However, there appears to be considerable evidence that this may not be the case. Many numerical studies have used the similarity form of velocity deficit profiles to initialize numerical simulations (principally DNS & LES). Currently lacking in literature are calculations behind the wake of a self-propelled body where the characteristics of the downstream flow are linked to the difference between thrust and drag.

(c) As noted by Tennekes & Lumley (1972), the constant turbulent viscosity model is quite approximate and largely serves to demonstrate that the velocity deficit decays much more rapidly than for a fixed body in a stream. Since this model is really the classic self-propelled model, it does not require further examination. However, other turbulence models should be considered to examine the robustness of the Tennekes & Lumley (1972) predictions.

A critical analysis of literature has identified a number of important areas worthy of examination. These are

1. near self-propelled states,
2. including geometry and explicitly defining the self-propelled state,
3. influence of turbulence models.

To answer these questions, we propose the following approach:

1. turbulence models - There are many turbulence models that can be applied to examine the development of a turbulent wake. These include LES, K-ϵ, Spalart Allmaras (SA) and mixing length models. These can be applied to two-dimensional, axisymmetric and three-dimensional flow fields. The computational resources required to run three-dimensional calculations are considerable, and at the outset, this was not considered. The characteristic scales of the wake velocity deficit and contaminant concentration are sensitive to the flow being planar or axisymmetric. In terms of turbulence models, the most robust is the mixing length model as it has a strong foundation base on the Prandtl (1925) mixing length hypothesis and is already the basis of most prior studies of self-propelled wakes and mixing. A description of this approach is given later. LES turbulence models require significantly more computational resources than K-ϵ, SA or mixing length models, therefore, the proposed approach is to examine in detail the choice of (I) a constant turbulent viscosity model and (II) a mixing length model. The choice of (I) is so that we can understand the implications of the Tennekes & Lumley (1972) approach, since this type of model also corresponds to a DNS solution (with a low Re based on the turbulent viscosity).

2. characteristic form of a ship - Fundamentally, in plan view, ships are streamlined at the bow an have a boxy structure at the stern. As a consequence, a similar design was chosen based on the experimental study of Cimbala & Park (1990) where fluid was injected out of the rear of the body to generate a self-propelled wake. In the following numerical analysis (6), the body used is 4 times shorter in comparison to Cimbala & Park (1990) (as a consequence of computational resource constraints), however, the characteristic features, *e.g.* streamlined bow

and bluff stern remain. The reason for this is to reduce the amount of boundary layer that needs to be resolved. As described in Chapter 5, it takes considerable computational resource to fully resolve the flow features around solid objects.

3. choice of forcing - Different approaches exist including the use of distributed forcing (not physical) and volumetric forcing (relates to thrusters).

4. boundary influence - Computational domains generally have a finite size and its influence may render certain approaches infeasible. Which method is least affected by the effect of boundedness for determining the self-propelled state of the calculation?

Chapter 5

Computational model

5.1 Introduction

The Navier-Stokes equation can only be solved analytically for very simple flow field assumptions, however, computers can produce accurate approximate solutions with the use of numerical schemes for a wide variety of flows. This technique, commonly referred to as Computational Fluid Dynamics (CFD), involves taking a problem, generating a numerical solution that captures some, but perhaps not all, of the salient features of the problem and presenting the data in a meaningful manner. As described in the literature presented in Chapter 4 there is a subtlety in studying self-propelled bodies. It is clear that in a numerical study of self-propelled state a thorough understanding would be needed on the internal structure and diagnostics of the code. The purpose of this chapter and the reason for writing my own code is to cover the fundamentals of CFD as well as develop and validate various solvers.

5.2 Overview of computational methods

There are two fundamental representations of fluid flow which have a strong bearing on the mesh, model equations and numerical techniques used for solving them: Lagrangian and Eulerian (Lamb, 1932). A Lagrangian description involves following a parcel of information (flow field variables) which moves with the flow. This is computationally challenging and only used for specialist problems (*e.g.* dispersed multiphase flows). Alternatively the flow information is tracked at fixed points - the Eulerian description - and this is generally used in engineering. We focus our attention on the Eulerian models.

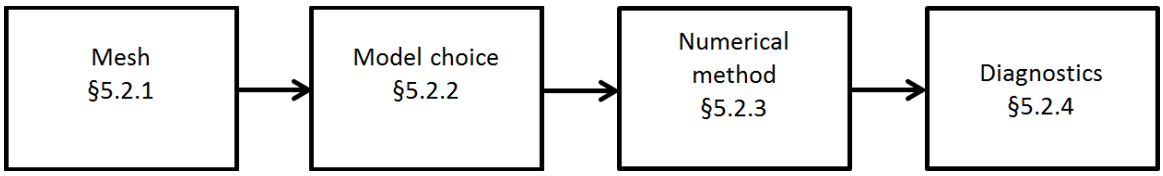

Figure 5.1: Steps involved in a CFD analysis of a flow field.

Many numerical codes have been developed, the most prominent are OpenFOAM (open source `http://www.openfoam.com/`) and Fluent (proprietary `http://www.ansys.com/`). The main benefit of proprietary software is that within the advertised range of functionality it can be expected to perform well and ample technical support is available. The disadvantage is that once limitations within the framework of the program are reached it can be very difficult to implement further functionality. In academia it is common to also use in-house research codes one of which is ACEsim (`http://acesim.co.uk/`) that is used in UCL. The reason for developing my own code is because ACEsim does not have turbulence models at this stage. Regardless of the choice of numerical code the general steps in CFD analysis can be grouped into four main steps (see figure 5.1), for which there are many choices.

An important part of any mathematical or computational method is validation and verification of results (Velten, 2008), underlying the importance of continued experimental work in fluid mechanics. For general purpose numerical codes a wide range of validation studies need to be performed. In CFD it must be understood what effect different boundary conditions and choice of numerical method have on the final results. Most validation studies are based on experimental and analytical data, however, comparisons can also be made against other validated codes.

5.2.1 Meshing

Very broadly, fluid flow problems tend to fall under either external (*e.g.* flow around a cylinder) or internal flows (*e.g.* pipe flow) (Hunt, 1999), which can have quite different properties. Regardless of the problem type the computational domain, in most cases, is bounded and finite. The bounded region is filled with a number of nodes (N_p), which are the basis of a group of tessellating geometric shapes that make up the mesh. The purpose of a mesh is to reduce a problem with infinite degrees of freedom to one with a finite number. For unstructured meshes the most common shapes are triangular

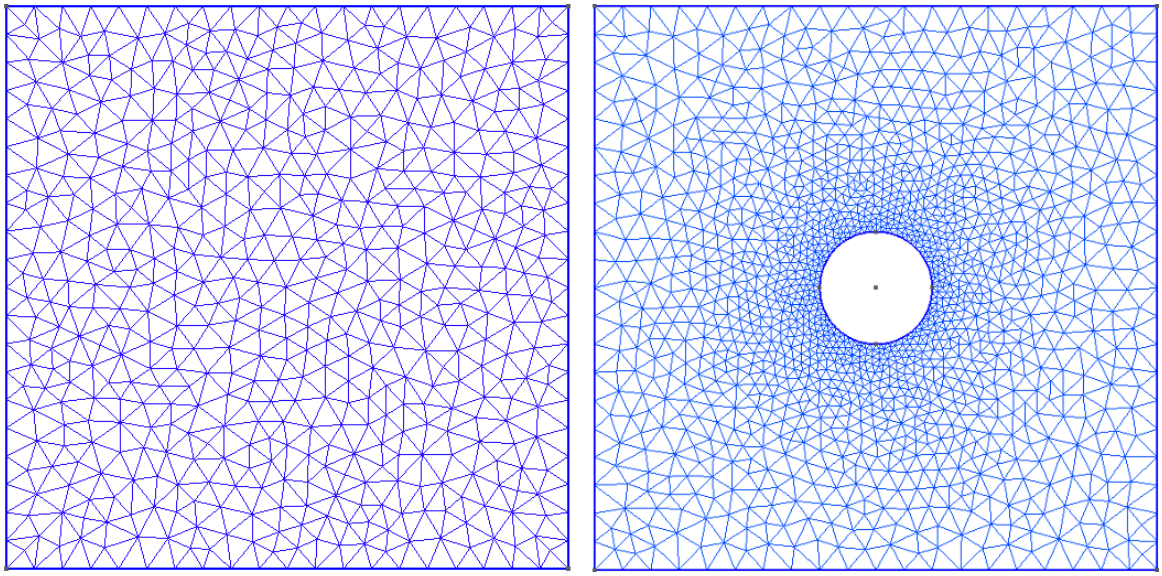

Figure 5.2: Two unstructured meshes composed of triangular elements created in Gmsh. The advantage of the unstructured mesh is illustrated by placing a curved surface into the centre of the domain and increasing the mesh resolution locally. Similar gradual mesh refinement is not easily reproduced with structured meshes.

(two-dimensional) and tetrahedral (three-dimensional), while in structured meshes, quadrilateral and hexahedral shapes are the most common (Hirsch, 2007). In order to calculate the solution, the governing equations need to be closed by appropriate boundary conditions on the boundaries of the computational domain.

The advantage of unstructured meshes over structured meshes is that they can be applied to complex geometries (see figure 5.2), however, they are not compatible with some simpler numerical methods such as the finite difference method. Most of the disadvantages of unstructured meshes originate from the storage and calculation of nodal connections and geometric gradients at each point. This results in a larger memory footprint and additional calculations when determining the elemental areas and the various matrices that are dependent on them. Additionally, certain diagnostics require a structured mesh (*e.g.* calculating the turbulent energy spectrum) resulting in the need of additional steps to reinterpret the unstructured mesh onto a structured grid.

Ideally the elements of a triangular mesh should be as close to equilateral triangles as possible resulting in an isotropic mesh. The most common mesh quality criterion for two-dimensional unstructured triangular elements is the Delaunay triangulation method (Delaunay, 1934). Under this method the requirement is that the nodes are

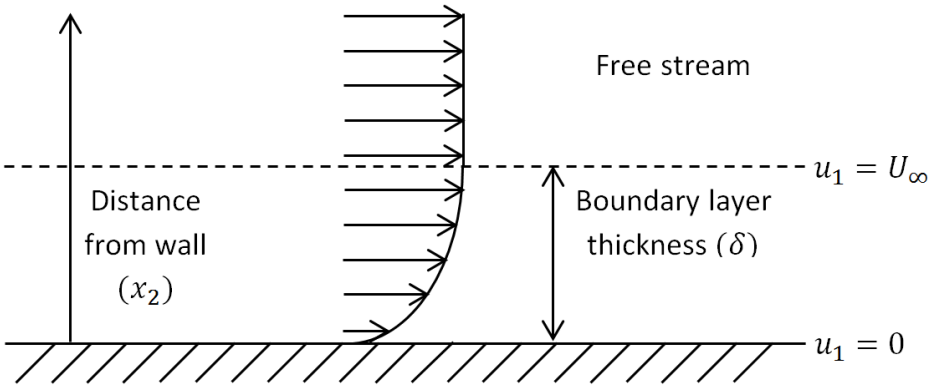

Figure 5.3: The velocity profile within the boundary layer of the flow past a rigid surface.

separated in such an arrangement where there are no more than three nodes within the circumcircle of a triangular element. The result is that obtuse triangles are avoided where possible.

One of the most common triangular mesh generators is Triangle (Shewchuk, 1996) (`http://www.cs.cmu.edu/~quake/triangle.html`), which can be accessed through graphical user interfaces such as Gmsh (`http://geuz.org/gmsh/`). For tetrahedral meshes Netgen (`http://www.hpfem.jku.at/netgen/`) is the preferred method that is also included with Gmsh. Structured meshes are much simpler to generate and most codes implement their own methods.

5.2.2 Model choice

The choice of the fluid mechanics model depends on the Reynolds number defined as

$$Re = \frac{U_\infty D}{\nu}, \tag{5.1}$$

where U_∞ is the characteristic flow velocity past a body, D is the characteristic length scale of the body and ν is the kinematic viscosity. As Re increases so does the range of flow field lengthscales resulting in very fine flow features (*e.g.* boundary layer and filament vortices) that are usually much smaller than the local grid scale and have to be represented by using a subgrid scale model.

The boundary condition for a rigid surface is that the relative velocity is zero. In the cases studied the surfaces are stationary which results in the boundary condition being $\boldsymbol{u} = 0$. This results in the formation of a boundary layer which is a region

adjaisent to the rigid surface where the velocity goes from 0 to the free stream (see figure 5.3). As the inertial forces are of the same order of magnitude as the viscous forces the Re of the boundary layer is approximately 1. The x_1 component of the Navier-Stokes equation is

$$\rho\left(\frac{\partial u_1}{\partial t}+\boxed{u_1\frac{\partial u_1}{\partial x_1}}+u_2\frac{\partial u_1}{\partial x_2}\right)=-\frac{\partial p}{\partial x_1}+\mu\left(\frac{\partial^2 u_1}{\partial u_1^2}+\boxed{\frac{\partial^2 u_1}{\partial x_2^2}}\right). \tag{5.2}$$

Considering a steady shear flow, assuming that $\partial u_1/\partial x_2 \gg \partial u_1/\partial x_1$ and $u_2 \sim 0$ (5.2) reduces to the highlighted parts that can be expressed as

$$\rho u_1\left(\frac{u_1}{L}\right)\sim\mu\left(\frac{u_1}{\delta^2}\right), \tag{5.3}$$

where L is a lengthscale and δ is the boundary layer thickness. Rearranging and expressing in terms of the Reynolds number results in

$$\delta \sim LRe^{-1/2}, \tag{5.4}$$

which has the same dependence on Re for two- and three-dimensional flows (Davidson, 2003). To fully resolve it at least 4 elements across the boundary layer are required (Nicolle, 2009).

To illustrate how the flow characteristics change with Re consider the streamline structure in figure 5.4 for a two-dimensional flow past a rigid cylinder. At $Re \ll 1$ the streamlines are symmetrical around across the vertical and horizontal axis. The symmetry reduces to that of horizontal axis only at $Re \approx 10$ when counter rotating recirculating regions develop at the back of the cylinder. At $Re \approx 90$ instabilities develop and the cylinder starts shedding vortices known as the von Karman vortex street. When $Re > 1000$ the vortices are mixed together to become a turbulent flow that is irregular in space and time. Flow past cylinders for a range of Re been studied in great detail by Blevins (1990) and Singh & Mittal (2005).

The transition between laminar and turbulent flow is gradual, however, a critical point can be determined beyond which the flow can be considered turbulent. Direct Numerical Simulations (DNS) simulate the full range of turbulent fluctuations on all relevant length scales. This becomes increasingly computationally resource intensive as Re increases due to the increase in the range of smallest to largest flow feature lengthscales. Therefore, calculations at high Re become unfeasible with DNS, therefore,

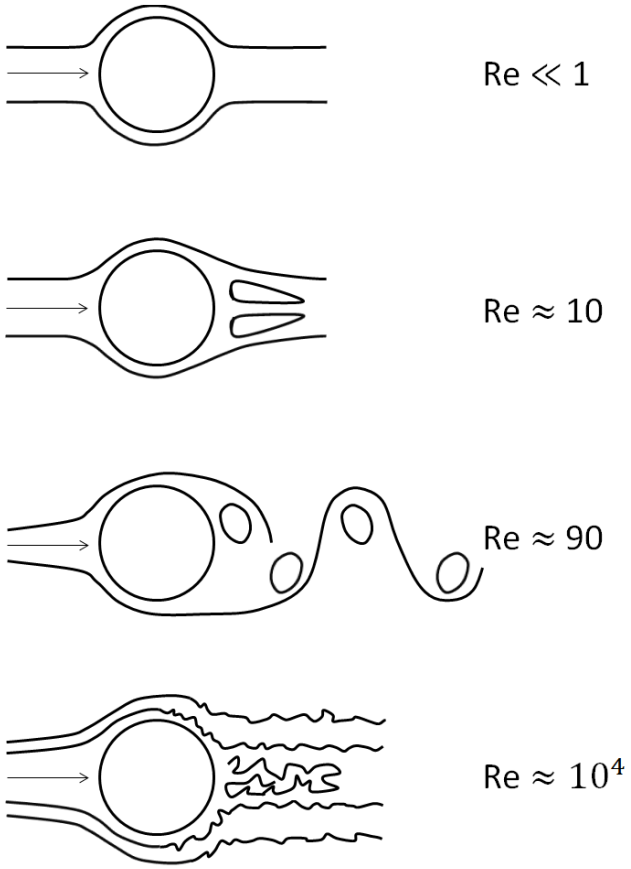

Figure 5.4: Qualitative streamlines of a flow past a cylinder for a range of Reynolds numbers. At very low $Re \ll 1$ the flow does not separate from the surface of the cylinder. At $Re \approx 10$ a recirculating region appears at the end of the cylinder. At $Re \approx 90$ two flow regimes develop with laminar vortex streets. At $Re \approx 10^4$ the boundary layer has become fully turbulent and the wake has become narrower and chaotic.

turbulence models need to be considered. There are two types of modelling approaches based on conceptually different treatments of modelling the unresolved scales.

The first is based on an ensemble averaging of the flow (Reynolds average Navier-Stokes (RANS) method) where the flow has clear partitions between fast and slow scales (Pope, 2000). $K-\epsilon$ is one of the simpler RANS models and it is also weakly dependent on Re. It is a two equation model that includes two transportation equations to describe the development of turbulent kinetic energy and turbulent dissipation. This model ignores turbulent fluctuations and only deals with the average flow. $K-\epsilon$ is the most common turbulence model used in research and industry but it does not perform well when dealing with large pressure gradients (Wilcox, 1994). Another popular example is the Spalart-Allmaras model (Spalart & Allmaras, 1992) described in Appendix C.

The second is the Large Eddy Simulations (LES) method. The Navier-Stokes operations are filtered and averaged over small scales (Davidson, 2003). Small scale eddies on the subgrid scale are represented as effective turbulent viscosity on the larger scale flow. The computational resource required increases significantly when walls and obstructing objects are introduced into the geometry. The flow field around the boundary is important because viscous effects play a larger role in the downstream development of vortices.

In conclusion the model choice needs to be based on the required Re of the flow and the computational resources available. Figure 5.5 gives an indication of the computational resources required for a specific problem. It should also be noted that there are differences between two- and three-dimensional flows. In the case of three-dimensional flows vortices break down due to instabilities to smaller scales until the diffusive length scale. In the case of two-dimensional flows there is no stretching of vortices. Smaller vortices are smeared out resulting in the cascade to large-scales.

5.2.3 Numerical method

Most CFD models are based on approximating the non-linear Navier-Stokes equation with a system of linear equations. The common element is to represent a solution to a system of PDE's as a discrete set of points in time, space or both. Regardless of the numerical method, the solution is reached by projecting current flow field values forward in time by a small increments based on the local flow information.

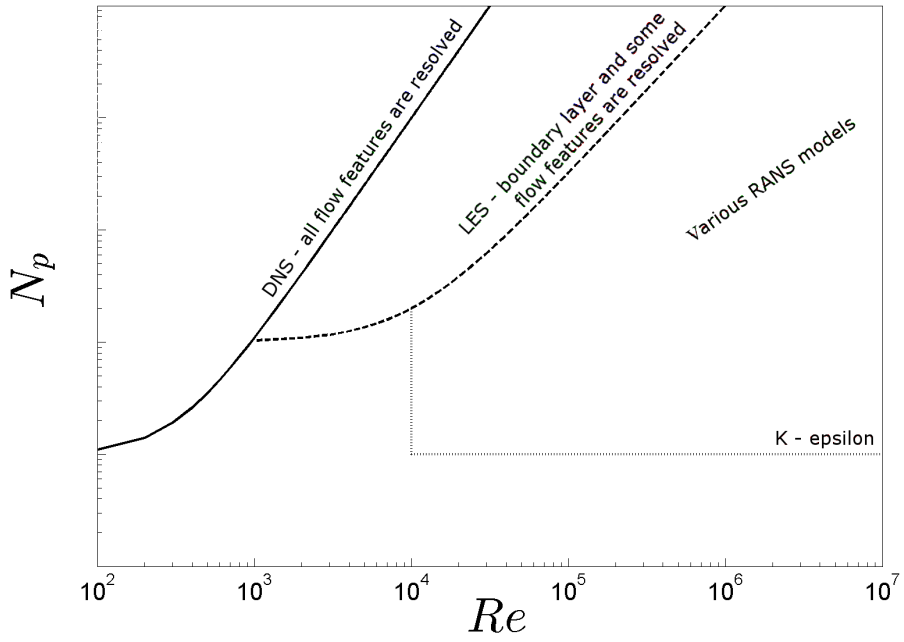

Figure 5.5: Schematic showing how the number of nodes N_p required for calculating the flow past a two-dimensional cylinder depends on the modelling approach used. The solid, dashed and dotted lines correspond to DNS, LES and $K-\epsilon$ models. This is an estimate based on the general assumptions about the calculations.

This projection is called the time step and it is affected by the element size and the advective and diffusive timescales. Depending on the application, an appropriate numerical scheme must be chosen because errors are amplified by the discretization process and time stepping. There are three widely applied CFD methods that are likely to be used for the foreseeable future. We illustrate these techniques through a discussion of a generic partial differential equation represented as

$$\mathcal{L}(\boldsymbol{u}) = \mathbf{0}, \tag{5.5}$$

where $\mathcal{L}$ is an operator on the field $\boldsymbol{u}$. The following three numerical methods are the most common approaches to CFD.

1. Finite Difference Method (FDM) - A basic numeric method based on the properties of the Taylor expansion (Lomax *et al.*, 2001). It is extremely simple to apply, however, the grid points are usually set up in a structured n-dimensional space where the points are located at the intersections of n families of lines that are unique to that point.

2. Finite Volume Method (FVM) - A conceptually simple scheme that is easy to implement to structured and unstructured grids (Versteeg & Malalasekera, 2007). The grid points in this numerical domain are associated with the centre of a finite volume. Across the edge of each element an integral conservation law is applied. The volume integrals contain a divergence term that is converted to surface integrals which are used to evaluate the fluxes entering and leaving the volume surrounding each node. The FVM involves integrating (5.5) over a control volume

$$\int_{\Omega_e} \mathcal{L}(\boldsymbol{u}) \mathrm{d}\Omega = \mathbf{0}. \tag{5.6}$$

This ensures that the divergence of momentum or force can be expressed in terms of

$$\int_{\Omega_e} \boldsymbol{\nabla} \cdot \boldsymbol{A} \mathrm{d}\Omega = \int_{S_e} \boldsymbol{A} \cdot \hat{\boldsymbol{n}} \mathrm{d}S, \tag{5.7}$$

where Ω is the volume and S the surface in three-dimensions. In two-dimensions Ω and S are area and a line. The benefit of this technique is that mass and momentum are explicitly conserved. The disadvantage of the FVM is that velocity and pressure values may not be collocated. This makes applying boundary conditions to complex geometries challenging.

3. Finite Element Method (FEM) - A more advanced numerical tool that is extremely flexible and can be applied to a large number of problems (Lewis *et al.*, 2004). Traditionally FEM has been the basis of Computational Solid Mechanics (CSM) to calculate mechanical stresses, vibrations and deformations of rigid structures. Its main advantage is that it can be used to obtain approximate numerical solutions to complex geometry problems to which exact solutions are impossible or impractical to find. The principal feature of FEM is that the domain is divided into small interconnected and non-overlapping elements where each element gives its approximation to the governing partial differential equation. This technique involves first defining an approximation

$$\boldsymbol{u}_a = \sum_{i=1}^{N_p} u_i \boldsymbol{N_i}, \tag{5.8}$$

where $\boldsymbol{N}$ is a set of basis functions. The solution is chosen so that the residual

is zero, *i.e.*

$$R_i = \int_\Omega \mathcal{L}(\boldsymbol{u}_a) N_i \mathrm{d}\Omega = 0. \tag{5.9}$$

The disadvantage of FEM is that it does not conserve momentum locally only globally.

The accuracy of the simulation depends on a wide variety of factors. Usually increasing the number of elements (increasing mesh density) reduces the simulation error but it also increases the number of calculations and, therefore, the computational power requirement. Other factors that affect simulation accuracy are the initial conditions and appropriateness of the numerical model. Regardless of the numerical method it is important to understand its fundamentals and the initial flow conditions need to be applied appropriately.

5.2.4 Diagnostics

Diagnostic tools are a very powerful part of CFD allowing the user to extract quantitative data from any region of the flow field, however, they are very problem specific. Commonly used diagnostics include the calculation of drag, lift, vorticity, pressure loss and so on. Qualitative results commonly involve the visualisation of the data. In relation to a flow past a rigid body, the relevant diagnostics are described in §5.4.3. It can also be important to know before running the simulation what diagnostics need to be calculated as they may have to be hard coded or data may need to be extracted at specific time intervals.

5.2.5 Critical analysis

Considering that the intent is to analyse mixing in the wake of a rigid body, the following choices can be made:

a) programming environment - Matlab was chosen due to its accessibility and ease of debugging. It would have been better to write the code in C from a performance standpoint but the ease at which data can be visualized in Matlab allows for the development and prototyping of additional features such as solvers, turbulence models and diagnostics. There are already numerous codes available that have already been written in C and to my knowledge this is the first CBS-FEM code written in Matlab.

b) two-dimenions - Matlab has significant computational overhead, therefore, working in three-dimensions would not be useful due to mesh size limitations. The exception is axisymmetric flows that could be considered, due to only marginal performance decreases, to be two-dimensional.

c) meshing - Unstructured triangular meshes were chosen because of the geometry requirements and the chosen meshing tool is Gmsh. The use of structured triangular meshes is also possible with the same implementation. In the case of structured quadrilateral meshes the option to create an unstructured mesh is not possible, therefore, the use of triangular meshes is more flexible.

d) CBS-FEM - Under this scheme it is very straightforward to implement boundary conditions to complex geometries. In comparison to FVM, FEM is much easier to program for as it does not require the use of ghost elements. Additionally, there is considerable support available for FEM at UCL (Nicolle, 2009; Klettner, 2010).

5.3 Numerical scheme

The Characteristic Based Split (CBS) scheme (Lewis *et al.*, 2004) is a numerical method that can be applied to solve the two- and three-dimensional Navier-Stokes equations. It is composed of two parts, the first being the split where the pressure gradient term is dropped from the momentum equation, which allows for the use of equal interpolation for both pressure and velocity. The second part is the Characteristic Galerkin method where a stabilisation term, a second-order operator from the spatial Taylor series expansion, is added to the momentum equation to dampen oscillations from the discretization of the convective term.

5.3.1 Two-dimensional formulation

The governing equations need to satisfy the conservation of momentum and mass. The conservation of mass is described by the continuity equation

$$\frac{\partial \rho}{\partial t} + \boldsymbol{\nabla} \cdot \boldsymbol{u} = 0. \tag{5.10}$$

In this study the fluid is assumed to be incompressible, therefore, the expression in (5.10) reduces to

$$\boldsymbol{\nabla} \cdot \boldsymbol{u} = 0. \tag{5.11}$$

The conservation of momentum for an isothermal fluid is expressed as

$$\rho \frac{\mathrm{D}\boldsymbol{u}}{\mathrm{D}t} = -\boldsymbol{\nabla} p + \boldsymbol{\nabla} \cdot \boldsymbol{\tau}, \tag{5.12}$$

where $\boldsymbol{u} = (u_1, u_2)$ is the velocity vector field and p is the pressure field. The velocities u_1 and u_2 correspond to x_1 and x_2 in Cartesian coordinates. The term $\boldsymbol{\tau}$ consists of

$$\boldsymbol{\tau} = \rho(\nu_t + \nu)\boldsymbol{S}, \tag{5.13}$$

where ν_t is the turbulent kinematic viscosity in the case the case when a turbulence model with the Boussinesq eddy viscosity assumption is being used, ν is the molecular kinematic viscosity and $\boldsymbol{S}$ is the rate of strain defined as

$$\boldsymbol{S} = \boldsymbol{\nabla u} + (\boldsymbol{\nabla u})^T. \tag{5.14}$$

The formulation of the Spalart Allmaras turbulence model is in Appendix C. We illustrate the numerical techniques for CBS–FEM by applying it to the Navier-Stokes equation

$$\rho \frac{\mathrm{D}\boldsymbol{u}}{\mathrm{D}t} = \rho \left[\underbrace{\frac{\boldsymbol{u}^{n+1} - \boldsymbol{u}^n}{\Delta t}}_{\text{unsteady}} + \underbrace{(\boldsymbol{u} \cdot \boldsymbol{\nabla})\boldsymbol{u}}_{\text{convective}} \right] = - \underbrace{\boldsymbol{\nabla} p}_{\text{pressure gradient}} + \underbrace{\mu \boldsymbol{\nabla}^2 \boldsymbol{u}}_{\text{diffusion}}. \tag{5.15}$$

In order to solve this equation numerically it must first be discretized in time and space.

Temporal Discretization

1. The intermediate velocity fields are calculated while excluding the pressure gradient term.
2. A pressure equation is used to calculate the pressure field.
3. The velocity components are corrected using the pressure calculation that projects the intermediate velocity into solenoidal space.

Step 1

The intermediate velocity field without the pressure gradient term in a semi-discrete form is expressed as

$$\rho\left[\frac{\tilde{\boldsymbol{u}}-\boldsymbol{u}^n}{\Delta t}+(\boldsymbol{u}\cdot\boldsymbol{\nabla})\boldsymbol{u}\right]=\mu\boldsymbol{\nabla}^2\boldsymbol{u}. \tag{5.16}$$

Rearranging and adding the stabilisation term results in

$$\frac{\tilde{\boldsymbol{u}}-\boldsymbol{u}^n}{\Delta t}=-(\boldsymbol{u}\cdot\boldsymbol{\nabla})\boldsymbol{u}+\nu\boldsymbol{\nabla}^2\boldsymbol{u}^n-\underbrace{[(\boldsymbol{u}\cdot\boldsymbol{\nabla})(\boldsymbol{u}\cdot\boldsymbol{\nabla}\boldsymbol{u})]\Delta t}_{\text{stabilisation}}. \tag{5.17}$$

Step 2

The resulting pressure equation from the decoupling of the momentum equation is

$$\frac{\tilde{\boldsymbol{u}}-\boldsymbol{u}^n}{\Delta t}=-\frac{1}{\rho}\boldsymbol{\nabla}p^{n+1}. \tag{5.18}$$

The pressure is calculated so that the velocity field at (n+1) satisfies the divergence free condition

$$\frac{(\boldsymbol{\nabla}\cdot\boldsymbol{u}^{n+1}-\boldsymbol{\nabla}\cdot\tilde{\boldsymbol{u}})}{\Delta t}=-\frac{1}{\rho}\boldsymbol{\nabla}^2p^{n+1}. \tag{5.19}$$

The reduced continuity equation for incompressible flows results in the $\boldsymbol{\nabla}\cdot\boldsymbol{u}^{n+1}$ term equalling zero leading to an elliptic equation for p

$$\frac{\boldsymbol{\nabla}\cdot\tilde{\boldsymbol{u}}}{\Delta t}=\frac{1}{\rho}\boldsymbol{\nabla}^2p^{n+1}. \tag{5.20}$$

Computationally this is the most challenging of the three as the other steps are parabolic.

Step 3

This is the momentum correction step where the pressure term derived in Step 2 can be expressed as

$$\frac{\boldsymbol{u}^{n+1}-\tilde{\boldsymbol{u}}}{\Delta t}=-\frac{1}{\rho}\boldsymbol{\nabla}^2p^{n+1}, \tag{5.21}$$

and added onto the intermediate velocities derived in Step 1 resulting in

$$\frac{\boldsymbol{u}^{n+1}-\tilde{\boldsymbol{u}}}{\Delta t}=-(\boldsymbol{u}\cdot\boldsymbol{\nabla})\boldsymbol{u}+\nu\boldsymbol{\nabla}^2\boldsymbol{u}^n-[(\boldsymbol{\nabla}\cdot\boldsymbol{u})(\boldsymbol{u}\cdot\boldsymbol{\nabla}\boldsymbol{u})]\Delta t-\frac{1}{\rho}\boldsymbol{\nabla}^2p^{n+1}. \tag{5.22}$$

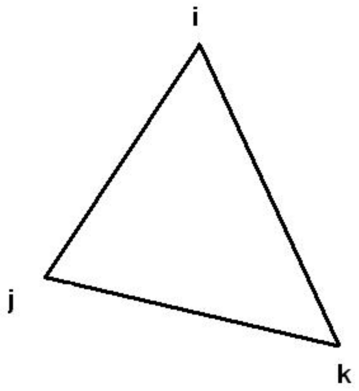

Figure 5.6: Linear triangular element notations on the previously defined two-dimensional plane. The labels i, j and k are given in an anticlockwise sense so that the area A_e in (5.26) is positive.

Spatial Discretization

Now that temporal discretization is complete the next step is spatial discretization for a triangular element assuming linear interpolation functions. Linear spatial variation in a field variable ϕ (*e.g.* u_1, u_2 or p) is described by the following equation where $\boldsymbol{N}$ is the shape function

$$\phi = N_i\phi_i + N_j\phi_j + N_k\phi_k = [\boldsymbol{N}]\{\boldsymbol{\phi}\}. \tag{5.23}$$

After the application of the Galerkin weighting to ϕ or in this case u we obtain the global mass matrix

$$\int_\Omega [\boldsymbol{N}]^T[\boldsymbol{N}]\frac{\{\boldsymbol{u}^{n+1}\} - \{\boldsymbol{u}^n\}}{\Delta t}\mathrm{d}\Omega = [\boldsymbol{M}]\frac{\Delta\{\boldsymbol{u}\}}{\Delta t}, \tag{5.24}$$

where $[\boldsymbol{M}]$ is the mass matrix which, for a single element in the CBS scheme is defined to be

$$[\boldsymbol{M}_e] = \frac{A_e}{12}\begin{bmatrix} 2 & 1 & 1 \\ 1 & 2 & 1 \\ 1 & 1 & 2 \end{bmatrix}. \tag{5.25}$$

The elemental area is calculated as

$$A_e = \frac{1}{2}\det\begin{vmatrix} x_i & y_i & 1 \\ x_j & y_j & 1 \\ x_k & y_k & 1 \end{vmatrix}. \tag{5.26}$$

The convection matrix for a single element is integrated as

$$[\boldsymbol{C}_e] = \int_\Omega [\boldsymbol{N}]^T \left(u\frac{\partial[\boldsymbol{N}]}{\partial x_1} + v\frac{\partial[\boldsymbol{N}]}{\partial x_2} \right) \mathrm{d}\Omega. \tag{5.27}$$

In matrix form it is expressed as

$$[\boldsymbol{C}_e] = \frac{1}{24}\begin{bmatrix} (usu+u_{1i})b_i & (usu+u_{1i})b_j & (usu+u_{1i})b_k \\ (usu+u_{1j})b_i & (usu+u_{1j})b_j & (usu+u_{1j})b_k \\ (usu+u_{1k})b_i & (usu+u_{1k})b_j & (usu+u_{1k})b_k \end{bmatrix}$$

$$+\frac{1}{24}\begin{bmatrix} (vsu+u_{2i})c_i & (vsu+u_{2i})c_j & (vsu+u_{2i})c_k \\ (vsu+u_{2j})c_i & (vsu+u_{2j})c_j & (vsu+u_{2j})c_k \\ (vsu+u_{2k})c_i & (vsu+u_{2k})c_j & (vsu+u_{2k})c_k \end{bmatrix}, \tag{5.28}$$

where

$$usu = u_{1i} + u_{1j} + u_{1k},$$

$$vsu = u_{2i} + u_{2j} + u_{2k},$$

and

$$b_i = y_j - y_k; \quad c_i = x_k - x_j,$$

$$b_j = y_k - y_i; \quad c_j = x_i - x_k,$$

$$b_k = y_i - y_j; \quad c_k = x_j - x_i.$$

By substituting in the values of the derivatives of the shape functions, the diffusion matrix for a single element can be integrated

$$[\boldsymbol{K}_e] = \int_\Omega \left(\frac{\partial[\boldsymbol{N}]^T}{\partial x_1}\frac{\partial[\boldsymbol{N}]}{\partial x_1} + \frac{\partial[\boldsymbol{N}]^T}{\partial x_2}\frac{\partial[\boldsymbol{N}]}{\partial x_2} \right) \mathrm{d}\Omega. \tag{5.29}$$

In matrix form it is expressed as

$$[\boldsymbol{K}_e] = \frac{1}{4A_e}\begin{bmatrix} b_i^2 & b_ib_j & b_ib_k \\ b_jb_i & b_j^2 & b_jb_k \\ b_kb_i & b_kb_j & b_k^2 \end{bmatrix} + \frac{1}{4A_e}\begin{bmatrix} c_i^2 & c_ic_j & c_ic_k \\ c_jc_i & c_j^2 & c_jc_k \\ c_kc_i & c_kc_j & c_k^2 \end{bmatrix}. \tag{5.30}$$

By integrating the characteristic Galerkin term within the domain, the elemental stabilisation matrix is obtained

$$[\boldsymbol{K}_{se}] = u_1\frac{\Delta t}{2}\left[\int_\Omega u_1 \frac{\partial[\boldsymbol{N}]^T}{\partial x_1}\frac{\partial[\boldsymbol{N}]}{\partial x_1}\mathrm{d}\Omega + \int_\Omega u_2 \frac{\partial[\boldsymbol{N}]^T}{\partial x_2}\frac{\partial[\boldsymbol{N}]}{\partial x_2}\mathrm{d}\Omega \right]$$

$$+ u_2 \frac{\Delta t}{2} \left[\int_\Omega u_1 \frac{\partial [\boldsymbol{N}]^T}{\partial x_1} \frac{\partial [\boldsymbol{N}]}{\partial x_1} \mathrm{d}\Omega + \int_\Omega u_2 \frac{\partial [\boldsymbol{N}]^T}{\partial x_2} \frac{\partial [\boldsymbol{N}]}{\partial x_2} \mathrm{d}\Omega \right], \tag{5.31}$$

that in matrix form is expressed as

$$[\boldsymbol{K}_{se}] = \frac{u_{1av}}{12A} usu \begin{bmatrix} b_i^2 & b_i b_j & b_i b_k \\ b_j b_i & b_j^2 & b_j b_k \\ b_k b_i & b_k b_j & b_k^2 \end{bmatrix} + \frac{u_{1av}}{12A} vsu \begin{bmatrix} b_i c_i & b_i c_j & b_i c_k \\ b_j c_i & b_j c_j & b_j c_k \\ b_k c_i & b_k c_j & b_k c_k \end{bmatrix}$$

$$+ \frac{u_{2av}}{12A} usu \begin{bmatrix} c_i b_i & c_i b_j & c_i b_k \\ c_j b_i & c_j b_j & c_j b_k \\ c_k b_i & c_k b_j & c_k b_k \end{bmatrix} + \frac{u_{2av}}{12A} vsu \begin{bmatrix} c_i^2 & c_i c_j & c_i c_k \\ c_j c_i & c_j^2 & c_j c_k \\ c_k c_i & c_k c_j & c_k^2 \end{bmatrix}, \tag{5.32}$$

where u_{1av} and u_{2av} are average values of u_1 and u_2 over an element. The gradient vectors in the x_1 and x_2 direction are

$$[\boldsymbol{G}_1] = \frac{1}{6} \begin{bmatrix} b_i & b_j & b_k \\ b_i & b_j & b_k \\ b_i & b_j & b_k \end{bmatrix} = \frac{1}{6} \begin{bmatrix} 1 \\ 1 \\ 1 \end{bmatrix} \boldsymbol{b}, \tag{5.33}$$

$$[\boldsymbol{G}_2] = \frac{1}{6} \begin{bmatrix} c_i & c_j & c_k \\ c_i & c_j & c_k \\ c_i & c_j & c_k \end{bmatrix} = \frac{1}{6} \begin{bmatrix} 1 \\ 1 \\ 1 \end{bmatrix} \boldsymbol{c}. \tag{5.34}$$

In conclusion the above terms are assembled in order to make up the following steps that enable the solving of an isothermal problem with the CBS scheme.

1. Intermediate velocity calculation:

$$[\boldsymbol{M}] \frac{\Delta \{\tilde{\boldsymbol{u}}_1\}}{\Delta t} = -[\boldsymbol{C}] \{\boldsymbol{u}_1\}^n - \nu [\boldsymbol{K}_e] \{\boldsymbol{u}_1\}^n - [\boldsymbol{K}_{se}] \{\boldsymbol{u}_1\}^n \Delta t + \{\boldsymbol{f}_1\} \tag{5.35}$$

$$[\boldsymbol{M}] \frac{\Delta \{\tilde{\boldsymbol{u}}_2\}}{\Delta t} = -[\boldsymbol{C}] \{\boldsymbol{u}_2\}^n - \nu [\boldsymbol{K}_e] \{\boldsymbol{u}_2\}^n - [\boldsymbol{K}_{se}] \{\boldsymbol{u}_2\}^n \Delta t + \{\boldsymbol{f}_2\} \tag{5.36}$$

2. Pressure calculation:

$$[\boldsymbol{K}] \{\boldsymbol{p}\}^{n+1} = -\frac{1}{\Delta t} \left([\boldsymbol{G}_1] \{\tilde{\boldsymbol{u}}_1\} + [\boldsymbol{G}_2] \{\tilde{\boldsymbol{u}}_2\} \right) + \{\boldsymbol{f}_3\} \tag{5.37}$$

3. Velocity correction:

$$[\boldsymbol{M}]\{\boldsymbol{u}_1\}^{n+1} = [\boldsymbol{M}]\{\tilde{\boldsymbol{u}}_1\} - \Delta t[\boldsymbol{G}_1]\{\boldsymbol{p}\}^{n+1} \tag{5.38}$$

$$[\boldsymbol{M}]\{\boldsymbol{u}_2\}^{n+1} = [\boldsymbol{M}]\{\tilde{\boldsymbol{u}}_2\} - \Delta t[\boldsymbol{G}_2]\{\boldsymbol{p}\}^{n+1} \tag{5.39}$$

The forcing terms $\{\boldsymbol{f}_1\}$, $\{\boldsymbol{f}_2\}$ and $\{\boldsymbol{f}_3\}$ have not been described. The reason is that the focus will be on Dirichlet boundary conditions where the desired values are prescribed onto the boundaries. Alternatively Neumann boundary conditions could be used where the gradient of a field variable is prescribed instead. In the latter case the forcing terms need to be included in the above CBS formulation. The relevant matrices can be summarised as

$$[\boldsymbol{M}] = \frac{A}{12}\begin{bmatrix} 2 & 1 & 1 \\ 1 & 2 & 1 \\ 1 & 1 & 2 \end{bmatrix}, \quad [\boldsymbol{C}] = \frac{[\boldsymbol{M}]}{2A}(\{\boldsymbol{u}_1\}^n\boldsymbol{b} + \{\boldsymbol{u}_n\}^n\boldsymbol{c}), \tag{5.40}$$

$$[\boldsymbol{K}_s] = \frac{[M]\{\boldsymbol{u}_1\}\Delta t}{8A^2}[\{\boldsymbol{u}_1\}^T\boldsymbol{b}^T\boldsymbol{b} + \{\boldsymbol{u}_2\}^T\boldsymbol{b}^T\boldsymbol{c}] + \frac{[\boldsymbol{M}]\{\boldsymbol{u}_2\}\Delta t}{8A^2}[\{\boldsymbol{u}_1\}^T\boldsymbol{c}^T\boldsymbol{b} + \{\boldsymbol{u}_2\}^T\boldsymbol{c}^T\boldsymbol{c}], \tag{5.41}$$

$$[\boldsymbol{K}] = \frac{1}{4A}[\boldsymbol{b}^T\boldsymbol{b} + \boldsymbol{c}^T\boldsymbol{c}], \quad [\boldsymbol{G}_1] = \frac{1}{6}\begin{bmatrix} 1 \\ 1 \\ 1 \end{bmatrix}\boldsymbol{b}, \quad [\boldsymbol{G}_2] = \frac{1}{6}\begin{bmatrix} 1 \\ 1 \\ 1 \end{bmatrix}\boldsymbol{c}. \tag{5.42}$$

An elemental time step is calculated but the smallest value is used as the global time step

$$\Delta t = \min\left(\frac{h}{|\boldsymbol{u}|}, \frac{h^2}{\nu}\right). \tag{5.43}$$

In the CBS scheme the projection of nodal data forward in time must not interfere with the projections of neighbouring nodes, *e.g.* information can not travel across an element over the time period Δt. As a result the global time step is set by the smallest element with the largest velocity.

5.4 Numerical code development

The numerical scheme was implemented in Matlab 2013b to create a general purpose CFD code. The intention was to gain expertise in developing a code and to have a useful tool that can easily be interpreted and developed further by anyone without extensive programming skills. The advantage of using Matlab over other scripting

languages is that the data can easily be visualized at any stage of the calculation. This gives a significant advantage to troubleshooting when developing and prototyping new pieces of code. The disadvantage of using Matlab on the other hand is that the computational performance is not competitive with open source codes such as OpenFOAM.

5.4.1 Structure

The code and data structures changed significantly throughout development. The drivers behind this were optimisation as well as code management. The total code length is more than 2000 lines. As additional features were being added it became important to pick and choose which ones were required for a specific problem. The simplest way to achieve this is to divide the code into purpose built self contained functions.

Code

These various functions are drawn together into a main Matlab file where the user can specify the initial variables and the order of execution for the functions. The main functions can be grouped into four areas identified in figure 5.1:

Mesh

reading a mesh - The purpose is to read in a data file, structure the data in the required manner and calculate the elemental areas. Three different mesh file types have been implemented that cover ASCII as well as binary meshes. The advantage of ASCII meshes is that they are human readable, the ASCII character-encoding scheme contains 128 characters that are based on the English alphabet, and are specially useful when debugging. The disadvantage, however, is that they take significantly longer for the computer to interpret.

Model choice

setup - The purpose of this function is to calculate and compile all of the matrices and vectors required by the CBS scheme that are mesh dependent and do not change with every time step. Boundary conditions are also implemented into the global $[\boldsymbol{M}]$ and $[\boldsymbol{K}]$ matrices.

Numerical method

1. time step - This function calculates the time step for each element and picks the smallest one.

2. solver - This function goes through the three steps of the CBS scheme.

Diagnostics

1. diagnostics - Calculates the required diagnostics defined by the user.

2. write pos - A post processing file is written that can be opened in Gmsh visualizing the specified data. Both binary and ASCII versions have been implemented.

3. write mesh - Mesh files can be printed out either at the end of the calculation or during calculation. These files can be loaded in again to allow the user to continue a calculation from a checkpoint. As was the case with reading mesh files, three different file formats have been implemented.

Data

Throughout the calculation variables are being created and deleted, however, data that is kept is stored in four categories:

1. boundary - boundary line labels, nodes on boundary lines

2. mesh - node data values, node coordinates, node h values, element i, j and k labels, element types, element areas, *etc.*

3. parameter - directory names, file names, safety factor, the value of ν, diagnostics requirements

4. solver - various matrices and vectors required by the CBS scheme, simulation execution limits, current simulation time, time step

5.4.2 Implementation

The way in which the CBS-FEM method is implemented is quite flexible, however, trade-offs have to be made. Generally trade-offs tend to fall into categories of ease of programmability, accuracy and performance. Some of these choices are highlighted in this section.

Elemental area

Calculating the elemental areas provides a test point to whether the triangles have been labelled correctly with i, j and k in an anticlockwise order as shown in figure 5.6. When a mesh is loaded, nodes for each element are labelled randomly. If $A_e < 0$, the j and k labels are switched around resulting in a anticlockwise labelling as needed and the absolute value for the area is stored.

Time step

A separate time step is calculated for each element and this is undertaken at each time step. There are a number of methods that can be used (Lewis *et al.*, 2004). The first one is to calculate the shortest height of all of the triangular elements from the current node. Using this information the shortest height is used to calculate the nodal time step. Another method is to use the height of the triangle in the direction of flow movement. The simplest method, and the one used, is to use the shortest element side length originating from the node. The advantage is that the number of operations performed is kept low, increasing the performance of the code. The time step is multiplied by a safety factor to improve stability. It is standard practice to use a safety factor of 1/2 for two-dimensional calculations (Nicolle, 2009).

File types

The loading and writing of six different file types was implemented, the reason for this was the transition of the code from the development stage to calculation stage where performance became increasingly important. The first file format was the Gmsh v1 mesh that is written in ASCII and has a human-readable structure. The second file format was a modified version of the Gmsh v1 mesh that also included flow field information, this was important for checkpointing the simulations. The disadvantage of using files written in ASCII is that they are written and loaded very slowly due to binary to ASCII conversions. As mesh and problem sizes became bigger it became important to implement a binary file format.

The first stage in writing a binary file format was to implement the Gmsh v2 ASCII mesh that has the same data structure as the Gmsh v2 binary mesh in order to have a comparable data template for debugging. After the creation of a function for writing and loading in Gmsh v2 binary meshes an extension needed to be written that

would also include flow field variables.

The fifth and sixth file formats are ASCII and binary post processing files. The post processing files can be opened in Gmsh and are used to visualize the relevant flow field information.

5.4.3 Diagnostics

In relation to the practical application described in Chapter 4 it is essential to calculate the force balance on a rigid body. Similarly the vorticity field and instantaneous streamlines are needed to visualize the flow field.

Forces

The force, $\boldsymbol{F}$, on a rigid body (with no through surface flow) is

$$\boldsymbol{F} = \int_{S_B} (-p\boldsymbol{I} + \boldsymbol{\tau}) \cdot \hat{\boldsymbol{n}} \mathrm{d}S, \tag{5.44}$$

where S_B is the surface of the body, I an identity matrix, $\hat{\boldsymbol{n}}$ is the unit normal to the surface and $\boldsymbol{\tau}$ is the viscous stress tensor. To calculate the force, we need to identify the line elements on the bounding surface and their normal vectors. In this chapter we consider two-dimensional flows. Consider a surface boundary composed of a series of connected line elements where the coordinates of the ends are represented by x_{1i}^E, x_{2i}^E and x_{1j}^E, x_{2j}^E in Cartesian coordinates (see figure 5.7). Surrounding triangular elements are identified by searching the list of elements containing the two points at the ends of each line element belonging to the boundary (*e.g.* $[\boldsymbol{B}]$). Since no line element will contain the same two points the generated lists are unique. The unit normal vector is determined from

$$\hat{\boldsymbol{n}} = \left(\frac{x_{2j}^E - x_{2i}^E}{|\boldsymbol{x}_i - \boldsymbol{x}_j|}, -\frac{x_{1j}^E - x_{1i}^E}{|\boldsymbol{x}_i - \boldsymbol{x}_j|} \right). \tag{5.45}$$

The surface edge has a length of

$$\mathrm{d}l = |\boldsymbol{x}_i - \boldsymbol{x}_j|. \tag{5.46}$$

The viscous stress tensor is

$$\tau_{ij} = \begin{bmatrix} 2\mu \frac{\partial u_1}{\partial x_1} & \mu \left(\frac{\partial u_1}{\partial x_2} + \frac{\partial u_2}{\partial x_1} \right) \\ \mu \left(\frac{\partial u_1}{\partial x_2} + \frac{\partial u_2}{\partial x_1} \right) & 2\mu \frac{\partial u_2}{\partial x_2} \end{bmatrix}, \tag{5.47}$$

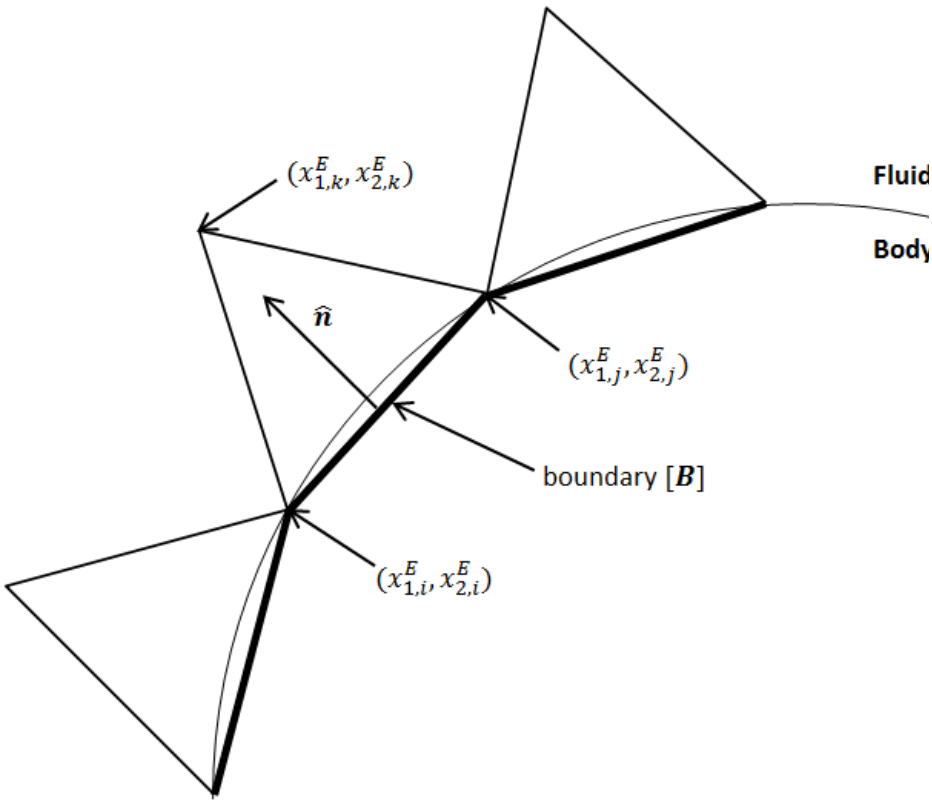

Figure 5.7: Triangular mesh elements approximating a boundary around a curved shape. The normal $\hat{\boldsymbol{n}}$ is pointing out of the body.

is symmetric and determined from the velocity gradients. For a two-dimensional incompressible flow

$$\frac{\partial u_1}{\partial x_1} + \frac{\partial u_2}{\partial x_2} = 0, \tag{5.48}$$

so that there are only three velocity gradients that must be calculated, *e.g.*

$$\frac{\partial u_1}{\partial x_1}, \quad \frac{\partial u_1}{\partial x_2}, \quad \frac{\partial u_2}{\partial x_1}. \tag{5.49}$$

Within the FEM approach, we illustrate how $\partial u_1/\partial x_1$ is estimated. The first step is to define

$$u_{1,i} = \frac{\partial u_1}{\partial x_1}. \tag{5.50}$$

In combination with the linear basis function $\boldsymbol{N}$ the elemental gradients are

$$\frac{\partial u_1}{\partial x_1} = [\boldsymbol{N}]\{u_{1,i}\}. \tag{5.51}$$

Multiplying by $[\boldsymbol{N}]^T$ and integrating over each triangular element results in

$$\int_{l_e} [\boldsymbol{N}^T][\boldsymbol{N}]\{u_{1,i}\}\mathrm{d}\Omega = \int_{\Omega_e} [\boldsymbol{N}^T]\frac{\partial}{\partial x_1}[\boldsymbol{N}]\{\boldsymbol{u}\}\mathrm{d}\Omega, \tag{5.52}$$

or

$$[\boldsymbol{M}]\{u_{1,i}\} = [\boldsymbol{G}_1]\{\boldsymbol{u}\}, \tag{5.53}$$

where $[\boldsymbol{G}_1]$ is defined in (5.33). The velocity gradients are evaluated by creating a global sparse mass matrix and inserting the RHS vector from each element. No boundary conditions are stencilled onto $\{u_1\}$. An identical approach is applied to calculate the force contribution from a triangular element

$$\begin{aligned}\int_{l_e} (-p\boldsymbol{I} + \boldsymbol{\tau}) \cdot \hat{\boldsymbol{n}}\mathrm{d}l_e \simeq \hat{\boldsymbol{x}}\mathrm{d}l(-pn_x + (2\mu u_{1,i}n_x + \mu(u_{1,j} + u_{2,i})n_y) \\ + \hat{\boldsymbol{y}}\mathrm{d}l(-pn_y + \mu(u_{1,j} + u_{2,i})n_x + 2\mu u_{2,i}n_y)).\end{aligned} \tag{5.54}$$

Vorticity and streamlines

In a two-dimensional flow, vorticity is defined as

$$\omega = \frac{\partial u_2}{\partial x_1} - \frac{\partial u_1}{\partial x_2}. \tag{5.55}$$

Writing

$$\boldsymbol{\omega} = [\boldsymbol{N}]\{\boldsymbol{\omega}\}, \tag{5.56}$$

the FEM approach requires weighting with $\boldsymbol{N}^T$ and integrates to yield

$$\int_{\Omega_e} \boldsymbol{N}^T \boldsymbol{N}\{\boldsymbol{\omega}\} \mathrm{d}\Omega = \int_{\Omega_e} \boldsymbol{N}^T \left(\frac{\partial u_2}{\partial x_1} - \frac{\partial u_1}{\partial x_2} \right) \mathrm{d}\Omega, \tag{5.57}$$

or

$$[\boldsymbol{M}]\{\boldsymbol{\omega}\} = \frac{1}{3} A_e \begin{bmatrix} 1 \\ 1 \\ 1 \end{bmatrix} ([\boldsymbol{G}_1]\{\boldsymbol{u}_2\} - [\boldsymbol{G}_2]\{\boldsymbol{u}_1\}). \tag{5.58}$$

Streamlines are particularly useful for understanding the flow field especially where there are recirculating regions. There are two general methods to calculating the streamlines - either directly by integrating the instantaneous trajectory of fluid elements using fictitious time, *e.g.*

$$\frac{\mathrm{d}x_1}{\mathrm{d}S} = u_1, \quad \frac{\mathrm{d}x_2}{\mathrm{d}S} = u_2, \tag{5.59}$$

or by calculating the stream function where the streamlines are determined from the isocontours. The difficulty of using the first method is that it can be very difficult to determine where particles should be injected to capture recirculating regions. In the case of the latter the velocity field is related to the stream function, ψ, through

$$u_1 = -\frac{\partial \psi}{\partial x_2}, \quad u_2 = \frac{\partial \psi}{\partial x_1}, \tag{5.60}$$

or

$$\frac{\partial^2 \psi}{\partial x_1^2} + \frac{\partial^2 \psi}{\partial x_2^2} = \omega = \frac{\partial u_1}{\partial x_2} - \frac{\partial u_2}{\partial x_2}. \tag{5.61}$$

Defining

$$\boldsymbol{\psi} = [\boldsymbol{N}]\{\boldsymbol{\psi}\}, \tag{5.62}$$

substituting and integrating gives

$$\int_{\Omega_e} \boldsymbol{N}^T \left(\frac{\partial^2}{\partial x_1^2} \boldsymbol{N}\{\boldsymbol{\psi}\} + \frac{\partial^2}{\partial x_2^2} \boldsymbol{N}\{\boldsymbol{\psi}\} \right) \mathrm{d}\Omega = \int_{\Omega_e} \left(\boldsymbol{N}^T \frac{\partial}{\partial x_2} \boldsymbol{N}\{\boldsymbol{\psi}\} - \boldsymbol{N}^T \frac{\partial}{\partial x_1} \boldsymbol{N}\{\boldsymbol{\psi}\} \right) \mathrm{d}\Omega. \tag{5.63}$$

Using Green's Theorem, the left hand side becomes

$$-\int_{\Omega_e} \left(\frac{\partial \boldsymbol{N}^T}{\partial x_1} \frac{\partial \boldsymbol{N}}{\partial x_1} + \frac{\partial \boldsymbol{N}^T}{\partial x_2} \frac{\partial \boldsymbol{N}}{\partial x_2} \right) \{\boldsymbol{\psi}\} \mathrm{d}\Omega. \tag{5.64}$$

In combination this becomes

$$-[\boldsymbol{K}]\{\boldsymbol{\psi}\} = \frac{1}{3}A_e \begin{bmatrix} 1 \\ 1 \\ 1 \end{bmatrix} ([\boldsymbol{G}_2]\{\boldsymbol{u_1}\} - [\boldsymbol{G}_1]\{\boldsymbol{u_2}\}), \tag{5.65}$$

where

$$[\boldsymbol{K}] = \frac{1}{4A_e}(b^T b + c^T c). \tag{5.66}$$

The boundary conditions for ψ must be stencilled in. For rigid boundaries with no through surface flow the boundary condition is

$$\psi = \text{constant}. \tag{5.67}$$

For inlet flows (in the case of a uniform horizontal flow), *e.g.*

$$u_1 = U_\infty, \quad u_2 = 0, \tag{5.68}$$

we see from (5.60) that

$$\psi = -U_\infty x_2, \tag{5.69}$$

where x_2 varies from $-H/2$ to $H/2$ for a channel of height H. On the bottom and top walls the boundary conditions are equal to $-H/2$ and $H/2$, respectively.

5.5 Validation

Once a code has been written it needs its output needs to be validated against a number of standard test cases. In relation to the required diagnostics described in §5.4.3 two validation cases were chosen. The first is a lid driven flow in a cavity that reaches a steady state (Ghia *et al.*, 1982) and the second is a flow past a cylinder resulting in an unsteady wake (Schäfer & Turek, 1996). The steady state validation case is undertaken to determine the correctness of the numerical code testing the CBS and boundary condition implementation. The unsteady validation case is performed to determine that there are no temporal errors that may not show up in a steady state calculation and it also shown that the implementation of force measurements on rigid bodies is correct (used in Chapter 6).

5.5.1 Two-dimensional cavity flow

The validation study of Ghia *et al.* (1982) is one of the standard two-dimensional cases that is frequently used. A cavity driven flow with its geometry and boundary conditions, as shown in figure 5.8, is simulated to a steady state. At steady state the flow field variables become unaltered in time. In this case, steady state was reached when the following condition was met

$$\text{steadystate} = \frac{\sum_{i=1}^{n} \sqrt{(|\boldsymbol{u}_{n+1}| - |\boldsymbol{u}_n|)^2}}{\Delta t \sum_{i=1}^{n} \sqrt{(|\boldsymbol{u}_{n+1}|)^2}} < 10^{-6}. \tag{5.70}$$

The characteristic Re is calculated using the driving velocity and the height of the cavity. Two cases were run for $Re = 100$ and 400. An unstructured constant density mesh is used with 129 elements across each edge of the cavity resulting in a total of 44542 triangular elements ($N_p = 22270$) on the domain. Meshes of the same density were used in the study of Ghia *et al.* (1982). The results are additionally compared against the results from another numerical code, ACEsim, on the same mesh.

Figures 5.9 and 5.10 display the streamline and the vorticity fields. The contour values are defined in tables 5.1 and 5.2 from Ghia *et al.* (1982). A qualitative comparison is made between the published figures, the Matlab code and the results from ACEsim. Finally, velocity profiles horizontally (see figure 5.11) and vertically (see figure 5.12) across the cavity are taken and compared. The cavity validation study showed that there was good agreement between the Matlab code and the benchmark study. Additionally, the same agreement was reached when compared against another numerical code. This gives confidence that the CBS scheme and the boundary conditions were implemented appropriately.

5.5.2 Two-dimensional cylinder

The second validation case deals with a flow past a cylinder. The results are compared against those published by Schäfer & Turek (1996). The geometry and the boundary conditions of the domain are shown in figure 5.13. The inlet condition is described as follows

$$u_1 = 4U_{max} x_2 (H - x_2)/H^2; \quad u_2 = 0, \tag{5.71}$$

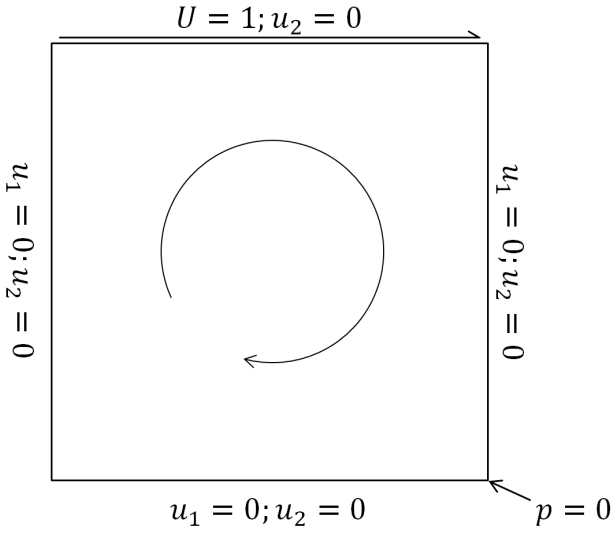

Figure 5.8: Boundary conditions for the lid driven cavity flow.

Contour label	ψ	Contour label	ψ
a	-1.0×10^{-10}	0	1.0×10^{-8}
b	-1.0×10^{-7}	1	1.0×10^{-7}
c	-1.0×10^{-5}	2	1.0×10^{-6}
d	-1.0×10^{-4}	3	1.0×10^{-5}
e	-0.0100	4	5.0×10^{-5}
f	-0.0300	5	1.0×10^{-4}
g	-0.0500	6	2.5×10^{-4}
h	-0.0700	7	5.0×10^{-4}
i	-0.0900	8	1.0×10^{-3}
j	-0.1000	9	1.5×10^{-3}
k	-0.1100	10	3.0×10^{-3}
l	-0.1150		
m	-0.1175		

Table 5.1: Stream function (ψ) contour line values from Ghia *et al.* (1982). The comparison is shown in figure 5.9.

Contour label	ω
0	0.0
±1	±0.5
±2	±1.0
±3	±2.0
±4	±3.0
5	4.0
6	5.0

Table 5.2: Vorticity (ω) contour line values from Ghia *et al.* (1982). The comparison is shown in figure 5.10.

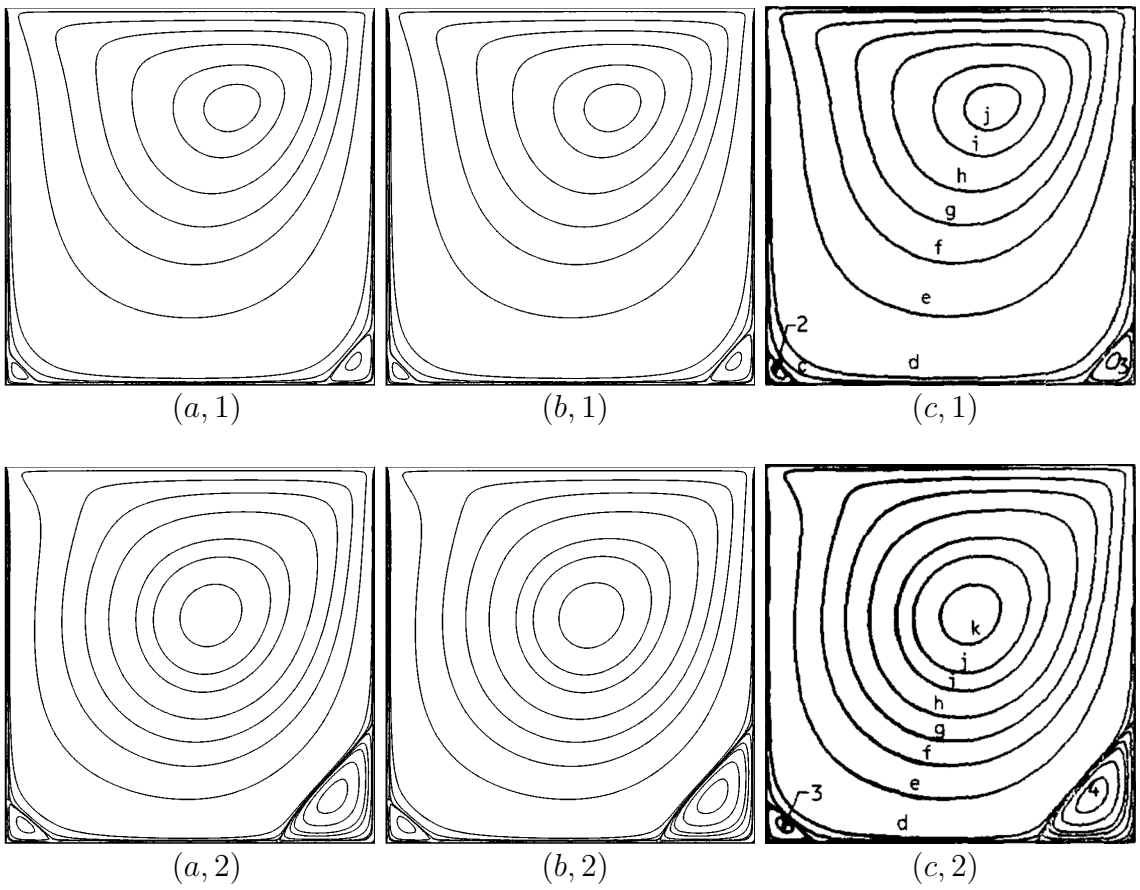

$(a, 1)$ $(b, 1)$ $(c, 1)$

$(a, 2)$ $(b, 2)$ $(c, 2)$

Figure 5.9: Streamlines for $Re = 100$ on top and $Re = 400$ on the bottom. The figures with (a) are from ACEsim, (b) are from the Matlab code and (c) were published in Ghia *et al.* (1982). The contours correspond to the values listed in table 5.1.

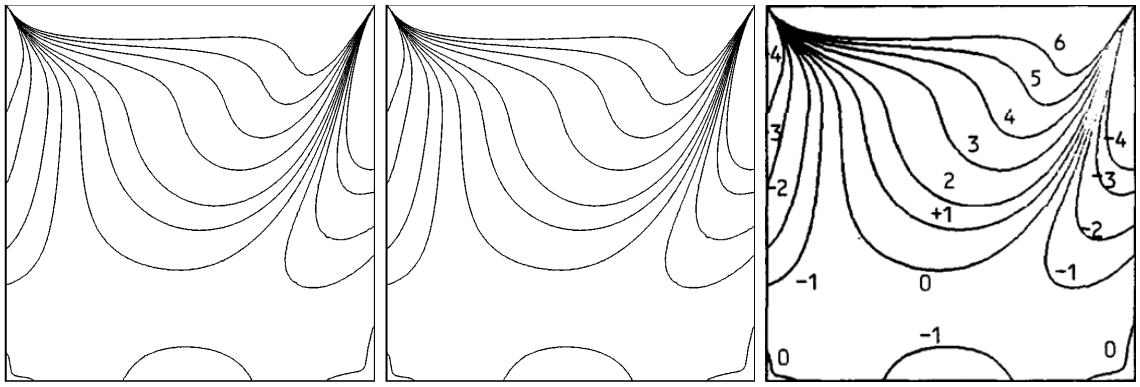

$(a, 1)$ $(b, 1)$ $(c, 1)$

$(a, 2)$ $(b, 2)$ $(c, 2)$

Figure 5.10: Vorticity field for $Re = 100$ on top and $Re = 400$ on the bottom. The figures with (a) are from ACEsim, (b) are from the Matlab code and (c) were published in Ghia *et al.* (1982). The contours correspond to the values listed in table 5.2.

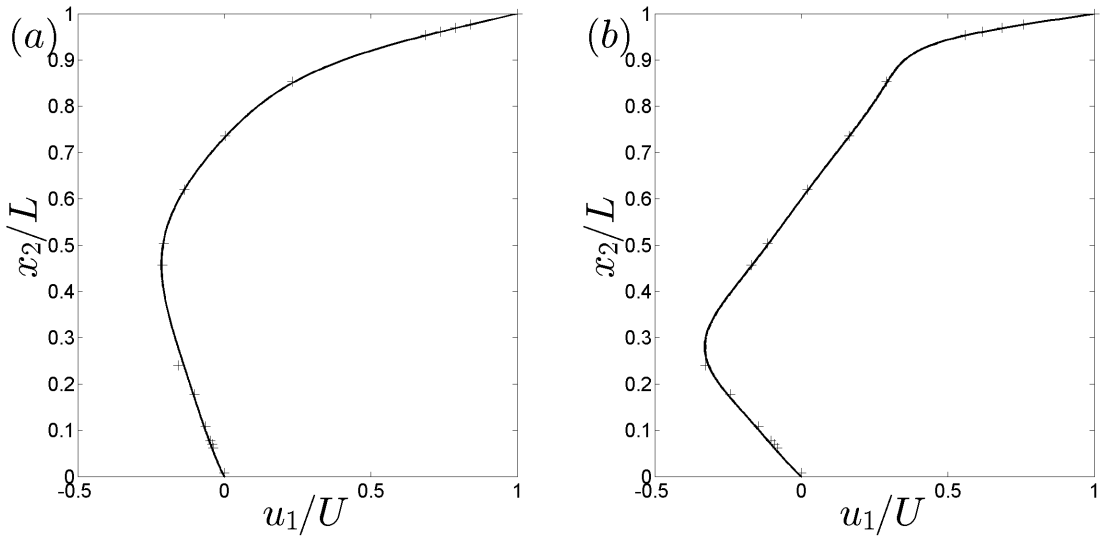

Figure 5.11: Horizontal velocity along the vertical centre line of the domain in (*a*) $Re = 100$ and in (*b*) $Re = 400$. The crosses correspond to the data published in Ghia *et al.* (1982) and the solid and dashed lines that have collapsed onto each other originate from the Matlab code and ACEsim.

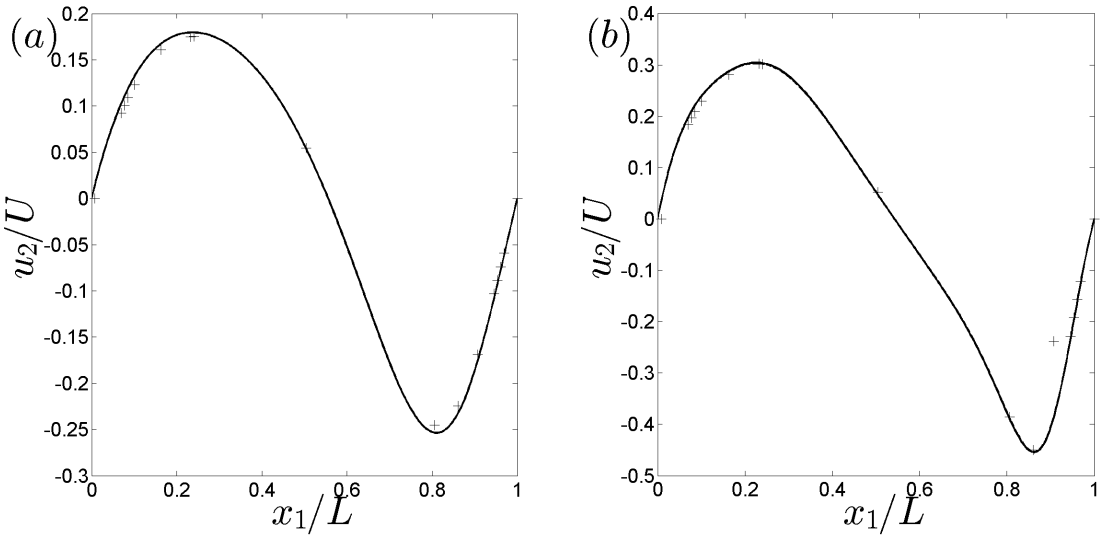

Figure 5.12: Vertical velocity along the horizontal centre line of the domain in (*a*) $Re = 100$ and in (*b*) $Re = 400$. The crosses correspond to the data published in Ghia *et al.* (1982) and the solid and dashed lines that have collapsed onto each other originate from the Matlab code and ACEsim.

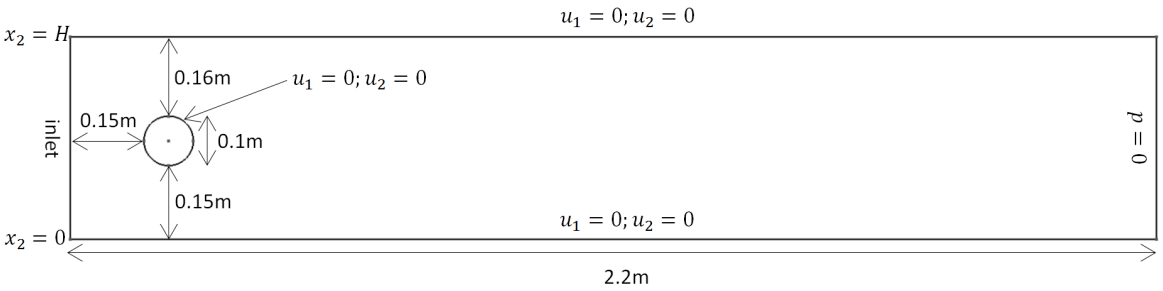

Figure 5.13: Geometry and boundary conditions for a two-dimensional flow past a cylinder validation case.

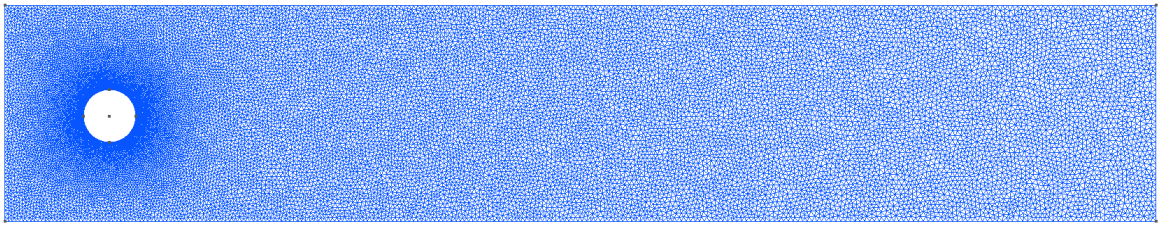

Figure 5.14: The mesh used in the cylinder validation case, it consists of 44798 triangular elements ($N_p = 22007$). The mesh density was significantly increased in the vicinity of the cylinder to accurately capture the boundary layer. In the case of $Re = 20$ the boundary layer thickness is approximately 8 elements and in the case of $Re = 100$ it is approximately 4 elements. In both cases, the number of elements across the boundary layer meet the requirement of 4 elements across it as suggested in (**??**).

where H is the total height of the domain in the x_2 direction. Two simulations were run with a characteristic Re of 20 and 100 defined on the inlet as

$$Re = \frac{2HU_{mean}}{\nu}, \tag{5.72}$$

where

$$U_{mean} = \frac{2U_{max}}{3}. \tag{5.73}$$

The kinematic viscosity is chosen to be $\nu = 10^{-3}$ m^2/s and the values of U_{max} are 0.3 m/s and 1.5 m/s. The mesh used for the calculations is shown in figure 5.14. There is a region of significantly higher mesh resolution around the cylinder than in the rest of the domain. This is necessary to resolve the boundary layer of the flow and obtain accurate data to calculate the drag and lift forces. The rest of the domain does not need as high a mesh resolution, therefore, to reduce the computational time required it can be significantly coarsened.

Lift F_L and drag forces F_D are calculated on the cylinder throughout the simulation and the results are shown in figures 5.15 and 5.16. The drag and lift coefficients are calculated from the forces as

$$C_D = \frac{2F_D}{\rho U_{mean}^2 D}, \quad C_L = \frac{2F_L}{\rho U_{mean}^2 D}, \tag{5.74}$$

where ρ is the density (1kg/m^3) and D is the diameter of the cylinder (0.1m). In the case of $Re = 20$ the length of the recirculating region L_a and the pressure difference between the leading and trailing edges of the cylinder ΔP also needed to be recorded. In the case of $Re = 100$ the pressure difference between is calculated when $C_L \approx 0$ and the frequency of oscillation is determine from the C_L in order to calculate the Strouhal number. The results and their comparison with the benchmark results is shown in table 5.3.

The streamlines on the inlet follow the following expression

$$\psi = \int_{-H/2}^{H/2} u_1 \mathrm{d}x_2, \tag{5.75}$$

where H is the height of the channel. Due to the inlet having a parabolic profile the following boundary condition needs to be used

$$\psi = U_{mean}\left(x_2 - \frac{x_2^3}{3H^2}\right), \tag{5.76}$$

		published min.	published max.	published median	current
$Re = 20$	C_{Dmax}	5.4450	5.8190	5.5755	5.5422
(steady)	C_{Lmax}	-0.0060	0.2085	0.0107	0.0204
	L_a	0.0660	0.8315	0.0837	0.0833
	ΔP	0.0998	3.2277	0.1170	0.1183
$Re = 100$	C_{Dmax}	2.8920	4.7330	3.2232	3.1931
(unsteady)	C_{Lmax}	0.5540	2.0600	0.9840	0.9931
	St	0.2336	0.3380	0.2973	0.3000
	ΔP	1.9727	3.4300	2.4833	2.1410

Table 5.3: Comparison of current simulation results with that of the data published in Schäfer & Turek (1996).

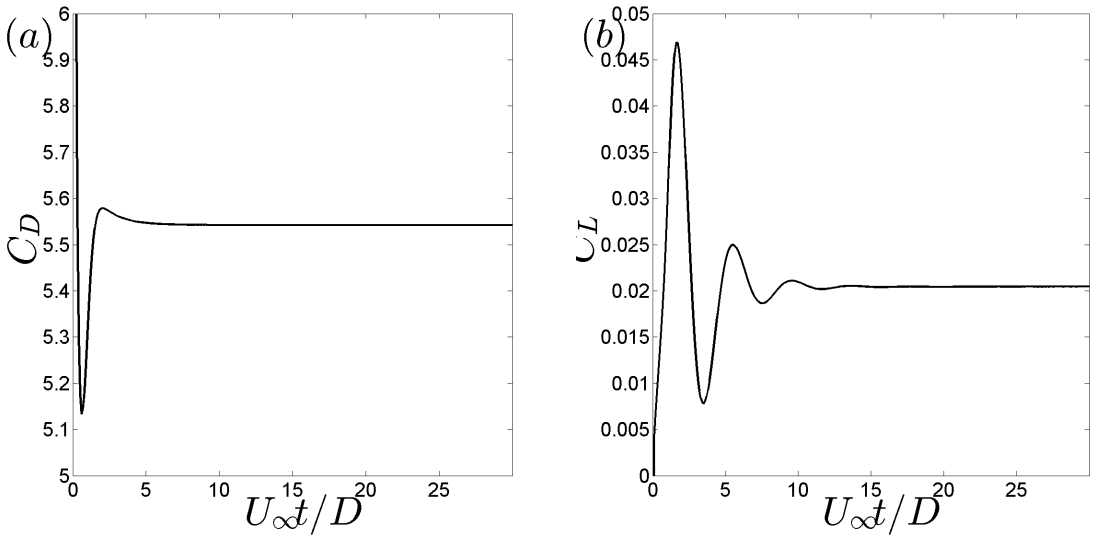

Figure 5.15: Numerical results for a flow past a cylinder at $Re = 20$. In (a) the drag coefficient and in (b) for the lift coefficient is plotted against time.

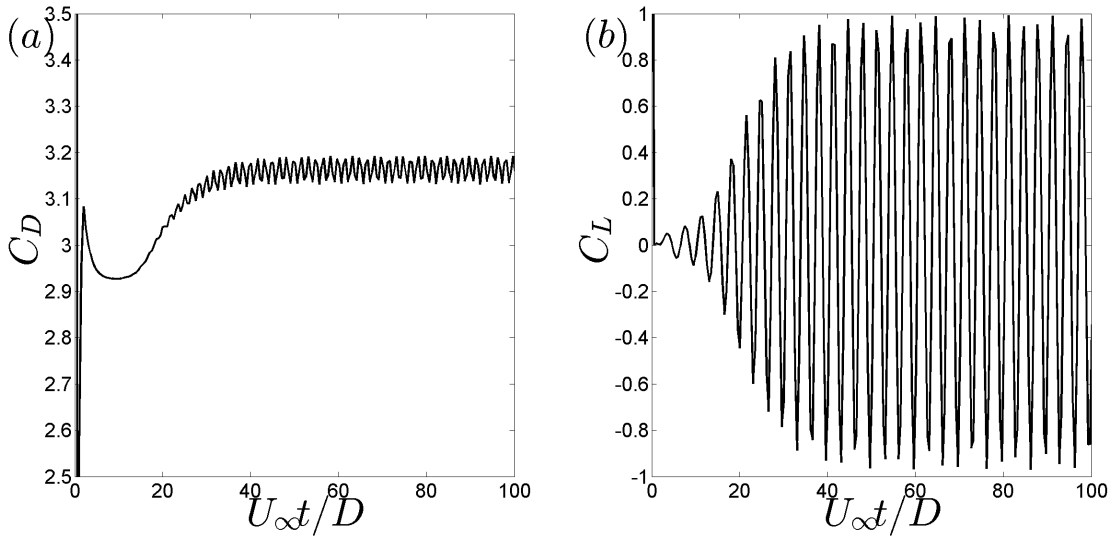

Figure 5.16: Numerical results for a flow past a cylinder at $Re = 100$. In (a) the drag coefficient and in (b) for the lift coefficient is plotted against time.

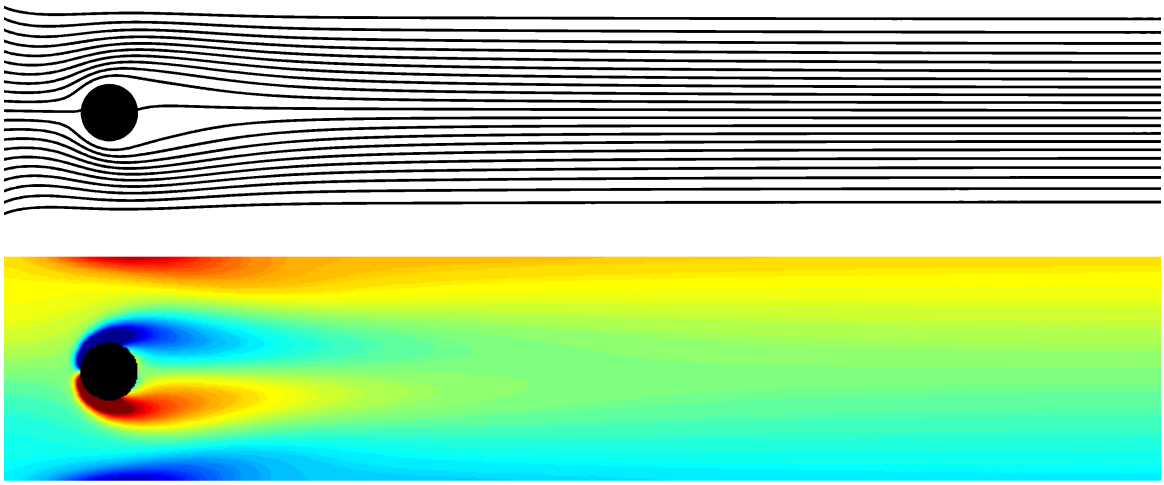

Figure 5.17: The streamlines (top) and vorticity field (bottom) for the flow past a cylinder at $Re = 20$. The vorticity contours are capped from -10 to 10.

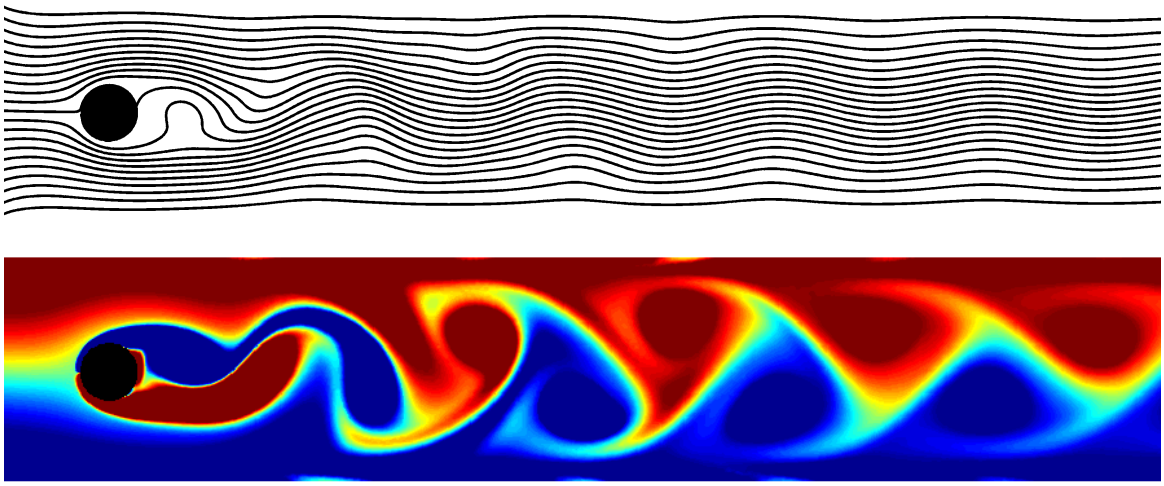

Figure 5.18: The streamlines (top) and vorticity field (bottom) for the flow past a cylinder at $Re = 100$. The vorticity contours are capped from -10 to 10.

where y ranges from $-H/2$ to $H/2$. The vorticity field and streamlines are shown in figures 5.17 for $Re = 20$ and on 5.18 for $Re = 100$.

5.6 Conclusions

An overview of CFD applied to incompressible flows was given. In relation to the problem set out in Chapter 4, a numerical code was developed in Matlab and validated for steady and unsteady cases giving confidence in its accuracy. Based on the validation cases it can be concluded that the implementation of vorticity and streamfunction diagnostics is also accurate. The novelty of writing a CBS-FEM code in Matlab is that it is easily accessible to people interested in learning the basics of CFD without having extensive programming knowledge and as a consequence is an excellent platform for testing various extensions to the code, such as turbulence models, additional solvers or diagnostics. The code is extended with an axisymmetric formulation in Appendix B and the Spalart Allmaras turbulence model in Appendix C. This gives a solid basis for the code and demonstrates its general purposiveness. The code will be applied to flows past bluff bodies to verify the analytical analysis in Chapter 4 and the computational results are presented in Chapter 6.

Chapter 6

Computational results

6.1 Introduction

This chapter presents the numerical results from the computational analysis of flow past a ship without the effects of the free surface. The basis for these calculations is the computational model in Chapter 5 with the extension of axisymmetry (Appendix B) and the Spalart Allmaras (SA) turbulence model (see Appendix C). The main challenges involved are capturing and identifying the self-propelled state because it is very sensitive to the velocity of the propelling jet at the rear of the ship. An iterative approach was taken to reaching the self-propelled state which was time and resource intensive because a steady state had to be reached before the data could be analysed. The self-propelled profiles captured in the following calculations are approximate and further downstream the wake tends to the profile of a non self-propelled wake.

6.2 Geometry and boundary conditions

The propulsion of the model ship is due to a jet of fluid expelled from the stern. This results in a proportional increase of the downstream volume flow rate. Two sets of calculations (planar and axisymmetric) are undertaken for a constant turbulent Reynolds number (Re_T) and the SA turbulence model (Spalart & Allmaras, 1992) for the under-propelled (decelerating), self-propelled (moving at a steady velocity) and over-propelled (accelerating) cases. The constant Re_T calculations are consistent with the basis of Tennekes & Lumley (1972) original theory. The Reynolds number $Re = U_\infty D/\nu$ for a ship is very large ($Re \sim 10^6$) but Re_T is much smaller and weakly dependent on Re provided that Re is large enough. For the SA turbulence model, the

Re of the flow was set to be 10^6. The SA turbulence model enables the gross features of the flow to be captured that are weakly dependent on Re. The SA turbulence model is based on an evolution equation describing ν_T so that we can then examine how Re_T varies spatially. An illustration of the resulting modelled ship shape is shown in figure 6.1. The geometry of the planar ship is similar to the one used in the experimental study of wakes by Cimbala & Park (1990).

Figure 6.2 shows the geometry and boundary conditions of the computational domain and the values of thrusting velocity (exit velocity of the jet) at the rear of the ship is shown in table 6.1. In the case of planar calculations for $Re_T = 10$ the domain (a) was used and in the case of SA the domain in (b) was used. It was discovered that the thrusting velocity for the self-propelled state is very sensitive to the boundedness of the domain and the value of ν_T. In order to mitigate this the domain was made as wide and as long as possible. Due to computational constraints the maximum downstream distance from the ship was set to 100 ship widths ($D = 100$). The meshes used in the calculations is shown in Appendix D.

In order to optimise computational resources various stages of mesh refinement are used. The domain in figure 6.2 is divided into a number of different regions of varying mesh density. In (a) mesh refinement is used around the boundary layer and an additional region of refinement is used to capture the near field wake dynamics. From the calculations with the domain in (a) it became clear that the flow features of interest are very close to the wake centre line and that the velocity perturbation is very rapid, therefore, a revised design, shown in (b), is used for the SA calculations. For axisymmetric calculations half the domain in (b) is used and the boundary conditions involving ν_T are applicable to the SA turbulence model case only. In the case of (b) the domain is divided into three regions of mesh density across the length of the domain. The middle region (immediately around the ship) is used to capture the boundary layer and the wake dynamics. It contains 64% of the nodes on the domain while it only has an area of 9.6% of the domain. The regions immediately to the sides are a transition region to lower mesh density and the density is reduced even further at the extremes to the top and bottom of the domain. Images of the meshes used are shown in Appendix D.

Figure 6.1: Illustration of the modelled ship shapes for the planar (top) and axisymmetric calculations (bottom). The regions where the propulsion jet emerges are highlighted in red.

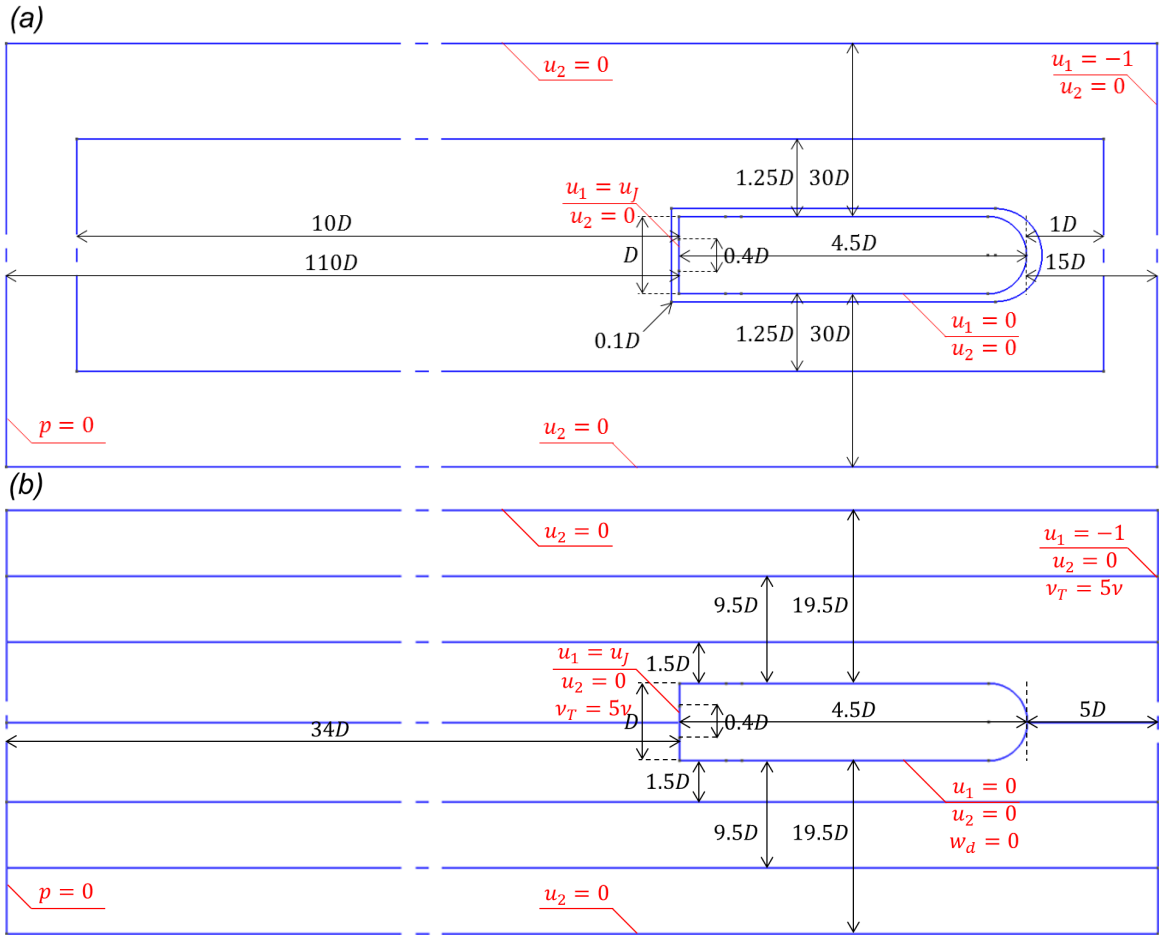

Figure 6.2: The geometry and boundary conditions of the computational domains. The geometry in (a) is used in the planar constant turbulent viscosity calculations and the geometry in (b) is used in the planar SA calculations. In the case of the axisymmetric calculations, half of the domain shown in (b) is used.

	under-propelled	self-propelled	over-propelled
planar	0	3.6	5
planar SA	0	1.4	4
axisymmetric	0	7	10
axisymmetric SA	0	1.72	4

Table 6.1: The ratio of u_J/U_∞ used in the calculations to achieve the under-, self- and over-propelled states.

	u_J/U_∞	$\rho u_J^2 A$	F_D	$F_T + F_D$
under-propelled	0	0	-0.96215	-0.96215
self-propelled	3.6	2.4624	-1.86424	0.5982
over-propelled	5	4.75	-2.43801	2.3120

Table 6.2: Force balance between the thrust $F_T = \rho u_J^2 A$ and the drag F_D for the planar constant Re_T case.

6.3 Force balance

The logical first step to determining the self-propelled state is to examine the force balance on the ship. Fluid is being ejected from the rear of the ship and in figure 6.2 it is shown that the width of the thrusting region is $0.4D$, however, from calculating the variation of Q across the whole width of the domain it was determined that the width of the thrusting region is reduced by 5% due to interpolation on the edges. Based on this information the force balance on the ship can be calculated and the results are shown in table 6.2. The width of the thrusting region was intended to be as narrow as possible, however, the number of elements across it was the limiting factor. From preliminary tests it was determined that a region with 20 line elements was suitable for these calculations. Increasing the number of line elements by increasing the mesh resolution would have impacted the timestep of the calculation too much.

The force balance analysis does not indicate that the ship is close to the self-propelled state, this is because additional factors need to be considered. The first is that FEM does not conserve momentum, therefore, the momentum flux budget needs to be understood. The second is the introduction of a source flow to generate thrust. The consequence of this is the introduction of a Lamb force (see Chapter 2) that may have some significance. The third is the effects of the computational boundary and the net mean flow increase downstream of the thrust source. Each of these three elements could modify the self-propelled state ($F_D = F_T$). Using the force balance to determine

the self-propelled state in FEM is challenging and a significantly simpler approach is to examine the wake maximum absolute vorticity decay across the width of the wake with distance downstream.

6.4 Integral relationships

The flow field is assessed through three integral quantities: volume flux (Q), momentum flux (M) and the Tennekes & Lumley (1972) integral (I). The velocity deficit u_d is defined as

$$u_d = u - U_\infty - u_{\text{wall}}, \tag{6.1}$$

where u_{wall} is the velocity along the edges of the computational domain as a result of boundedness. As a function of downstream distance the integral relationships are

$$Q = \int_{A_D} u_d \mathrm{d}A, \tag{6.2}$$

$$M = \int_{A_D} u_d^2 \mathrm{d}A, \tag{6.3}$$

$$I = \int_{A_D} x_2^2 u_d \mathrm{d}A, \tag{6.4}$$

where A_D is the cross-sectional area of the domain leading to $\mathrm{d}A = \mathrm{d}x_2$ in the planar case and $\mathrm{d}A = 2\pi x_2 \mathrm{d}x_2$ in the axisymmetric case. The results are shown in figure 6.3 for M and in figure 6.4 for I. The value of Q experiences a jump at the point where the jet propelling the ship enters the domain but no other variation is experienced. This is to be expected and it confirms that mass is being conserved.

Figure 6.3 shows that the momentum decays very rapidly for the self-propelled states and reaches approximately 0 within $x_1/D = 5$. As the self-propelled state was reached through iteration, it became clear that the momentum deficit is not a very good measure of determining the self-propelled state because it decayed in a very rapid manner even when the calculations were as much as 10% off from the self-propelled state.

The integral relationship in figure 6.4 is a useful indicator of whether the self-propelled state has been reached because it conforms to $\mathrm{d}I/\mathrm{d}x_1 = 0$ (black lines). For the under- and over-propelled cases there is significant variance and a single trend could not be found.

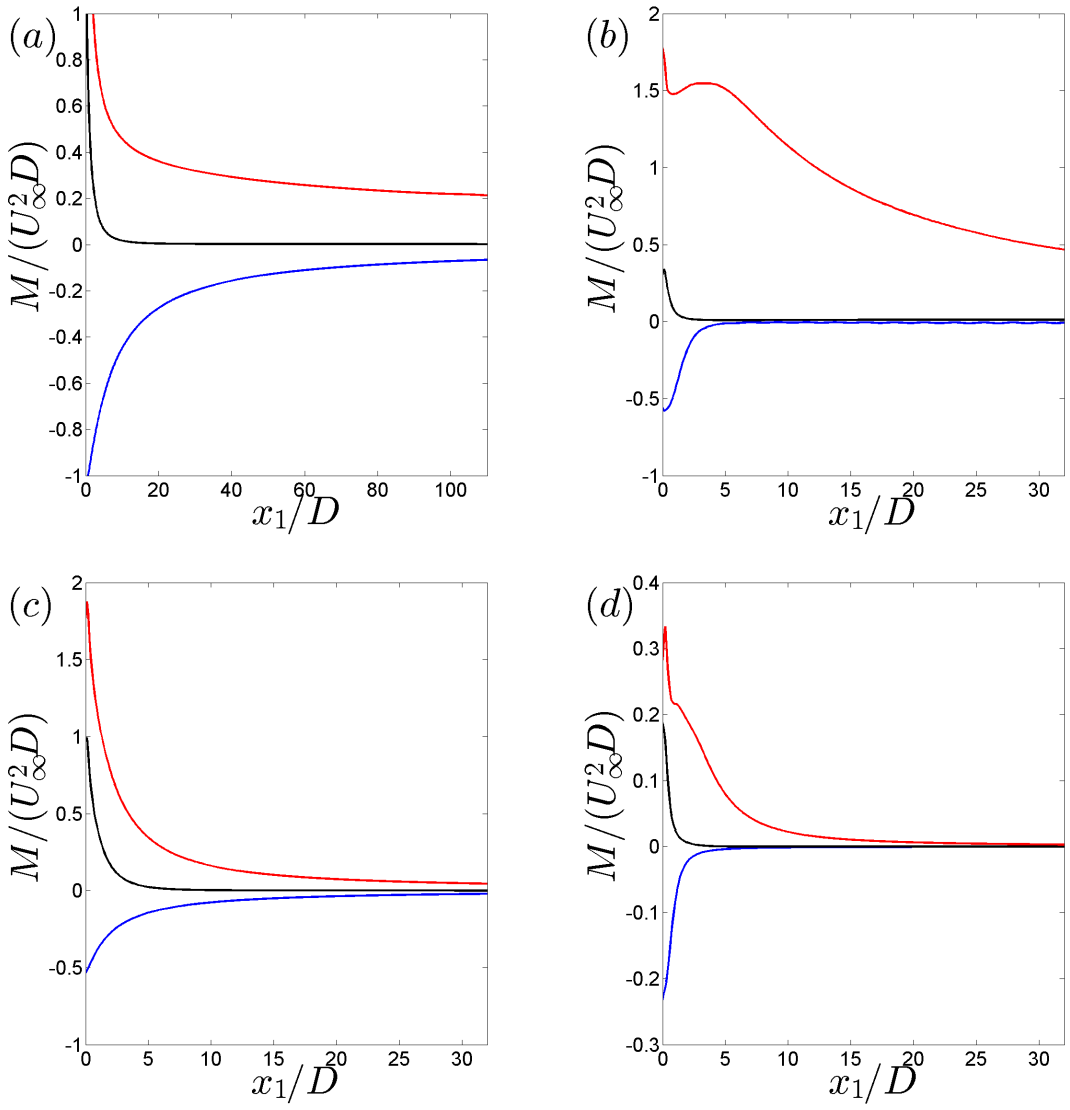

Figure 6.3: The variation of momentum flux with distance downstream. The plots in the case of a planar wake are (*a*) $Re_T = 10$, (*b*) SA and in the case of an axisymmetric wake (*c*) $Re_T = 10$, (*d*) SA. The blue, black and red lines are for the under-, self- and over-propelled cases.

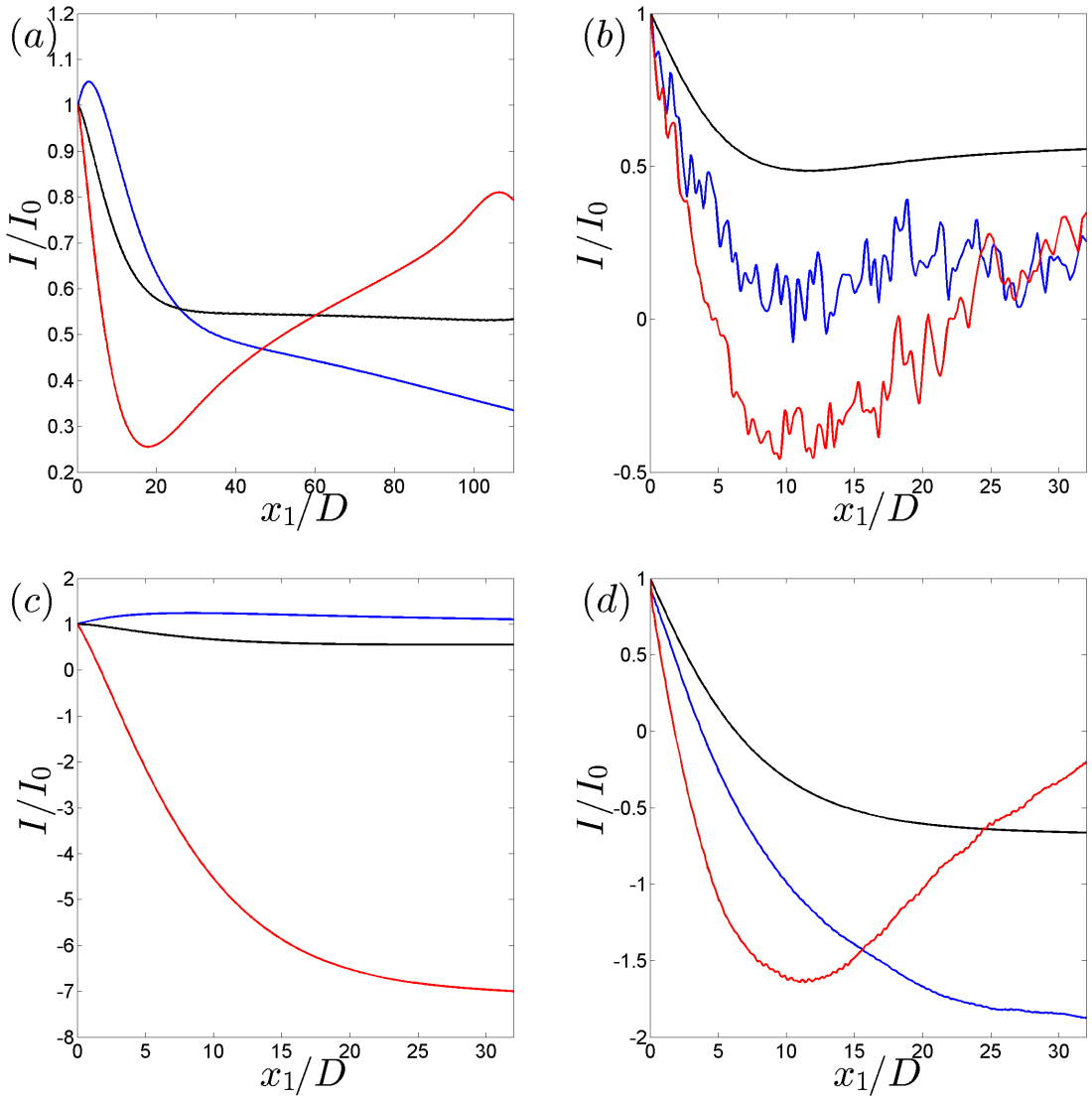

Figure 6.4: The variation of the Tennekes & Lumley (1972) integral with distance downstream. The plots in the case of a planar wake are (*a*) $Re_T = 10$, (*b*) SA and in the case of an axisymmetric wake (*c*) $Re_T = 10$, (*d*) SA. The blue, black and red lines are for the under-, self- and over-propelled cases.

$\frac{\max(\lvert\omega\rvert)D}{U_\infty} = \left(\frac{x_1}{D}\right)^\delta$	under-propelled	self-propelled	over-propelled
planar	-0.949 (-1)	-2.155 (-2)	-1.177 (-1)
planar SA	-0.147 (-1)	-2.343 (-1)	-1.623 (-1)
axisymmetric	-1.248 (-1.5)	-2.892 (-3)	-1.845 (-2)
axisymmetric SA	-1.294 (-1)	-2.868 (-1)	-2.176 (-2)

Table 6.3: The scalings for maximum vorticity magnitude decay across the width of the wake with distance downstream as observed in figure 6.5. The values of δ are shown in the table and the values in the brackets are those predicted in Chapter 4 table 4.1 for the under- and over-propelled cases. The scalings for the over-propelled case are based on the analysis in Chapter 2.

6.5 Vorticity field

The calculation of the vorticity field is a very useful tool in determining the self-propelled state. There is an interaction between the boundary layer of the ship and the jet, largely through diffusion. Without the thrusting jet the boundary layer is the dominant source of vorticity due to the no slip condition. As the strength of the jet increases it becomes the dominant source of vorticity in the flow. Ultimately the downstream state of the vorticity field depends on the relative strength of these two vorticity fields.

Looking at the centre line velocity decay in figure 6.5 it can be concluded that the vorticity decays very rapidly especially in the self-propelled case. The scalings for the vorticity decay are shown in table 6.3. The computational results are closer to the scalings predicted by the constant turbulent viscosity analysis in Chapter 4, table 4.1, for both $Re_T = 10$ and SA models. This confirms the hypothesis that Re_T of the wake is quite low even though the overall Re is very high. The variation of the computational results from the predicted results in the under-propelled case is due to the boundedness of the domain. As large of a computational domain as possible was used to mitigate this using larger and larger mesh elements towards the edges but there is a limit to how big the elements can get before causing meshing failure. In the planar $Re_T = 10$ case the domain used is significantly wider than in the other case and the observed scaling is much closer to the prediction. In these calculations the self-propelled state is captured approximately, therefore, the scalings are affected by this in addition to boundedness. The predicted scalings from the over-propelled case are obtained from the analysis in Chapter 2. The planar SA case varies significantly from the predicted value, this is most likely due to the thrusting velocity not being

high enough for the flow to fully exit the self-propelled regime. Additionally, the computational result for the under-propelled planar SA case is different from the prediction because of vortex shedding.

The vorticity fields are shown in figures 6.6, 6.7, 6.8 and 6.9 and the corresponding vorticity profiles across the width of the wake are shown in Appendix E. From the vorticity field we can determine the wake width. In this case the wake width is defined by the point where the maximum absolute vorticity has dropped to 5% of its maximum value and the results are shown in figures 6.12 and 6.13. The wake width growth occurs very slowly with distance downstream and in the axisymmetric cases the growth of the self-propelled wake comes to a halt at about $x_1/D = 10$. This suggests that after the rapid near field dilution of contaminant any further dilution occurs very slowly.

In the figures 6.10 and 6.11 the spatial variation of the Re_T is shown. We can see that the value of Re_T decays rapidly, however, the width of the turbulent region of the wake remains constant. The main point here is to show that within the wake the level of turbulence is much higher than in the ambient leading to the contaminant in the wake to be localised within this region. The values of Re_T measured in the SA calculations range from 10 to 125 indicating that the choice of $Re_T = 10$ for the fixed turbulent Re calculations is appropriate.

The wake width, determined from the vorticity field, is shown in figure 6.12 for the planar case and in figure 6.13 for the axisymmetric case. A necking region can be observed in the propelling jet in the proximity of the ship. This only occurs in the SA calculations, however, it is consistent with the observations of Chou (1996) who stated that the dilution in the wake width should be considered in two regimes *i.e.* $x_1/D < 7, > 7$. In the $Re_T = 10$ over-propelled planar and axisymmetric cases it can be observed that there is a drop in the overall wake width. This is due to the vorticity from the boundary layer of the ship model being pushed away from the centre line and as it gets annihilated a short distance downstream the wake width drops. It is probable that a similar necking region would be observed in the $Re_T =$ constant case if a higher Re_T value were to be used. As u_J/U_∞ increases there is a gradual change to the regime showed by the red lines, however, additional increases beyond that point did not result in a wider wake.

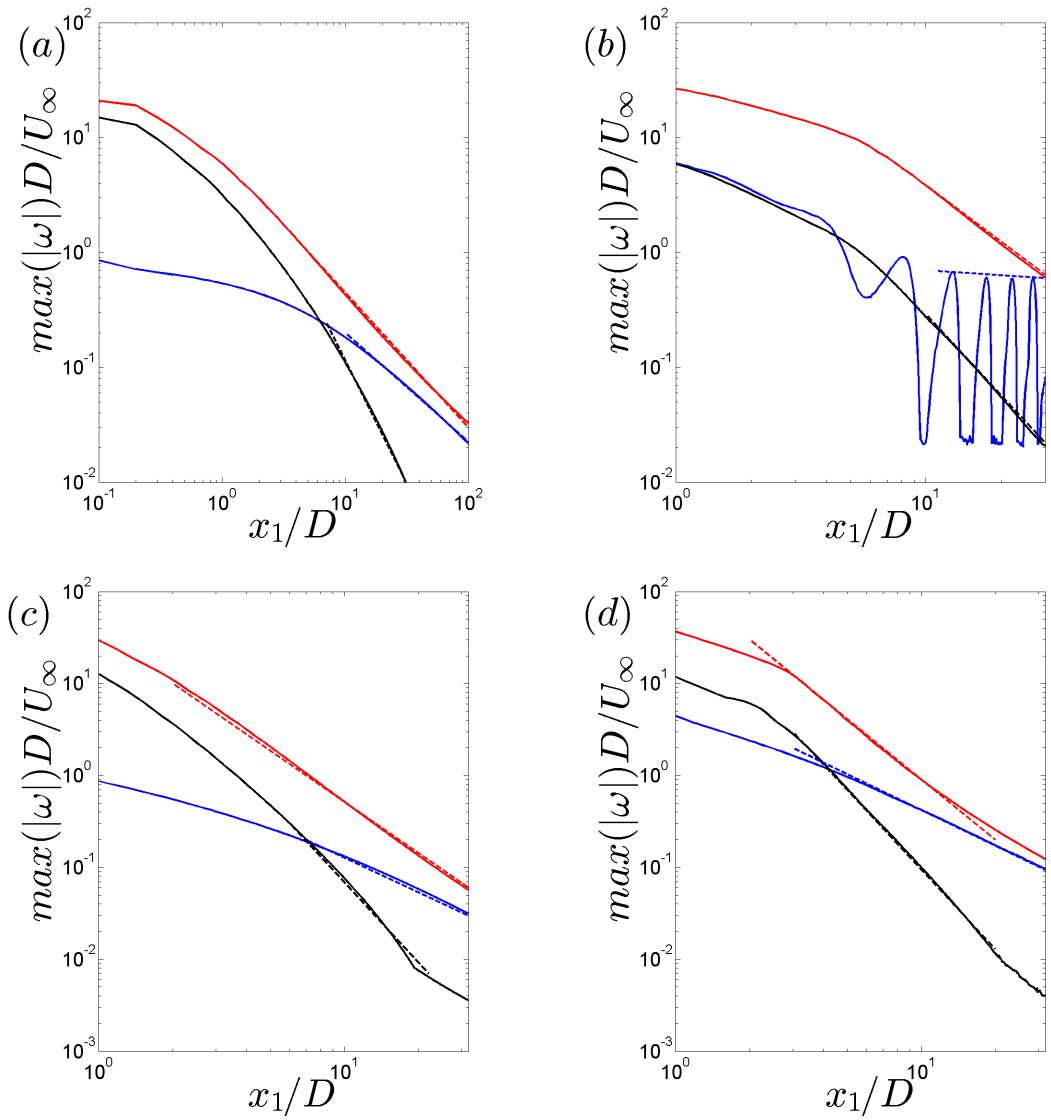

Figure 6.5: The variation of the maximum vorticity magnitude across the width of the wake with distance downstream. The plots in the case of a planar wake are (*a*) $Re_T = 10$, (*b*) SA and in the case of an axisymmetric wake (*c*) $Re_T = 10$, (*d*) SA. The blue, black and red lines are for the under-, self- and over-propelled cases.

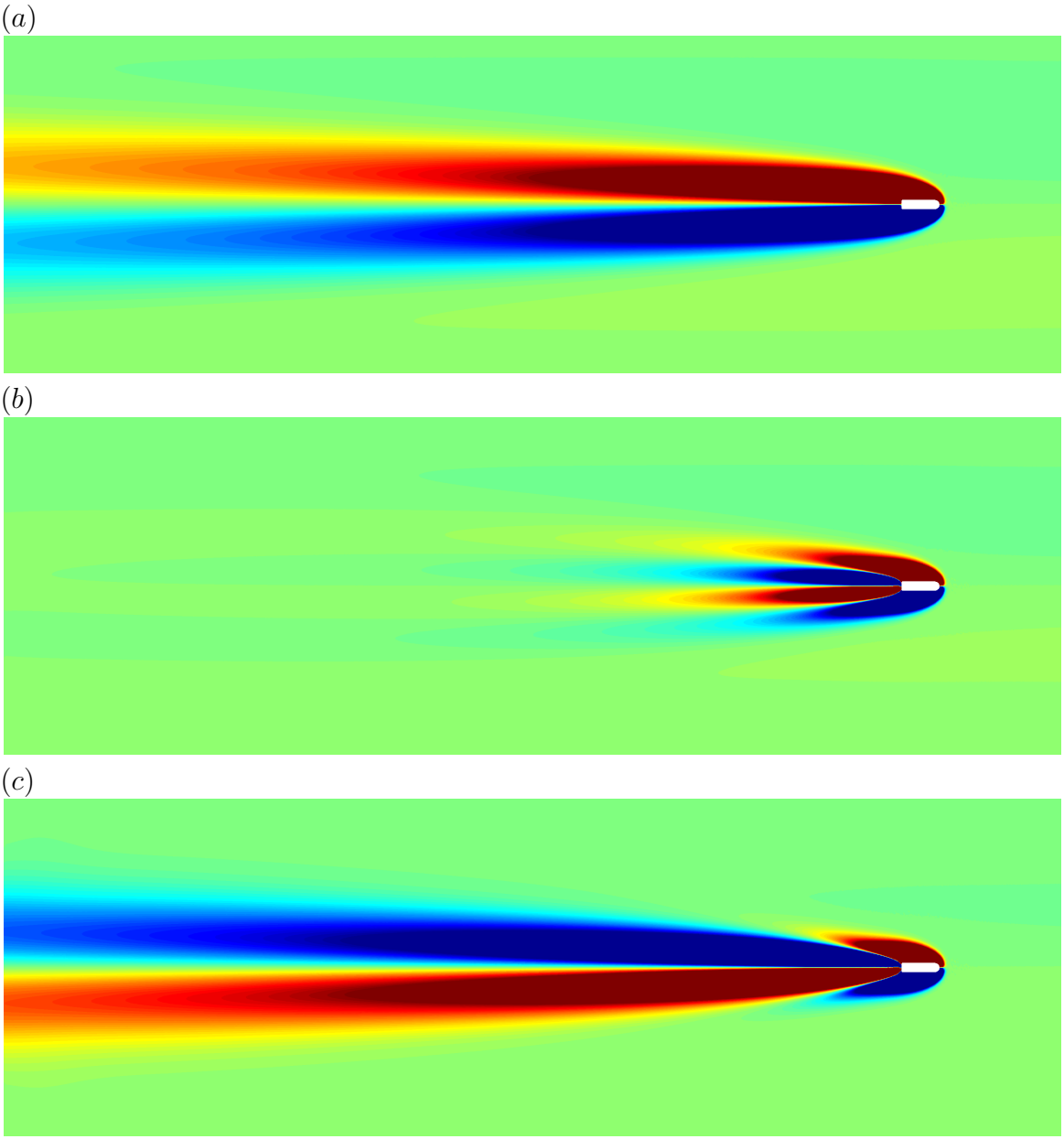

Figure 6.6: The vorticity field for the planar and Re_T = constant calculations. The under-propelled state is shown in (a), the self-propelled state in (b) and the over-propelled state in (c). The vorticity field has been limited into the range of $0.05U_\infty/D$ to $-0.05U_\infty/D$ to capture data far downstream, this has the effect of exaggerating the vorticity field in the near wake.

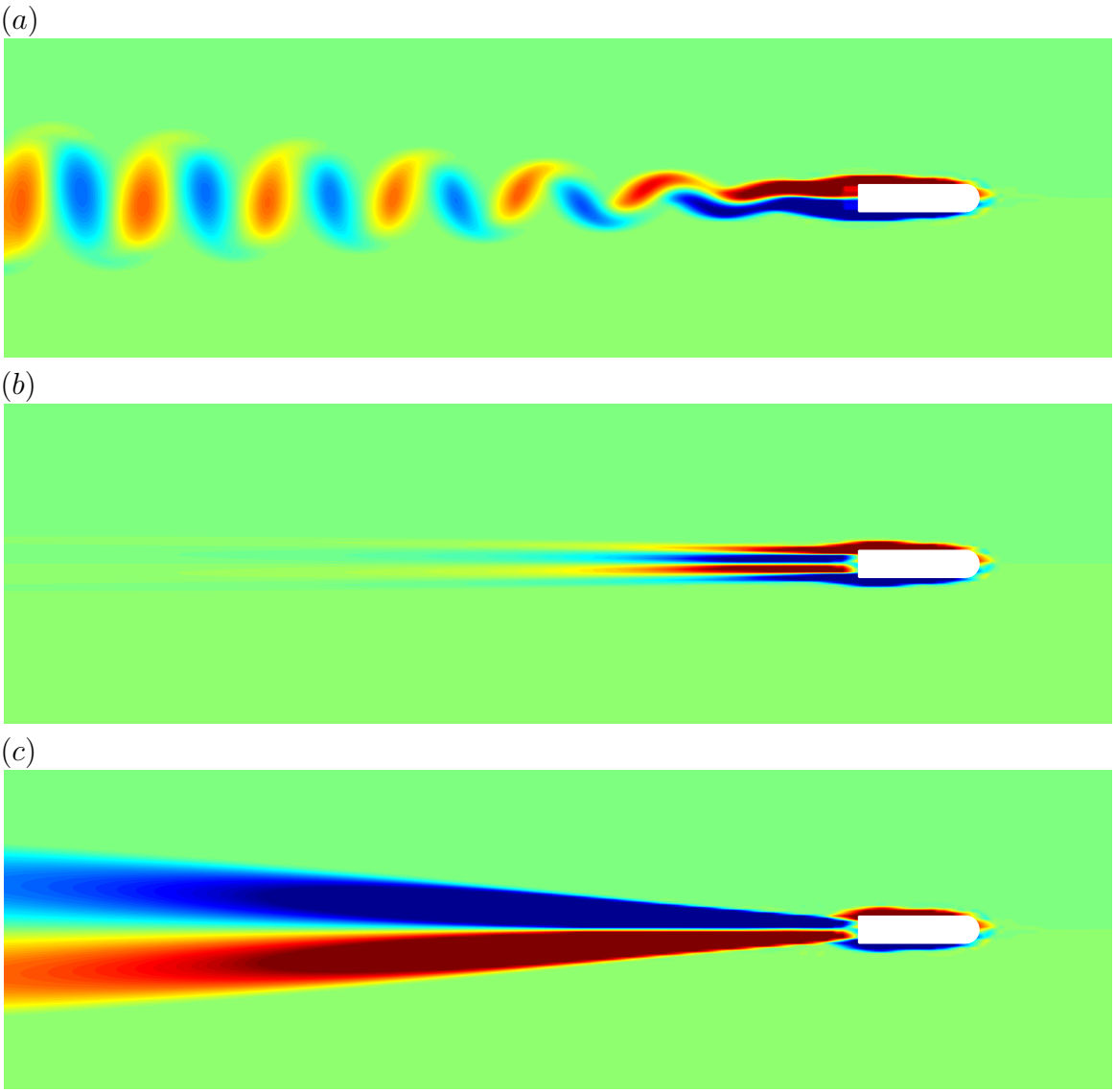

Figure 6.7: The vorticity field for a planar flow past a ship with the SA turbulence model. The vorticity field has been capped from $0.5U_\infty/D$ to $-0.5U_\infty/(D)$ and the under-, self- and over-propelled cases are shown in (a), (b) and (c) respectively.

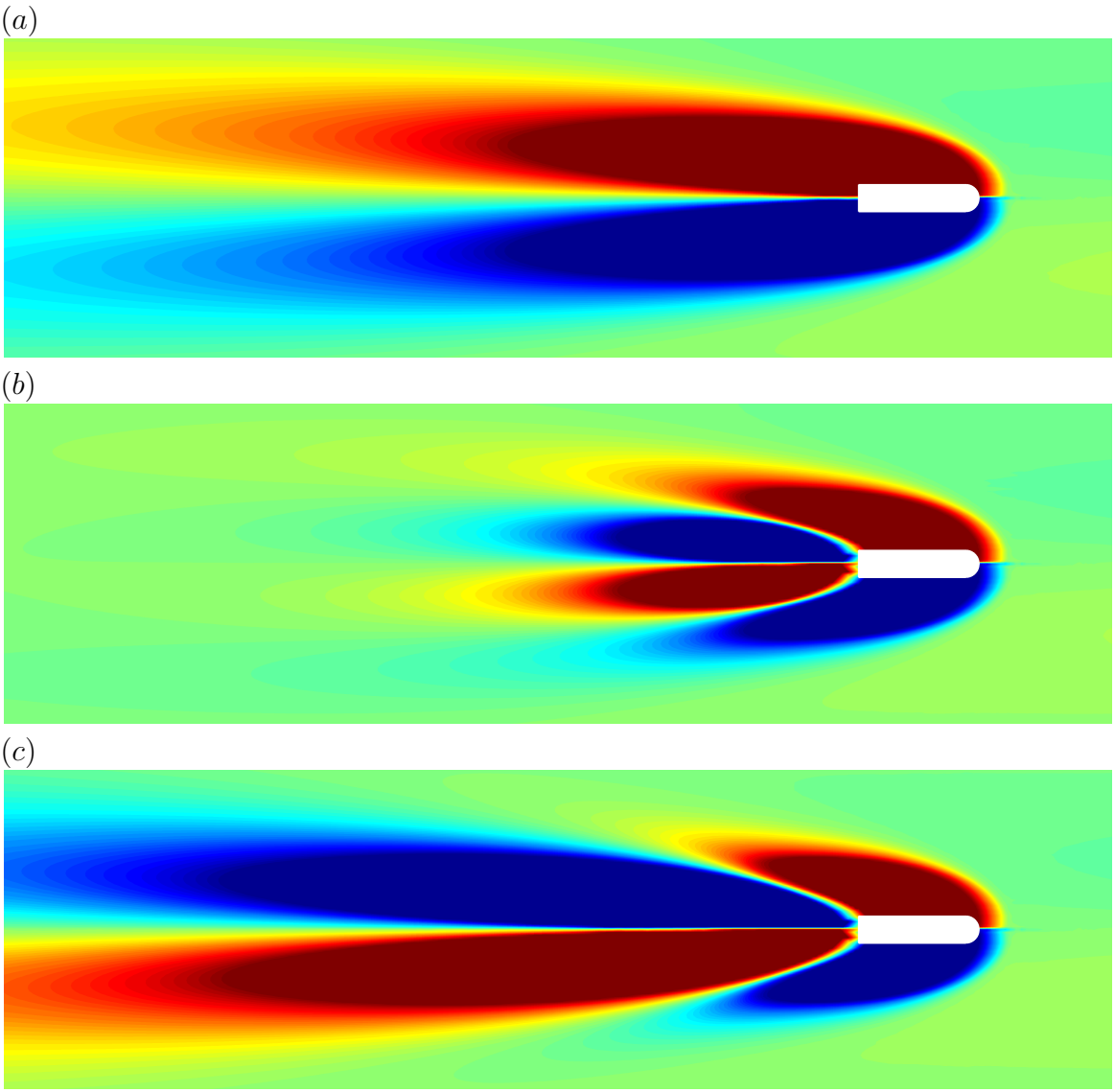

Figure 6.8: The vorticity field for the axisymmetric flow past a ship. The vorticity field has been capped from $0.05U_\infty/D$ to $-0.05U_\infty/D$ and the under-, self- and over-propelled cases are shown in (a), (b) and (c) respectively.

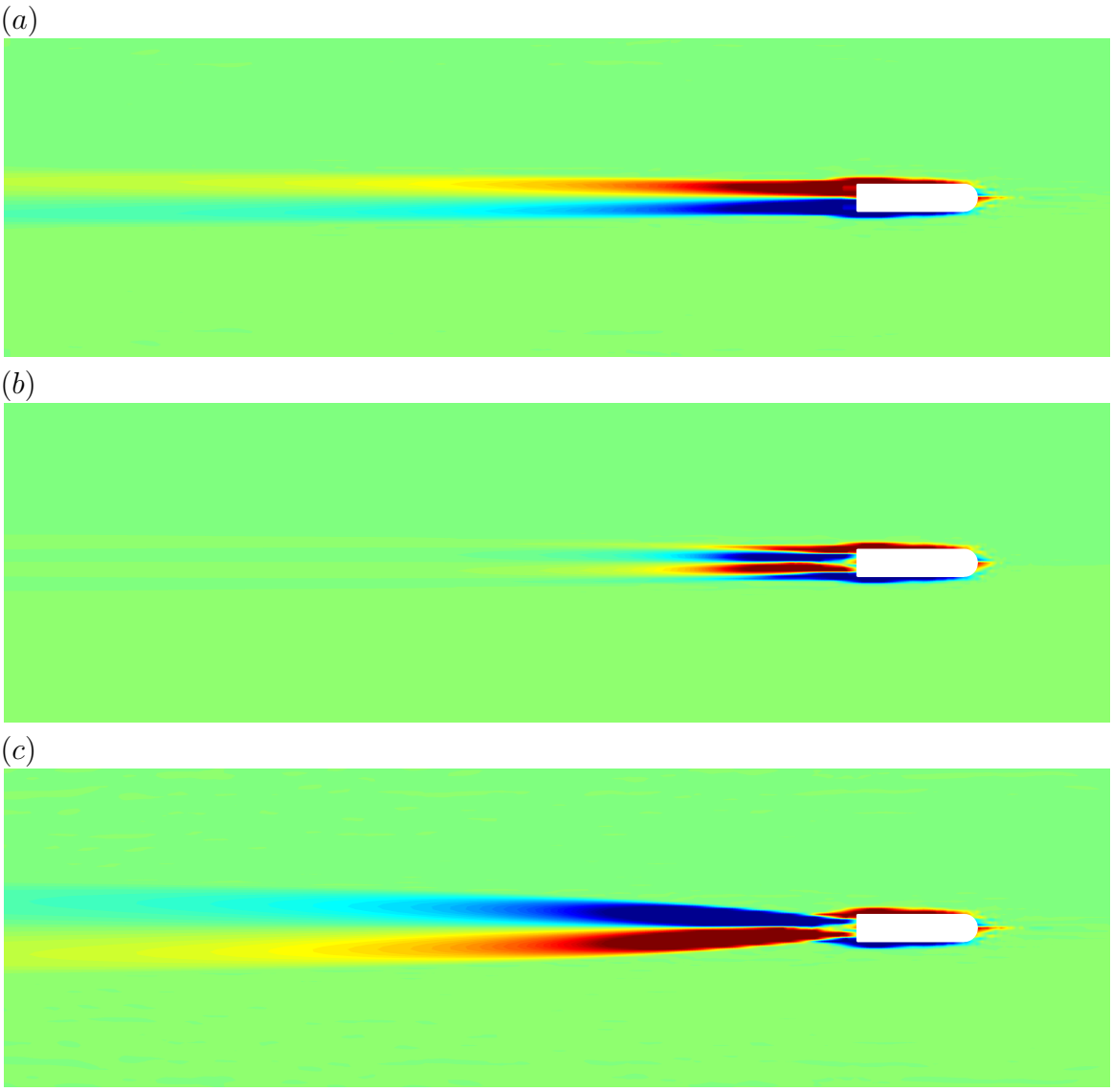

Figure 6.9: The vorticity field for the axisymmetric flow past a ship with the SA turbulence model. The vorticity field has been capped from $0.5U_\infty/D$ to $-0.5U_\infty/D$ and the under-, self- and over-propelled cases are shown in (a), (b) and (c) respectively.

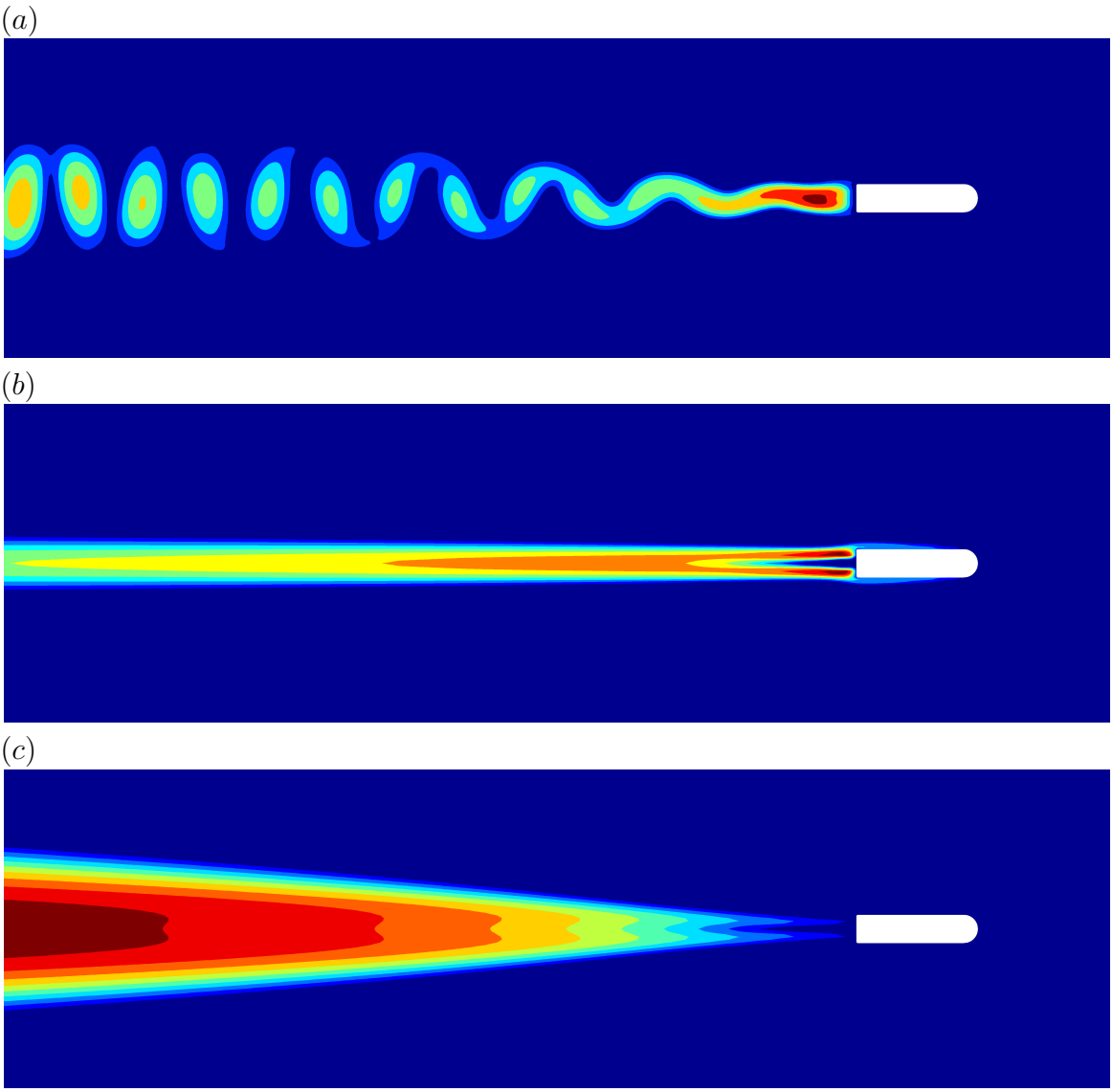

Figure 6.10: The turbulent Reynolds number, Re_T, for the planar wake calculations with the SA turbulence model. The under-, self- and over-propelled cases are shown in (a), (b) and (c) respectively. The maximum values of Re_T are (a) 38.5, (b) 125 and (c) 10.

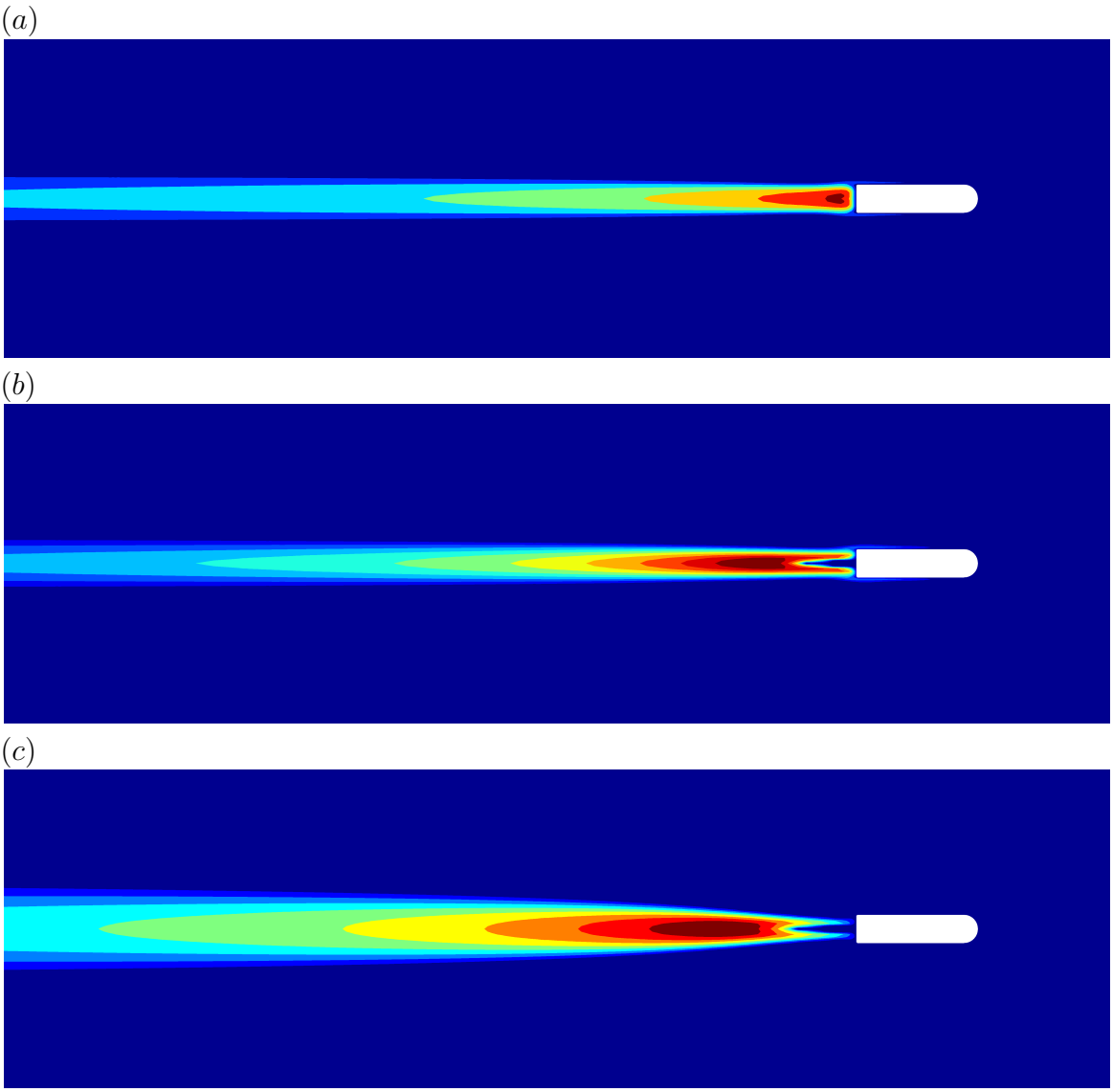

Figure 6.11: Axisymmetric flow past a ship with the SA turbulence model showing the spatial variation of Re_T. In (a), (b) and (c) the maximum value of Re_T is 80.5, 90.9 and 28.2 respectively.

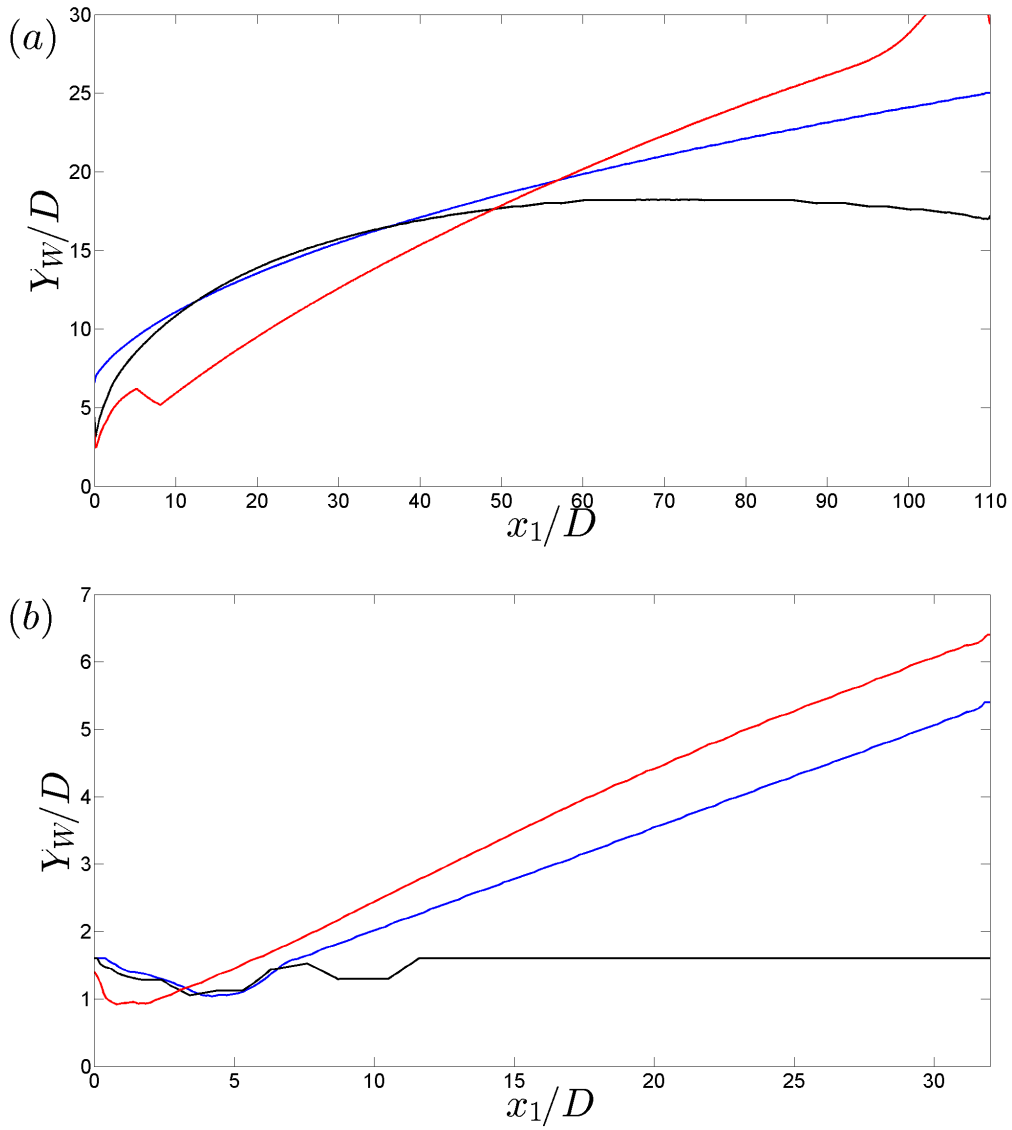

Figure 6.12: The wake width for the planar wake calculations. In (a) $Re_T = 10$ and in (b) the SA turbulence model is used. The under- (blue line), self- (black line) and over-propelled (red line) cases are shown. The edge of the wake is defined where the vorticity field drops to 5% of its maximum value along the x_2 axis. The wake width in the under-propelled case is obtained from a time-averaged vorticity field due to vortex shedding. Approximately 30 periods of shedding were recorded with data extracted at 300 equally sized segments.

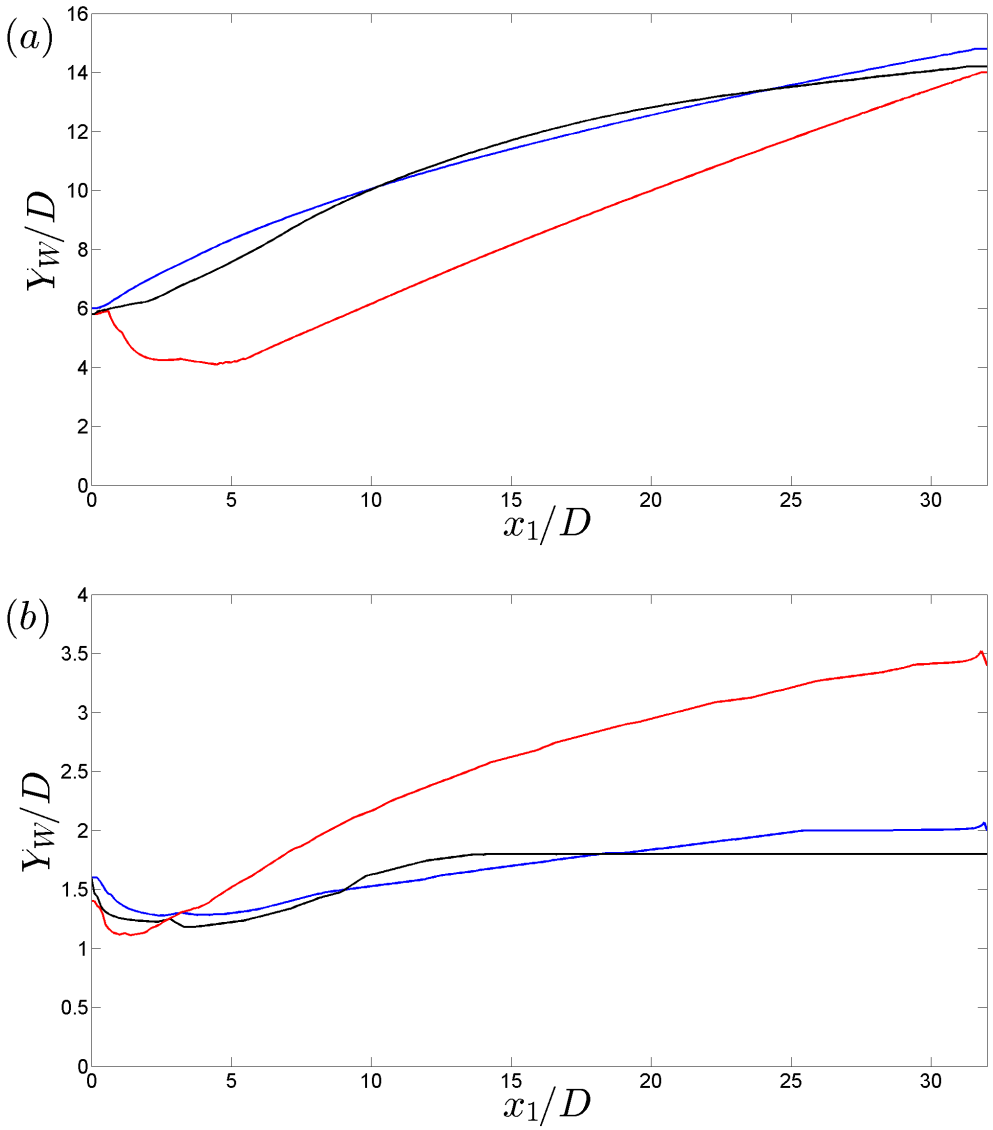

Figure 6.13: The wake width for the axisymmetric wake calculations. In (*a*) $Re_T = 10$ and in (*b*) the SA turbulence model is used. The under- (blue line), self- (black line) and over-propelled (red line) cases are shown. The edge of the wake is defined where the vorticity field drops to 5% of its maximum value along the x_2 axis.

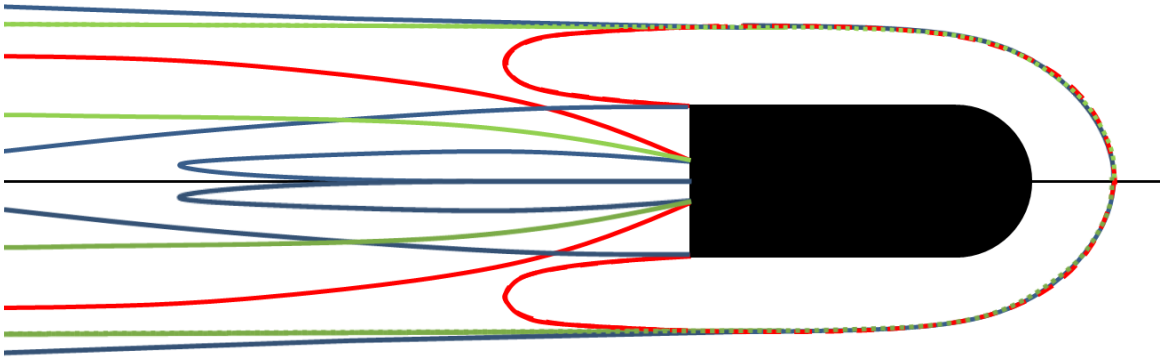

Figure 6.14: A schematic of the overlapping vorticity magnitude fields for the under- (blue lines), self- (green lines) and over-propelled (red lines) cases.

6.6 Conclusions

As Tennekes & Lumley (1972) highlighted, the properties of the downstream wake profile depend subtly on how close the flow is to the self-propelled state. To understand the possible influence of the mode of propulsion (*e.g.* under-, self- or over-propelled) three cases were considered, using either the constant turbulent viscosity model of Tennekes & Lumley (1972) or the SA turbulence model.

The detailed numerical calculations showed the dramatic influence of the thrusting jet on the downstream development of the ship wake. For the under-propelled state, the boundary layer vorticity from the sides of the ship dominates and as it progresses downstream, the diffusion of opposite signed vorticity into one another leads to an annihilation shown in figure 6.14. The constant turbulent Re_T results agree with the self-similar model. In the planar wake case with the SA turbulence model, vortex shedding occurs and since the opposite signed vortical patches are well separated, vorticity cancellation does not occur and instead the maximum vorticity decays slowly with distance downstream. The vortex shedding that would occur in three-dimensions is suppressed due to the axisymmetric form of the model. For the case of the self-propelled state, the vorticity flux caused by the thrusting jet and the boundary layer are oppositely signed and equal. A triple shear layer is created downstream (see the self-propelled images in figures 6.6, 6.7, 6.8 and 6.9) and within the wake and the vorticity annihilation is more effective leading to an extremely rapid decrease in the vorticity maximum. For an over-propelled state, the thrusting jet vorticity dominates and spread more widely that the other two cases.

The analysis of Tennekes & Lumley (1972) suggests that the wake width grows

more slowly for the case of the self-propelled state and this is confirmed in this study for both constant Re_T and the SA turbulence model. However, the rate of increase is too small to confirm the scaling analysis of Tennekes & Lumley (1972). The mean concentration within the wake scales as $C = C_0 Q_0 / A_w$, where A_w is the wake cross-sectional area. The calculations suggest that the wake width is approximately constant over the distance $x_1/D < 30$ and thus the mean concentration of contaminants in the wake is also constant. While the flow dramatically changes, the effect on the concentration field is weak in the near field. As suggested in Chapter 4, the growth of the wake width is relatively slowl due to the fact that the wake is initially so large. From Chapter 4 (4.29), we find $Y_W = Y_W(0)(1 + \lambda x/D)^{1/(\beta+1)}$. The level of turbulence in the wake is typically about αU_∞, where $\alpha \sim 0.1$ (see the experimental study), which can be used to estimate $\lambda \sim 0.1$. Over a distance of $D/\lambda \sim 10D$ the wake width has increased from $Y_W(0)$ to $2^{1/(\beta+1)} Y_W(0)$. This suggests that the turbulent region of the wake in the near field is not observably widening. A photograph of a ferry wake is shown in Chapter 4, figure 4.5 confirming the computational observation.

In relation to dilution in the wake it can be concluded that the mode of propulsion, *e.g.* under-, self- or over-propelled, has a very weak effect on the wake width in the near to mid fields. This indicates that the dilution in the wake is approximately the same in all three cases.

Chapter 7

Scrubber design implications

7.1 Introduction

Chapter 1 highlighted the regulatory requirement, a pH of 6.5 or greater 4 m from the point of discharge. Compliance is tested in ports where the ship is held at rest with the engines running creating the typical conditions for fuel consumption (worst case scenario) and therefore, scrubber flow rate and acid concentration. A typical scrubber configuration is shown in figure 7.1.

In Chapter 2, the jet/plume behaviour of the acidic discharge was examined analytically. Analytical expression were developed and later tested in Chapter 3. The numerical study in Chapter 6, highlighted that mixing in the wake of the ship is very high, reinforcing the hypothesis that acidity will have the highest impact on the marine environment while the ship is being held at rest. The purpose of this chapter is to develop simplified analytical expressions based on which design decisions can be made to best meet regulatory compliance.

7.2 Physics of dilution

Open loop scrubbers are required to use 45 m^3 of seawater per megawatt-hour (MWh) at 80% of the fuel combustion power rating (MEPC 59/24/Add.1 Annex 9). The scrubbing of sulphur oxides from the exhaust gases produces an effluent with a pH of approximately 3 (USEPA, 2013). A typical vessel used in the technical report MARINTEK (2006) had a horizontal discharge port at depth of 8 m. Even though the configuration of the discharge port will vary from vessel to vessel, it is reasonable to assume that the discharge depth will always be well below the free surface. In the case

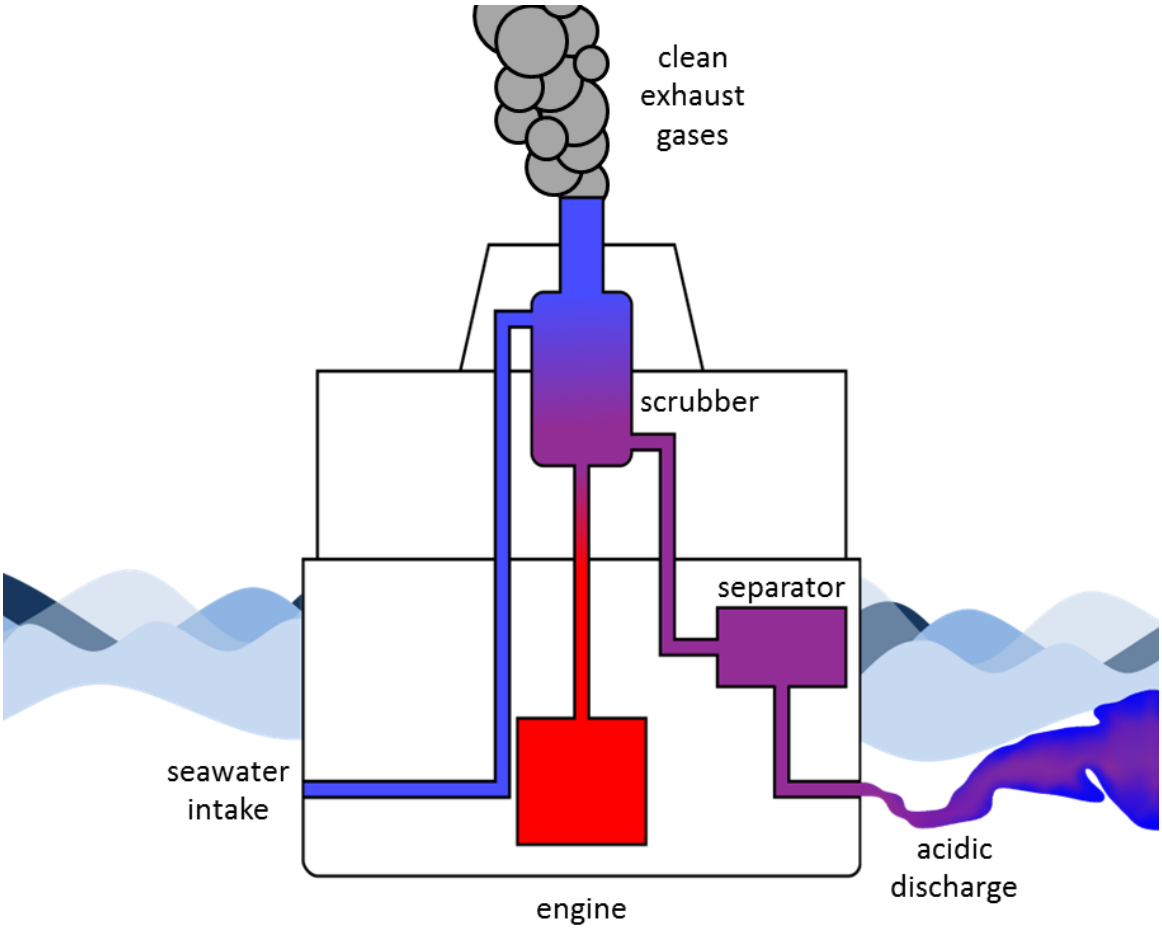

Figure 7.1: Cross-sectional view from the rear of the ship highlighting the key components to a wet scrubber setup. The colour from red to blue is an indicator of temperature from hot (combustion) to cold (seawater).

of the Pride of Kent, the scrubber discharge temperature was at 37 ^{o}C (USEPA, 2013). The density variation between the ambient and the discharge due to temperature in standard mean ocean water (SMOW) will be less than 1% (Lide, 2004), although seawater density is dependent both on its temperature and salt content (Wang *et al.*, 2010).

Consider a scrubber generating acidic exhaust gas wash water from seawater with a volume flux Q_s and acidity C_a^s. Onboard the ship, the wash water may be diluted with an additional volume flux of seawater (Q_w) resulting in a total volume flux $Q_0 = Q_s + Q_w$. The onboard dilution factor $\mathcal{D}_{onboard}$ and reduced acidity at the point of discharge are

$$\mathcal{D}_{onboard} = \frac{Q_w}{Q_s}, \quad C_a^0 = \frac{(C_a^s - C_b^0)Q_s}{Q_s + Q_w}, \tag{7.1a, b}$$

where C_b^0 is the alkalinity of the ambient seawater. The inclusion of $\mathcal{D}_{onboard}$ may be useful to ensure pH recovery for large values of Q_s in the case of large ships. At the outlet Q_0 can be increased by installing a larger number of nozzles N (while maintaining the same discharge velocity and port radius)

$$Q_0 = Q_s(1 + \mathcal{D}_{onboard}) = \pi b_0^2 u_0 N, \tag{7.2}$$

where b_0 is the radius of the nozzle. Between the wash water leaving the ship and reaching a distance of 4 m, the fluid has been diluted by a factor of $\mathcal{D}_{jet}$. The total dilution ($\mathcal{D}_T$) that has occurred from the scrubber to the distance of 4 m from the discharge nozzle is

$$\mathcal{D}_T = (1 + \mathcal{D}_{jet})(1 + \mathcal{D}_{onboard}) - 1. \tag{7.3}$$

In a time-averaged jet, $\mathcal{D}_{jet}$ indicates the amount of dilution on the jet centre line, a region where dilution will be at its lowest.

7.3 Constraints on velocity

Two characteristic velocities are of importance in this problem, the flow velocity in the pipes (u_p) and the discharge jet velocity u_0 at the nozzle. The constraint on the flow within the pipe is that cavitation does not occur requiring that the pressure P satisfies

$$P \left(= P_a + \rho g h - \frac{\rho u_p^2}{2} \right) > P_v, \tag{7.4}$$

where P_v is the cavitation pressure of the water, P_a is the atmospheric pressure, ρ is the the density of the wash water, g is acceleration due to gravity and h is the depth of discharge. Observations on the phenomena of cavitation were first published by Reynolds (1873). The potential to cavitate depends on water depth, water quality and the smoothness of the pipe internal surface. The flow velocity can be increased by reducing the friction coefficient of the pipe through acrylic coating. The outlet nozzle radius can be designed to be much smaller than the discharge pipe radius, therefore, u_0 can be much higher than u_p, however, additional material considerations need to be taken into account (Krivchenko, 1994), *i.e.* higher tensile strength materials. Entrainment is a mechanism leading to the growth of the jet radius and volume flux with distance from the point of discharge by capturing ambient fluid (Turner, 1973). When the jet speed is small, the discharged flow becomes laminar and the entrainment of ambient fluid into the discharge is significantly reduced (Morton, 1967). This introduces a constraint

$$Re \left(= \frac{2b_0 u_0}{\nu} \right) > Re_c, \tag{7.5}$$

where Re_c is a critical Reynolds number and ν is the kinematic viscosity of water. Certainly $Re_c = 3000$ is sufficient for the jet to be turbulent (McNaughton & Sinclair, 1966).

7.4 Near field discharge deflection

In the following analysis we use the jet/plume model with cross flow as described in Chapter 2 §2.4. The jet is directed along the y-axis, rises due to buoyancy along the z-axis and is swept by an ambient flow along the x-axis. Two forces act on the buoyant jet in the presence of an ambient flow U_∞, the Lamb force (see Chapter 2) and buoyancy. The temperature difference between the discharge and the ambient seawater generates buoyancy, in this case the ambient temperature is taken as 10 ^{o}C (the typical maximum sea surface temperature in the northern parts of the Baltic Sea) and the temperature difference between the ambient and the discharge is $\Delta T_0 = 5$, 10, 20 and 30 ^{o}C. The values of ΔT result in the density contrast at the nozzle ($(\rho_a - \rho_0)/\rho_a$) of 0.0006, 0.0015, 0.0040 and 0.0075 kg/m^3 for Standard Mean Ocean Water (SMOW) (Tanaka *et al.*, 2001). The system of equations in Chapter 2 §2.4 is solved using the Euler method in Matlab R2013b for $b_0 = 0.05$ m, the results are plotted in figure 7.2

and discussed in the following section.

The typical form of discharge is a jet (*i.e.* $u_0 \gg \sqrt{gb_0(\rho_a - \rho_0)/\rho_a}$, U_∞), therefore, the influence of buoyancy and ambient flow are negligible in the near field. The benefit of a high discharge velocity is that it also results in a more coherent jet within 4 m from the nozzle. In this limit the following linear relationships can be established

$$\frac{b}{b_0} = 1 + \mathcal{D}_{jet}, \quad \mathcal{D}_{jet} = \frac{2\alpha y}{b_0}. \tag{7.6a, b}$$

Jet dilution and volume flux increase (Morton *et al.*, 1956) along the centre line are related to each other through the following relationship

$$Q = 1 + \mathcal{D}_{jet}. \tag{7.7}$$

The comparison with the full model in Chapter 2 and the estimates in (7.6*a,b*) are plotted in figure 7.2*a*. The jet results in a cone with an angle $\tan^{-1}(4\alpha) = 21.8\ ^o$ and over a distance of $y = 4$ m, the jet fluid has been diluted by a factor of

$$\mathcal{D}_{jet} = \frac{0.8}{b_0}. \tag{7.8}$$

The decay in u and ΔT of the jet with distance y due to entrainment of ambient fluid (dilution) can be estimated as

$$\frac{u}{u_0} = \frac{1}{1 + \frac{2\alpha y}{b_0}}, \quad \frac{\Delta T}{\Delta T_0} = \frac{1}{1 + D}. \tag{7.9a, b}$$

By inserting the terms in (7.6*a*) and (7.9*a*) into (7.5) it can be shown that the local Reynolds number within a momentum dominated jet cone will stay constant, so if the jet is initially turbulent at the outlet it will be turbulent along its path.

When measuring the location of the jet centre line at 4 m it is important to make a correction due to the effect of U_∞ and ΔT. The influence of ΔT causes the jet to rise above the point of discharge. This rise can be estimated from

$$M_0 \frac{\mathrm{d}^2 z}{\mathrm{d}y^2} \simeq \pi b^2 g \left(\frac{\rho_a - \rho_0}{\rho_a} \right). \tag{7.10}$$

Since the buoyancy flux is conserved, we can integrate (7.10) to obtain

$$z \simeq \frac{g y^2}{u_0^2} \left(\frac{1}{2} + \frac{\alpha y}{3 b_0} \right) \left(\frac{\rho_a - \rho_0}{\rho_a} \right). \tag{7.11}$$

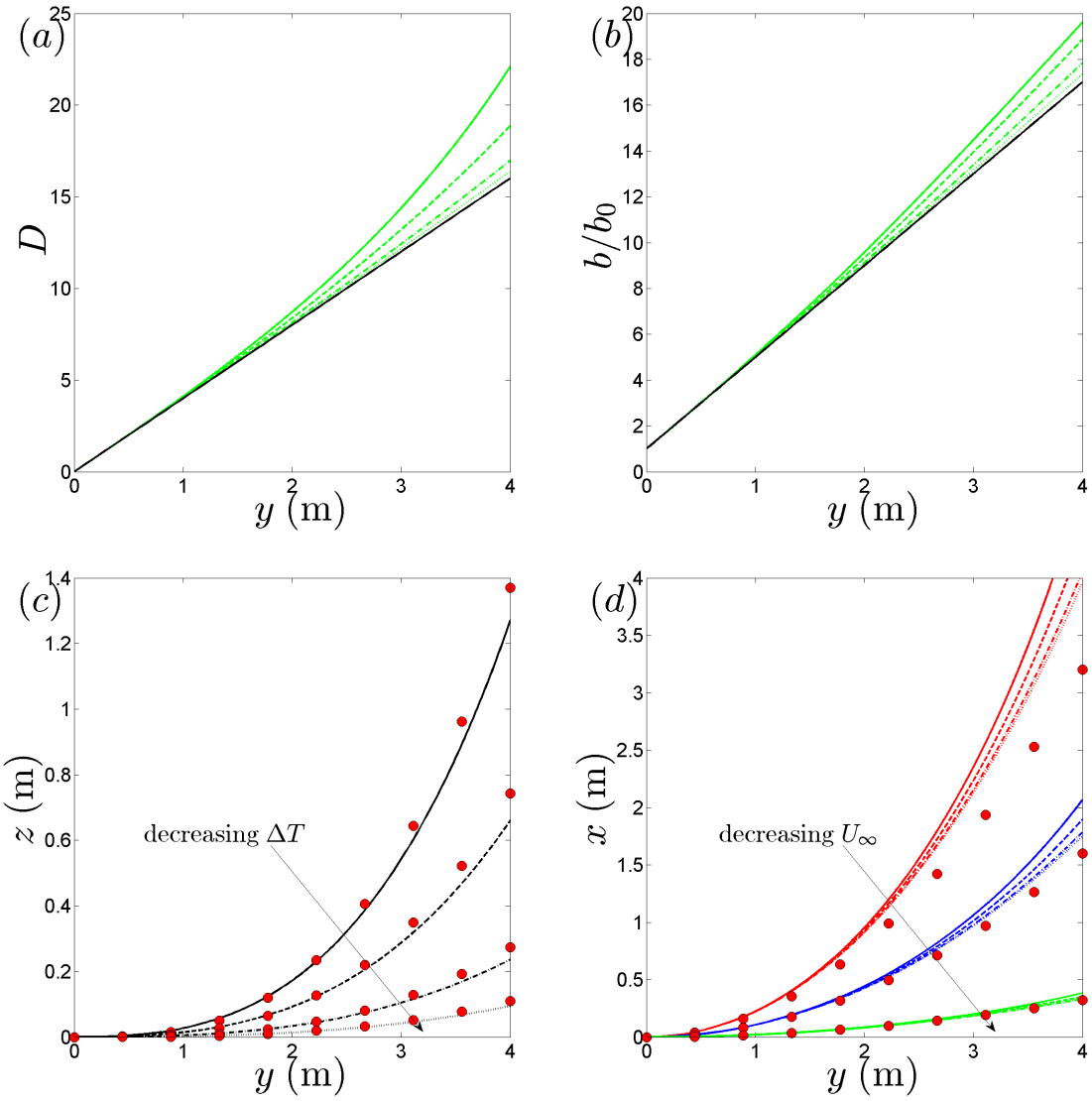

Figure 7.2: The influence of buoyancy with $b_0 = 0.05$ m is investigated for $\Delta T_0 = 5$ ^{o}C (dotted line), 10 ^{o}C (dash-dot line), 20 ^{o}C (dashed line), 30 ^{o}C (solid line) on all of the subplots. In (a) and (b) a comparison is made between the models presented in Chapter 2 (solid black lines) and §7.4. In (c), the influence of buoyancy on the deflection of the jet along the z axis is compared with (7.11), plotted as red circles. In (d), the influence of buoyancy and U_∞ on the deflection of the jet along the x axis is compared with (7.13), plotted as red circles. The red, blue and green sets of lines correspond to $U_\infty/u_0 = 0.1$, 0.05 and 0.01.

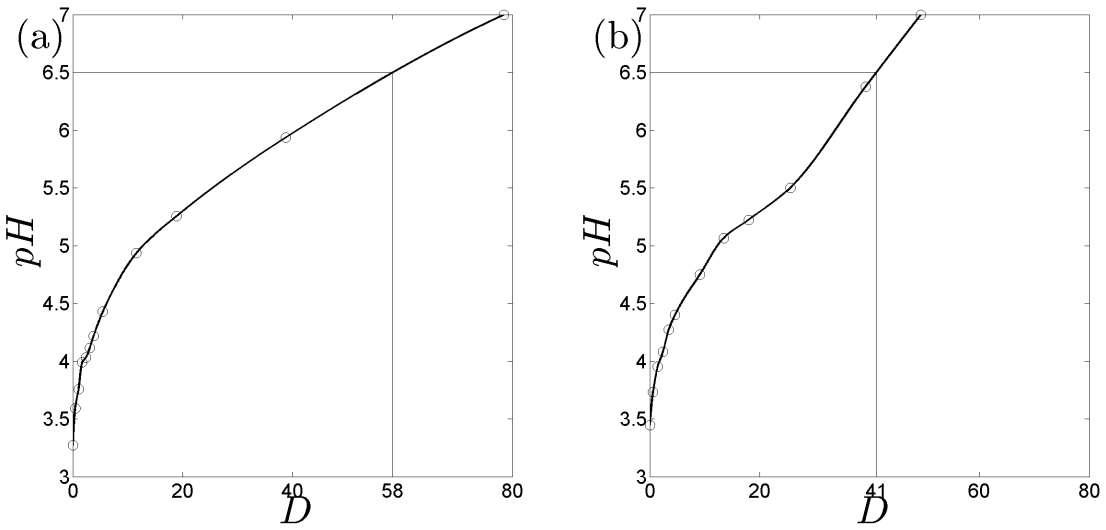

Figure 7.3: Empirical titration curves, with a cubic spline fitted to the data, for acidified (a) Thames River and (b) Brighton marina water samples. The samples were acidified with nitric acid resulting in pH = 3.27 for Thames water and pH = 3.45 for Brighton Marina. The number of points indicates the number of dilutions performed to reach pH = 6.5.

Similarly the jet trajectory deflection due to a weak cross flow is estimated to be

$$M_0 \frac{\mathrm{d}^2 x}{\mathrm{d}y^2} \simeq 2\pi u_E U_\infty b_0 \simeq 2\pi \alpha u_0 U_\infty b_0, \tag{7.12}$$

where entrainment (u_E) is simplified to αu_0. Integrating (7.12) results in an approximate expression for the jet deflection downstream

$$x \simeq \frac{\alpha U_\infty y^2}{u_0 b_0}. \tag{7.13}$$

A comparison between the full numerical model in Chapter 2 and (7.11) and (7.13) is shown in figure 7.2b,c respectively. The agreement is good for $|\Delta T_0|< 20$ ^{o}C and $U_\infty/u_0 < 0.01$.

7.5 Titration of acidified seawater

The key element to this chapter are the titration experiments that need to be undertaken to determine the amount of dilution required by $\mathcal{D}_{onboard}$ and $\mathcal{D}_{jet}$ to reach the pH of 6.5 at 4 m from the point of discharge as shown in figure 7.3 (the experimental procedure is described in Appendix A). The chemistry of a strong acid reacting with

seawater is more complex than the alkaline solution used in the experimental study due to a wide variety of dissolved salts in seawater. To closely mimic the typical reaction between an acid and seawater, we titrated acidified samples from the River Thames (taken a week before the Olympics at Embankment on Saturday the 21st of July 2012 at 2pm) and from Brighton Marina (taken on Saturday the 22nd of September 2012 at 2pm). Both samples were taken on days where there was no rain. The Thames is a tidal river, however, at the point and time the sample was taken, the water was essentially fresh with suspended clay sediments. These titration curves are of singular importance in trying to understand pH recovery from jets and they must be obtained from experiments because of the complex and highly variable chemistry of seawater. The instructions for undertaking these can be found in Appendix A. The 100 ml samples were acidified with 4 ml of 1 mol/l nitric acid (HNO_3) resulting in pH = 3.27 for Thames water and pH = 3.45 for Brighton Marina. For low dilution factors, the dependence of pH on dilution is similar for both samples (see figure 7.3*a,b*) because the molarity of the acid is much stronger than the alkalinity; in this instance the initial pH increase is largely due to dilution with the pH recovering by slightly more than 1 unit when $D = 10$. From these titration curves we can determine the dilution required to bring the discharge to a pH = 6.5. In this example, Brighton seawater has an alkalinity of 770 μmol/l and River Thames water has an alkalinity of 480 μmol/l. The former is typical for the low alkalinity waters in the Baltic seas (see Chapter 1). These titrations were done over a period of 15 minutes, with less than a minute for each step; much faster than a number of published studies (Behrends *et al.*, 2005). This is to mimic the rapid mixing processes that occur within the jet - the travel time of the acidic jet fluid from the nozzle to a distance of 4 m is typically < 10 s. It is worth noting that these experiments are very sensitive to contamination and should be performed rather quickly to minimize the release of CO_2 from solution.

7.6 Design solutions

We examine the engineering constraints on $\mathcal{D}_{jet}$ and chemistry constraints on $\mathcal{D}_T$ to achieve the necessary pH recovery. The design of the port discharge hole may be optimised to ensure pH = 6.5 at 4 m, for a single circular discharge port. An example discharge of pH = 3.5 is used, which was obtained with a monoprotic acid with molarity 0.0385 mol/l. Extension to other values of discharge pH and seawaters

is straightforward.

7.6.1 Without prior dilution or treatment ($\mathcal{D}_{onboard} = 0$)

To enable large volumes to be discharged multiple ports may be required and the number can be estimated to be

$$N = \frac{Q_s \mathcal{D}_T^2}{4\pi u_0 \alpha^2 x^2}. \tag{7.14}$$

From (7.8), the jet nozzle radius that ensures a dilution $\mathcal{D}_T$, is

$$b_0 = \frac{2\alpha x}{\mathcal{D}_T}. \tag{7.15}$$

Figure 7.4 shows how the number and size of the discharge ports are selected. We consider the example of a 20, 40 and 60 MW ships (where $Q_s = 45$ t/hr/MW) which are in waters with a low alkalinity of 1500 μmol l^{-1}. This alkalinity is typical for the main shipping routes in the Baltic Sea (see Chapter 1). The alkalinity determines the total dilution required which is $\mathcal{D}_T = 19.25$ and this sizes the discharge port radius to 0.04 m from (7.15). We have chosen $u_0 = 5$ m/s which is a conservative estimate of the discharge speed. The number of ports is shown in figure 7.4*c*. For 20, 40 and 60 MW ships 10, 19 and 28 outlet nozzles are required.

Figure 7.4*d* shows the influence of separation of the ports (of radius 0.04 m) on the overlapping entrainment fields for a stationary ship. Having 10 ports on the side of a ship still remains a practical solution for regulatory compliance, especially if laid out in a staggered arrangement with no overlapping within 4 m. In the case of a moving ship the dilution is increased drastically due to the ambient turbulence and overlapping due to the ambient flow will not be a problem to meeting regulatory compliance. Increasing the flow rate from 5 m/s to 7 m/s, for instance, would reduce the number of ports from 9 to 6. When the discharge port holes are close together or form of a slot, the entrainment rate is reduced because the perimeter available for entrainment is reduced. For example a slot of width $2b_0$, the jet width grows as $b = b_0 + \alpha x$ and $u/u_0 = 1/(1 + \alpha x/b_0)^{1/2}$. The dilution increases with distance, but at a slower rate than for a circular jet, *i.e.* $\mathcal{D}_{jet} = (1 + \alpha x/b_0)^{1/2} - 1$.

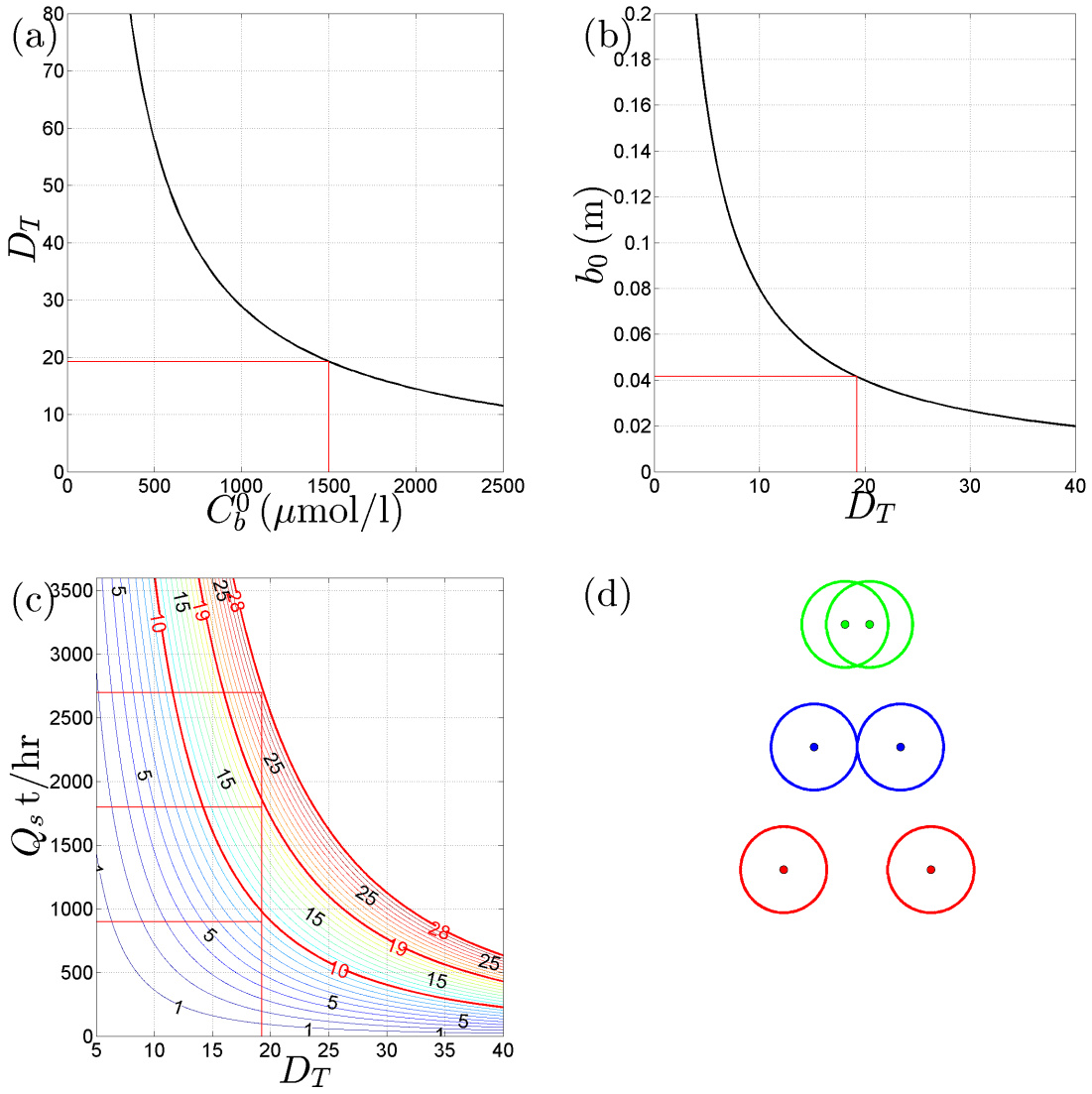

Figure 7.4: In (a), the total dilution ($\mathcal{D}_T$) required to give a pH of 6.5 is plotted against the alkalinity of seawater (C_b). In (b), the nozzle radius required, at a discharge rate of 5 m/s, to reach the required dilution in the $\mathcal{D}_{jet}$. In (c), the number of discharge ports required for a range of flow rates Q_s at the speed of 5 m/s to reach the required dilution $\mathcal{D}_T$. In (d) the influence of separation of the discharge ports (of radius 0.05 m) on the overlapping entrainment fields is illustrated. In the case of green circles the ports are separated by 0.5 m and the edges overlap reducing in a reduced entrainment and poor dilution. The blue circles indicate optimal separation 1.75 m ($= 4\alpha x + 2b_0$) and in the case of red circles the separation is 2.5 m.

7.6.2 With prior dilution or treatment ($\mathcal{D}_{onboard} > 0$)

For large ships and low alkaline waters, it is impractical to add multiple discharge ports using pipes. The engineering alternative is to form a discharge tank in the hull of the ship or sea chest and cut the holes with the separations suggested in figure 7.4*d*. Additional technologies are available that rely on multiple jets issuing from a single discharge port which could be employed. When these are not available, the remaining solution is to either add an alkaline agent or to dilute on board, both of these processes can be represented as an equivalent dilution $\mathcal{D}_{onboard}$. In this case, the outlet port radius (b_0) and number of ports (N) are determined from an implicit equation

$$\mathcal{D}_{onboard} = \frac{1+\mathcal{D}_T}{1+2\alpha x/b_0} - 1, \quad N = \frac{Q_s(1+\mathcal{D}_{onboard})}{\pi b_0^2 u_0}. \tag{7.16a,b}$$

For the results to be physically meaningful in (7.16) the value of $\mathcal{D}_{onboard}$ would need to be greater than or equal to 0. Figure 7.5*a,b,c* highlight the effects of onboard dilution on a 20, 40 and 60 MW ship and figure 7.5*d* shows the reduced need for dilution due to alkali addition.

In the case that the discharge velocity is very low and a plume develops then onboard dilution raises the initial pH but decreases the initial buoyancy flux of the discharge. This is due to a reduction in temperature resulting in reduced entrainment by the plume. The density contrast between the discharge and the ambient can be estimated in terms of the temperature difference ΔT

$$\rho_0 - \rho_{a0} = \gamma \Delta T, \tag{7.17}$$

where γ is the thermal expansion coefficient of water that varies with temperature. The discharge characteristics are assumed to be pH = 3.27 and $T = 40$ ^{o}C ($\gamma = 3.84 \times 10^{-4}$ /^{o}C). The ambient is assumed to have a temperature of 10 ^{o}C ($\gamma = 0.88 \times 10^{-4}$ /^{o}C) and the relationship between pH and dilution featured in figure 7.3. We are interested in an unstratified environment where the plume is characterised by

$$\Gamma_0 = \frac{5\Delta\rho g \pi^2 b_0^5}{8\alpha\rho_0 Q_0^2}, \tag{7.18}$$

which is expressed in terms of parameters that would be part of any design procedure such as the discharge pipe radius b_0 and volume flux Q_0. The scrubber volume flux (quantity of water used to spray the exhaust gas) is proportional to the rate at which

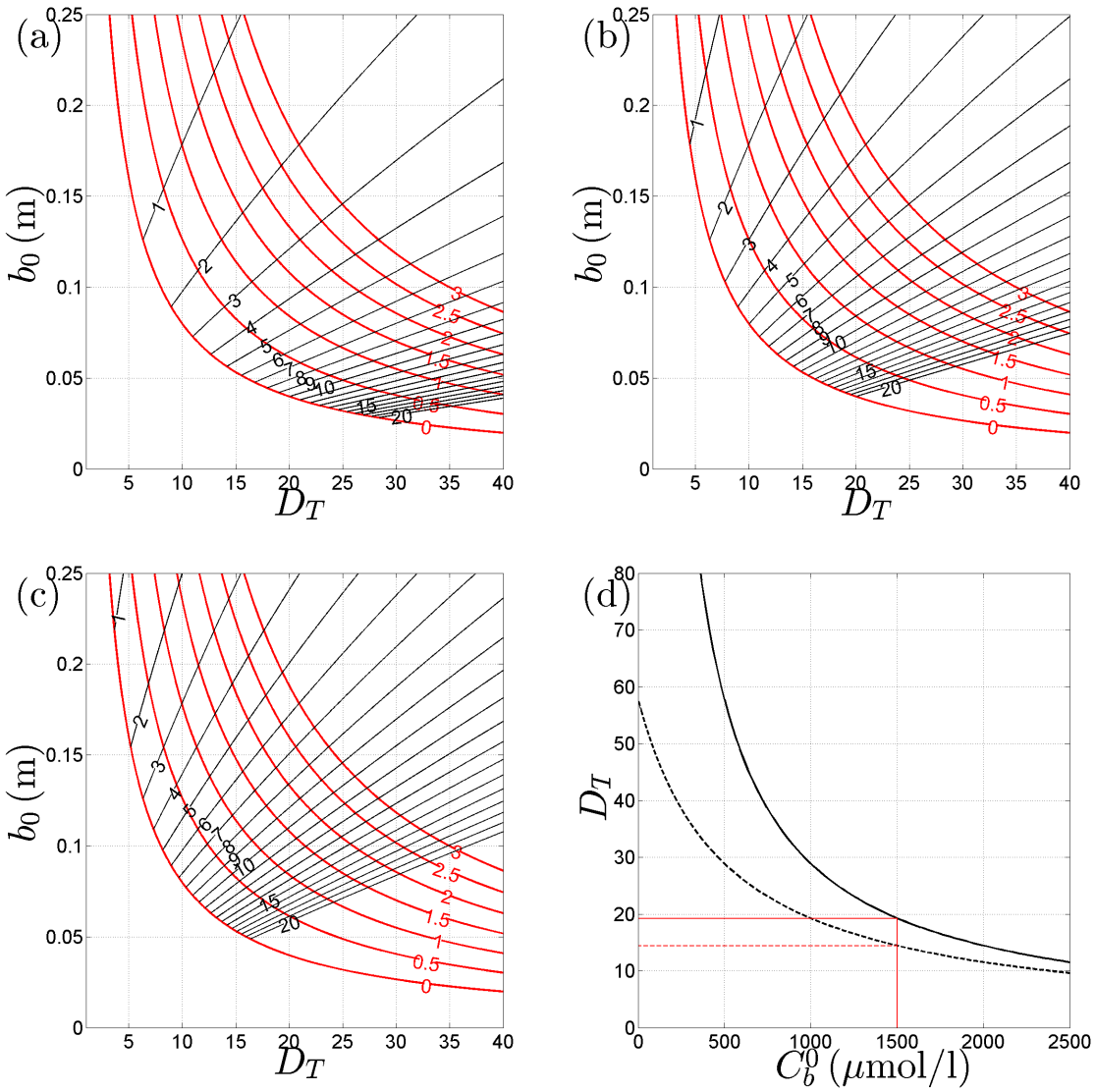

Figure 7.5: In (a), (b) and (c) the discharge pipe radius (b_0) is plotted against total dilution ($\mathcal{D}_T$) for 20, 40 and 60 MW ships, respectively. The red contour lines raise the total dilution with dilution done prior to discharge. The black contour lines highlight the number of nozzles required to achieve the necessary scrubber flow rate. The jet exit velocity at each nozzle is 5 m/s. In (d) the effect of alkali addition to the scrubber discharge is presented. The solid line corresponds to figure 7.4a and the dashed line corresponds to an addition of 500 μmol/kg of calcium carbonate to the discharge.

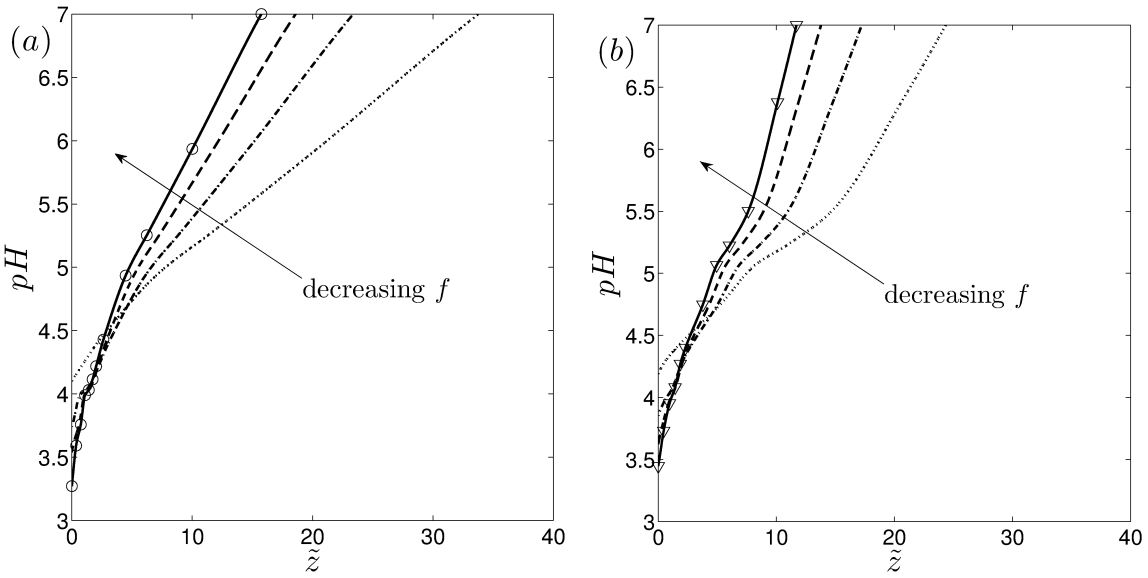

Figure 7.6: Estimating the effect of dilution prior to a vertical discharge into (a) River Thames and (b) Brighton Marina water. If the nozzle diameter remains unchanged then increasing the dilution prior to discharge has an inverse effect on Γ_0. The solid, dashed, dash-dot and dotted lines correspond to $f = 0\%$, 25%, 50%, 75% and $\Gamma_0 =$ 4.78, 2.02, 0.60, 0.08. The symbols in (a) and (b) match the experimentally determined values in figure 7.3.

fuel is consumed in the engine and the fuel sulphur molarity. The volume flux of the discharge into seawater can be higher depending on how it is diluted (frequently various fluids such as engine cooling water are combined and discharged from one source).

Figure 7.6 shows the variation of the pH of an acidic discharge with distance when the wash water has been diluted between 0 and 75%, for $b_0 = 0.2$ m and a discharge of $Q_f = 0.015$ m^3/s from the scrubber. The value of $Q_0 = Q_f(1 + f)$ increases proportionally to the additional dilution (f) done prior to discharge. The relationship between $\mathcal{D}$ and $\hat{z}$ is determined by solving (2.49) numerically and relating the dilution factor to the pH in the plume. The initial dilution has an effect of increasing the initial pH but decreasing the gradient of the pH with distance. In this configuration, the vertical neutralisation distances are so large that pH recovery would certainly need to be supplemented with the addition of an alkaline agent.

7.7 Conclusions

In this chapter we have examined the implications of the MEPC 59/24/Add.1 Annex 9 (II) policy on engineering solutions to ensure pH recovery to 6.5 or higher at a distance of 4 m from the ship depends on the nozzle radius (b_0) and the alkalinity of the seawater (C_b^0) in which the ship operates. The number of ports (N) (arranged in a configuration for optimal entrainment as shown in figure 7.4) is then determined by the total discharge flux of the scrubber (Q_s). The practical challenge of introducing multiple ports can be met using a sea chest with circular holes. Further increases in the scrubber discharge flux (for instance 60 MW ships, in low alkalinity waters) can be met by additional dilution onboard the ship ($\mathcal{D}_{onboard}$). The detailed analysis has identified some specific issues related to compliance.

The scrubber discharge rises due to buoyancy and is also swept past the outlet nozzle by a flow induced by the propeller during the compliance test. This leads to a significant deflection of the discharge jet. Empirically measuring the jet dilution a distance of a jet radius from the jet centre line leads to an over estimation of dilution by a factor of 3-10 (see figure 3.13*b*) resulting in a pH difference of 1-1.5 units (see figure 7.3). The measurement of pH requires a small boat with someone collecting samples by drawing fluid from locations beneath the free surface. In order to get meaningful pH readings the jet position 4 m from the ship ($y = 4$ m) needs to be estimated (see figure 7.2). A number of samples need to be taken and time-averaged to account for the turbulent 'flapping' of the discharge. The accuracy of measuring the pH at a specific depth is problematic and requires calibrated and temperature corrected probes. An alternative method to validate the discharge port designs is to measure the temperature as a series of points along the discharge jet. The temperature measurements can be used to infer the dilution at 4 m and the pH determined from titration curves.

Chapter 8

Summary and conclusions

8.1 Introduction

The motivation for this thesis comes from current legislative discussion by the shipping industry on the use of open loop exhaust gas scrubbers and the discharge of acidic wash water into seawater. This technique is used to comply with air pollution related legislation that is becoming increasingly stringent. The focus was on IMO Regulation 14 that limits the amount of sulphur oxides and soot that ships may release into the atmosphere.

The purpose of this thesis was to provide a detailed examination of the physics of mixing and dilution of a continuous acidic discharge from a ship into seawater. A wide range of fluid mechanical and chemistry processes contribute to this, therefore, a number of techniques had to be covered. These included the development of a detailed fundamental analytical model (Chapter 2), design and undertaking of a programme of laboratory scale jet and plume experiments with acid-alkali reactions (Chapter 3) and the development, coding, validation and application of a CFD model from scratch (Chapters 4, 5 and 6). The result is an overview of the problem that could be used to advise industry and legislative bodies in the context of environmental legislation (Chapter 7).

8.2 Research questions

In response to the questions raised in Chapter 1 we can conclude with the following:

1. What processes affect the pH recovery in the ambient seawater?

In the near and mid fields where the discharge is still coherent as a jet or a plume, we argue in Chapter 2 that the pH recovery to the ambient state is due to a combination of dilution and chemistry. Dilution is caused by the fluid mechanical aspects, specifically entrainment of fluid, at the edges of the jet/plume. The process of neutralisation is the result of the chemical reactions between the acidic discharge and the weakly alkaline ambient seawater. Here the excess H^+ ions, introduced by the acid, are buffered by the carbonate ions (HCO_3^-; CO_3^{2-}) in seawater. The acid absorption capacity of seawater is not indicated in the pH because a significant amount of carbonate ions remain trapped in particulate form until their aqueous concentration drops.

An analytical model was developed in Chapter 2 to explore the pH recovery. The model showed that dilution is responsible for the initial increase in the discharge pH but the chemistry component becomes increasingly dominant as the point of neutralisation is approached. A detailed experimental study is described in Chapter 3 that was used to validate the analytical model. This process took two forms - the titration and dilution experiments of seawater and the measurement of neutralisation distance for a jet and a plume.

2. How is the trajectory of the discharge affected by buoyancy and cross flow?

A continuous tangential discharge to the direction of travel from a moving ship is affected both by cross flow and buoyancy. Due to the action of the Lamb force, the entrainment field causes the jet/plume to be accelerated in the streamwise direction, while buoyancy force causes it to rise. There are a number of integral models that could have been applied to understand the jet/plume dynamics, some of which include fictitious drag forces to account for entrainment. As with Woodhouse *et al.* (2013), we have included the two principle forces. A simple model for entrainment was selected that enables new closed form expressions to be derived to explain how jets/plumes behave in a cross flow. Focussing on horizontal injection, the majority of practical ship discharges, the discharge is momentum dominated and the analysis of Chapter 2 (§2.4.3) indicates that in the near field the deflection is characterised by $\tilde{y} \sim \sqrt{2}\tilde{x}^{1/2}/(\Lambda(1+\Lambda))^{1/2}$ and $\mathcal{D} \sim (1+\Lambda)\tilde{s}$. The influence of cross flow is to significantly increase entrainment leading to additional dilution in the jet. This results in a reduction of the neutralisation distance as described in Chapter 2 (§2.3.3) *i.e.* $\tilde{s}_n = \mathcal{D}/(1+\Lambda)$. The increase in dilution is gradually lost as the jet is bent towards the direction of the ambient flow.

3. What are the mixing processes in the ship wake?

In the far field, the discharge is ultimately swept into the ship wake and mixed. A major challenge in determining the dilution far downstream is to first determine the form of the flow and the width of the wake. A steadily moving ship is self-propelled and in this state, about 5% of the total drag is generated by the wave field. In a self-propelled state, the wake flow has special properties with the velocity deficit, and in particular the vorticity field, decaying extremely rapidly with distance downstream. To explore these processes, a CFD code was developed and validated in Chapter 5. The code was applied to analyse the wake development behind a ship shape model similar to that described in the experimental paper of Cimbala & Park (1990). Two types of calculations were developed based on either a constant turbulent viscosity model and a Spalart-Allmaras turbulent model closure. These calculations demonstrate that while there is a rapid decrease in the flow signature behind approximately self-propelled bodies, the growth of the wake width has a weak dependence on the state of propulsion and distance, at least in the near field. This means that after the rapid initial dilution of the discharge in the turbulence caused by propulsion additional dilution due to wake width growth is negligible in the near field. The dilution in the wake rapidly reaches $U_\infty A/Q_0$, which remains approximately constant over a distance of $x_1/D \sim 10$.

4. What are the design and engineering best practices for scrubber discharge nozzle sizes and configurations?

In Chapter 7 we create an optimisation problem and propose a number of solutions for scrubber discharges to comply with the regulation MEPC 59/24/Add.1 Annex 9. We show that the compliance tests in the case of measuring the pH of the discharge at 4 m from the point of discharge are sensitive to the position of the point of measurement due to the jet movement caused by buoyancy and deflection caused by the flow of the propeller. In our analysis the dilution of the discharge can be used to determine the point where the required pH of 6.5 is reached. Practical solutions to estimating dilution of the discharge at 4 m have been made, such as using temperature as a proxy for passive mixing.

8.3 Novelty

There are a number of aspects to the thesis which could be considered novel. These include:

1. Scientific assessment of IMO MEPC environmental legislation. The science behind acidic scrubber discharges is complex because it combines chemical and fluid mechanical aspects. The near field processes have been analysed in this thesis based on which practical engineering comments have been made in Chapter 7 and Ülpre & Eames (2014). The presentation based on this thesis titled 'Environmental policy constraints for acidic exhaust gas scrubber discharges from ships' was awarded the 'Most innovative topic' award at the Marine Technology Postgraduate Conference in 2014.

2. The combination of reversible chemistry with a jet/plume (described in Chapter 2) analysis is new. An experimental study was undertaken (see Chapter 3) to validate the theory and the analysis has been recently published (Ülpre *et al.*, 2013).

3. There are a great deal of literature on self-propelled wakes - both from the experimental and theoretical communities. Nearly all the computational studies have employed a prescribed velocity field to initialize the calculations (usually the Tennekes & Lumley (1972) self-propelled profile). Therefore, the new aspect in this thesis is the analysis of wakes behind a streamlined body that is either in an under-, self- or over-propelled state. As expected velocity and vorticity profiles in the wake vary significantly between the three modes but what was unexpected was that the wake width remained approximately constant.

8.4 Future work

Due to the broad scope of this project, a number of future research threads have been identified which could be taken forward:

1. In the natural environment, ambient turbulence is present and its effects on the spreading of the jet or plume in a cross flow should be considered. A recent experimental study by Khorsandi *et al.* (2013) showed that the entrainment

processes in the jet are reduced due to the presence of homogeneous and isotropic turbulence. The effect of ambient turbulence will lead to a rapid widening and flapping of the jet/plume. This will cause the jet/plume to reach a finite distance which is different from when there is no ambient turbulence (the jet/plume grows to infinity). Presently, the influence of a external turbulence is not included in the jet/plume models that are described in Chapter 2.

2. The analysis of the self-propelled state (in Chapter 6) was an unusually difficult challenge because of determining and reaching the self-propelled state computationally. From our analysis it is clear that the $F_D = F_T$ is not appropriate because of the introduction of a Lamb force due to the ejection of fluid by the ship and it is also clear that boundedness of the flow is important. These problems have also been encountered in experimental work on self-propelled wakes. A lot of studies use a momentum thickness measure or observations to determine the self-propelled state. The starting point should be the development of an automatic method for reaching the self-propelled state.

8.5 Concluding remarks

Environmental policy is inherently a very difficult topic to tackle in a manner that can be achievable met by the industry in the given time frame. Expertise from various fields is necessary in order to provide a complete picture of the problem as was demonstrated in this thesis, *e.g.* fluid mechanics, chemistry, numerics. Flexibility should be exercised from regulatory and industry bodies to revise legislation if desired environmental goals are not being achieved in a reasonable manner.

Bibliography

Abel, N.H. 1826 Auflösung einer mechanischen Aufgabe. *J. für die Reine & Angew. Math.* **1**, 153–157.

Arora, S.C. & Domkundwar, S. 1997 *A course in power plant engineering*. Delhi, India: Dhanpat Rai & Sons.

Atkins, P.W. & De Paula, J. 2006 *Atkins' Physical Chemistry*. Oxford, UK: Oxford Univ. Press.

Baines, W.D. 1983 A technique for the direct measurement of volume flux of a plume. *J. Fluid Mech.* **132**, 247–256.

Batchelor, G.K. 2001 *An introduction to fluid dynamics*. Cambridge, UK: Cambridge University Press.

Behrends, B., Liebezeit, G. & Hufnagl, M. 2005 *Effects on seawater scrubbing*. UK: BP Marine/Research Centre Terramare.

Bell, H.L. & Nebeker, A.V. 1969 Preliminary studies on the tolerance of aquatic insects to low pH. *J. Kansas Entomol. Soc.* **42**, 230–236.

Betz, A. 1925 Ein verfahren zur direkten ermittlung des profilwiderstandes. *Z. Flugtechn. Motorluftschiffahrt* **16**, 42–44.

Bisset, D.K., Hunt, J.C.R. & Rogers, M.M. 2002 The turbulent/non-turbulent interface bounding a far wake. *J. Fluid Mech.* **451**, 383–410.

Blatcher, D.J. & Eames, I. 2013 Compliance of Royal Navy ships with nitrogen oxide emissions legislation. *Mar. Pollut. Bull.* **74**, 10–18.

Blevins, R.D. 1990 *Flow-induced vibrations*. New York, USA: Van Nostrand-Reinhold.

Boussinesq, J. 1903 *Théorie analytique de la chaleur, Vol. 2*. Paris: Gauthier-Villars.

Brønsted, J.N. 1923 Some remarks on the concept of acids and bases. *Recl. Trav. Chim. des Pays-Bas* **42**, 718–728.

Byrne, C.D., Law, R.J., Hydson, P.M., Thain, J.E. & Fileman, T.W. 1988 Measurements of the dispersion of liquid industrial waste discharged into the wake of a dumping vessel. *Water Res.* **22**, 1577–1584.

Campbell, A.N. & Cardoso, S.S.S. 2010 Turbulent plumes with internal generation of buoyancy by chemical reaction. *J. Fluid Mech.* **655**, 122–151.

Cardoso, S.S.S. & McHugh, S.T. 2010 Turbulent plumes with heterogeneous chemical reaction on the surface of small buoyant droplets. *J. Fluid Mech.* **642**, 49–77.

Carlotti, P. & Hunt, G.R. 2005 Analytical solutions for turbulent non-Boussinesq plumes. *J. Fluid Mech.* **538**, 343–359.

Casagrande, D.J. 1987 Sulphur in peat and coal. *Geological Society, London, Special Publications* **32**, 87–105.

Chou, H.-T. 1996 On the dilution of liquid waste in ships' wakes. *J. Mar. Sci. Technol.* **1**, 149–154.

Cimbala, J.M. & Park, W.J. 1990 An experimental investigation of the turbulent structure in a two-dimensional momentumless wake. *J. Fluid Mech.* **213**, 479–509.

Coelho, S.L.V. & Hunt, J.C.R. 1989 Vorticity dynamics of the near field of strong jets in cross flow. *J. Fluid Mech.* **200**, 95–120.

Conroy, D.T. & Llewellyn-Smith, G. 2008 Endothermic and exothermic chemically reacting plumes. *J. Fluid Mech.* **612**, 291–310.

Corriveau, A.F. & Baines, W.D. 1993 Diffusive mixing in turbulent jets as revealed by a pH indicator. *Experiments in Fluids* **16**, 129–136.

da Silva, C.B., Hunt, J.C.R., Eames, I. & Westerweel, J. 2014 Interfacial layers between regions of different turbulence intensity. *Annu. Rev. Fluid Mech.* **46**, 567–590.

Dahl, J.B. & Tollan, O. 1972 *Measurement of dilution of tank waste water in the wake of M/T 'Esso Bergen'*. Kjeller, Norway: Institute for Atomic Energy.

Dahl, J.B. & Tollan, O. 1973 *Dilution in the ship's wake of tank washings released from M/T 'Esso Slagen'*. Kjeller, Norway: Institute for Atomic Energy.

Dahl, J.B. & Tollan, O. 1975 *Measurement of the dilution of tank washings in the wake of M/T 'Esso Slagen'*. Kjeller, Norway: Institute for Atomic Energy.

Darmon, A., Benzaquen, M. & Raphaël, E. 2014 Kelvin wake pattern at large Froude numbers. *J. Fluid Mech.* **738**, 1–8.

Davidson, G.A. 1986 Gaussian versus top-hat profile assumptions in integral plume models. *Atmospheric Environment* **3**, 471–478.

Davidson, P.A. 2003 *Turbulence: An introduction for scientists and engineers*. Cambridge, UK: Cambridge University Press.

Delaunay, B. 1934 Sur la sphère vide. A la mémoire de Georges Voronoï. *Bulletin de l'Académie des Sciences de l'URSS. Classe des sciences mathématiques et na* **6**, 793–800.

Delvigne, G.A.L. 1983 *North Sea experiments on wake dilution capacity of dumping tankers*. Delft, Netherlands: Waterloopkundig Laboratorium.

Diamessis, P.J., Spedding, G.R. & Domaradzki, J.A. 2011 Similarity scaling and vorticity structure in high-Reynolds-number stably stratified turbulent wakes. *J. Fluid Mech.* **671**, 52–95.

Dias, F. 2014 Ship waves and Kelvin. *J. Fluid Mech.* **746**, 1–4.

Dimotakis, P.E. & Brown, G.L. 1976 The mixing layer at high Reynolds number: large-structure dynamics and entrainment. *J. Fluid Mech.* **78**, 535–560.

Dong, R.R., Katz, J. & Huang, T.T. 1997 On the structure of bow waves on a ship model. *J. Fluid Mech.* **346**, 77–115.

Drever, J.I. 1988 *The geochemistry of natural waters*. Toronto, CA: Prentice-Hall.

Eames, I. & Hunt, J.C.R. 2004 Forces on bodies moving in rapidly compressed flows. *J. Fluid Mech.* **505**, 349–364.

Eames, I., Johnson, P.B., Roig, V. & Risso, F. 2011*a* Effect of turbulence on the downstream velocity deficit of a rigid sphere. *Phys. Fluids* **23**, 095103.

Eames, I., Jonsson, C. & Johnson, P.B. 2011*b* The growth of a cylinder wake in turbulent flow. *J. Turbul.* **12**, 1–16.

Eigen, M. 1954 Methods for investigation of ionic reactions in aqueous solutions with half-times as short as 10^{-9}sec. *Discuss. Faraday Soc.* **17**, 194–205.

Fan, L.-N. 1967 *Turbulent buoyant jets into stratified or flowing ambient fluids*. Tech. Rep. No. KH-R-18: W. M. Keck Lab. Hydraul. & Water Res., Calif. Inst. Tech. Pasadena, Calif. 104.

Frankignoulle, M. 1994 A complete set of buffer factors for acid/base CO_2 system in seawater. *J. Mar. Syst.* **5**, 111–118.

Gertler, M. 1954 A reanalysis of the original test data for the Taylor standard series. *David Taylor Model Basin Rep.* p. 806.

Ghia, U., Ghia, K.N. & Shin, C.T. 1982 High-Re solutions for incompressible flow using the Navier-Stokes equations and a multigrid method. *J. Comp. Phys.* **48**, 387–411.

Gordus, A.A. 1985 *Theory and problems of analytical chemistry*. New York, N.Y.: McGraw-Hill.

Graff, W., Kracht, A. & Weinblum, G. 1964 Extensions of D.W. Taylor's standard series. *Trans. Soc. Nav. Architects Mar. Eng.* **72**, 374.

Hansen, J. & Nazarenko, L. 2004 Soot climate forcing via snow and ice albedos. *Proc. Nati. Acad. Sci.* **101** (2), 423–428.

Hirsch, C. 2007 *Numerical computation of internal and external flows. The fundamentals of computational fluid dynamics*. Oxford; Burlington, MA: Elsevier/Butterworth-Heinemann.

Hunt, G.R. & van den Bremer, T.S. 2011 Classical plume theory: 1937-2010 and beyond. *IMA J. App. Math.* **76**, 424–448.

Hunt, G.R. & Kaye, N.G. 2001 Virtual origin correction for lazy turbulent plumes. *J. Fluid Mech.* **435**, 377–396.

Hunt, G.R. & Kaye, N.B. 2005 Lazy plumes. *J. Fluid Mech.* **533**, 329–338.

Hunt, G.R. & Linden, P.F. 2001 Steady-state flows in an enclosure ventilated by buoyancy forces assisted by wind. *J. Fluid Mech.* **426**, 355–386.

Hunt, J.C.R. 1999 Environmental forecasting and turbulence modeling. *Physica D* **133**, 270–295.

Hunt, J.C.R., Eames, I., da Silva, C.B. & Westerweel, J. 2011 Interfaces and inhomogeneous turbulence. *Philos. Trans. A Math. Phys. Eng. Sci.* **369**, 811–832.

Hunt, J.C.R., Eames, I. & Westerweel, J. 2006 Mechanics of inhomogeneous turbulence and interfacial layers. *J. Fluid Mech.* **554**, 499–519.

ICES 2011 *Dataset on Ocean Hydrography*. Copenhagen: The International Council for the Exploration of the Sea.

Jacobson, M.Z. 2010 Short-term effects of controlling fossil-fuel soot, biofuel soot and gases, and methane on climate, Arctic ice, and air pollution health. *J. Geophysical Research* **115** (D14), D14209.

Jirka, G.H. 2004 Integral model for turbulent buoyant jets in unbounded stratified flows. Part I: Single round jet. *Env. Fluid Mech.* **4**, 1–56.

Kaminski, E., Tait, S. & Carazzo, G. 2005 Turbulent entrainment in jets with arbitrary buoyancy. *J. Fluid Mech.* **526**, 361–376.

Kaye, N.B. 2008 Turbulent plumes in stratified environments: A review of recent work. *Atmosphere-Ocean* **46**, 433–441.

Key, R.M., Kozyr, A., Sabine, C.L., Lee, K., Wanninkhof, R., Bullister, J.L., Feely, R.A., Millero, F.J., Mordy, C. & Peng, T.H. 2004 A global ocean carbon climatology: Results from GLODAP. *Global Biogeochemical Cycles* **18**, GB4031.

Khorsandi, B., Gaskin, S. & Mydlarski, L. 2013 Effect of background turbulence on an axisymmetric turbulent jet. *J. Fluid Mech.* **736**, 250–286.

Kitamura, Y. & Itoh, T. 1987 Reaction volume of protonic ionization for buffering agents. Prediction of pressure dependence on pH and pOH. *J. Sol. Chem.* **16**, 715–725.

Klettner, C. 2010 *On the fundamental principles of waves propagating over complex geometry*. University College London: Doctoral thesis.

Knutzen, J. 1981 Effects of decreased pH on marine organisms. *Mar. Pollut. Bull.* **12**, 25–29.

Krivchenko, G.I. 1994 *Hydraulic machines: Turbines and pumps*. FL, USA: Lewis Publishers.

Lamb, H. 1932 *Hydrodynamics*. Cambridge, UK: Cambridge University Press.

Lewis, R.E. 1985 The dilution of waste in the wake of a ship. *Water Res.* **19**, 941–945.

Lewis, R.W., Nithiarasu, P. & Seetharamu, K.N. 2004 *Fundamentals of the finite element method for heat and fluid flow*. Chichester, UK: John Wiley & Sons, Ltd.

Lide, D. 2004 *CRC handbook of chemistry and physics : a ready-reference book of chemical and physical data*. Boca Raton, Fla.: CRC Press.

Linden, P.F. 2011 The efficiency of pulsed-jet propulsion. *J. Fluid Mech.* **668**, 1–4.

List, E.J. 1982 Turbulent jets and plumes. *Annu. Rev. Fluid Mech.* **14** (1), 189–212.

Lomax, H., Pulliam, T.H. & Zingg, D.W. 2001 *Fundamentals of computational fluid dynamics*. Toronto, Canada: Springer.

Lowry, T.M. 1923 The uniqueness of hydrogen. *Chem. and Ind.* **42**, 43–47.

MARINTEK 2006 Washwater criteria for sea water exhaust gas SOx scrubbers. *Norwegian Marine Technology Research Institute report to Norwegian Shipowners' Association/Research Council of Norway* .

Maxworthy, T. 1972 The structure and stability of vortex rings. *J. Fluid Mech.* **51**, 15–32.

Maxworthy, T. 1974 Turbulent vortex rings. *J. Fluid Mech.* **64**, 227–240.

Maxworthy, T. 1977 Some experimental studies of vortex rings. *J. Fluid Mech.* **81**, 465–495.

McNaughton, K.J. & Sinclair, C.G. 1966 Submerged jets in short cylindrical flow vessels. *J. Fluid Mech.* **25**, 367–375.

Meunier, P. & Spedding, G.R. 2006 Stratified propelled wakes. *J. Fluid Mech.* **552**, 229–256.

Morton, B.R. 1959 Forced plumes. *J. Fluid Mech.* **5**, 151–163.

Morton, B.R. 1967 Entrainment models for laminar jets, plumes, and wakes. *Physics of Fluids* **10**, 2120–2127.

Morton, B.R., Taylor, G. & Turner, J.S. 1956 Turbulent gravitational convection from maintained and instantaneous sources. *Proc. Roy. Soc. London* **234A**, 1–23.

Nicolle, A. 2009 *Flow through and around groups of bodies*. University College London: Doctoral thesis.

Nicolle, A. & Eames, I. 2011 Numerical study of fluid flow through and around a circular array of cylinders. *J. Fluid Mech.* **679**, 1–31.

Pope, S.B. 2000 *Turbulent flows*. Cambridge, UK: Cambridge University Press.

Prandtl, L. 1925 Magnuseffekt und Windkraftschiff. *Die Naturwissenschaften* **13**, 93–108.

Prandtl, L. 1954 *Essentials of fluid mechanics*. Glasgow: Blackie.

Raja, A.K., Srivastava, A.P. & Dwivedi, M. 2006 *Power plant engineering*. New Delhi, India: New Age International.

Raven, J., Caldeira, K., Elderfield, H., Hoegh-Guldberg, O., Liss, P., Riebesell, U., Shepherd, J., Turley, C. & Watson, A. 2005 Ocean acidification due to increasing atmospheric carbon dioxide. *The Royal Society* .

Redford, J.A., Castro, I.P. & Coleman, G.N. 2012 On the universality of turbulent axisymmetric wakes. *J. Fluid Mech.* **710**, 419–452.

Reichardt, H. 1941 Über eine neue Theorie der freien Turbulenzen. *ZAMM* **21**, 257–264.

Reichardt, H. 1942 Gesetzmäßigkeiten der freien Turbulenzen. *VDI-Forschungsheft* **414**.

Reynolds, O. 1873 The causes of the racing of the engine of screw streamers investigated theoretically and by experiment. *Trans. Inst. Naval Arch.* **14**, 56–63.

Ricou, F.P. & Spalding, D.B. 1961 Measurements of entrainment by axisymmetrical turbulent jets. *J. Fluid Mech.* **11**, 21–32.

Rind, E. & Castro, I.P. 2012 Direct numerical simulation of axisymmetric wakes embedded in turbulence. *J. Fluid Mech.* **710**, 482–504.

Roshko, A. 1961 Experiments on the flow past a circular cylinder at very high Reynolds number. *J. Fluid Mech.* **10**, 345–356.

Scase, M.M., Caulfield, C.P. & Dalziel, S.B. 2006*a* Boussinesq plumes and jets with decreasing source strengths in stratified environments. *J. Fluid Mech.* **563**, 463–472.

Scase, M.M., Caulfield, C.P., Dalziel, S.B. & Hunt, J.C.R. 2006*b* Time-dependent plumes and jets with decreasing source strengths. *J. Fluid Mech.* **563**, 443–461.

Schäfer, M. & Turek, S. 1996 Benchmark computations of laminar flow around a cylinder. *Notes on Numerical Fluid Mechanics* **52**, 547–566.

Schindler, D.W. 1988 Effects of acid rain on freshwater ecosystems. *Science.* **239** (4836), 149–157.

Secondo, C. 1935 *Reaction-propulsion method and plant*. U.S. Patent 2024274.

Shewchuk, J.R. 1996 Triangle: Engineering a 2D quality mesh generator and Delaunay triangulator. *Applied Computational Geometry: Towards Geometric Engineering* **1148**, 203–222.

Singh, S.P. & Mittal, S. 2005 Flow past a cylinder: shear layer instability and drag crisis. *Int. J. Numer. Meth. Fluids* **47**, 75–98.

Sørensen, S.P.L. 1909 Enzymstudien II: uber die Messung und die Bedeutung der Wasserstoffionenkonzentration bei enzymatischen Prozessen. *Biochem. Zeit.* **21**, 131–200.

Spalart, P.R. & Allmaras, S.R. 1992 A one-equation turbulence model for aerodynamic flows. *AIAA* **92**, 0439.

Tanaka, M., Girard, G., Davis, R. & Peuto, A. 2001 Recommended table for the density of water between 0 ^{o}C and 40 ^{o}C based on recent experimental reports. *Metrologia* **38**, 301–309.

Tennekes, H. & Lumley, J.L. 1972 *A first course in turbulence*. Cambridge, Massachusetts and London, England: The MIT Press.

Trent, L.L., Hestand, R.S. III & Carter, C.C. 1978 Toxicity of sulfuric acid to aquatic plants and organisms. *J. Aquat. Plant Manage.* **16**, 40–43.

Turner, J.S. 1969 Buoyant plumes and thermals. *Annu. Rev. Fluid Mech.* **1**, 29–44.

Turner, J.S. 1973 *Buoyancy effects in fluids*. Cambridge, UK: Cambridge Univ. Press.

Ülpre, H. & Eames, I. 2014 Environmental policy constraints for acidic exhaust gas scrubber discharges from ships. *Mar. Pollut. Bull.* **88**, 292–301.

Ülpre, H., Eames, I. & Greig, A. 2013 Turbulent acidic jets and plumes injected into an alkaline environment. *J. Fluid Mech.* **734**, 253–274.

USEPA 2013 *Exhaust gas scrubber washwater effluent*. Washington, DC, USA: Bibliogov.

Van Den Bremer, T.S. & Hunt, G.R. 2010 Universal solutions for Boussinesq and non-Boussinesq plumes. *J. Fluid Mech.* **644**, 165–192.

Velten, K. 2008 *Mathematical modeling and simulation: Introduction for scientists and engineers*. Weinheim, Germany: Wiley VCH.

Versteeg, H.K. & Malalasekera, W. 2007 *An introduction to computational fluid dynamics: The finite volume method*. Harlow, UK: Pearson Prentice Hall.

Wang, C., Dong, S. & Munoz, E. 2010 Seawater density variations in the North Atlantic and the Atlantic meridional overturning cirulation. *Clim. Dyn.* **34**, 953–968.

Westerweel, J., Fukushima, C., Pedersen, J.M. & Hunt, J. C.R. 2005 Mechanics of the turbulent-nonturbulent interface of a jet. *Phys. Rev. Lett.* **95**, 174501.

Westerweel, J., Fukushima, C., Pedersen, J.M. & Hunt, J. C.R. 2009 Momentum and scalar transport at the turbulent/non-turbulent interface of a jet. *J. Fluid Mech.* **631**, 199–230.

Wilcox, D.C. 1994 *Turbulence modeling for CFD*. Anaheim, CA: DCW Industries.

Williamson, C.H.K. 1996 Vortex dynamics in the cylinder wake. *Annu. Rev. Fluid Mech.* **28**, 477–539.

Woodhouse, M.J., Hogg, A.J., Phillips, J.C. & Sparks, R.S.J. 2013 Interaction between volcanic plumes and wind during the 2010 Eyjafjallajökull eruption, Iceland. *J. Geophys. Res. Solid Earth* **118**, 92–109.

Woods, A.W. 1997 A note on non-Boussinesq plumes in an incompressible stratified environment. *J. Fluid Mech.* **345**, 347–356.

Woods, A.W. 2010 Turbulent plumes in nature. *Annu. Rev. Fluid Mech.* **42**, 391–412.

Appendix A

Titration procedure for acidified seawater

The important element to processing the experimental data (see table A.1) is that the number of moles of acid must be tracked as the acidified seawater is diluted. In step 1, two 10 ml samples are removed from the beaker and 56 ml of unacidified seawater are added. In step 2, two 10 samples are again removed and 70 ml of unacidified seawater is added. The reason for taking out two 10 ml samples is that each one of them can be titrated against a strong base allowing for the calculation of the mean value. The pH is calculated from

$$\text{pH} = -log_{10}\left(\frac{V_b}{1000} \times C_b\right), \tag{A.1}$$

where V_b is the volume of NaOH added in ml and C_b is the molar concentration of NaOH solution in mol/l. The example calculations are performed with the assumption that the added litmus solution had a neutral pH. A flowchart of the procedure can be found on the following page.

step	0	1	2
beaker (ml)	114	$114 - 20 + 56 = \text{A}$	$\text{A} - 20 + 70 = \text{B}$
acid/total (ml)	$\frac{4}{114} = \text{C}$	$\frac{114\times\text{C}-20\times\text{C}}{\text{A}} = \text{D}$	$\frac{\text{A}\times\text{D}-20\times\text{D}}{\text{B}} = \text{E}$
D	$\text{C}/\text{C} - 1$	$\text{C}/\text{D} - 1$	$\text{C}/\text{E} - 1$
NaOH (ml)	17.05	8.85	5.30
pH	3.45	3.73	3.95

Table A.1: Example calculation of D and pH from experimental data.

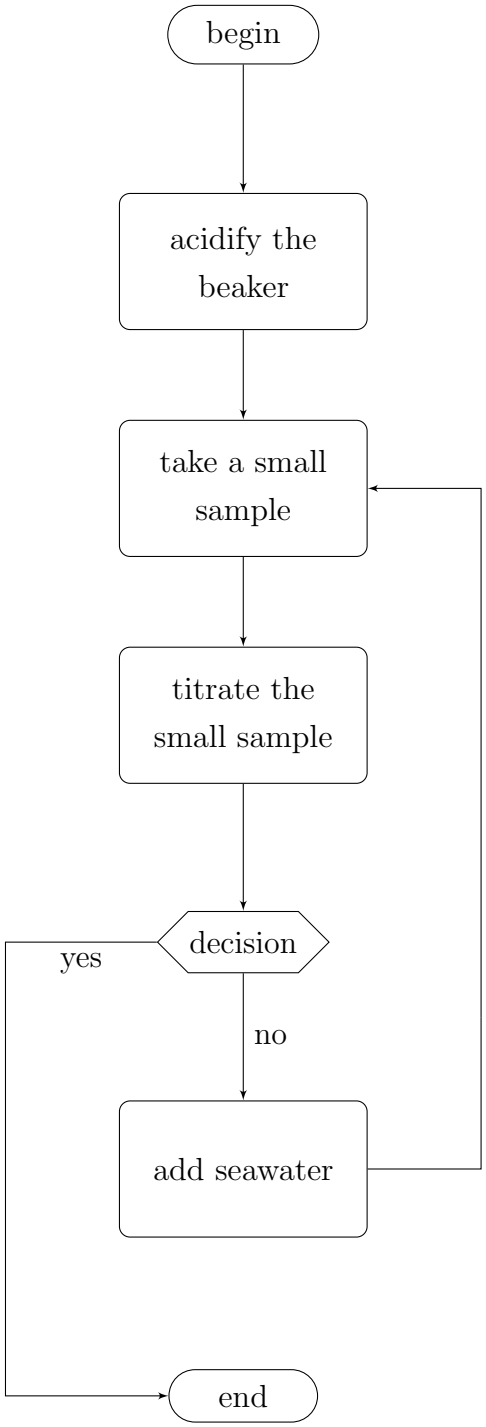

Prepare a 100 ml sample of seawater in a glass beaker and add 10 ml of litmus solution.

Add 4 ml of 1 mol/l monoprotic strong acid resulting in a total volume of 114 ml.

Take a two 10 ml samples from the beaker reducing the total volume to 94 ml.

Titrate the 10 ml sample against a strong base. Record the amount of base added for the litmus dye within the small sample to turn blue.

Is the sample blue without the need to titrate against a strong base?

Dilute the solution in the beaker by adding more unacidified seawater and if the litmus solution becomes too dilute then record the volume added.

The recorded volumes of acid, seawater, litmus and alkali can now be processed.

Appendix B

Axisymmetric formulation

The following formulation is similar to the one in Nicolle & Eames (2011) where the Navier-Stokes equation for an axisymmetric flow (u_r, u_z) is

$$\rho\left(\frac{\partial u_r}{\partial t}+u_r\frac{\partial u_r}{\partial r}+u_z\frac{\partial u_r}{\partial z}\right)=-\frac{\partial p}{\partial r}+\mu\left(\frac{1}{r}\frac{\partial}{\partial r}\left(r\frac{\partial u_r}{\partial r}\right)+\frac{\partial^2 u_r}{\partial z^2}\right)-\frac{u_r}{r^2},$$

$$\rho\left(\frac{\partial u_z}{\partial t}+u_r\frac{\partial u_z}{\partial r}+u_z\frac{\partial u_z}{\partial z}\right)=-\frac{\partial p}{\partial z}+\mu\left(\frac{1}{r}\frac{\partial}{\partial r}\left(r\frac{\partial u_z}{\partial r}\right)+\frac{\partial^2 u_z}{\partial z^2}\right),$$

where r is the radial and z is the axial position. The mass conservation equation can be written as

$$\frac{1}{r}\frac{\partial}{\partial r}(ru_r)+\frac{\partial u_z}{\partial z}=0.$$

In the CBS scheme a set of linear basis functions, $[\boldsymbol{N}]=[N_i,N_j,N_k]$, are introduced which depend on z and r. Within each element the velocity and pressure components are $u_z=[\boldsymbol{N}]\{\boldsymbol{u}_z\}$ and $u_r=[\boldsymbol{N}]\{\boldsymbol{u}_r\}$ and they vary as $\partial[\boldsymbol{N}]/\partial r=\boldsymbol{b}/2A_e$ and $\partial[\boldsymbol{N}]/\partial z=\boldsymbol{c}/2A_e$ across the area of the local element A_e. As described in §5 the CBS scheme is solved numerically in three step:

Step 1: Momentum step

$$[\boldsymbol{M}]\frac{\tilde{\boldsymbol{u}}_r-\boldsymbol{u}_r^{(n)}}{\Delta t}=-[\boldsymbol{C}]\{\boldsymbol{u}_r\}^{(n)}-\nu[\boldsymbol{K}]\{\boldsymbol{u}_r\}^{(n)}-\frac{\nu}{r^2}[\boldsymbol{M}]\{\boldsymbol{u}_r\}^{(n)}-[\boldsymbol{K}_s]\{\boldsymbol{u}_r\}^{(n)}+\nu[\boldsymbol{F}]\{\boldsymbol{u}_r\}^{(n)},\tag{C1}$$

and

$$[\boldsymbol{M}]\frac{\tilde{\boldsymbol{u}}_z-\boldsymbol{u}_z^{(n)}}{\Delta t}=-[\boldsymbol{C}]\{\boldsymbol{u}_z\}^{(n)}-\nu[\boldsymbol{K}]\{\boldsymbol{u}_z\}^{(n)}-[\boldsymbol{K}_s]\{\boldsymbol{u}_z\}^{(n)}+\nu[\boldsymbol{F}]\{\boldsymbol{u}_z\}^{(n)}.\tag{C2}$$

Step 2: Pressure step

$$[\boldsymbol{K}]\{\boldsymbol{p}\}^{(n+1)} = -\frac{\rho}{\Delta t}\bigg([\boldsymbol{G}_r]\{\tilde{\boldsymbol{u}}_r\} + \frac{1}{r}[\boldsymbol{M}]\{\tilde{\boldsymbol{u}}_r\} + [\boldsymbol{G}_z]\{\tilde{\boldsymbol{u}}_z\}\bigg) + [\boldsymbol{F}]\{\boldsymbol{p}\}.$$

Step 3: Velocity correction step

$$[\boldsymbol{M}]\{\boldsymbol{u}_r\}^{(n+1)} = [\boldsymbol{M}]\{\tilde{\boldsymbol{u}}_r\} - \frac{\Delta t}{\rho}[\boldsymbol{G}_r]\{\boldsymbol{p}\}^{(n+1)},$$

and

$$[\boldsymbol{M}]\{\boldsymbol{u}_z\}^{(n+1)} = [\boldsymbol{M}]\{\tilde{\boldsymbol{u}}_z\} - \frac{\Delta t}{\rho}[\boldsymbol{G}_z]\{\boldsymbol{p}\}^{(n+1)}.$$

The matrices and vectors in the above steps are:

$$[\boldsymbol{M}] = \frac{2\pi r A}{12}\begin{bmatrix} 2 & 1 & 1 \\ 1 & 2 & 1 \\ 1 & 1 & 2 \end{bmatrix}, \quad [\boldsymbol{C}] = \frac{[\boldsymbol{M}]}{2A}\bigg(\{\boldsymbol{u}_r\}\{\boldsymbol{b}\} + \{\boldsymbol{u}_z\}\{\boldsymbol{c}\}\bigg),$$

$$[\boldsymbol{K}_s] = \frac{[\boldsymbol{M}]\{\boldsymbol{u}_r\}\Delta t}{8A^2}\bigg[\{\boldsymbol{u}_r\}^T\boldsymbol{b}^T\boldsymbol{b} + \{\boldsymbol{u}_z\}^T\boldsymbol{b}^T\boldsymbol{c}\bigg] + \frac{[\boldsymbol{M}]\{\boldsymbol{u}_z\}\Delta t}{8A^2}\bigg[\{\boldsymbol{u}_r\}^T\boldsymbol{c}^T\boldsymbol{b} + \{\boldsymbol{u}_z\}^T\boldsymbol{c}^T\boldsymbol{c}\bigg]$$

$$[\boldsymbol{K}] = \frac{2\pi r}{4A}\bigg[\boldsymbol{b}^T\boldsymbol{b} + \boldsymbol{c}^T\boldsymbol{c}\bigg], [\boldsymbol{G}_r] = 2\pi r\begin{bmatrix}1\\1\\1\end{bmatrix}\boldsymbol{b}, [\boldsymbol{G}_z] = 2\pi r\begin{bmatrix}1\\1\\1\end{bmatrix}\boldsymbol{c}, [\boldsymbol{G}_{r2}] = 2\pi\begin{bmatrix}1\\1\\1\end{bmatrix}\boldsymbol{b}.$$

The forcing term is

$$[\boldsymbol{F}] = \frac{1}{2A}\int_{\Gamma_e}\bigg(\boldsymbol{N}^T n_1 \mathrm{d}\Gamma\boldsymbol{b} + \boldsymbol{N}^T n_2 \mathrm{d}\Gamma\boldsymbol{c}\bigg),$$

where Γ_e is a boundary element. Dirichlet boundary conditions are used where values are stenciled into the global $[\boldsymbol{M}]$ and $[\boldsymbol{K}]$ matrices.

Appendix C

Spalart Allmaras turbulence model

This is a one equation turbulence model for turbulent viscosity (Spalart & Allmaras, 1992) that is implemented as shown in §5 equation (5.13). The turbulent viscosity is given as

$$\nu_t = \tilde{\nu} f_{v1}, \tag{C.1}$$

where

$$f_{v1} = \frac{X^3}{X^3 + c_{v1}^3}, \quad X \equiv \frac{\tilde{\nu}}{\nu}. \tag{C.2}$$

The term $\tilde{\nu}$ is a variable defined by

$$\frac{\mathrm{D}\tilde{\nu}}{\mathrm{D}t} = P - D + \frac{1}{\sigma}\left[\nabla \cdot ((\nu + \tilde{\nu})\nabla\tilde{\nu}) + c_{b2}(\nabla\tilde{\nu})^2\right], \tag{C.3}$$

where P and D are the production and wall destruction terms, *e.g.*

$$P = c_{b1}(1 - f_{t2})\tilde{S}\tilde{\nu}, \quad D = \left(c_{w1} f_w - \frac{c_{b1}}{k^2} f_{t2}\right)\left(\frac{\tilde{\nu}}{d}\right)^2. \tag{C.4}$$

The laminar suppression term f_{t2} is

$$f_{t2} = c_{t3} \exp(-c_{t4} X^2), \tag{C.5}$$

and the modified vorticity term $\tilde{S}$ is

$$\tilde{S} \equiv S + \frac{\tilde{\nu}}{k^2 d^2} f_{v2}, \tag{C.6}$$

where

$$f_{v2} = 1 - \frac{X}{1 + X f_{v1}}. \tag{C.7}$$

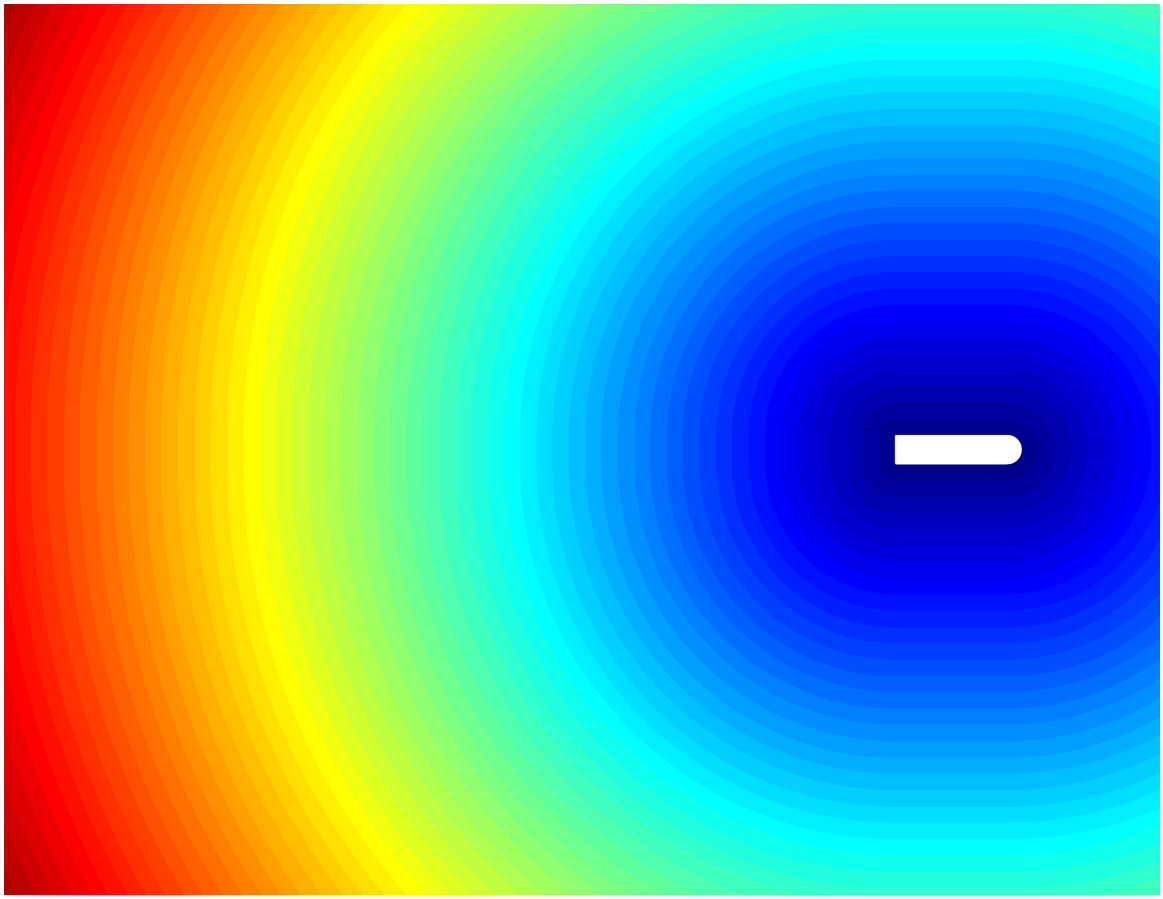

Figure C.1: The wall distance, d, variation with distance from the ship. It is used to scale the magnitude of the vorticity destruction term in the SA turbulence model. At the edges of the ship, wall distance is set to 0 and it increases linearly with distance to the edges of the domain where it reaches 18.7.

S is the vorticity magnitude and d is the wall distance. Wall distance variation is illustrated for the domain with the ship shaped object in figure C.1. Additionally,

$$f_w = g\left(\frac{1+c_{w3}^6}{g^6+c_{w3}^6}\right)^{1/6}, \tag{C.8}$$

where

$$g = r + c_{w2}(r^6 - r), \quad r = \min\left(\frac{\tilde{\nu}}{\tilde{S}k^2d^2}, r_{lim}\right). \tag{C.9}$$

The constants are $c_{b1} = 0.1355$, $\sigma = 2/3$, $c_{v2} = 0.622$, $k = 0.41$, $c_{w1} = c_{b1}/k^2 + (1 + c_{b2})/\sigma$, $c_{w2} = 0.3$, $c_{w3} = 2$, $c_{v1} = 7.1$, $c_{t3} = 1.2$, $c_{t4} = 0.5$ and $r_{lim} = 10$.

Appendix D

Wake calculation meshes

The meshes in figures D.1 and D.2 were generated with Gmsh (`http://geuz.org/gmsh/`). They were used in the calculations in Chapter 6. In the axisymmetric case half the domain in figure D.2 is used. The split is made across the horizontal centre line.

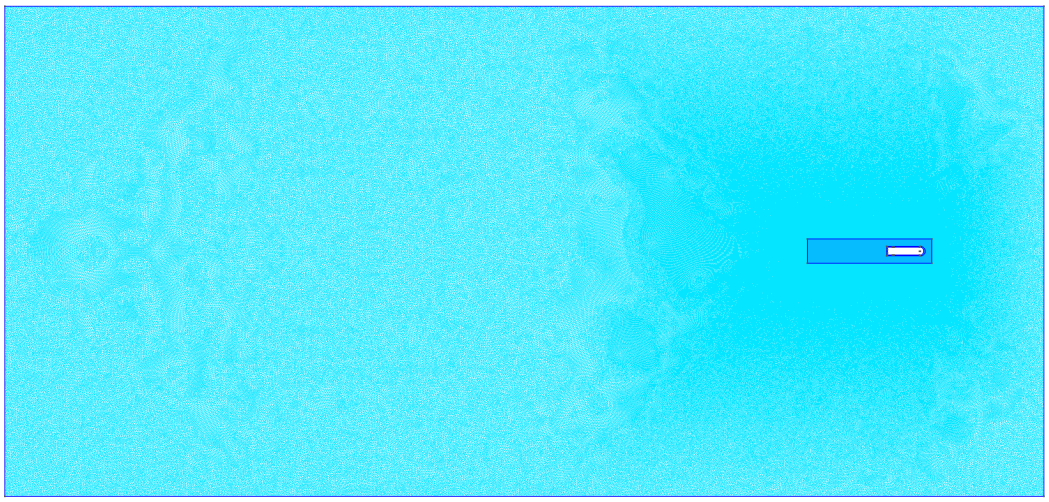

Figure D.1: The mesh used in the planar wake case for $Re_T = 10$. It consists of 434384 nodes and 873807 triangular elements.

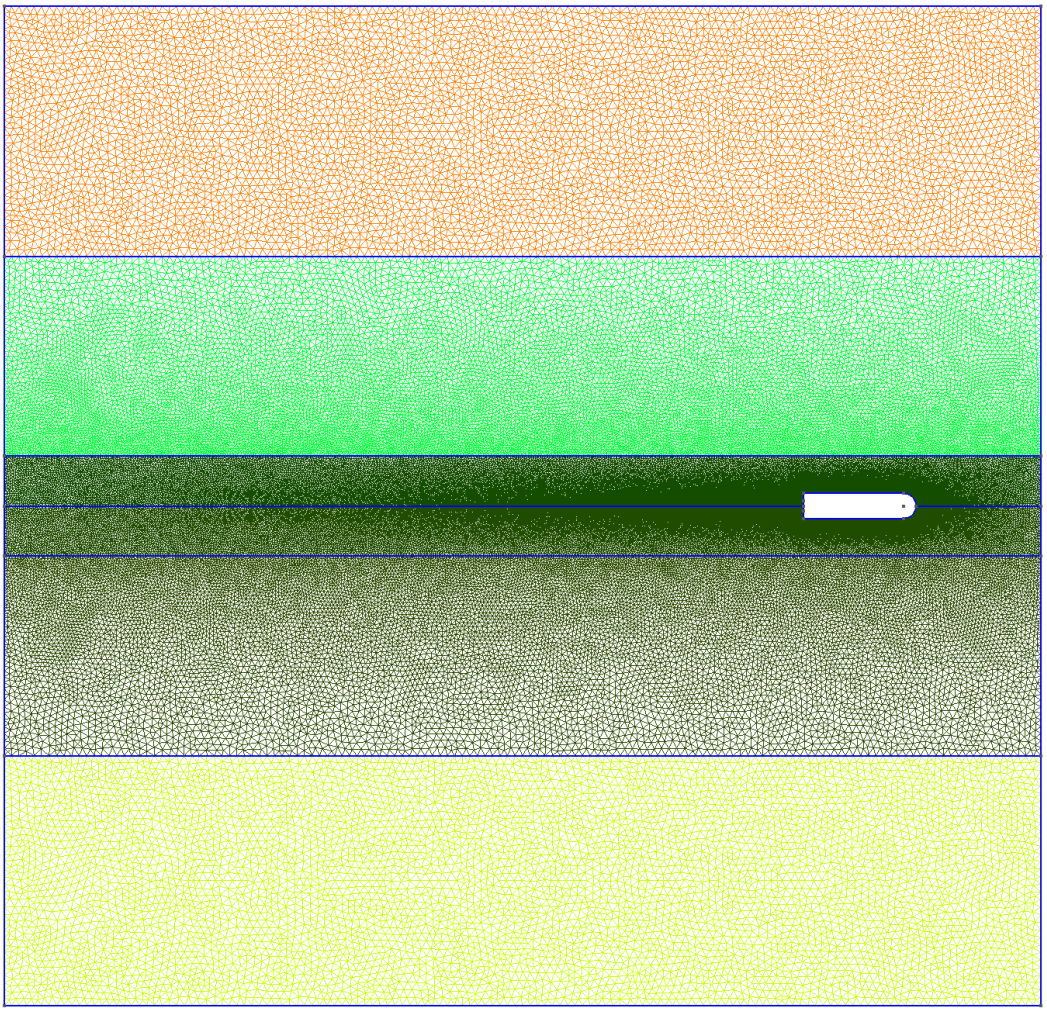

Figure D.2: The mesh used in the planar wake with the SA turbulence model case. It consists of 96867 nodes and 199528 triangular elements.

Appendix E

Vorticity fields across the wake

The vorticity fields in figures E.1, E.2, E.3 and E.4 correspond to the computational analysis in Chapter 6.

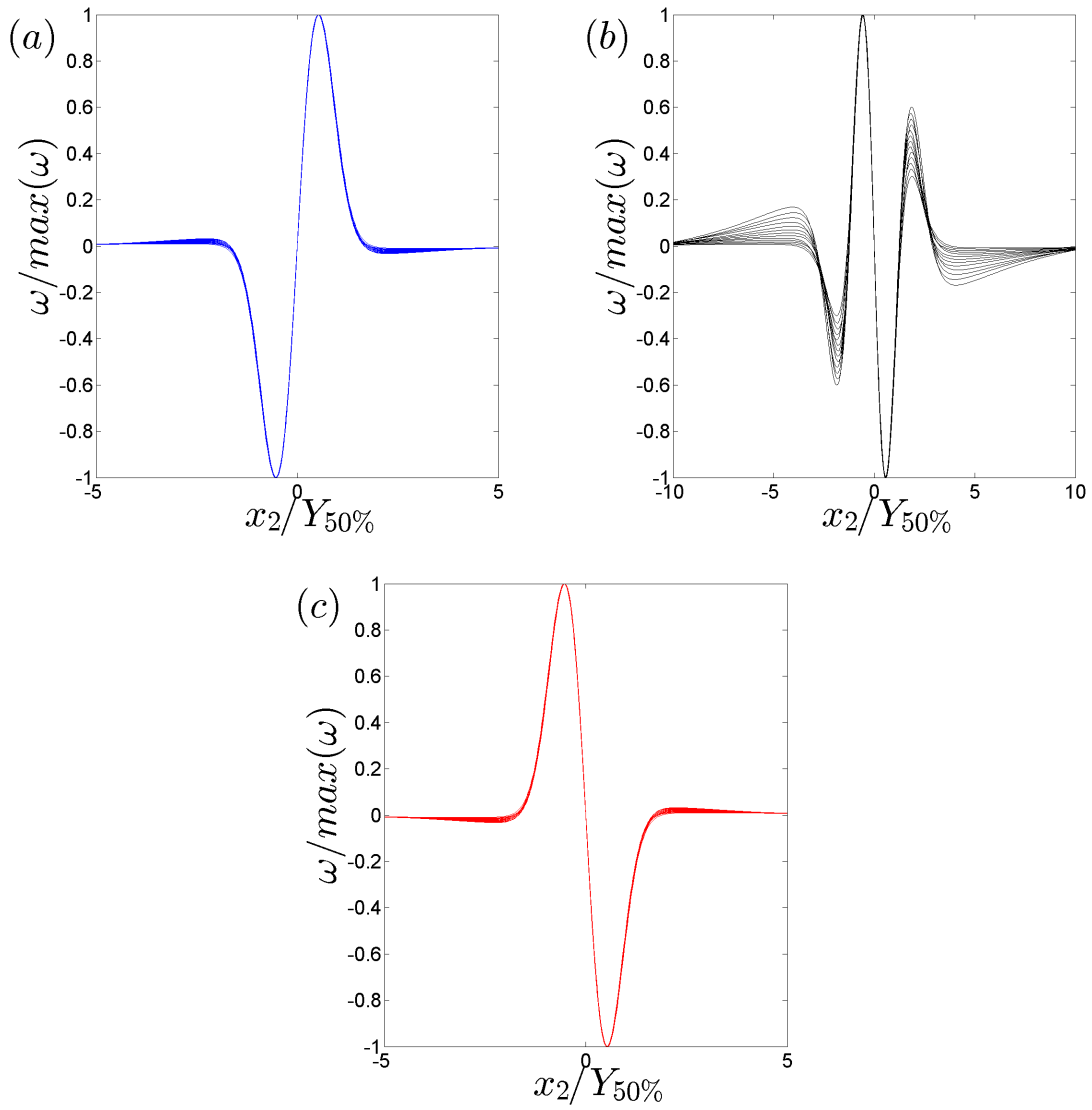

Figure E.1: $Re_T = 10$ vorticity fields across the width of a planar wake for (a) under-, (b) self- and (c) over-propelled cases. $Y_{50\%}$ corresponds to the point where 50% of the maximum vorticity value is observed.

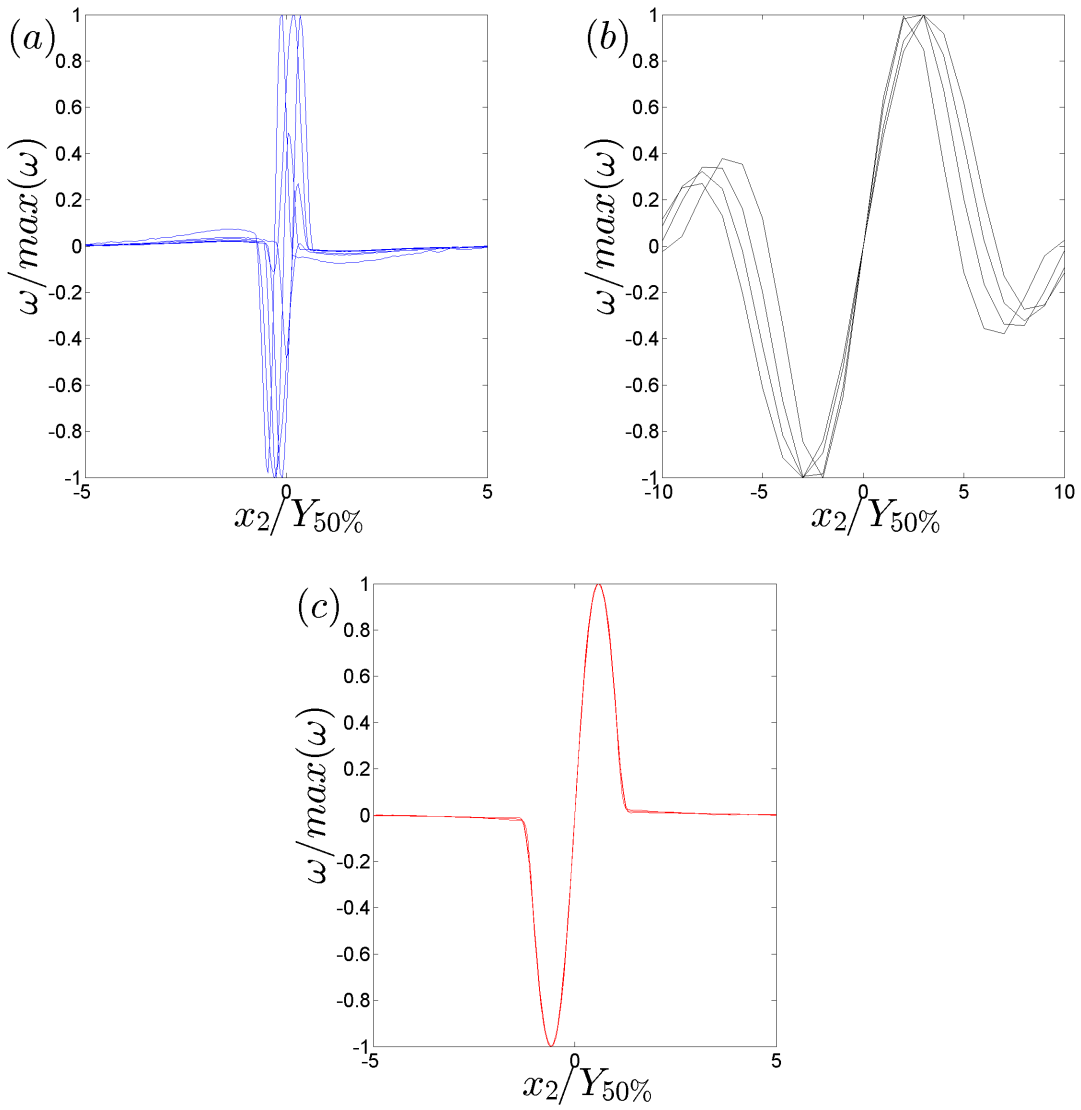

Figure E.2: SA turbulence model vorticity fields across the width of a planar wake for (a) under-, (b) self- and (c) over-propelled cases. $Y_{50\%}$ corresponds to the point where 50% of the maximum vorticity value is observed.

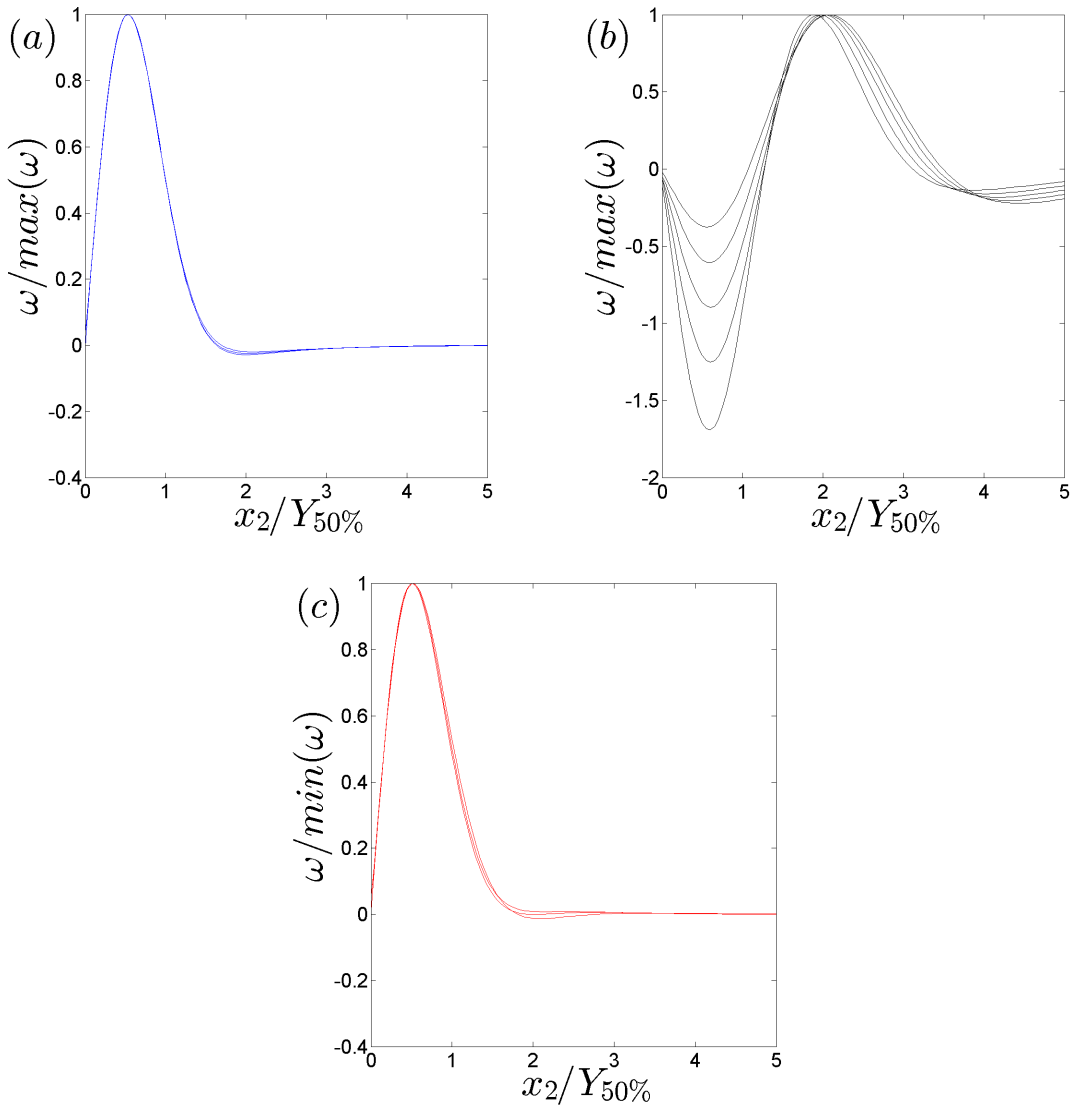

Figure E.3: $Re_T = 10$ vorticity fields across the width of a axisymmetric wake for (a) under-, (b) self- and (c) over-propelled cases. $Y_{50\%}$ corresponds to the point where 50% of the maximum vorticity value is observed.

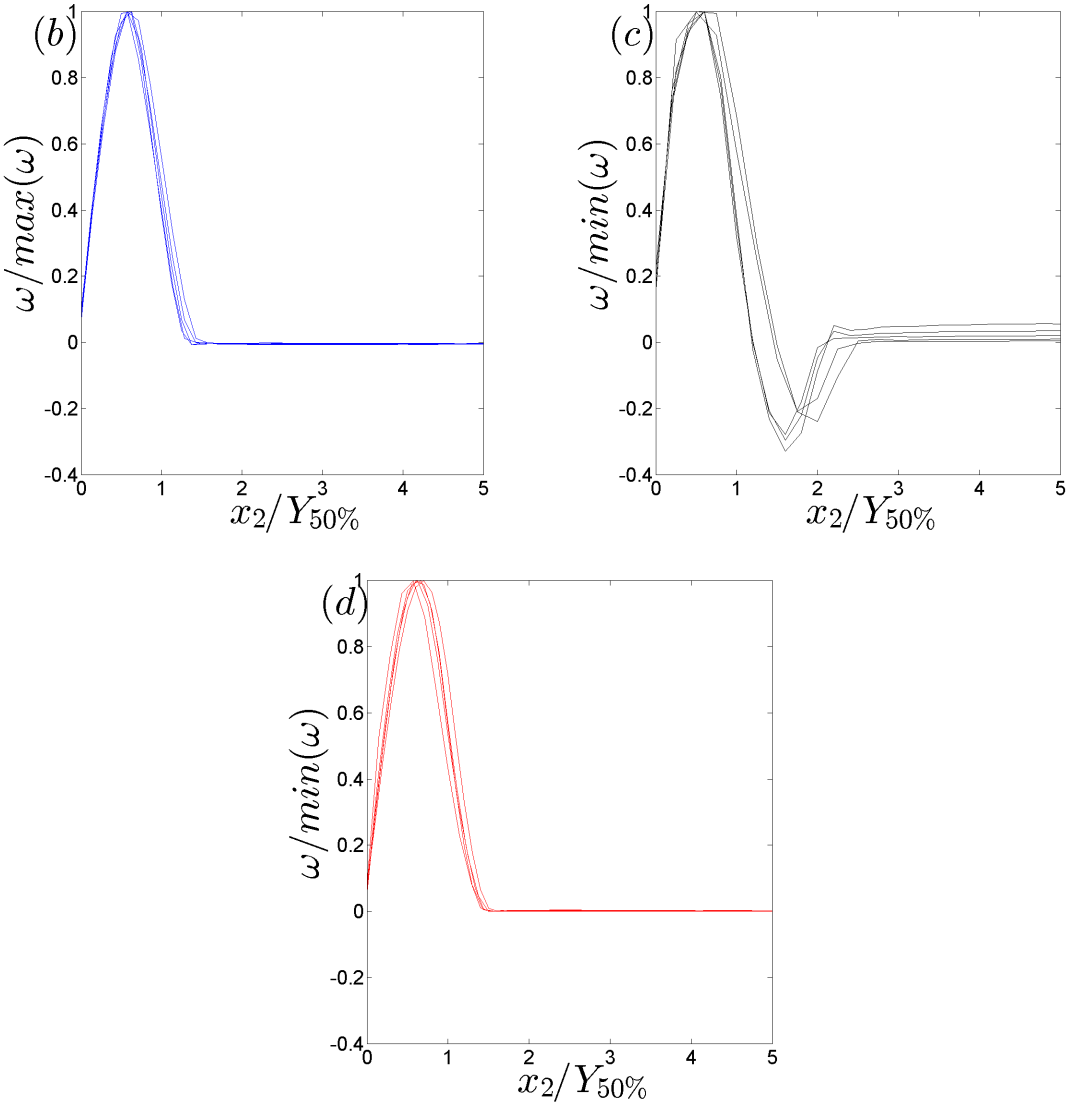

Figure E.4: $Re_T = 10$ vorticity fields across the width of a axisymmetric wake for (a) under-, (b) self- and (c) over-propelled cases. $Y_{50\%}$ corresponds to the point where 50% of the maximum vorticity value is observed.